4-2020

ACTIVATED CARBON NANOFIBERS FROM RENEWABLE (LIGNIN) AND WASTE RESOURCES (RECYCLED PET) AND THEIR ADSORPTION CAPACITY OF REFRACTORY SULFUR COMPOUNDS FROM FOSSIL FUELS

Efstratios Svinterikos

United Arab Emirates University

College of Engineering

ACTIVATED CARBON NANOFIBERS FROM RENEWABLE (LIGNIN) AND WASTE RESOURCES (RECYCLED PET) AND THEIR ADSORPTION CAPACITY OF REFRACTORY SULFUR COMPOUNDS FROM FOSSIL FUELS

Efstratios Svinterikos

This dissertation is submitted in partial fulfilment of the requirements for the degree of Doctor of Philosophy

Under the Supervision of Professor Mohamed H. Al-Marzouqi

April 2020

Declaration of Original Work

I, Efstratios Svinterikos, the undersigned, a graduate student at the United Arab Emirates University (UAEU), and the author of this dissertation entitled "*Activated Carbon Nanofibers from Renewable (Lignin) and Waste Resources (Recycled PET) and Their Adsorption Capacity of Refractory Sulfur Compounds from Fossil Fuels*", hereby, solemnly declare that this dissertation is my own original research work that has been done and prepared by me under the supervision of Professor Mohamed H. Al-Marzouqi, in the College of Engineering at UAEU. This work has not previously been presented or published, or formed the basis for the award of any academic degree, diploma or a similar title at this or any other university. Any materials borrowed from other sources (whether published or unpublished) and relied upon or included in my dissertation have been properly cited and acknowledged in accordance with appropriate academic conventions. I further declare that there is no potential conflict of interest with respect to the research, data collection, authorship, presentation and/or publication of this dissertation.

Student's Signature: _Efstratios Svinterikos_   Date: _27/04/2020_

Advisory Committee

1) Advisor: Mohamed H. Al-Marzouqi

Title: Professor

Department of Chemical & Petroleum Engineering

College of Engineering

2) Member: Nayef Mohamed Ghasem

Title: Professor

Department of Chemical & Petroleum Engineering

College of Engineering

3) Member: Md Monwar Hossain

Title: Associate Professor

Department of Chemical & Petroleum Engineering

College of Engineering

4) Member: Ioannis Zuburtikudis

Title: Professor

Department of Chemical Engineering

Abu Dhabi University, United Arab Emirates

Approval of the Doctorate Dissertation

This Doctorate Dissertation is approved by the following Examining Committee Members:

1) Advisor (Committee Chair): Mohamed H. Al-Marzouqi

   Title: Professor

   Department of Chemical & Petroleum Engineering

   College of Engineering

   Signature ___Mohamed AlMarzouqi___   Date ___27/04/2020___

2) Member: Basim Abu Jdayil

   Title: Professor

   Department of Chemical & Petroleum Engineering

   College of Engineering

   Signature _____   Date ___27/04/2020___

3) Member: Yaser Greish

   Title: Professor

   Department of Chemistry

   College of Science

   Signature _____   Date ___26/04/2020___

4) Member (External Examiner): Satish Kumar

   Title: Professor

   School of Materials Science and Engineering

   Institution: Georgia Institute of Technology, U.S.A.
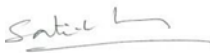
   Signature _____   Date ___26/04/2020___

This Doctorate Dissertation is accepted by:

Dean of the College of Engineering: Professor Sabah Alkass

Signature _____   Date __10/6/2020_____

Dean of the College of Graduate Studies: Professor Ali Al-Marzouqi

Signature _____   Date __June 11, 2020_____

Copy ____ of ____

Abstract

The development of advanced engineering materials such as carbon nanofibers from low-cost, renewable and/or waste resources is a key aspect of sustainability. In addition, escalating concerns related to the presence of noxious sulfur compounds in commercial fuels are driving the need to develop more efficient desulfurization technologies. In this PhD dissertation research, activated carbon nanofibers were produced from a blend of lignin with recycled poly(ethylene terephthalate) (r-PET) and they were successfully tested for the adsorption of refractory sulfur compounds from a model diesel fuel. Starting from different lignin/r-PET mass ratios, precursor nanofibers of different morphologies were initially prepared using the electrospinning technique. With the aid of a Design-of-Experiments statistical methodology, electrospun nanofibrous mats with a minimum average diameter of 80 nm were produced. The electrospun nanofibers were characterized with Differential Scanning Calorimetry, Attenuated Total Reflection-Fourier Transform Infrared Spectroscopy, Thermogravimetry and Scanning Electron Microscopy. Subsequently, electrospun precursor nanofibers consisting of different lignin/r-PET mass ratios and of varying average diameters were carbonized into carbon nanofibers (CNFs). It was discovered that the morphology of the CNFs depends on a synergy between the average fiber diameter and the lignin/r-PET mass ratio of the precursor electrospun nanofibers. These conditions were mapped and CNFs with average fiber diameter close to 100 nm were prepared. The CNFs were characterized using N_2 physisorption, Transmission Electron Microscopy, Raman spectroscopy, X-Ray Diffraction and Energy-Dispersive X-Ray Spectroscopy. Their structure consists mostly of disordered carbon, while the CNFs derived from 50/50 lignin/r-PET with ~400 nm average fiber diameter present the highest BET surface area (353 m^2/g). Their chemical activation with KOH boosted their BET surface area to 1413 m^2/g, while a further treatment with HNO_3 anchored oxygen functional groups on their surface. These activated CNFs (ACNFs) were tested for the adsorption of 4,6-dimethyldibenzothiophene (DMDBT) and of dibenzothiophene (DBT) from a model diesel fuel (n-dodecane). It was found that they exhibit a very high adsorption capacity (120.3 mg_{DMDBT}/g_C and 77.82 mg_{DBT}/g_C respectively), combined with remarkably fast adsorption kinetics. Therefore, the ACNFs have a great potential to be used as desulfurization adsorbents.

Keywords: Carbon Nanofibers, Lignin, Recycled PET, Electrospinning, Adsorption, Refractory Sulfur Compounds, Desulfurization.

Title and Abstract (in Arabic)

ألياف الكربون النانوية المنشطة من الموارد المتجددة (اللجنين) وموارد النفايا (PET) المعاد تدويرها وقدرتها على امتصاص مركبات الكبريت الحرارية الناتجة عن الوقود الأحفوري

الملخص

يعد تطوير المواد الهندسية المتقدمة مثل ألياف الكربون النانوية من الموارد منخفضة التكلفة والمتجددة أو من النفايات جانبًا رئيسيًا في الاستدامة. بالإضافة إلى ذلك، المخاوف المتزايدة المتعلقة بوجود مركبات الكبريت الضارة في الوقود التجاري تدفع الحاجة إلى تطوير تقنيات أكثر كفاءة لإزالة الكبريت. في بحث أطروحة الدكتوراه، تم إنتاج ألياف الكربون النانوية المنشطة من مزيج من اللجنين مع بولي (إيثيلين تيريفثاليت) المعاد تدويره (r-PET) وتم اختبارها بنجاح لامتصاص مركبات الكبريت الحرارية من وقود الديزل النموذجي. بدءاً من نسب كتلة اللجنين/-r PET المختلفة، تم تحضير ألياف النانو السلائف من أشكال مختلفة في البداية باستخدام تقنية الدعم الكهربائي. بمساعدة منهجية إحصائية لتصميم التجارب، تم إنتاج حصائر ليفية متناهية الصغر بقطر متوسط يبلغ 80 نانومتر على الأقل. تميزت ألياف النانو الكهربائية مع قياس المسعر التفاضلي بالمسح الضوئي، الانعكاس الكلي الموهن-التحليل الطيفي للأشعة تحت الحمراء لتحويل فورييه، قياس الحرارة الحراري، الفحص المجهري الإلكتروني. في وقت لاحق، تم تفحيم ألياف النانو التي تتكون من نسب كتلة مختلفة من اللجنين، r-PET وبأقطار متفاوتة بأقطار متناهية الصغر إلى ألياف نانوية كربون. لقد تم اكتشاف أن تشكل CNFs يعتمد على التآزر بين متوسط قطر الألياف ونسبة كتلة اللجنين r-PET. تم تعيين هذه الشروط وتم إعداد CNFs بقطر ليفي متوسط يصل إلى 100 نانومتر. تميزت CNFs باستخدام N$_2$ (physisorption) المجهر الإلكتروني للإرسال، مطياف رامان، حيود الأشعة السينية وطيفي الأشعة السينية المشتتة من الطاقة. يتكون هيكلها في الغالب من كربون مضطرب، في حين أن مركبات الكربون النانوية (CNF) المشتقة من 50/50 اللجنين مع قطر ألياف يبلغ متوسطه حوالي 400 نانومتر تمثل أعلى مساحة سطحية (353 م^2/ جم). تم تعزيز مساحة سطح BET الخاصة بهذه المركبات إلى 1413 m^2/ جم عن طريق تنشيطها كيميائياً مع KOH في حين أن هناك علاجًا إضافيًا باستخدام مجموعات وظيفية من الأكسجين المرتبط HNO$_3$ على سطحها. تم اختبار هذه CNFs المنشط (ACNFs) لامتصاص 4،6-ثنائي ميثيل ديبنزوثيوفين (DMDBT) و dibenzothiophene من وقود الديزل نموذج (ن).

(n-dodecane) وقد وجد أنها تتميز بقدرة امتصاص عالية جدًا (120.3) ملغم/ديسيلتر g.C و 77.82 ملغ ديسيبل/غم على التوالي، بالإضافة إلى حركية امتزاز سريعة بشكل ملحوظ. لذلك، فإن ACNFs لديها إمكانات كبيرة لإستخدامها كمادة إزالة الكبريت.

مفاهيم البحث الرئيسية: ألياف الكربون النانوية، اللجنين، PET المعاد تدويره، الإلكتروسبين، الإدمصاص، مركبات الكبريت الحرارية، إزالة الكبريت.

Acknowledgements

issues arising. I also want to thank Botagoz Zhuman who helped me with some of my experiments at Khalifa University.

Special thanks to my fellow students and to my friends here in the UAEU with whom I spent many wonderful moments the last 5.5 years.

Last but not least, words are poor when it comes to express my gratefulness to my family and friends in Greece.

Dedication

To my beloved family and friends

Table of Contents

List of Tables

List of Figures

List of Abbreviations

ACNFs	Activated Carbon Nanofibers
ATR-FTIR	Attenuated Total Reflection-Fourier Transform Infrared Spectroscopy
BET Surface Area	Brunauer Emmett Teller Model for Specific Surface Area
C12	n-Dodecane
CA	Cellulose Acetate
CNFs	Carbon Nanofibers
DBT	Dibenzothiophene
DMDBT	4,6-Dimethyldibenzothiophene
DSC	Differential Scanning Calorimetry
EDS	Energy Dispersive X-Ray Spectroscopy
FWHM	Full Width at Half Maximum (for XRD Diffractograms)
PAN	Poly(Acrylonitrile)
PEO	Poly(Ethylene Oxide)
ppm	Parts Per Million
PVA	Poly(Vinyl Alcohol)
PVP	Polyvinylpyrrolidone
r-PET	Recycled Poly(Ethylene Terephthalate)
SEM	Scanning Electron Microscopy
TEM	Transmission Electron Microscopy
TGA	Thermogravimetry
XRD	X-Ray Diffraction

Nomenclature

A	Collision Frequency Factor, $[g_C/(mg_{DMDBT} \cdot min]$
C_e	Equilibrium Concentration, mg_{DMDBT}/kg_{C12} or mg_{DBT}/kg_{C12}
C_{id}	Intercept of the Intraparticle Diffusion Model, mg_{DMDBT}/g_C
$d_{(002)}$	Average Interlayer Distance of sp^2-Carbon Layers, nm
E_a	Activation Energy, kJ/mol
g_C	Grams of Carbon (Mass of Adsorbent), g
k_1	Rate Constant of the Pseudo-First Order Model, min^{-1}
k_2	Rate Constant of the Pseudo-Second Order Model, $[g_C/(mg_{DMDBT} \cdot min)]$ or $[g_C/(mg_{DBT} \cdot min)]$
K_e	Dimensionless Equilibrium Constant for Adsorption
K_F	Freundlich Constant Related to the Adsorption Capacity, $[(mg_{DMDBT}/g_C)/(mg_{DMDBT}/kg_{C12})^{1/n}]$ or $[(mg_{DBT}/g_C)/(mg_{DBT}/kg_{C12})^{1/n}]$
k_{id}	Rate Constant of the Intraparticle Diffusion Model, $[mg_{DMDBT}/(g_C \cdot (min^{0.5}))]$
K_L	Langmuir Constant, kg_{C12}/mg_{DMDBT} or kg_{C12}/mg_{DBT}
K_{LF}	Langmuir-Freundlich Constant Related to the Adsorption Capacity, $[(mg_{DMDBT}/g_C)/(mg_{DMDBT}/kg_{C12})^{1/n}]$
L_a	Size of ab Plains of the Graphitic Domains, nm
L_c	Crystallite Size Along the c-Axis of the Graphitic Domains, nm
mg_{DMDBT}, mg_{DBT}, mgS	Milligrams of DMDBT, DBT or Sulfur Respectively, mg
M_w	Molecular Weight, g/mol
N_c	Average Number of Graphene Layers in Each Graphitic Crystallite, Dimensionless

n_F	Freundlich Constant Related to the Adsorption Intensity, Dimensionless
n_{LF}	Langmuir-Freundlich Constant Related to the Surface Heterogeneity, Dimensionless
q_e	Equilibrium Adsorption Capacity, mg_{DMDBT}/g_C or mg_{DBT}/g_C
q_{m-L}	Maximum Adsorption Capacity Predicted from the Langmuir Isotherm, Mg_{dmdbt}/G_c Or Mg_{dbt}/G_c
q_{m-LF}	Maximum Adsorption Capacity Predicted from the Langmuir-Freundlich Isotherm, mg_{DMDBT}/g_C or mg_{DBT}/g_C
q_t	Adsorbed Quantity at Time t, mg_{DMDBT}/g_C or mg_{DBT}/g_C
R	Ideal Gas Constant, 8.314 J/(K*mol)
T	Temperature, ^{o}C
t	Time, min
T_{cc}	Cold Crystallization Temperature, ^{o}C
T_g	Glass Transition Temperature, ^{o}C
T_m	Melting Temperature, ^{o}C
wt%	Weight%
ΔG^{o}	Standard Gibbs Free Energy Change, kJ/mol
ΔH^{o}	Standard Enthalpy Change, kJ/mol
ΔS^{o}	Standard Entropy Change, kJ/(K*mol)
θ	Diffraction Angle, $(^{o})$
λ	Wavelength During the XRD Measurements, nm

Chapter 1: Introduction

1.1 Overview

Sustainability has emerged as an issue of immense importance that will determine the prosperity of future generations. Based on the demand for sustainable growth, as well as due to the gradual depletion of natural resources, a significant part of the research and development in academia and in the industry is shifting towards the utilization of waste or renewable resources for the development of new, advanced engineering materials. This concept has been the main motivation behind this PhD dissertation research, which describes the production of activated carbon nanofibers from a blend of lignin with recycled PET and their successful application in the adsorption of refractory sulfur compounds from fossil fuels.

Carbon nanofibers (CNFs) are a one-dimensional form of carbon with diameters in the submicron- and in the nano-scale, which carry an array of interesting properties that render them suitable for a variety of applications, such as in energy storage devices, for adsorption and catalysis and as electrodes of dye-sensitized solar cells [1, 2]. Their most striking feature is their very small diameter which translates into a very large external surface area per unit mass (the external surface of the fibers). Their surface can relatively easily be functionalized or doped with metals, according to a desired application. Moreover, activated carbon nanofibers (ACNFs) combine the advantages of CNFs with the very high porosity of activated carbon. However, an important limitation related to CNFs is that their most common precursor is poly(acrylonitrile) (PAN) [3], a relatively expensive petroleum-based polymer, the cost of which limits their more widespread use [4]. Therefore, alternative CNF precursors have been proposed, the most important of which is lignin.

Lignin is the second most abundant natural polymer of Earth behind cellulose [5]. It is a relatively low-cost biorenewable polymer which is obtained as a waste by-product of the paper industry, while it can also be extracted from agricultural waste [6]. Its complex structure, which depends on the plant source and the method of extraction, hinders its widespread use; it has been estimated that only 2% of the annual lignin quantity extracted from the paper industry is commercialized [6, 7]. However, lignin shows a great potential for being used as carbon nanofiber precursor [3].

Poly(ethylene terephthalate) (PET) is one of the most common commodity polymers and a major component of municipal waste. As the global consumption of plastics rises annually by 5-6% [8], the development of alternative uses of the plastic waste, and especially of recycled PET (r-PET), will be instrumental in upgrading the municipal waste management.

Therefore, the combination of an abundant natural polymer (lignin), the large potential of which is still unexploited, with a major municipal waste (PET) can provide an alternative low-cost precursor for the manufacture of CNFs.

In addition, significant environmental issues are increasing the need for cleaner fuels. Sulfur compounds existing in fossil fuels pose an important environmental concern as they contribute to air pollution and they are related to detrimental health issues. Over the last 10 years the competent authorities in most developed countries, including the U.A.E., have introduced stringent regulations which limit the content of sulfur in automobile fuels to 10-15 ppm [9-11]. Nevertheless, the long-standing industrial catalytic hydrodesulfurization is very energy consuming as it takes place at high temperatures and pressures, and it is not very efficient for removing the heavier aromatic sulfur compounds [12, 13]. These compounds, such as dibenzothiophene

(DBT) and 4,6-dimethyldibenzothiophene (DMDBT) are termed as refractory sulfur compounds [12].

Hence, there is a need to develop alternative ways to upgrade the industrial desulfurization practice, in order to achieve the more efficient removal of these refractory sulfur compounds. For this purpose, adsorptive desulfurization at ambient conditions is a very promising process [13]. In this PhD dissertation research, activated CNFs are produced from lignin/r-PET and they are proposed as desulfurization adsorbents. The work presented in this dissertation is schematically outlined in Figure 1.1.

1.2 Research objectives

On the basis of the above-mentioned problems, the objectives of this PhD dissertation research are the following:

i) The preparation of precursor nanofibers from lignin/recycled PET using a well-established nanomanufacturing technique, the electrospinning.

ii) The investigation of the electrospinning process conditions that minimize the average fiber diameter of the electrospun fibers, and the characterization of these nanofibers.

iii) The carbonization of the electrospun nanofibers, in order to transform them into CNFs. The investigation of the process conditions that yield well-formed filamentous carbon structures and the characterization of the CNFs.

iv) The activation of the CNFs in order to raise their porosity.

v) The application of activated CNFs (ACNFs) for the adsorption of refractory sulfur compounds from a model fossil fuel. The calculation of their adsorption capacity and the assessment of their potential as desulfurization adsorbents.
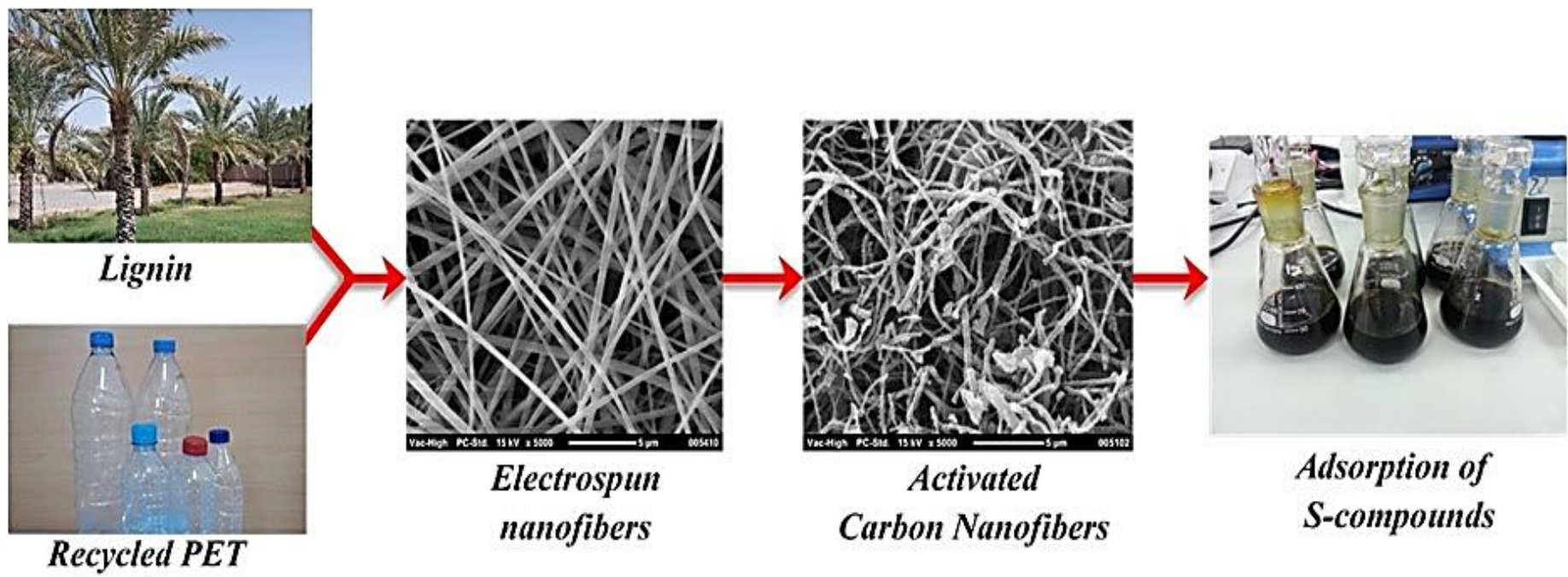
Figure 1.1: Graphical outline of the dissertation

1.3 Organization of the dissertation

This dissertation consists of six chapters.

In this chapter (Chapter 1), a brief introduction to the subject of this PhD dissertation was presented, the research problems were analyzed and the research objectives were stated.

Chapter 2 presents a literature review on the subject of CNFs. Particularly, the structure, properties and applications of CNFs are analyzed, the electrospinning technique is described, and the structure, properties and extraction methods of lignin are presented. Moreover, a complete literature summary of the state-of-the-art related to lignin-based electrospun CNFs is presented and analyzed.

The problems arising from the presence of sulfur compounds in fossil fuels are delineated in Chapter 3. In addition, the current industrial practice is presented, together with its limitations, and the alternative methods proposed. Applications of CNFs related to adsorptive desulfurization are also presented.

Chapter 4 is the experimental part of this research, in which sufficient details about the research methodology are given.

Chapter 5 is the "results and discussion" part of this dissertation. This chapter is divided in four sections. In the first Section (5.1), the fabrication of electrospun lignin/r-PET nanofibers is presented, together with characterization of their morphology, structure and thermal properties. In the second Section (5.2), the carbonization process is outlined, and the mapping of conditions that lead to a well-formed filamentous morphology is presented. In the third Section (5.3) the CNFs are characterized in terms of their BET surface area and their structure. Also, the activation process is presented here, together with the morphology and the textural properties of

the ACNFs. In the fourth Section (5.4), the adsorption results are presented for the removal of DBT and DMDBT from a model diesel fuel (n-dodecane).

Finally, Chapter 6 presents the conclusions. The major findings are summarized and analyzed together with recommendations for future research in this field.

Chapter 2: Lignin-Based Electrospun CNFs: Literature Review

2.1 Carbon nanofibers: structure, properties and applications

An overview of the structure of the CNFs is presented in the following paragraphs, together with their porosity characteristics and their applications.

2.1.1 Morphology and structure

Carbon materials have revolutionized the materials science in the last few decades and they are projected to be at the forefront of emerging technological advances. Carbon nanofibers (CNFs), a one-dimensional form of carbon, belong to this class of materials and they show a promising potential for a wide range of engineering applications. While conventional carbon fibers have typically diameters of few micrometers up to few tens of micrometers, CNFs have diameters in the range between few tens of nanometers up to submicron values. A strict definition would require the use of the prefix "nano-" for dimensions up to 100 nm, however, the term "nanofibers" is commonly encountered in the literature for fibers with diameters of up to few hundreds of nanometers [3]; here, this convention will be followed. In applications where the surface area is important, lowering the average diameter to this range is highly beneficial.

The morphology of CNFs is characterized by a continuous network of long carbonaceous filaments which usually have a varying degree of interconnection (Figure 2.1). Unlike carbon nanotubes (CNT) which consist of perfectly wrapped concentric graphene layers, the structure of CNFs is more random, although it mainly consists of sp^2-hybridized carbon, as well [3]. Their structure comprises graphitic regions, which have a higher degree of order consisting of stacked graphene layers

(graphitic regions), and more disordered regions with randomly oriented defective graphene layers [3, 14]. The degree of order depends on the method of production and on the precursor materials [2, 3].
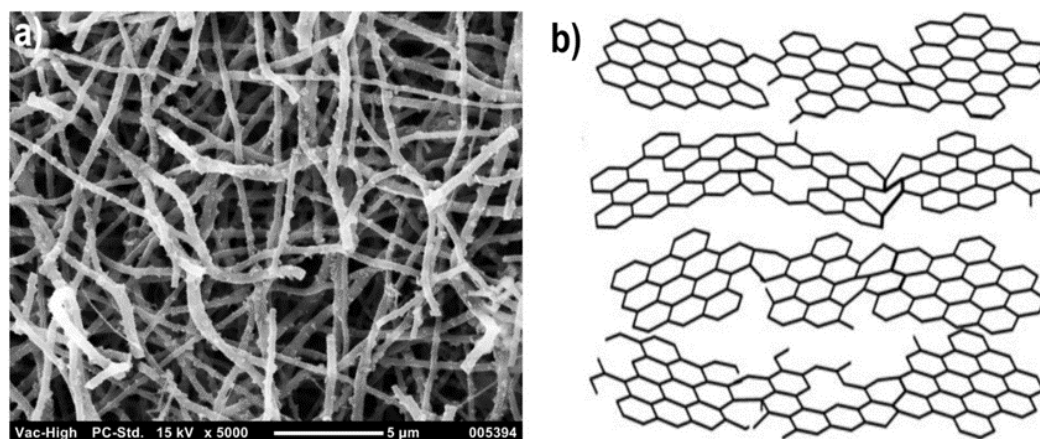
Figure 2.1: Morphology and structure of CNFs; a) SEM image of lignin-based electrospun CNFs (image taken during this research); b) the stacking of defective graphene layers constituting the structure of CNFs [14]

The structure of CNFs is typically examined via X-ray diffraction (XRD) and Raman spectroscopy. The domains of disordered graphene layers in carbonaceous materials are sometimes termed as "turbostratic", although this term has been criticized (see [15] for a thorough discussion on this issue). Figure 2.1b presents a model for the stacking of defective graphene layers in the structure of carbon fibers (adapted from [14]). These layers comprise regions which have a perfect hexagonal structure (the stacking of which builds the graphitic regions) and others in which the graphene layers are flawed (containing 5- or 7-carbon rings, open rings, etc). These defects induce curvature which disrupts the parallel stacking of graphene layers, forming disordered regions resembling the shape of crumpled paper (see [16] for a detailed discussion about these structures). The disordered regions contain more unoccupied space, which translates into higher porosity [16].

2.1.2 Fabrication methods

CNFs are mainly fabricated using the following methods:

a) Chemical vapor deposition (CVD): according to this method, CNFs are produced from the decomposition of gaseous hydrocarbon precursors (such as CH_4, C_2H_6, C_2H_2, etc.) in the presence of metal catalysts inside a reactor [2, 3, 17]. This process is performed at high temperatures (700-1200 K) [2, 3]. The catalysts used in this case are metal nanoparticles consisting of Ni, Co, Fe, or various alloys [2, 3, 17]. As the gases are heated until they decompose, C atoms precipitate on the catalyst surface and develop graphitic filamentous structures [2, 3]. Their diameter ranges from few tens to few hundreds of nanometers, while their length from less than a micron till few millimeters [17]. The shape of the graphitic structure (e.g. platelet-stacked or cup-stacked) is determined by the type of catalyst used [2]. The CNFs produced with this method have excellent thermal conductivities, however their production cost is rather high [3].

b) Spinning: Carbon fibers, with diameters higher than 5 μm, are traditionally fabricated from a polymeric precursor using a spinning technique, such as wet spinning, gel spinning, dry spinning or melt spinning [3]. In all these techniques, the precursor polymer is initially formed into fibers, followed by their thermal treatment at high temperatures (>600°C) under inert atmosphere [2, 3]. In the melt spinning technique, the precursor polymer is heated until it melts and then it is drawn through a spinneret for the formation of microfibers. In the other techniques, the polymer is dissolved in a suitable solvent and then it is ejected through a spinneret [3]. The fiber diameters are adjusted via the spinneret size and the drawing speed.

Nevertheless, these techniques are not suitable for producing nanometer-sized carbon fibers. Instead, the most suitable method for this purpose is electrospinning, which is a variation of dry spinning. As CNFs are the main topic of this review, the electrospinning technique and the polymer precursors used for their manufacture will be described in more details in Section 2.2.

Besides these two techniques, template-based strategies and biomass methods have also been reported for the preparation of CNFs. These, however, are beyond the scope of this review; further information about them can be found in [2].

2.1.3 Properties and applications

The main advantage of CNFs is their very small diameter which translates into a very high aspect ratio (over a few hundreds) and into a very high specific surface area [3]. They can also be thermally or chemically treated in order to increase their porosity and their BET surface area to values as high as 2500 m^2/g [3]. Their large surface area can facilitate the doping with metals or metal oxides and, thus, enhance their applicability. Moreover, their surface can relatively easily be functionalized in order to introduce functional groups and alter their surface properties and their dispersion in various matrices [1, 3]. CNFs possess good flexibility and mechanical strength depending on the degree of order of their microstructure, which in turn is dependent on the choice of the precursor and the fabrication method [17]. Their tensile strength can reach values of up to 4.8 GPa, which, however, is an order of magnitude less than that of carbon nanotubes [1, 17]. These factors also influence their electrical conductivity which can vary significantly from 10^{-7}-10^3 S/cm [3]. Defects in their structure lower their crystallinity, but this can be advantageous in applications related to energy storage as their energy density is enhanced through higher charge storage in

these defects [3]. Moreover, although they generally have lower thermal conductivity (<1600 W/(mK)) compared to carbon nanotubes (2000-6000 W/(mK)), they possess the advantages of easier dispersion and lower fabrication cost [3, 17].

Due to their high specific surface area, chemical resistance and thermal stability, CNFs have successfully been used in catalysis (catalyst support) [1], as adsorbents for the removal of sulfur compounds from fuels [18, 19], for air and water purification [1], in biomedical applications, e.g. as templates for cell growth [1], for polymer-based nanocomposites [1, 3], in dye-sensitized solar cells, in sensors [1] and in energy storage applications, particularly as electrodes for lithium-ion batteries, sodium-ion batteries and supercapacitors [2, 3, 20, 21].

2.2 Electrospinning for nanofiber manufacturing

The main features of the electrospinning technique, which was used in this research, are described in the following sections.

2.2.1 The electrospinning technique

Electrospinning is a well-established technique for the fabrication of micro- and nanosized polymer fibers. Although it was first patented in 1934, it has received greater attention since the 1990's and it has also been applied at industrial level [17].

In contrast to other fiber-spinning techniques such as melt spinning or dry spinning, which rely on mechanical forces to produce fibers by drawing the polymer through a spinneret, this technique relies on electrostatic forces [17]. A typical setup of the process is presented in Figure 2.2 (the setup can have either vertical or horizontal orientation) [1].
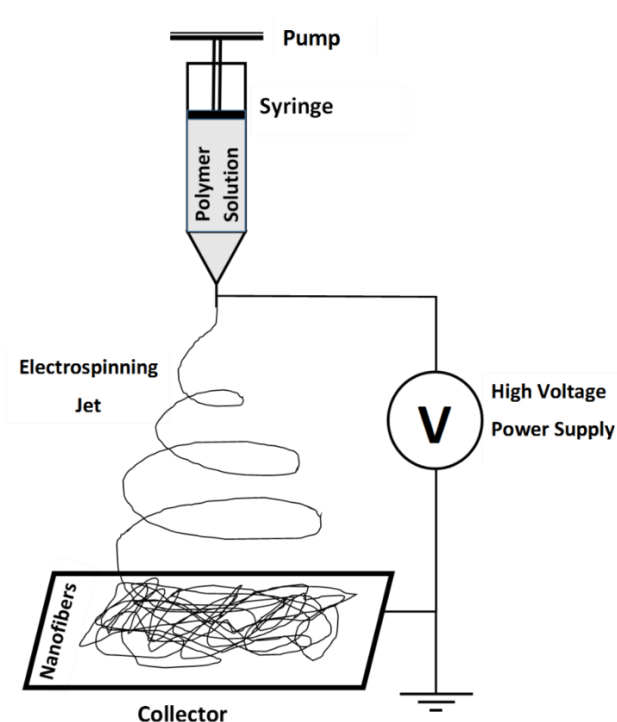
Figure 2.2: Typical electrospinning setup with vertical orientation

The polymer or the blend of polymers is initially dissolved into an appropriate solvent and loaded into a syringe which is connected to a pump offering a controlled flow rate. The metallic needle of the syringe is connected to a metallic collector through a high-voltage power supply. As the polymer solution is pumped through the needle, it is subjected to the electrostatic force from the electric field between the syringe and the collector. The shape of the pendant polymer droplet is, then, transformed into a cone (termed as the "Taylor cone"). When the electrostatic force overcomes the surface tension of the polymer solution, a jet is formed, which immediately breaks into a number of smaller jets. These jets follow looping trajectories and fall on the collector. During the ejection, the solvent evaporates and the jet is transformed into polymer fibers, which are usually solid and smooth [22]. In a typical setup, the fibers are randomly oriented and they form a nonwoven mat. However, variations of the collector allow the formation of aligned fibers (e.g. using a rotating

drum) [3, 22]. Other variations of the setup allow the formation of core/shell structured fibers, in which the core polymer is different from the shell polymer, or hollow fibers [3, 22].

The fiber morphology is influenced by various process and material parameters. The most important of them are discussed in the following lines.

a) Solution concentration and viscosity: The solution concentration increases the solution viscosity, which in turns results in higher average fiber diameters [3, 17]. When the concentration is below a certain point, the viscosity is too low, and then the jets breaks easily into droplets. In this case, many spherical beads form during the spinning, resulting in "beads-on-strings" morphology, or only beads (electrospray) [3, 17]. Therefore, a sufficiently high concentration is needed for bead-free fibers. At very high concentrations, however, the continuous flow is disrupted.

b) Molecular weight of the polymer: The longer the chain length, the higher the molecular weight of the polymer is [17]. This translates into more chain entanglements, resulting in higher average diameters and fewer beads [17]. When the polymer molecular weight is too low, then there is electrospray instead of fiber formation. This is a very usual case for lignin. Therefore, a high-MW polymer (binder polymer) is added to the lignin solution to increase its spinnability [23, 24].

c) Solvent boiling point: A low boiling point is preferable for fast evaporation and dry fiber formation [17]. Nevertheless, a too volatile solvent can solidify in the needle and block it [3]. Moreover, the solvent evaporation affects the viscoelastic properties of the jet; fast evaporation results in a higher viscoelastic force, which in turn prevents the jet from stretching further. This produces fibers of larger diameters, as it has been reported in the case of polystyrene in tetrahydrofuran (boiling point 66°C) vs. polystyrene in dimethylformamide (boiling point 153°C) [17].

d) Surface tension: In most cases, it is better if the surface tension is kept rather low, so that a very high voltage is not necessary for the fiber formation [3]. Hence, the choice of solvent should be the appropriate one. Moreover, when the surface tension is low the formation of beads is avoided [3]. However, exceptions to this rule have been reported [17].

e) Electrical conductivity: It has been reported that the addition of salts into the solution produces finer, beadless fibers [17]. This is the result of higher elongational forces acting on the jet inside the electrostatic field [17].

f) Temperature: This parameter influences the viscosity of the solution and the evaporation of the solvent. As an example, better spinnability of polyurethane fibers at relatively high temperature (70°C) has been reported [17]. Nevertheless, there is no universal rule in this case.

g) Humidity: This is another important factor which affects the evaporation of the solvent. High humidity translates into slower evaporation, which in turn prevents the viscosity of the jet from increasing abruptly. On the other hand, high humidity can affect the charge density on the fiber surface [17]. Moreover, when more wet fibers are deposited on the collector, the slower evaporation can leave behind pores or a rough surface [17].

h) Applied voltage: The electrostatic force acting on the jet is influenced by the applied voltage. There is a voltage threshold above which the fiber formation is successful, and this depends on the surface tension and the viscosity of the solution [3]. In most cases a higher voltage results in thicker fibers [17]. The voltage, usually, varies between 15-30 kV.

i) Spinning distance: Similar to the voltage, the spinning distance controls the electrostatic force. Here the effect is not always clear; at a constant voltage, larger

distance means weaker electrostatic field. However, in this case the jet has more time to stretch and dry [17]. Therefore, the effect is not always the same.

j) Flow rate: Various reports have stated that larger fiber diameters are produced at higher flow rates, because of the speed with which the jet travels towards the collector [3, 17]. At higher flow rates, higher voltage is required, as well [3]. The flow rate values for continuous fiber formation are, however, unique for each system.

There is a vast variety of more than 100 polymers which have been processed via electrospinning [22]. The popularity of this technique is justified by a number of advantages, such as its simple setup, the easiness in controlling the fibrous morphology by simply adjusting the process parameters and the huge variety of polymers or polymer blends that can be used. Furthermore, it is a versatile technique since interesting variations have been developed, e.g. different configurations for producing core/shell or hollow fibers, the production of composite fibers by incorporating micro- or nano-sized fillers, multichannel structures, aligned fibers, or even the fabrication of ceramic fibers [25, 26]. The most important drawbacks of this technique are the use of harmful solvents and sometimes the viability of scaling up at industrial level, especially when low concentrations or low flow rates have to be used. Electrospun nanofibers have been used in diverse applications including the manufacture of filters, in biomedical applications (tissue scaffolds), for sensors, in electrochemical applications (electrodes, photovoltaic devices, etc), in controlled drug delivery, in protective clothing and as reinforcing fibers in composites [17, 26].

2.2.2 Manufacturing electrospun-based CNFs

In addition to the applications mentioned in the previous section, electrospun nanofibers made of certain precursors are used for the fabrication of CNFs. Despite

the variety of polymers processed via electrospinning, only a few of them have been used as precursors for the preparation of CNFs, that is, polyacrylonitrile (PAN), lignin, pitch, polyimide (PI), poly(vinylidene fluoride) (PVDF), polyvinyl alcohol (PVA) and more recently cellulose acetate [3, 25, 27, 28]. The reason is that the precursor must satisfy some criteria in order to be carbonizable to CNFs. The most important is that it should not melt when heated at very high temperatures (above 800°C), or at least that it can undergo some thermal or chemical treatment to become infusible during heating [29]. In this context, polymers containing heteroatoms (N, O, S, P, halogens), double bonds and aromatic rings in their chains are more appropriate [29]. Furthermore, the polymer must dissolve into an electrospinning-appropriate solvent and it should give a considerable carbon yield. PAN is the most common polymeric precursor for CNFs because it gives a high carbon yield (>50%) and it produces CNFs with very good mechanical properties [3]. It can only be carbonized after it is first thermo-stabilized through heat treatment in air at 200-280°C.

Lignin-based electrospun CNFs were first reported in 2007, although the production of lignin-derived carbon microfibers using other methods had previously been reported [30]. Details about the properties and the structure of lignin can be found in Section 2.3. Although a few research groups have reported the successful electrospinning of lignin alone and its carbonization into CNFs [30-35], in most cases the electrospinning of lignin yields spray instead of fibers. Therefore, the presence of another polymer of higher MW is necessary in the electrospinning solutions. This is usually PAN, PVA or PEO (polyethylene oxide).

Moreover, in order to prevent the lignin-based electrospun mats from melting and losing their fibrous morphology, they are first subjected to a stabilization step. During this stage, the precursor nanofibers are heated at a very slow rate (usually

$<1^{o}$C/min, depending on the lignin type) under oxidative atmosphere (air) until they reach temperatures between 200-280°C, where they are kept for a few hours. Detailed stabilization and carbonization conditions for every lignin-based electrospun CNFs found in the literature is presented in Table 2.1. This process can be very time-consuming (sometimes lasting for days) and it is a drawback for industrial scale-up; however, the slow heating is necessary for effective diffusion of O_2 into the bulk of the fibers [33]. During this step, oxygen-containing functional groups (carbonyl, carboxyl, ester groups) are incorporated into the lignin macromolecules and cross-linking reactions take place [30]. This procedure raises the T_g of lignin significantly and it prevents the fusion among the fibers [30]. It should be noted, however, that some degree of fusion among the fibers is desirable in many cases. Interconnected fibers exhibit better mechanical properties, increased electrical conductivity and enhanced performance in electrochemical applications [36, 37]. In rare cases the stabilization can be totally omitted [21].

After the fibers have been stabilized, they are carbonized for their transformation into CNFs. During this process, the nanofibers are heated under inert atmosphere (N_2 or Ar) until they reach a temperature between 600-1200°C, where they are kept for ~1 hour in most cases. Detailed carbonization conditions can be found in Table 2.1. Here, the fibers decompose slowly and release volatile products (H_2, CH_4, H_2O, CO, CO_2, phenolic compounds), while their structure is transformed into sp^2-hybridized carbon as described in the previous sections. After the carbonization, a step of activation is optionally added, for increasing the porosity of CNFs. The activation can be either chemical (e.g. treatment with KOH or NaOH) or physical (heating under CO_2 or steam) (see Table 2.1).

2.3 Lignin: structure, extraction methods and properties

Lignocellulosic biomass extracted from plants is considered the most promising biorenewable carbon-containing resource on earth. This biomass consists of cellulose (35-83% dry weight basis), lignin (1-43% dry weight basis) and hemicellulose (0-30% dry weight basis). The relative content of each of these three components depends on the plant source [6].

Lignin is the second most abundant natural polymer on Earth after cellulose, accounting for around 30% of the organic carbon existing in the biosphere, while it is the main biorenewable source of aromatic structures [5, 38]. Its main function as a structural component in the plants is to inhibit the diffusion of enzymes or solutions into the wood, rendering the cell walls stronger and more rigid [6, 39].

The structure of lignin is complex and amorphous, as it is highly branched [5, 39]. It is constructed from the polymerization of three phenylpropane monomers (coniferyl, sinapyl and p-coumaryl alcohols); inside the lignin structure these three units are termed as guaiacyl (G), syringyl (S), and p-hydroxyphenyl (H) respectively [5, 6] (Figure 2.3). The configuration of the lignin structure differs according to the plant species and it is also influenced by the environment. Generally, in softwoods (coniferous wood) the G units are prevalent, in hardwoods (deciduous trees) the amounts of G and S are almost equal and only traces of H are present, whereas in monocot grasses the ratio of the three monomers G/S/H is around 70/25/5 [6, 39].

a)

b)
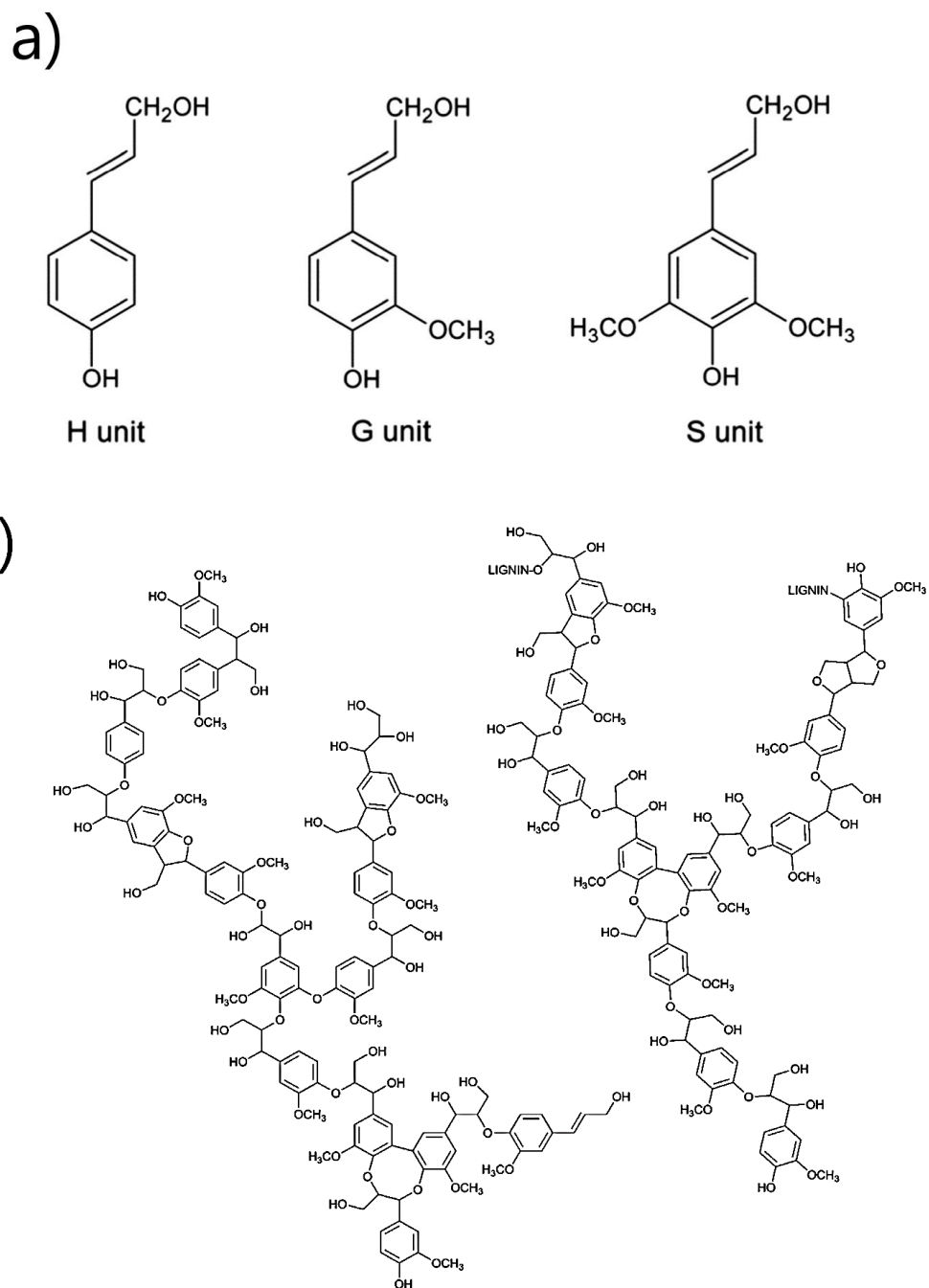
Figure 2.3: The structure of the lignin macromolecules; a) the three lignin monomer units; b) typical structure of softwood lignin. Adapted from [38]

The extraction of lignin from the lignocellulosic biomass is industrially achieved through one of the following paper pulp processes, which aim at solubilizing lignin in order to obtain pure cellulose.

a) The kraft process: it is the most widely used method (approximately 85% of the produced lignin is extracted with the kraft process) [5]. It is performed at high temperatures (~ 170°C) and high pH values (~13-14) in which lignin is dissolved in solutions of NaOH and Na$_2$S [5, 38]. Kraft lignin contains small amounts of ash and sulfur and it usually has a molecular weight of around 1000-15000 Da [5, 6]. The ash can, however, be removed with proper chemical treatment [40].

b) The sulfite process: this method is very common in the pulp and paper industry [5]. It proceeds through the reaction of lignin with a metal sulfide and SO$_2$ at high temperatures (120-180°C) for 1-5 hours [5]. The lignosulfonates produced here are water-soluble, they contain a considerable amount of sulfur (4-8%) and ash, but also a higher molecular weight compared to kraft lignin (1000-50000 Da) [5, 6].

c) The soda process: This process is applied to non-wood lignocellulosic biomass (grass, sugarcane, etc) [5, 38]. It is similar to the kraft process as the biomass is digested at high temperatures (140-170°C) in NaOH solution in the presence of anthraquinone [5]. Soda lignins are sulfur-free and they have a range of molecular weight between 1000-3000 Da [5, 6].

d) The organosolv process: This extraction method is based on the treatment of the lignocellulosic biomass with organic solvents (methanol, ethanol, acetic and formic acid) mixed with water at high temperatures (170-190°C) in the presence of catalysts. It produces sulfur-free, more pure lignin, with low ash content and low molecular weight (500-5000 Da). Disadvantages of this method include the corrosion of the equipment, the high cost of the solvents and the presence of undesirable side reactions [5, 6, 38]. Alcell lignin is a type of organosolv lignin commercialized by Lignol Innovations [41].

In addition to the above, lignin derived from the enzymatic hydrolysis of biomass has also been reported [42]. The lignins produced from these processes have some structural differences which affect their physicochemical properties. Kraft and sulfite lignin contain sulfur (1-8%) and ash (mainly salts of alkali metals), while soda and organosolv lignin are sulfur-free [7]. In terms of their solubility, sulfite lignin is soluble in water, while kraft lignin becomes water-soluble after sulfonation, as well [5]. Kraft and organosolv lignin are soluble in organic solvents, while soda lignin dissolves in alkaline solutions [5, 29]. Moreover, sulfite lignin has the highest polydispersity index (6-8), while the other three types have polydispersity values between 1.5-3.5 [7].

The heterogeneous structure and the relatively high polydispersity are obstacles in the wider use of lignin. This can be overcome by filtration or selective precipitation to produce more homogeneous fractions, however, the large quantities of solvents needed are a disadvantage for the industrial scale-up [38]. These issues, together with its immiscibility with various polymer matrices and its poor mechanical properties, have rendered this significant biorenewable resource rather unexploited. It has been estimated, that out of 50-70 million tons of lignin extracted from the paper industry in 2010, only 2% was commercialized for applications such as adhesives, dispersants, antioxidants and surfactants [6]. Most of the lignin produced is used as low-grade burning fuel or it is simply discarded as waste [7].

Nevertheless, lignin can potentially emerge as a significant, versatile raw material through chemical modification. This includes amination, nitration, hydroxyalkylation, esterification and alkylation of its hydroxyl groups among others [8]. These processes can in turn lead to its use as a precursor for a wide range of products such as biodiesel, pharmaceutical precursors or polymers [5, 6, 39]. Without

chemical modification, lignin is a very attractive precursor for the manufacture of carbon materials, such as carbon fibers and activated carbon. Its suitability for this purpose is based on its low cost, its large availability, the relatively high carbon content in its structure (around 60 wt%) and the absence of toxic by-products during its thermal treatment [29]. The thermal decomposition of lignin during its conversion to carbon consists of multiple steps over a wide temperature range. Usually, there is an initial decomposition step between 150-275°C (dehydration from hydroxyl groups), then the aliphatic chains start to break away from the aromatic rings at around 300°C, at 370-400°C carbon-carbon cleavages occur in the lignin backbone and, finally, at 500-700°C the rearrangements in the lignin structure lead to char formation (mainly polyaromatic graphitic and disordered carbon) [6]. During this process, volatile compounds are released, mainly H_2, H_2O, CH_4, CO, CO_2 and phenolic compounds [43, 44].

2.4 Lignin-based electrospun carbon nano- and submicron-fibers: a review of the relevant literature

Table 2.1 concisely presents a summary of the relevant literature related to lignin-based electrospun carbon nano- and submicron-fibers, focusing on the experimental conditions (material and electrospinning parameters, thermal treatment) and on some key properties of the fibers (average diameters, porosity, mechanical and electrical properties).

In the following sections, a more detailed account of the methodologies leading to the successful fabrication of lignin-based electrospun carbon nano- and submicron-fibers is presented, focusing on the precursor formulation and on their features arising from the preparation method.

Table 2.1: Lignin-based electrospun carbon nano- and submicron-fibers: literature summary

Reference & Purpose[1]	Material parameters[2]	Electrospinning parameters	Thermal treatment[4]	Average fiber diameter	Porosity characteristics	Properties[5]
	Lignin type/solvent	Voltage/Distance	Stabilization	Electrospun	BET Surface area	Tensile str.
	Polymer mass ratio	Flow rate	Carbonization	Carbonized	Total pore volume	Y. Modulus
	Additives	Concentration[3]	Activation		Meso-/microporous	Conductivity
[30]	Organosolv/ethanol	12 kV/20-25 cm	0.25ºC/min, 200ºC, 24 h	400-2000 nm	1200 m^2/g	-
(Properties)	- / -	0.5-1 mL/h	10ºC/min, 900ºC	200 nm	0.484 cm^3/g	-
	-	L/EtOH: 1/1 w/w	-		Microporous	-
[35]	Organosolv/ethanol	12 kV/20-25 cm	0.05ºC/min, 200ºC, 36 h	800-3000 nm	505-1195 m^2/g	-
(Properties)	- / -	0.8 mL/h	10ºC/min, 600-1000ºC	400-1000 nm	0.233-0.523 cm^3/g	-
	Pt-prec.: 0.2 & 0.4 wt%	L/EtOH: 1/1 w/w	-		Microporous	-
[32]	Organosolv/ethanol	14-22 kV/25 cm	0.08ºC/min, 200ºC, 100 h	N/A	747-1289 m^2/g	-
Catalysis	- / -	1-3 mL/h	10ºC/min, 900ºC	600-3000 nm	0.18-0.51 cm^3/g	-
	H$_3$PO$_4$ 30 wt% & Pt<3 wt%	L/EtOH: 1/1 w/w	-		Meso- & Micro-	-
[33]	Organosolv/ethanol	24 kV/30 cm	0.08ºC/min,200ºC,60 h	400-1000 nm	850-2000 m^2/g	303 MPa
Catalysis	- / -	3 mL/h	10ºC/min, 900ºC	400-1000 nm	0.329-0.849 cm^3/g	4 GPa
Electrodes	H$_3$PO$_4$ 30 wt%	L/EtOH: 1/1 w/w	N$_2$/O$_2$: 97/3 v/v, 900ºC		Mostly microporous	-
[45]	Organosolv/Ac/CCl$_4$	38 kV/13 cm	2ºC/min, 250ºC, 1 h	1300-5200 nm	532-2447 m^2/g	-
Supercapacitor	- / -	0.2 mL/min	1000ºC, 1 h	1300-2500 nm	0.28-1.58 cm^3/g	-
	Hexamine 7.5-10%	35 wt%	Steam, 900ºC		Meso- & Micro-	-

Table 2.1: Lignin-based electrospun carbon nano- and submicron-fibers: literature summary (continued)

Reference & Purpose[1]	Material parameters[2]	Electrospinning parameters	Thermal treatment[4]	Average fiber diameter	Porosity characteristics	Properties[5]
	Lignin type/solvent	Voltage/Distance	Stabilization	Electrospun	BET Surface area	Tensile str.
	Polymer mass ratio	Flow rate	Carbonization	Carbonized	Total pore volume	Y. Modulus
	Additives	Concentration[3]	Activation		Meso-/microporous	Conductivity
[31]	Kraft/DMF	N/A/13 cm	0.5°C/min, 250°C, 15 min	769 nm	676-1204 m^2/g	-
Supercapacitor	- / -	1 mL/h	3°C/min, 900°C, 30 min	567 nm	0.22-0.55 cm^3/g	-
	-	50 wt%	CO_2, 600°C, 1 h		Meso- & Micro-	-
[46]	N/A /DMF	15 kV/10cm	1°C/min, 250°C, 3 h	(submicron)	6.3-12.9 m^2/g	-
LIB	L/PAN: 0/100-50/50	0.02 mL/min	10°C/min, 1000°C, 1 h	(submicron)	N/A	-
	-	12 wt%	-		N/A	-
[47]	Lignosulfonate/DMF	25 kV/20 cm	250°C, 1 h	200-500 nm	~10-30 m^2/g	-
SIB	L/PAN: 10/90-50/50	1 mL/h	800-1300°C, 30 min	N/A	N/A	-
	-	12 wt% (PAN)	-		Microporous	-
[48]	N/A /DMF	20 kV/15 cm	250°C, 3 h	N/A	17.5-68.8 m^2/g	-
LIB	L/PAN: 50/50	1.5 mL/h	1200°C, 1 h	150 nm	0.026-0.081 cm^3/g	-
	Pluronic P 123	12 wt% (PAN)	-		Mesoporous	-
[49]	Kraft/DMF	19 kV/16 cm	2°C/min, 280°C, 1 h	N/A	2331-2543 m^2/g	-
Supercapacitor	L/PAN:10/90-30/70	0.8 mL/h	5°C/min, 1000°C	79-184 nm	$V_{mes,max}$: 0.955 mL/g	-
	-	10 wt%	CO_2, 1000°C, 1 h		Meso- & Micro-	530 S/m

Table 2.1: Lignin-based electrospun carbon nano- and submicron-fibers: literature summary (continued)

Reference & Purpose[1]	Material parameters[2]	Electrospinning parameters	Thermal treatment[4]	Average fiber diameter	Porosity characteristics	Properties[5]
	Lignin type/solvent	Voltage/Distance	Stabilization	Electrospun	BET Surface area	Tensile str.
	Polymer mass ratio	Flow rate	Carbonization	Carbonized	Total pore volume	Y. Modulus
	Additives	Concentration[3]	Activation		Meso-/microporous	Conductivity
[42]	EHL/DMF	25 kV/15 cm	1°C/min, 250°C, 1.5 h	N/A	578-631 m^2/g	-
Supercapacitor	L/PAN: 0/100-70/30	4.8 mL/h	10°C/min, 800°C, 1 h	172-421 nm	0.25-0.27 m^2/g	-
	-	12 wt%	-		Microporous	-
[50]	N/A /DMF/THF	N/A	280°C, 1 h	310-650 nm	376-1194 m^2/g	-
Supercapacitor	L/PAN/pitch: 0.78/7/3	N/A	5°C/min, 800°C, 1 h	~370 nm	N/A	-
	Zn-prec.: 0-10 wt%	N/A	-			-
[51]	Kraft/DMF	8.5kV/20 cm	1°C/min, 280°C, 1 h	N/A	-	-
Supercapacitor	L/PAN: 20/80 & 50/50	N/A	5°C/min, 1000°C	270-590 nm	-	-
	NiCo$_2$O$_4$: 1.59 mg/cm^2	12-18 wt%	-	doped: >800 nm	-	-
[52]	EHL/DMF	15 kV/15 cm	0.5°C/min, 260°C, 3 h	N/A	1008-2439 m^2/g	-
Supercapacitor	L/PAN: 50/50	1 mL/min	5°C/min, 1400°C, 1 h	N/A	0.54-1.29 cm^3/g	2.82 GPa
	Graphene: 0-0.3 wt%	20 wt%	KOH/CNFs: 6/1, 800°C		Meso- & Micro-	-
[53]	N/A /DMF	24 kV/ N/A	1°C/min, 225°C, 2 h	105-250 nm	-	-
Sensor	L/PAN: 50/50-75/25	0.3 mL/h	1200°C	<100 nm	-	-
	Graphene: 0-5 wt%	10-20 wt%	-		-	-

Table 2.1: Lignin-based electrospun carbon nano- and submicron-fibers: literature summary (continued)

Reference & Purpose[1]	Material parameters[2]	Electrospinning parameters	Thermal treatment[4]	Average fiber diameter	Porosity characteristics	Properties[5]
	Lignin type/solvent	Voltage/Distance	Stabilization	Electrospun	BET Surface area	Tensile str.
	Polymer mass ratio	Flow rate	Carbonization	Carbonized	Total pore volume	Y. Modulus
	Additives	Concentration[3]	Activation		Meso-/microporous	Conductivity
[36]	Organosolv/DMF	N/A / 10-15 cm	200-275ºC, 1-12 h	250-270 nm	-	-
Thermoelectric	L/PAN: 0/100-70/30	10 µL/min	900 or 1100ºC, 1 h	130-150 nm	-	-
generator	-	10-15 wt%	-		-	27.47 S/cm
[54]	Kraft/DMF	16 kV / N/A	10ºC/min, 250ºC	283-412 nm	-	160 GPa*mm^3/g
(Properties)	L/PAN: 10/90-30/70	0.8 µL/min	1400ºC/ 30 mins	185-253 nm	-	14,000
	Copolymer 10-30 wt%	10 wt%	-		-	GPa*mm^3/g
[55]	N/A /DMF	15 kV/12 cm	200-280ºC, 2 h in total	150-200 nm	-	-
(Properties)	L/PAN: 50/50	0.04 mm/min	600-1000ºC, 2-3 h	~100 nm	-	-
		12 wt%	-		-	-
[56]	Kraft/DMF	17 kV/20 cm	-	~3500 nm	-	-
(properties)	L/PAN: 50/50	0.03 mL/h	1st step: 550ºC, 2 h, H$_2$	~3500 nm	-	-
	Cellulose nanofibrils	17 wt%	2nd step: 1000ºC, 1 h, Ar		-	-
[57]	Kraft/DMF	17 kV/25 cm	-	1000-1200 nm	~15-31 m^2/g	-
(Properties)	L/PAN: 50/50	0.1 mL/h	1st step: 550ºC, 2 h, H$_2$	615-989 nm	-	-
	Fe-, Pd-precursors	15 wt%	2nd step: 1000ºC, 1 h, Ar		-	-

Table 2.1: Lignin-based electrospun carbon nano- and submicron-fibers: literature summary (continued)

Reference & Purpose[1]	Material parameters[2]	Electrospinning parameters	Thermal treatment[4]	Average fiber diameter	Porosity characteristics	Properties[5]
	Lignin type/solvent	Voltage/Distance	Stabilization	Electrospun	BET Surface area	Tensile str.
	Polymer mass ratio	Flow rate	Carbonization	Carbonized	Total pore volume	Y. Modulus
	Additives	Concentration[3]	Activation		Meso-/microporous	Conductivity
[58]	Kraft/DMF	8.5-10 kV/15 cm	10°C/min, 250°C, 2 h	N/A	-	89.4 MPa
(properties)	L-g-PAN copolymer	0.85-10.5 µL/min	600-1400°C, 30 mins	561-926 nm	-	2.5 GPa
	-	15-18 wt%	-		-	21.3 S/cm
[59]	Organosolv/DMF	10 kV/20 cm	0.2-2°C/min, 220°C, 1 h	N/A	-	89 MPa
(Properties)	L/PAN: 50/50	1 mL/h	4°C/min, 1400°C, 2 h	N/A	-	5.3 GPa
	Iodine vapor, 70°C	20 wt%	-		-	-
[60]	Organosolv/DMF	15 kV/20 cm	0.2°C/min, 200°C, 12 h	1300-1800 nm	-	83 MPa
(properties)	L/PAN: 30/70-70/30	5 µL/min	5°C/min, 1000°C, 30min	1000-1100 nm	-	6.1 GPa
	(Butyration)	20 wt%	-		-	-
[61]	Soda, kraft/DMF	15 kV/15 cm	0.3°C/min, 280°C, 1 h	273-701 nm	-	142 MPa
(properties)	L/PAN: 0.25/1-1/0.75	N/A	3°C/min, 1000°C	177-522 nm	-	10 GPa
	-	15 wt%	-		-	-
[62]	Kraft/Water	26 kV/25 cm	Stepwise, 220°C, >24 h	~200 nm	583 m^2/g	-
Adsorption	L/PVA: 70/30	1.2 mL/min	5°C/min, 1200°C, 1 h	~200 nm	0.29 cm^3/g	-
	-	12 wt%	-		Meso- & Micro-	-

Table 2.1: Lignin-based electrospun carbon nano- and submicron-fibers: literature summary (continued)

Reference & Purpose[1]	Material parameters[2]	Electrospinning parameters	Thermal treatment[4]	Average fiber diameter	Porosity characteristics	Properties[5]
	Lignin type/solvent	Voltage/Distance	Stabilization	Electrospun	BET Surface area	Tensile str.
	Polymer mass ratio	Flow rate	Carbonization	Carbonized	Total pore volume	Y. Modulus
	Additives	Concentration[3]	Activation		Meso-/microporous	Conductivity
[63]	Kraft/Water	26 kV/25 cm	Stepwise, 220ºC, >24 h	~200 nm	583 m^2/g	-
Supercapacitor	L/PVA: 70/30	1.2 mL/min	5ºC/min, 1200ºC, 1 h	~200 nm	0.29 cm^3/g	-
	MnO$_2$ nanowhiskers	12 wt%	-		Meso- & Micro-	-
[64]	Kraft/Water	26 kV/25 cm	Stepwise, 220ºC, >24 h	~200 nm	583 m^2/g	-
LIB	L/PVA: 70/30	1.2 mL/min	5ºC/min, 1200ºC, 1 h	~200 nm	0.29 cm^3/g	-
	Fe$_2$O$_3$: 22-45 wt%	12 wt%	-		Meso- & Micro-	-
[24]	Kraft/Water	26 kV/25 cm	Stepwise, 220ºC, >24 h	~200 nm	583 m^2/g	-
Supercapacitor	L/PVA: 70/30-30/70	1.2 mL/min	5ºC/min, 1200ºC, 1 h	~200 nm	0.29 cm^3/g	-
	-	12 wt%	-		Meso- & Micro-	-
[65]	Kraft/Water	26 kV/25 cm	Stepwise, 220ºC, >24 h	~200 nm	583 m^2/g	-
Electrocatalyst	L/PVA: 70/30	1.2 mL/min	5ºC/min, 1200ºC, 1 h	~200 nm	0.29 cm^3/g	-
	Ag-prec.: 11-25 wt%	12 wt%	-		Meso- & Micro-	-
[66]	Kraft/Water	22 kV/20 cm	Iodine, 100ºC, 12 h	~570-770 nm	1049 m^2/g	-
LIB/SIB	L/PVA: 50/50	1 mL/h	2ºC/min, 600ºC, 1 h	514-875 nm	0.49 cm^3/g	-
	KOH: 5 wt%	15 wt%	No additional treatment		Microporous	-

Table 2.1: Lignin-based electrospun carbon nano- and submicron-fibers: literature summary (continued)

Reference & Purpose[1]	Material parameters[2]	Electrospinning parameters	Thermal treatment[4]	Average fiber diameter	Porosity characteristics	Properties[5]
	Lignin type/solvent	Voltage/Distance	Stabilization	Electrospun	BET Surface area	Tensile str.
	Polymer mass ratio	Flow rate	Carbonization	Carbonized	Total pore volume	Y. Modulus
	Additives	Concentration[3]	Activation		Meso-/microporous	Conductivity
[67]	Kraft/Water	20 kV/15 cm	2°C/min, 250°C, 1 h	210-600 nm	1370-2170 m^2/g	-
Supercapacitor	L/PVA: 90/10-75/25	0.8 mL/h	5°C/min, 1000°C, 1 h	166-220 nm	0.36-0.53 cm^3/g	-
	-	24 wt%	CO_2, 800°C, 30 min		Meso- & Micro-	-
[68]	Kraft/Water	17 kV/20 cm	4°C/min, 250°C, 2 h, N_2	148 nm	1689-2005 m^2/g	-
Supercapacitor	L/PVA: 75/25	8-10 µL/min	4°C/min, 600°C, 1 h	148 nm	0.60-0.71 cm^3/g	-
	-	17.4 wt%	KOH/CNFs: 1/1, 900°C		Mesoporous	386 S/m
[69]	Kraft/DMSO	15-20 kV/20 cm	2.5°C/min, 250°C, 1 h	410-750 nm	-	526.3 MPa
Microelectrode	L/PVA: 100/0-50/50	0.5 mL/h	550-1200°C, 1 h	N/A	-	26 GPa
	-	30 wt%	-		-	21.9 S/cm
[70]	Kraft/Water	15-20 kV/20 cm	5°C/min, 250°C, 1 h	N/A	193-941 m^2/g	-
DSSC	L/PVA: 50/50-80/20	1 mL/h	800-1500°C, 1 h	200-250 nm	0.12-0.53 cm^3/g	-
	-	10-25 wt%	-		Meso- & Micro-	502 S/m
[71]	Kraft/H_2O/Acetic Acid	18 kV/ N/A	200°C, 3 h	N/A	478-1147 m^2/g	-
Adsorption	L/PVA: 1/0.1	0.4 mL/h	600-1000°C, 1 h	N/A	0.43-0.73 m^2/g	-
	-	27.5 wt%	Steam, KOH, Nitrates		Meso- & Micro-	-

Table 2.1: Lignin-based electrospun carbon nano- and submicron-fibers: literature summary (continued)

Reference & Purpose[1]	Material parameters[2]	Electrospinning parameters	Thermal treatment[4]	Average fiber diameter	Porosity characteristics	Properties[5]
	Lignin type/solvent	Voltage/Distance	Stabilization	Electrospun	BET Surface area	Tensile str.
	Polymer mass ratio	Flow rate	Carbonization	Carbonized	Total pore volume	Y. Modulus
	Additives	Concentration[3]	Activation		Meso-/microporous	Conductivity
[72]	Kraft/H_2O/Acetic Acid	18 kV/ N/A	200°C, 3 h	N/A	-	-
Adsorption	L/PVA: 1/0.1	0.4 mL/h	600-1000°C, 1 h	N/A	-	-
	-	27.5 wt%	KOH/CNFs: 3/1, 800°C		-	-
[73]	Kraft/H_2O/Acetic Acid	18 kV / N/A	200°C, 36 h	N/A	1466 m^2/g	-
Adsorption	L/PVA: 1/0.15	0.4 mL/h	10°C/min, 600°C, 1.5 h	700-1000 nm	0.89 m^2/g	-
	Fe_3O_4: 1.25% w/v	27.5 wt%	-		Meso- & Micro-	-
[74]	N/A /H_2O/Acetic Acid	22 kV/15 cm	0.5°C/min, 250°C	N/A	486-555 m^2/g	-
Sensors	L/PVA: 1/0.1	1 mL/h	800°C	~1000 nm	0.22-0.36 cm^3/g	-
	$ZnCl_2$: 1 wt%	27.5 wt%	-		Meso- & Micro-	-
[75]	Organosolv/DMF	25-30 kV/15-20 cm	0.2°C/min, 250°C, 1 h	400-600 nm	281-401 m^2/g	-
Supercapacitor	L/PEO: 90/10	0.4-1 mL/min	3°C/min, 900°C, 1 h	400-600 nm	0.193-0.394 cm^3/g	-
	Fe-prec.: 5-25 wt%	~42.8 wt%	-		Meso- & Micro-	-
[76]	Kraft/DMF	11-12 kV/17 cm	5°C/min, 250°C, 1 h	875 nm	374-456 m^2/g	76.3 MPa
(properties)	L/PEO: 28/0.2	2 mL/h	600-1000°C, 1 h	634 nm	N/A	4.8 GPa
	-	30 wt%	-		N/A	19.6 S/cm

Table 2.1: Lignin-based electrospun carbon nano- and submicron-fibers: literature summary (continued)

Reference & Purpose[1]	Material parameters[2]	Electrospinning parameters	Thermal treatment[4]	Average fiber diameter	Porosity characteristics	Properties[5]
	Lignin type/solvent	Voltage/Distance	Stabilization	Electrospun	BET Surface area	Tensile str.
	Polymer mass ratio	Flow rate	Carbonization	Carbonized	Total pore volume	Y. Modulus
	Additives	Concentration[3]	Activation		Meso-/microporous	Conductivity
[40]	Kraft/water	10-15 kV/12-20 cm	-	N/A	446-1444 m^2/g	-
(properties)	L/PEO: 7.4/2.6-9/1	1 mL/h	600-850°C, 30 min	100-500 nm	0.18-0.55 cm^3/g	-
	NaOH or KOH/L<0.5/1	10-11.7 wt%	-		Meso- & Micro-	-
[77]	Kraft/water	10-15 kV/12-20 cm	-	-	475-885 m^2/g	-
(properties)	L/PEO: 9/1	1 mL/h	600-900°C, 30 min	500-2000 nm	0.75-0.90 cm^3/g	-
	NaOH/L: 1/2	10 wt%	H$_2$SO$_4$, 110/150°C, 20 h		Meso- & Micro-	-
[78]	Kraft/DMF	V/D: 70×10^3 V/m	0.5-5°C/min, 250°C, 1 h	809 nm	-	0.0085 N/Tex
(properties)	L/PEO: 99/1	4.2×10^{-10} m3/s	5°C/min, 600-900°C, 1 h	N/A	-	N/A
	-	30 wt%	-		-	2.35 S/cm
[79]	Kraft/DMF	17.5 kV/15 cm	1°C/min, 250°C, 2 h	667 nm	-	51.25 MPa
(properties)	L/PEO: 30/1	0.1 mL/min	5°C/min, 1000°C, 2 h	474 nm	-	-
	Pd-precursor	N/A	-		-	-
[80]	Kraft/1M NaOH	19-25 kV/18-20 cm	-	172-478 nm	~905-1249 m^2/g	-
Supercapacitor	L/PEO: 1/0.14	1 mL/h	3°C/min, 800°C, 2 h→	163-331 nm	0.38-0.52 cm^3/g	-
	NaNO$_3$: 10-50 mol%	12 wt%	→(5% H$_2$ in N$_2$)		Meso- & Micro-	-

Table 2.1: Lignin-based electrospun carbon nano- and submicron-fibers: literature summary (continued)

Reference & Purpose[1]	Material parameters[2]	Electrospinning parameters	Thermal treatment[4]	Average fiber diameter	Porosity characteristics	Properties[5]
	Lignin type/solvent	Voltage/Distance	Stabilization	Electrospun	BET Surface area	Tensile str.
	Polymer mass ratio	Flow rate	Carbonization	Carbonized	Total pore volume	Y. Modulus
	Additives	Concentration[3]	Activation		Meso-/microporous	Conductivity
[37]	Kraft/DMF	20 kV/25 cm	5°C/min, 250°C, 1 h	300-1400 nm	-	-
(properties)	L/PEO: 99/1	0.01 mL/min	10°C/min, 1000°C, 1 h	N/A	-	-
	-	25-30 wt%	-		-	0.18 S/cm
[81]	Organosolv, kraft/DMF	20 kV/20 cm	0.2°C/min, 200°C, 12 h	~1000-1100 nm	-	15.58 MPa
(properties)	L/PEO: 95/5	0.5 mL/h	5°C/min, 1000°C, 30 min	~900-1000 nm	-	24.54 GPa
	-	30 wt%	-		-	-
[4]	Organosolv, kraft/DMF	7-9 kV/10 cm	1°C/min, 200°C, 2 h	N/A	-	-
Electrodes	L/PEO: 90/10	3 mL/min	5°C/min, 1000°C, 1 h	~100-250 nm	-	-
	Ketjen black: 1 wt%	20 wt%	-		-	-
[82]	Organosolv/DMF	7 kV/10cm	1°C/min, 200°C, 2 h	~1000 nm	381-473 m²/g	-
LIB	L/PEO:~9/1	1 mL/h	10°C/min, 900°C, 2 h	~500 nm	0.28-0.31 cm³/g	-
	N-doping (urea)	24.2% w/v	-		Meso- & Micro-	12.24 S/cm
[83]	Organosolv/DMF	30 kV/15 cm	0.2°C/min, 250°C, 1 h	N/A	-	-
Supercapacitor	L/PEO: 95/5	0.1 mL/h	10°C/min, 900°C, 1 h	400-500 nm	-	-
	Fe-prec.: 1-25 wt%	30 wt%	-		-	-

Table 2.1: Lignin-based electrospun carbon nano- and submicron-fibers: literature summary (continued)

Reference & Purpose[1]	Material parameters[2]	Electrospinning parameters	Thermal treatment[4]	Average fiber diameter	Porosity characteristics	Properties[5]
	Lignin type/solvent	Voltage/Distance	Stabilization	Electrospun	BET Surface area	Tensile str.
	Polymer mass ratio	Flow rate	Carbonization	Carbonized	Total pore volume	Y. Modulus
	Additives	Concentration[3]	Activation		Meso-/microporous	Conductivity
[84]	Kraft/DMF	20 kV/25 cm	5°C/min, 250°C, 1 h	~550-750 nm	-	33.7 MPa
(properties)	L/PEO: 99/1	0.01 mL/min	800-1000°C, 1 h	~300-550 nm	-	8 GPa
	NC Cellulose: 1-5 wt%	25-30 wt%	-		-	35 S/cm
[85]	Kraft/Water	10-15 kV/12-20 cm	-	N/A	same as [40]	-
Supercapacitor	L/PEO: 9/1	1 mL/h	10°C/min, 850°C, 30 min	(submicron)	same as [5]	-
	NaOH or KOH/L: 0.5/1	10 wt%	-		same as [5]	-
[86]	Kraft/DMF	15 kV/15 cm	150°C (24 h) + 350°C (4 h)	N/A	600-1140 m^2/g	-
Supercapacitor	L/PVP: 1/2	0.2 mL/h	3°C/min, 800°C, 1 h	100-200 nm	0.283-0.627 cm^3/g	-
	Mg-prec./L: 0.5/1-2/1	20 wt%	-		Meso- & Micro-	-
[87]	N/A / DMF	24 kV/30 cm	250°C, 2 h	~1500 nm	-	-
(properties)	LPF/PVP: 3/1	0.39 mL/h	800°C, 2 h	~1000 nm	-	-
	Polymeric precursor	30 wt%	-		-	-
[88]	Kraft/Ac/DCH:2/1	20 kV/20 cm	-	500 nm	541 m^2/g	-
SIB	L/CA: 1/1	0.75 ml/h	2°C/min, 1000°C, 1 h	300 nm	0.27 cm^3/g	-
	-	8 wt%	-		N/A	-

Table 2.1: Lignin-based electrospun carbon nano- and submicron-fibers: literature summary (continued)

Reference & Purpose[1]	Material parameters[2]	Electrospinning parameters	Thermal treatment[4]	Average fiber diameter	Porosity characteristics	Properties[5]
	Lignin type/solvent	Voltage/Distance	Stabilization	Electrospun	BET Surface area	Tensile str.
	Polymer mass ratio	Flow rate	Carbonization	Carbonized	Total pore volume	Y. Modulus
	Additives	Concentration[3]	Activation		Meso-/microporous	Conductivity
[89]	Organosolv/Ac/DMAc	16-18 kV/ 24 cm	2°C/min, 300°C, 2 h	400-500 nm	-	-
(properties)	L/CA: 1/1-4/1	0.7 mL/h	2°C/min, 600-1200°C, 1 h	200-300 nm	-	-
	Iodine vapor, 100°C	30 wt%	-		-	-

*"N/A" means that more details are not reported in the article; a dash "-" means that the specific procedure was not performed.

[1]Purpose of each article, classified in the following categories: properties, supercapacitor, Lithium-Ion Batteries (LIB), Sodium-Ion Batteries (SIB), electrodes, sensor, adsorption, thermoelectric generator, catalysis.

[2]Abbreviations: L: Lignin; prec.: precursor (e.g. Pt-precursor); Ac: Acetone; CCl$_4$: Carbon Tetrachloride; TFA: Trifluoroacetic acid;

DMF: N,N-Dimethylformamide; PAN: Polyacrylonitrile; EHL: Enzymatic Hydrolysis Lignin; THF: Tetrahydrofuran; PVA: Polyvinyl alcohol;

DMSO: Dimethyl sulfoxide; PEO: Polyethylene oxide; NC Cellulose: Nanocrystalline cellulose; PVP: Polyvinylpyrrolidone; LPF: Lignin-Phenol-Formaldehyde;

CA: Cellulose Acetate; DCH: N,N-Dimethylcyclohexylamine; DMAc: N,N-Dimethylacetamide

[3]Refers to total polymer concentration in the spinning solution.

[4]Described as: heating at a "x"°C/min heating rate, up to "T"°C temperature of treatment, hold for time "t" at this "T" temperature.

[5]Tensile strength, Young's modulus and electrical conductivity: only the maximum achieved values are reported here.

2.4.1 Electrospun carbon nano- and submicron-fibers prepared from lignin alone

Lallave et al. [30] were the first to report the preparation of lignin-based electrospun CNFs. Organosolv (alcell) lignin was used alone without any binder polymers in this case, and it was spun into precursor fibers via coaxial electrospinning. The tri-axial spinneret configuration consisted of (ethanol)/(lignin-in-ethanol)/(glycerine); the role of the outer ethanol sheath was to inhibit solidification, and the inner glycerine core acted as template fluid. After a lengthy stabilization step (24 h) which was necessary to prevent fusion, and the subsequent carbonization, highly microporous CNFs were produced with average diameters close to 200 nm. Their carbon content amounted to 94.3 wt%. The same research group elsewhere reported the production of carbon submicron-fibers doped with Pt [35]. The parameters of investigation here were the variation in carbonization temperature (600-1000°C) and the presence of Pt. It was found that although most of the precursor fibers had diameters above 1 μm, after carbonization their average diameter decreased to the submicron scale. Increasing the treatment temperature resulted in the highest carbon content (~95 wt% at 1000°C), higher structural order and increased porosity (reaching a BET surface area of 1195 m^2/g). The authors suggest that the high oxygen content in lignin functions as an activating agent for the development of porosity. The presence of Pt seemed to inhibit the structural ordering, while it didn't significantly affect the growth of porosity. The preparation of Pt-doped CNFs from alcell lignin was further reported by the same research group in another article, in which the CNFs were tested as catalysts for the electro-oxidation of alcohols [32]. The difference, here, was the addition of H_3PO_4 in the spinning solution which functioned as activation agent for the enhancement of porosity. The presence of H_3PO_4 allowed a vast decrease in the

stabilization time from 100 h for pure precursor fibers to just 1 h for those containing H_3PO_4. This vast difference was justified by the increased oxygen content which favored cross-linking during thermal treatment. Moreover, the presence of phosphorus boosted the development of microporosity, while mesoporous CNFs with lower surface area were prepared in its absence. Although phosphorus increased the electro-oxidation resistance of CNFs, it compromised their performance as electrocatalysts. Nevertheless, phosphorus-free CNFs containing well-dispersed Pt-nanoparticles with sizes of 2-3 nm performed very well in the electro-oxidation of methanol and ethanol. Similarly, an article of the same research group studying the properties of alcell lignin-based CNFs in the presence of H_3PO_4 as additive [33], emphasized on the role of the acid in the faster stabilization of the fibers and in their improved electrochemical stability. These CNFs displayed a tensile strength of ~300 MPa and a Young's modulus of 4 GPa, which are deemed satisfactory for adsorbents despite being insufficient for structural applications.

You et al. [45] prepared organosolv lignin-CNFs using a different approach to improve the stabilization step. Hexamine which decomposes to formaldehyde and acts as a cross-linker was added. Therefore, CNFs which retained their structural integrity could be produced. After steam activation, the CNFs exhibited a noteworthy BET surface area of 2447 m^2/g and they contained a significant percentage of mesoporosity. Moreover, it was shown that a narrow micropore distribution was more effective than a large BET surface area in terms of the performance of CNFs as electrodes for EDLC. Schlee et al. [31] used kraft lignin (Mw: 1900 g/mol) as CNF-precursor without the presence of any other binder polymers or additives. After activation with CO_2, the BET surface area of CNFs almost doubled from 676 m^2/g to 1204 m^2/g, accompanied by a widening of pores and by an increase of the graphitic domains (Figure 2.4). The

positive effect of pore widening was translated into an improved electrochemical performance in EDLC.
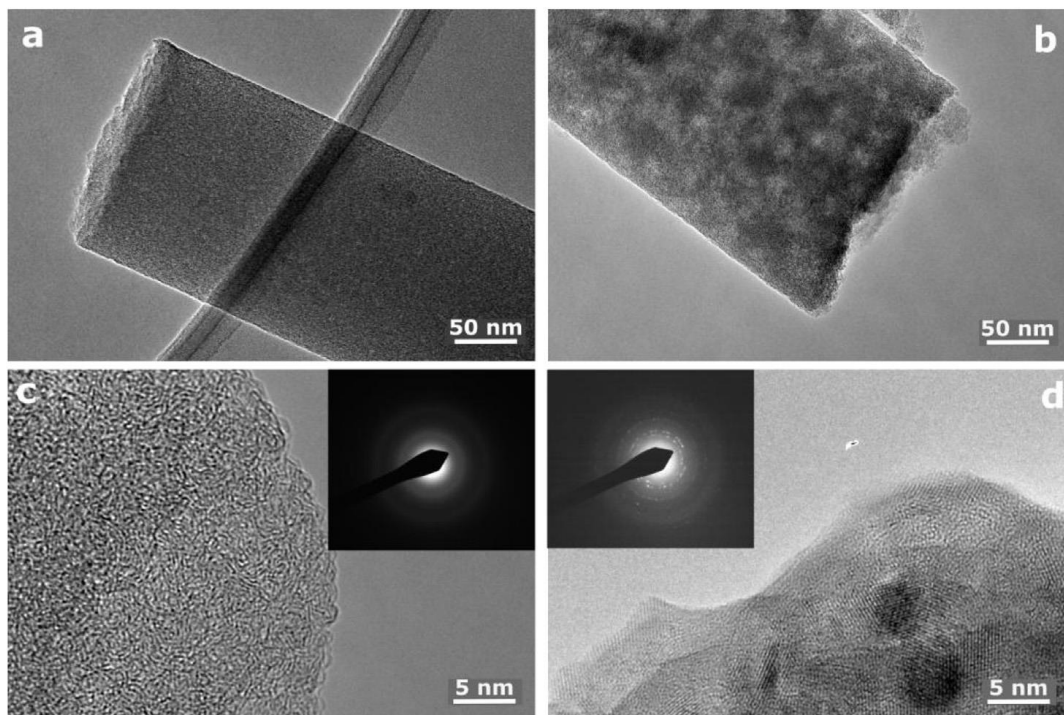
Figure 2.4: Typical TEM images of lignin-based CNFs; a) and c) non-activated CNF; b) and d) activated CNF. The diffraction pattern in (d) indicates the presence of polycrystalline graphite [31]

2.4.2 Electrospun carbon nano- and submicron-fibers prepared from lignin/PAN

PAN is very common as binder polymer for the fabrication of lignin-based CNFs due to its easy spinnability, its high molecular weight and the feasibility to be transformed into carbon fibers of relatively high mechanical strength.

Lignin/PAN-based electrospun CNFs have been commonly used as anodes for rechargeable batteries. Choi et al. [46] combined PAN with lignin at mass ratios ranging from 0/100 to 50/50 (lignin/PAN). It was observed that after carbonization, the average fiber diameters decreased by almost 50% (in the submicron scale), while

increasing the lignin content resulted in thinner fibers with lower BET surface area, probably due to some fusion between them, and lower coulombic efficiency when tested as anodes for LIB. In contrast, Jin et al. [47] report better electrochemical performance of lignin/PAN CNFs when lignin content increases, and a very good overall cycling stability when tested as anodes for SIB. This result is attributed to the more defective carbon structure created at lignin/PAN mass ratio of 50/50, as it provides more sites for ion adsorption. The same research group further tested lignin/PAN-based electrospun CNFs as anodes for LIB [48]. Keeping the same lignin/PAN ratio of 50/50, a triblock copolymer (Pluronic P 123) acting as a template for the development of mesoporosity was added. Although the CNFs had a low BET surface area (68.8 m^2/g), the abundant mesoporosity, as well as the fact that there was some fusion between the fibers which created a 3D interconnected network for the faster transportation of ions, resulted in a satisfactory capacity (127.7 mAh/g) at a high current density of 5 A/g with a discharge time of 91 seconds.

Besides anodes for rechargeable batteries, lignin/PAN-based CNFs have also been applied as supercapacitor electrodes. Jayawickramage et al. [49] blended kraft lignin with PAN at mass ratios ranging from 10/90 to 70/30 respectively. After carbonization and activation with CO_2, prepared activated mesoporous CNFs were prepared in which the BET surface area reached a maximum value for the fibers containing the highest amount of lignin (2543 m^2/g), while the mesoporous volume amounted to 0.955 cm^3/g. Here, lignin acted as a partially sacrificial polymer for the development of porosity. Moreover, the fibers containing the largest lignin percentage had the minimum average diameter (79 nm) and the most ordered structure. Another important feature induced by the high percentage of lignin was the rise in the electrical conductivity of CNFs, which almost doubled compared to the conductivity of the

fibers derived from the lowest lignin mass ratio (530 vs. 280 S/m respectively). Wang et al. [42] have also shown the positive effect of increasing lignin content (up to 60 wt%) in lowering the average diameter and increasing the BET surface area of lignin/PAN CNFs.

The doping of CNFs with metal-oxide nanoparticles or with heteroatoms is another strategy to increase their suitability for supercapacitor electrodes, by taking advantage of pseudocapacitive effects. With ZnO being a promising electrode material for supercapacitors, Yun et al. [50] fabricated ZnO-doped CNFs from a PAN/lignin/pitch precursor. Pitch, in this case, was added as a low-cost carbon source with higher electrical conductivity than PAN, while the oxygen-rich lignin promoted the development of porosity. The relative mass ratio of the three polymers was 0.78/7/3 for lignin/PAN/pitch respectively, with the only parameter of study here being the ZnO content (0-10 wt% of zinc acetate precursor in the spinning solution). In the absence of Zn, the CNFs were microporous (480 m^2/g), while the presence of zinc acetate boosted the porosity up to the value of 1194 m^2/g for 5 wt% Zn, creating a meso/microporous texture. Owing to pseudocapacitive effects, the presence of ZnO was found to augment the electrochemical performance of the CNFs, reaching a specific capacitance value of 165 F/g at current density of 1 mA/cm^2 and a power density of 22 Wh/kg. Another doping method has been reported through the hydrothermal deposition of $NiCo_2O_4$ on lignin/PAN based CNFs [51], which was achieved by dispersing the CNFs and the metal precursors in ethanol. Here, the metal oxides formed nanosheet-like and nano-needle hierarchical structures which grew axially on the surface of the fibers (Figure 2.5).
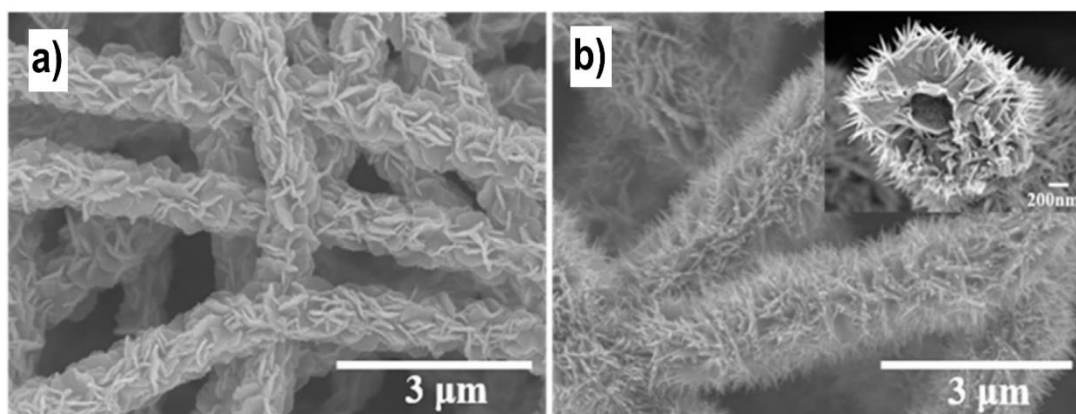
Figure 2.5: Nanostructures grown on lignin/PAN-based CNFs of different lignin content in the precursors; a) $NiCo_2O_4$ nanosheets; b) $NiCo_2O_4$ nano-needles. Lignin content is 20 wt% and 50 wt% respectively for (a) and (b) [51]

Dai et al. [52] implemented another doping strategy, as graphene nanosheets were added in the electrospinning solutions. Interestingly, it was found that the lignin/PAN-based CNFs doped with 0.3 wt% graphene had around 5 times higher N- and S-content than the undoped ones. It is suggested that the presence of graphene probably retained some of the amount of NH_3 and SO_2 being released from the polymers during carbonization. Moreover, the presence of graphene prompted a large increase in the BET surface area (2439 m^2/g), together with higher Young's modulus (2.82 GPa), higher degree of graphitization and lower hydrophobicity.

Mustafov et al. [53] report the doping of CNFs with graphene as well, although the application of interest here was biosensing. It was found that the presence of graphene lowers the degree of crystallinity of the electrospun nanofibers as the crystallization is disrupted, but it increases the degree of graphitization of the carbonized ones and their electrical conductivity although specific values are not mentioned. Here, CNFs of average diameter lower than 100 nm were produced. Similar magnitude for the average diameters of CNFs has been reported by Ma et al. [55] for a 50/50 mass ratio of corn straw lignin/PAN without any other additives. In

this case, it was observed that increasing the carbonization temperature (up to 1000°C) decreases the average diameter of the CNFs.

Another potential energy-related application associated with CNFs is that of thermoelectric generators. Dalton et al. [36] studied the thermoelectric properties of lignin/PAN-based CNFs, by measuring their Seebeck coefficient, which is defined as the voltage difference generated by the sample when a temperature gradient is applied on it. The results showed that increasing the lignin content to 70 wt% induces a high degree of fusion among the fibers and results in an interconnected CNF network. This high degree of fusion eliminates the contact resistance between the fibers. Hence, it was found that their electrical conductivity rises to 27.47 S/cm, much higher than the value of 7.64 S/cm for pure PAN-based CNFs which exhibit no fusion. The impact of this phenomenon could be also measured in the Seebeck coefficient which amounted to 10 µV/K, almost double that of pure PAN-based CNFs (4.5 µV/K).

Promoting the fusion and the interconnection among the fibers was the goal of Ding et al. [60] who esterified lignin with butyric anhydride. The butyration had a plasticizing effect as it transformed the hydroxyl groups of lignin into butyl esters, and, therefore, the T_g of lignin decreased due to a higher molecular thermal mobility. The morphology of the manufactured CNFs displayed a moderate inter-fiber bonding without losing their fibrous structure. As a result, the tensile strength of butyrated-lignin/PAN CNFs almost quadrupled compared to that of plain-lignin/PAN-based CNFs (83 MPa vs. 22 MPa).

Zhang et al. [61] proved that the lignin extraction process, which yields lignins of varying structural features, determines the mechanical properties of the CNFs. Soda lignin presented a more linear structure compared to kraft lignin, which was more complex and comprised many more polar functional groups. As a result, upon blending

with PAN and processing for CNF preparation, the soda lignin-derived CNFs had a less defective structure and exhibited much higher tensile strength (142 MPa) than kraft lignin-based CNFs (99 MPa).

Another important feature demonstrated by the blends of lignin with PAN is their flexibility to be modified in order to improve various properties of the CNFs. Park et al. [54] added a lignin-grafted-PAN copolymer (30 wt%) as compatibilizer between these two raw materials. This modification increased the specific tensile strength of the CNFs to around 160 GPa*mm^3/g and their Young's modulus to around 14,000 GPa*mm^3/g. Elsewhere, the same research group has reported the preparation of electrospun CNFs using as a precursor the lignin-grafted-PAN copolymer alone [58]. In this case, a tensile strength of 89.4 MPa was reported. The enhancement of mechanical properties was also the subject of study for Dai et al. [59], who treated the precursor fibers with iodine vapor prior to the stabilization step. Iodine is known to form charge transfer complexes with aromatic rings. Introducing it into the precursor fibers allowed them to be stabilized at a relatively high heating rate (2°C/min), therefore, more rigid CNFs with less structural defects and higher degree of graphitization were produced. Here, their tensile strength amounted to 89 MPa and their Young's modulus to 5.3 GPa.

Xu et al. [57] prepared Fe- and Pd-doped precursor lignin/PAN nanofibers by adding the appropriate precursors in the electrospinning solution. After the fabrication of the CNFs, the presence of catalysts promoted the growth of carbon nanotubes on their surface through a chemical vapor deposition process (Figure 2.6). The CNT-grown CNFs exhibited high thermal stability (98.3% residual weight at 950°C) due to their more graphitic structure, and a super-hydrophobic character because of the hierarchical nanostructures grown on their surface. Moreover, the same research group

has reported the preparation of porous CNFs through co-axial electrospinning, in which the lignin/PAN solution formed the shell of the precursor fibers and acetylated cellulose-nanofibrils the core [56]. The average external diameters of the core-shell CNFs produced here were in the micro scale (~3.5 μm).
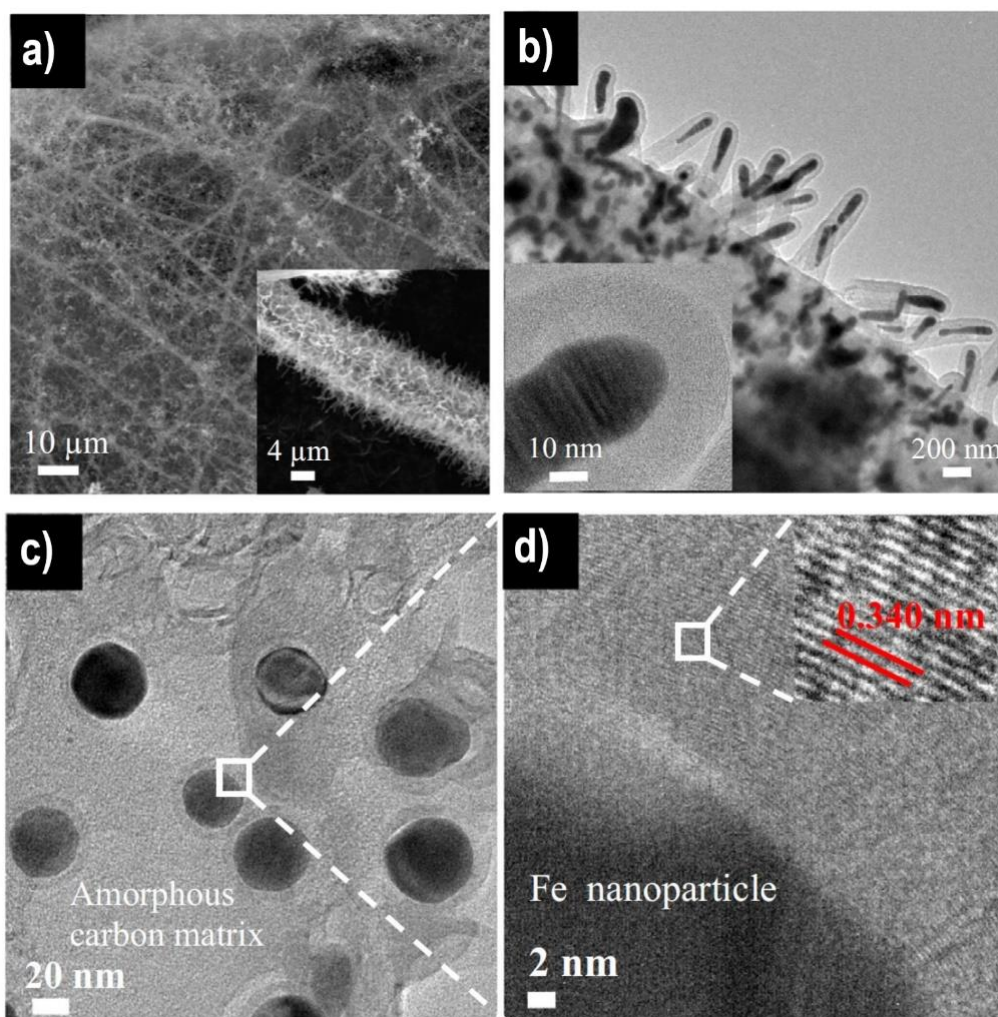
Figure 2.6: Carbon nanotubes grown on lignin/PAN-based CNFs doped with metals; a) and b) Pd-doped CNFs; c) and d) Fe-doped CNFs [57]. The red marks measure an interlayer spacing of 0.340 nm

2.4.3 Electrospun carbon nano- and submicron-fibers prepared from lignin/PVA

PVA is also very often combined with lignin for the preparation of electrospun CNFs. Although it gives a very low carbon yield when treated at elevated temperatures (<10 wt%) [8], it is soluble in water, therefore, it has high processability and the use of toxic solvents can be avoided. Moreover, similarly to lignin, the oxygen atoms in its macromolecule contribute to the development of microporosity [62].

Professor Hao Fong's group has reported in various articles the fabrication of lignin/PVA-based electrospun CNFs and their applications in adsorption, catalysis and energy storage [24,62-65]. Starting from a 70/30 lignin/PVA mass ratio, the precursor electrospun fibers are initially subjected to a lengthy stabilization step (>24 h) prior to carbonization. The CNFs have average diameters of less than 200 nm, and they possess a significant BET surface area of 583 m^2/g with an average pore size of 3.5 nm. These fibers were applied as adsorbents for the removal of methylene blue and tannic acid from aqueous solutions [62]. Comparing with commercial activated carbon of higher BET surface area (964 m^2/g), the CNFs exhibited almost 9-times higher adsorption capacity for methylene blue and 3.5 times higher adsorption capacity for tannic acid, accompanied with faster adsorption kinetics. The key property here was the relatively large average pore size, which posed less restrictions to the internal diffusion of the adsorbates into the adsorbent pores.

Furthermore, these fibers were tested as electrodes in supercapacitors, in which they exhibited a specific capacitance of 64 F/g at 400 mA/g current density, with 90% capacitance retention after 6000 cycles [24]. In order to improve their electrochemical performance, they were surface-decorated with varied amounts of MnO_2 nanowhiskers after treatment with $KMnO_4$ (Figure 2.7) [63]. In addition, the research group tested

the lignin/PVA-derived CNFs as electrocatalysts for the oxygen reduction reaction in alkaline fuel cells, after they were doped with Ag [65]. The deposition took place through the supercritical CO_2 method, after which Ag-nanoparticles sized ~2-10 nm were uniformly deposited on the fiber surface. For CNFs loaded with 15 wt% Ag, their electrocatalytic activity was higher than that of a commercial Pt/C catalyst, recording a mass activity of 119 mA/mg.
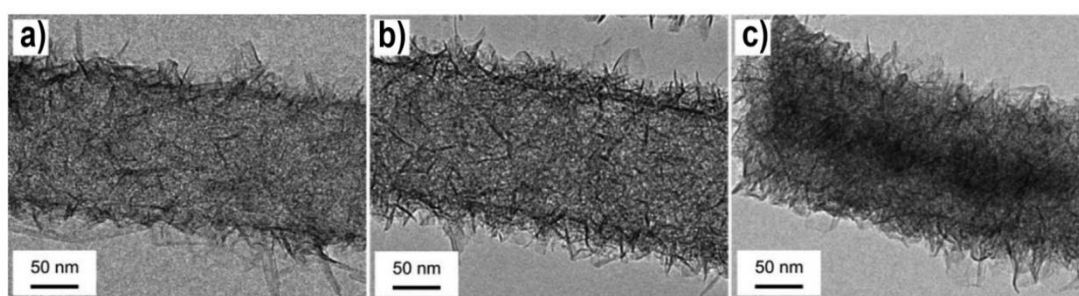
Figure 2.7: TEM images showing MnO_2 nanowhiskers grown on lignin/PVA based CNFs; the mass ratio between CNFs and MnO_2 is: a) 2/1; b) 1/1; c) 1/2 [63]

Another doping strategy has been implemented in order to use lignin/PVA-derived CNFs as electrodes in LIB [64]. Here, the CNFs were doped with F_2O_3, which is known to possess a high theoretical capacity (1007 mAh/g). After proper treatment of the CNFs with iron precursors, nanoparticles of 50 nm average size were uniformly deposited on the fiber surface. The electrochemical measurements revealed that the CNFs containing 35 wt% Fe_2O_3 nanoparticles showed a remarkable specific capacity of 715 mAh/g after 80 cycles, reflecting a good electronic conductivity and superior lithium permeability. Undoped Lignin/PVA-based CNFs activated with KOH have elsewhere exhibited a BET surface area of 1049 m^2/g and a capacity value of 272 mAh/g (at 50 mA/g) after 100 cycles [66].

Various other articles describe the utilization of lignin/PVA electrospun CNFs in energy-related applications (supercapacitors, LIB, dye-sensitized solar cells). Jayawickramage et al. [67] have reported the fabrication of mesoporous CNFs from a lignin/PVA blend of mass ratio ranging between 90/10 and 75/25. After activation with CO_2, the average fiber diameter dropped significantly from around 600 nm to less than 200 nm, mainly due to the decomposition of PVA. At 20 wt% PVA content, the activated CNFs exhibited a very large BET surface area of 2170 m^2/g. The role of PVA as a porosity-generating template has also been highlighted in the work of Ago et al. [68]. Here, the authors report that at 75/25 mass ratio between lignin and PVA, the PVA spontaneously segregated during electrospinning, producing precursor fibers with microphase separation. As PVA decomposes during carbonization, it acts as a sacrificial polymer inside the lignin scaffold. After activation with KOH, the CNFs possessed a high BET surface area (2005 m^2/g) of mesoporous texture, and they were used as free-standing working electrodes in supercapacitors. Their specific capacitance amounted to 205 F/g, with a capacity retention of 83% after 1500 cycles.

As a means to boost their mechanical and electrical properties, a twisted CNF yarn morphology has been elsewhere suggested, which can be fabricated after the electrospinning step using a rotating motor assembly (Figure 2.8) [69]. This twisted form enhances the tensile strength of the CNFs by an order of magnitude (523 MPa vs. 48.5 MPa of the untwisted mat) and their electrical conductivity (21.9 S/cm vs. 8.4 S/cm). However, their specific capacitance drops considerably (by more than 20 times) compared to the untwisted mat, because the twist produces more compact yarns and eliminates the voids among the fibers which are crucial for the ion transport.

On the other hand, Zhao et al. [70] focused more on the positive impact of the carbonization temperature on the electric properties of the CNFs. Raising the

temperature to $1500^{\circ}C$ produced mesoporous CNFs with 941 m^2/g BET surface area, which boosted their electrical conductivity (502 S/cm vs. 212 S/cm for CNFs carbonized at $1000^{\circ}C$) due to a higher degree of graphitization. These fibers were tested as binder-free counter electrodes of dye-sensitized solar cells, and exhibited a conversion efficiency of 7.60%, a value which is very close to that of a conventional Pt electrode.
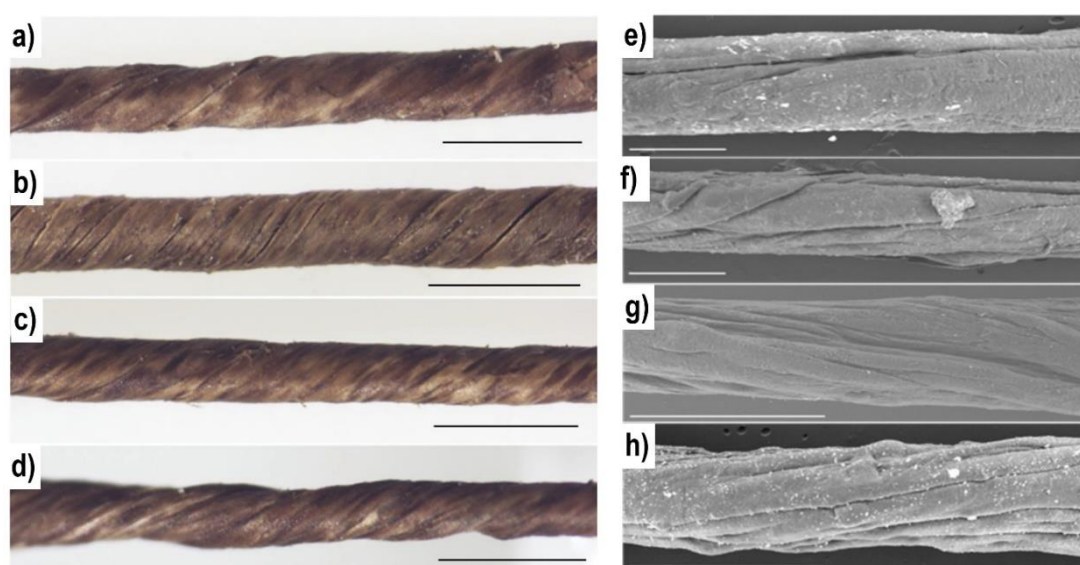
Figure 2.8: Images of twisted lignin/PVA electrospun fibers with different number of turns per cm; a) 23; b) 44; c) 54; d) 78 turns per cm (scale bar is 500 μm); e)-h) SEM images of the corresponding CNFs (scale bar is 200 μm) [69]

Moreover, Lignin/PVA-derived CNFs have been employed as adsorbents of high surface area. Activation with KOH has been reported to create a texture consisting of micro- and mesopores, reaching a BET surface area of 1147 m^2/g [71]. Meng et al. [72] studied the adsorption of volatile organic compounds (toluene, methanol, acetone) in the gas phase on a bed of activated CNFs. The activation process was performed through treatment with KOH, which altered the surface chemistry of the fibers by incorporating oxygen functionalities. BET surface area measurements are not reported

here, though. It was found that the non-polar toluene adsorbed to a larger extent through physical and chemical adsorption, and the lactone groups had a positive contribution in that. On the other hand, the more polar acetone and methanol showed a preference for adsorption on more polar sites. The same research group has further reported the enhancement of porosity through doping with Fe_3O_4 [73]. The presence of the metal oxide promoted the development of micropores in the CNFs and brought a huge increase in their BET surface area which reached the value of 1466 m^2/g, while the undoped ones had a BET surface area of 117 m^2/g. Elsewhere, the same group have reported the fabrication of ZnO-doped CNFs based on lignin/PVA which possessed a BET surface area of 486 m^2/g [74]. These fibers displayed a promising potential for being used as sensors in environmental-related applications.

2.4.4 Electrospun carbon nano- and submicron-fibers prepared from lignin/PEO

Small amounts of PEO (usually 1-10 wt%) are often added to lignin to improve its spinnability. PEO forms hydrogen bonds with the phenolic hydroxyl-groups of the lignin macromolecules; studies have shown that these interactions are dependent on the type of lignin (softwood/hardwood) [90]. Hence, it provides the necessary chain entanglements that facilitate electrospinning, while it doesn't interfere with the transformation of lignin to carbon [40].

Shi et al. [81] have reported the blending of lignin with PEO in mass ratios of 95/5 respectively, in order to study the carbonization behavior of three different types of lignin, namely, ethanol-organosolv lignin, formic acid/acetic acid-organosolv lignin and kraft lignin, named after their extraction method. It was found that the ethanol-organosolv lignin had a very low molecular weight and it could not be thermostabilized as it melted. Similar results about this type of lignin have been reported elsewhere [4].

On the other hand, formic acid/acetic acid-organosolv lignin contains many side-chains, thus, it yielded defective carbon fibers with poor mechanical properties. Kraft lignin, in contrast, produced smooth, compact fibers with a higher degree of graphitization and a tensile strength of 15.58 MPa, because its macromolecules have better orientation and fewer side-chains. Vivo-Vilches et al. [4] have further reported that phosphoric acid-lignin gives CNFs of higher mechanical stability than kraft lignin, due to its larger Mw and its higher purity.

The difference in the stabilization behavior depending on the type of lignin has also been highlighted by Cho et al. [37], who state that softwood kraft lignin can be stabilized at much faster heating rates (5-15°C/min) than the hardwood organosolv lignins (often ~0.1°C/min). Although the stabilization step aims at preventing the melting and collapse of the fibrous structure, the authors, here, stress the positive impact of a small degree of fusion in applications requiring mechanical stability. As the outer surface of the fibers softens, some "spot-welding" can be developed at junctions with other fibers. Following cross-linking reactions that take place during stabilization, these spots can act as strengthening knots that increase the tensile strength and the elastic resilience of the carbon nanofibrous mats. Moreover, the same research group has reported that this phenomenon boosts the electrical conductivity of the CNFs, as well, through facilitation of the electron transport [84]; adjusting the thermal treatment conditions to promote the interconnection between fibers boosted the electrical conductivity from 5 to 35 S/cm. Similar conclusions were drawn by Dallmeyer et al. [76] who measured improved tensile strength and electrical conductivity when interconnection between fibers occurred (Figure 2.9). Furthermore, Wang et al. [82] controlled the degree of fusion by incorporating an appropriate amount of PEO (10 wt%) in lignin. This resulted in an electrical conductivity of 10.53

S/cm. Therefore, the role of PEO in controlling the interconnection between the fibers is pivotal. In their case, the electrical conductivity was further increased to 12.24 S/cm after nitrogen doping via treatment with urea, while a specific capacity of 576 mAh/g (at 30 mA/g current density) was measured upon application in LIB [82]. Elsewhere, the conductivity of the CNFs has been shown to depend on the carbonization temperature, as the treatment at higher temperature (900^oC vs. 600^oC) was found to increase the conductivity by seven orders of magnitude due to the formation of a more ordered structure [78]. This observation agrees with other studies [70].
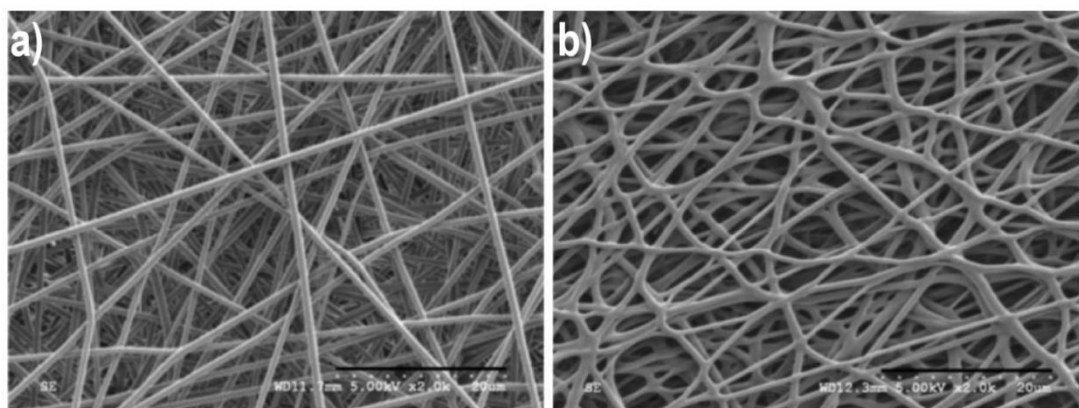
Figure 2.9: Lignin/PEO based CNFs with a different degree of interconnection [76]

Hu et al. [40, 77] have reported different approaches to raise the surface area of CNFs. Starting from a 90/10 lignin/PEO blend, NaOH or KOH were added at different ratios (10-50 wt% per lignin weight) in the electrospinning solutions. This quantity of alkali hydroxides is significantly smaller (only 0.1-0.25%) compared to the quantity usually needed when a post-carbonization treatment is performed for fiber activation. Here, activation of the fibers was conducted simultaneously with the carbonization at $850-900^o$C, for the production of micro-/mesoporous CNFs with a BET surface area of approximately 1400 m^2/g [40]. These fibers exhibited a specific

capacitance of 344 F/g with 96% cyclic stability after 5000 cycles [85]. Additional treatment with concentrated H_2SO_4 at 110-150°C for 20 h and hydrothermal treatment (water at 150°C, 5 atm for 24 h) caused fragmentation of the CNFs and widening of the pores, but it decreased the microporosity and the BET surface area (752-885 m^2/g) [77]. However, this treatment anchored sulfonic acid on the surface of CNFs, which were successfully applied in the hydrolysis of cellulose to glucose and nanocellulose.

Doping with Fe was applied by Wang et al. [83] and Yu et al. [75] to lignin/PEO precursors of 90/10 mass ratio in order to employ the CNFs as supercapacitor electrodes. Adding moderate amounts of Fe-acetylacetonate precursor (~20-25% per polymer mass) enhanced the electrochemical performance of CNFs in supercapacitors via the contribution of redox faradaic reactions; the specific capacitance in these cases amounted to 72.1-121.5 F/g. Another doping strategy has been reported through the coating of the CNF surface with Pd via electroless plating for enhancing their catalytic properties [79]. Schlee et al. [80], on the other hand, reported a significant increase in the volumetric energy density of CNFs in supercapacitors, by adding an oxidizing agent ($NaNO_3$) in the electrospinning solution which already contained NaOH. Without any stabilization, the fibers were directly carbonized in a reducing atmosphere (5% H_2 in N_2 at 800°C). The presence of $NaNO_3$ decreased the average fiber diameter by more than 50% compared to the undoped fibers (478 vs. 200 nm). Furthermore, this oxidizing salt enhanced the microporosity and anchored oxygen functionalities which contributed to pseudocapacitive effects.

2.4.5 Electrospun carbon nano- and submicron-fibers prepared from lignin blended with other polymers

Besides PAN, PVA and PEO, which are the most common binder polymers for the electrospinning of lignin, a few other polymers have been successfully used for

this purpose, each one contributing different features in the electrospun and in the carbonized fibers.

Jia et al. [88] blended kraft lignin with cellulose acetate at a 50/50 mass ratio. Cellulose acetate (CA) is the acetylated form of cellulose, which is an abundant, renewable, natural polymer like lignin. Hence, the production of CNFs in this case is totally based on natural precursors. Electrospun CNFs based on CA alone have been reported, as well [91]. An important issue that is associated with the use of this polymer for CNF preparation is that it must undergo deacetylation prior to carbonization to prevent its melting; this involves the treatment with a strong base, usually NaOH. Here it is reported, however, that after electrospinning, carbonization followed directly without stabilization, which in this case was not necessary probably due to the presence of lignin. The carbon fibrous structure, that was obtained, exhibited some fusion in the intersection of the fibers. Furthermore, Schreiber et al. [89] started from lignin/CA of different mass ratios (1/1-4/1 respectively), but stabilized the electrospun fibers initially with iodine vapor, and afterwards with heating in air at 300°C before carbonizing them. Iodine adsorbed in the lignin domains and helped stabilize the morphology, while the increasing lignin content resulted in a more disordered carbon structure.

Besides CA, polyvinylpyrrolidone (PVP) can also be used as a spinning agent for lignin. Although PVP gives a low carbon yield after carbonization, it can be dissolved in various solvents, so, it functions as a scaffold for the development of porosity after its thermal decomposition. Ma et al. [86] used a blend of lignin/PVP with 1/2 mass ratio respectively, which was also doped with Mg. After a long stabilization step at 150-50°C and carbonization at 800°C, highly porous CNFs were produced. In the absence of Mg, the fibers were microporous with BET surface area

of 600 m^2/g, while at the highest Mg-precursor/lignin mass ratio (2/1) the CNFs were highly mesoporous with a BET surface area of 1140 m^2/g. Guo et al. [87] combined PVP with a resin of lignin-phenol-formaldehyde (LPF), in which the lignin mass ratio was ~30%. The LPF/PVP mass ratio in the spinning solutions was 3/1. The precursor fibers were treated with a solution of a home-made polymeric precursor and then stabilized and carbonized. The polymeric precursor induced cross-linking and the fibers exhibited good dimensional stability. Porosity measurements in this case were not reported.

2.4.6 Conclusions drawn from the literature review

As it is described in the previous sections (2.4.1-2.4.5) the most important feature of electrospun lignin-based CNFs is the variety of manufacturing strategies including the choice of precursors, the additives, the conditions of thermal treatment and the feasibility of post-treatment. Based on the previous sections, a number of conclusions can be drawn:

i) Although a few articles describe the manufacture of electrospun CNFs from lignin alone, the usual case is the addition of a binder polymer that promotes the electrospinnability of lignin.

ii) Each of the binder polymers carries different features. PAN contributes to higher mechanical strength; PVA can be electrospun using non-toxic solvents; PEO contains oxygen which is beneficial for the stabilization and it can also control the degree of fusion among fibers; CA is derived from an abundant bioresource, thus, 100% bio-based CNFs can be produced from lignin/CA; PVP acts as a sacrificial polymer for the development of porosity.

iii) The electrospinning technique is suitable for minimizing the average fiber diameters and for controlling the morphology of CNFs. However, the use of organic solvents is an issue of consideration. Moreover, when low flow rates or low solution concentrations are required, the mass production of CNFs may not be viable.

iv) Using the electrospinning technique, CNFs with average diameters of as low as 100-200 nm can be manufactured. Lowering the average fiber diameter at these levels minimizes the mass transfer limitations when the CNFs are used as adsorbents, catalyst supports or electrodes.

v) The porosity of CNFs can be customized through physical or chemical activation and with a careful adjustment of the process conditions. BET surface areas with values higher than 1000 m^2/g are very common.

vi) The structure and the purity of lignin vary depending in its plant source and the method of extraction and these, in turn, influence the properties of CNFs. In general, kraft lignin can be stabilized faster than organosolv lignin but it contains a higher amount of ash.

vii) The slow stabilization is a limitation of the whole process especially for organosolv lignin, however, there are ways to accelerate it, e.g by adding H_3PO_4 in the electrospinning solution, or with iodine treatment of the precursor fibers.

viii) A very important feature of lignin-based CNFs is the interconnection among the fibers which comes as a result of controlled fusion. By adjusting this degree of interconnection, the electrical conductivity and the mechanical properties can be enhanced. However, excessive fusion compromises the surface area.

ix) Lignin-based CNFs can be easily doped with metals, metal oxides or nitrogen. Their surface chemistry can also be altered, e.g. through the anchoring of oxygen-containing functional groups.

x) Limitations arise from the structural complexity of lignin, the presence of impurities and its large polydispersity. Therefore, controlling its molecular structure, e.g. through fractionation, is desirable especially for improving the mechanical properties of CNFs.

Despite the limitations, it seems that lignin is a very attractive alternative for the production of CNFs. Replacing benchmark materials is a difficult task that requires the consideration of the cost arising from the disruption of established industrial practice. Nevertheless, the flexibility emerging from using lignin as a precursor allows the design of "bespoke" CNFs instead of relying to off-the-shelf materials. Furthermore, the long-term benefits of promoting a sustainable, circular economy should be decisive factors in the upgrade of existing technology.

2.5 Lignin blended with PET

In this research, lignin is blended for the first time with PET for the manufacture of electrospun CNFs. However, blends of lignin with PET as carbon fiber precursors have been reported before, using different techniques for the production of micro-sized fibers.

Kadla et al. [92] reported the fabrication of kraft lignin/PET fibers with melt spinning. The ratio of PET varied between 0-25 wt%. Although this blend exhibited better spinnability than the blends of lignin with poly(ethylene) and poly(propylene), the fiber formation was more difficult compared to pure lignin, so the researchers didn't proceed with the carbonization process. Kubo and Kadla [93] further reported the melt spinning of kraft lignin blended with PET. The PET ratio varied between 0-100 wt% and the processing temperature between 195-273°C. The diameter of the produced carbon fibers ranged between 30-45 μm, while improved tensile strength was reported

compared to carbon fibers derived from pristine lignin. Due to good miscibility of the two materials the fiber surface was smooth, but the carbon fiber yield decreased with increasing the PET content. The researchers suggested that the good miscibility of the two materials probably derives from π-type interactions of the aromatic rings that both polymers contain in their molecules. The same researchers report elsewhere [94] that, in lignin/PET blends, there is no hydrogen bonding, but only weak intermolecular interactions. Finally, Compere et al. [95] also reported the fabrication of lignin/PET fibers by melt spinning and subsequent carbonization. The fiber diameters ranged between 11-13 μm.

Despite the scarce reports of carbon fibers produced from lignin/PET and the absence of any research till now related to lignin/PET electrospun CNFs, the goal of combining lignin with PET is intriguing and it carries certain advantages. The total global consumption of plastics increases annually by 5-6% [8], while PET is one of the most widely used commodity plastics and the main material for the manufacture of water bottles, therefore it is a major component of municipal waste. Moreover, PET is one of the most widely recycled plastics in the world, and according to the relevant data the most widely recycled plastic in the USA in terms of weight of plastic material recycled [96]. Therefore, it would be desirable to investigate new potential applications for recycled PET. This task would contribute to more efficient waste management, as the concept of producing useful products from waste is a key concept of sustainability.

Chapter 3: The Need for Improved Desulfurization Technologies

3.1 The problem of sulfur in fuels

Crude oil is a complex mixture consisting mainly of hydrocarbons, but it also includes a small yet significant amount of compounds which contain sulfur, oxygen, nitrogen and metals. Generally, the range of sulfur content in crude oil is 0.05-10 wt%, but most commonly it varies between 1-4 wt% [97]. These crude oils that contain less than 1 wt% sulfur are termed as sweet or low-sulfur, while those with more than 1 wt% are termed as sour or high-sulfur. The sulfur compounds in petroleum can be either inorganic or organic. The former category includes elemental sulfur, COS (carbonyl sulfide), H_2S (hydrogen sulfide), and dissolved pyrites, while the latter includes compounds in which sulfur exists as a heteroatom bounded to a hydrocarbon molecule [13, 97]. Figure 3.1 summarizes the most common organic sulfur compounds encountered in crude oil. Alkyl-substituted derivatives of these molecules are usually encountered, as well [12].

The presence of sulfur in crude oil poses a serious concern as it is associated with various problems and adverse effects. First, many sulfur compounds are harmful to human health. For example, heavier thiophenes are carcinogenic upon exposure of humans to certain levels [13]. Thiols have an unpleasant repulsive odor and they can cause nausea, breathing problems, irritation to the eyes, the throat and the lungs, unconsciousness and muscular spasms [13]. Moreover, sulfur compounds raise environmental concerns as they contribute to the atmospheric pollution. SO_2 is produced during combustion, which contributes to the phenomenon of acid rain and to the photochemical smog, two serious threats to the flora and fauna [13].
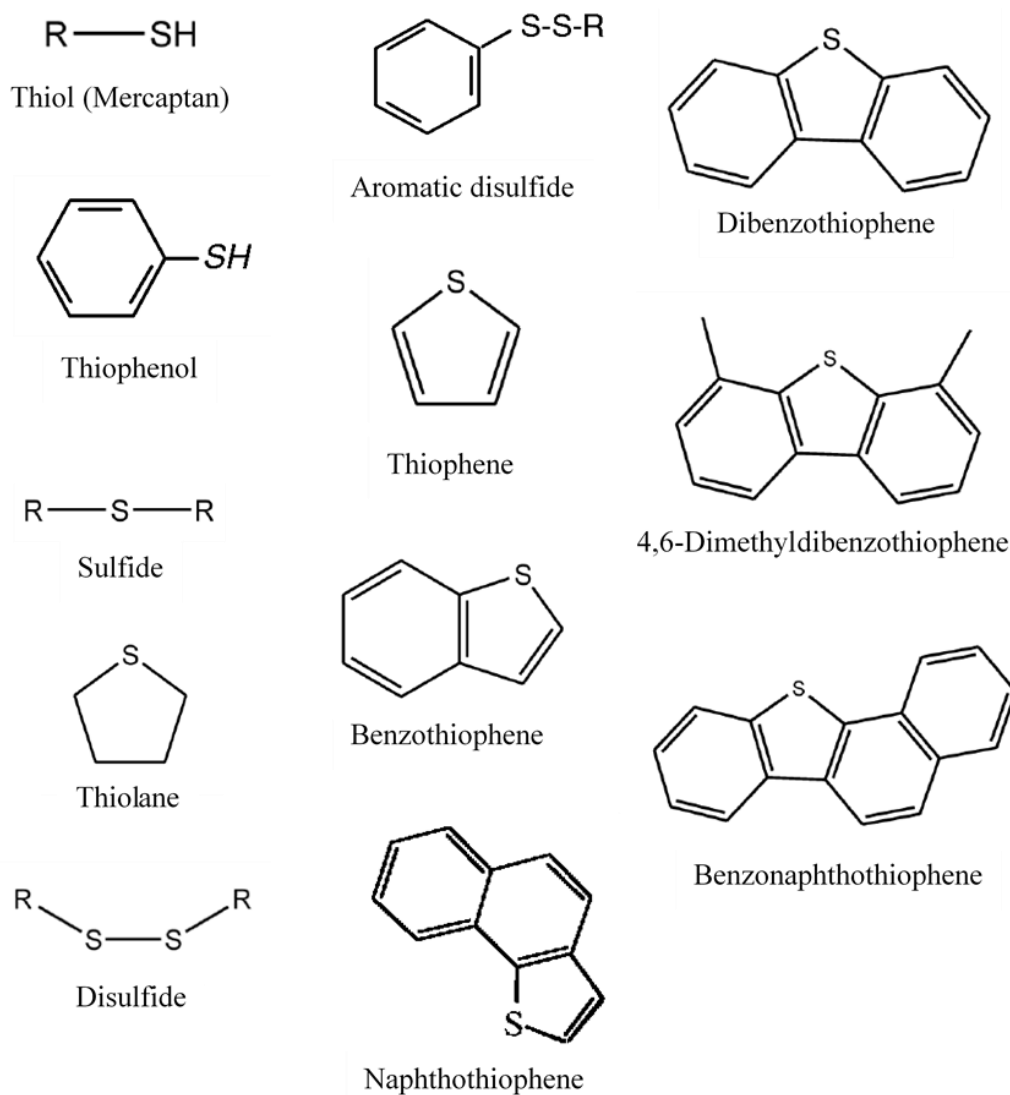
Figure 3.1: Common organic sulfur compounds in crude oil. Adapted from [12, 97]

In addition, some compounds such as H_2S and lower aliphatic sulfides and mercaptans cause corrosion to the distribution pipelines and to the equipment of the refineries, increasing the maintenance costs and obstructing their operation [13]. A serious concern to many refining processes is also caused by the deleterious effect of sulfur compounds on catalysts. These molecules are selectively adsorbed on the surface of metal catalysts, such as Cu, Ni, Co, Pb, Pt, and Ir, and they tend to deactivate

them [13]. Finally, the presence of sulfur in gasoline tends to decrease its octane number, therefore additional processing is required in order to reach the necessary specifications [13].

Because of the detrimental effects of sulfur compounds on human health and on the environment, the competent authorities in most countries apply regulations in order to limit the sulfur content of commercial fuels. These regulations have become even more stringent with time, especially in the USA and in the EU. In the EU during the 90's, the maximum sulfur content for diesel was set to 350 ppm and for gasoline to 150 ppm [10]. Since 2009 however, the limit is 10 ppm for both fuels [98]. Similarly, in the USA the current limits set by the US Environmental Protection Agency are set to 15 ppm for diesel and 10 ppm for gasoline [9, 99], while recent specifications in China and in Japan demand an upper limit of 10 ppm for diesel [100, 101]. In the United Arab Emirates, the Emirates Authority for Standardization and Metrology has issued a standard regulating the sulfur content of diesel fuel to 10 ppm, as well (UAE.S 477:2013) [11]. Moreover, the International Maritime Organization has decided to lower the limit of sulfur content for marine fuels from 3.5 wt% to 0.5 wt% starting in 2020 [102].

Furthermore, in the recent decades there has been a growing interest in the development of fuel cells, aiming to the transition towards cleaner fuel technologies. Under this concept, research has focused on the development of cars based on hydrogen-powered fuel cells, such as polymer electrolyte membrane fuel cells (PEMFC) and solid oxide fuel cells (SOFC) [12]. The problem is that these systems which use hydrocarbon fuels as feedstock are very sensitive to the presence of sulfur. PEMFCs demand a maximum sulfur content of 0.1 ppm, while solid oxide fuel cells can tolerate a maximum of 10 ppm [12]. Therefore, the regulations regarding the

specifications of automobile fuels as well as the universal need to promote the use of cleaner fuels constantly drive the effort to develop more efficient technologies for deep desulfurization.

3.2 Desulfurization strategies

Today, hydrodesulfurization (HDS) is the most common process in the refineries for the removal of sulfur compounds from petroleum distillates. This process was initially developed in the 1930s, and it is in use till now [12]. In HDS, the distillate is fed together with hydrogen gas in the catalytic reactor operating at elevated temperatures (320-440°C) and pressures (ranging from 15 up to around 200 atm) [12, 13]. The process conditions depend on the feedstock, with heavier petroleum fractions demanding higher operating temperatures and pressures [12]. Commonly used catalysts are sulfides of Mo or W supported on alumina and promoted by Co or Ni [12]. The HDS reaction proceeds through hydrogenation and hydrogenolysis [12].

Considering the variety of sulfur compounds found in petroleum and the differences in their structure and physicochemical properties, one should expect that each one exhibits different HDS reactivity. Indeed, HDS is very efficient for thiols, disulfides and sulfides, because they have higher electron density of the S atom and weaker C-S bonds [12]. In contrast, in the thiophenic compounds, the S atom conjugates with the π-electrons of the aromatic ring, therefore these bonds are stronger. There is also significant steric hindrance especially for the compounds which contain alkyl-substituents, so it is harder for the S atoms to reach the active centers of the catalyst. Hence, compounds such as 4,6-dimethyldibenzothiophene (higher thiophenes) present a very low HDS reactivity and are very difficult to be removed through this process; these compounds are termed as refractory sulfur compounds [12].

Table 3.1: Distribution of sulfur compounds in different petroleum distillates (wt%) [13]

Distillate fraction	Boiling Point range (°C)	Thiols	Sulfides	Thiophenes	Higher thiophenes
Naphtha	70-180	50	50	Rare	-
Kerosene	160-240	25	25	35	15
Diesel	230-350	15	15	35	35
Vacuum gas oil	350-550	5	5	30	60
Vacuum residue	>550	Rare	Rare	10	90

Table 3.1 shows the distribution of various sulfur compounds in different petroleum distillates, while Figure 3.2 summarizes the HDS reactivity of some representative molecules. Besides the problem of removing certain refractory compounds, reaching ultra-low concentrations of sulfur is more difficult to be achieved with HDS, as it requires extreme operating conditions; that is, very high temperature and pressure, and higher consumption of catalyst and H_2, in order to remove a greater amount of sulfur [12, 13].

As a consequence, alternative ways for the efficient deep and ultra-deep desulfurization of petroleum distillates have been investigated in the recent years. Some of the proposed alternatives are extractive desulfurization using specialized solvents, precipitative desulfurization, biodesulfurization using microorganisms, oxidative desulfurization, and adsorptive desulfurization on appropriate tailor-made adsorbents [12, 13].
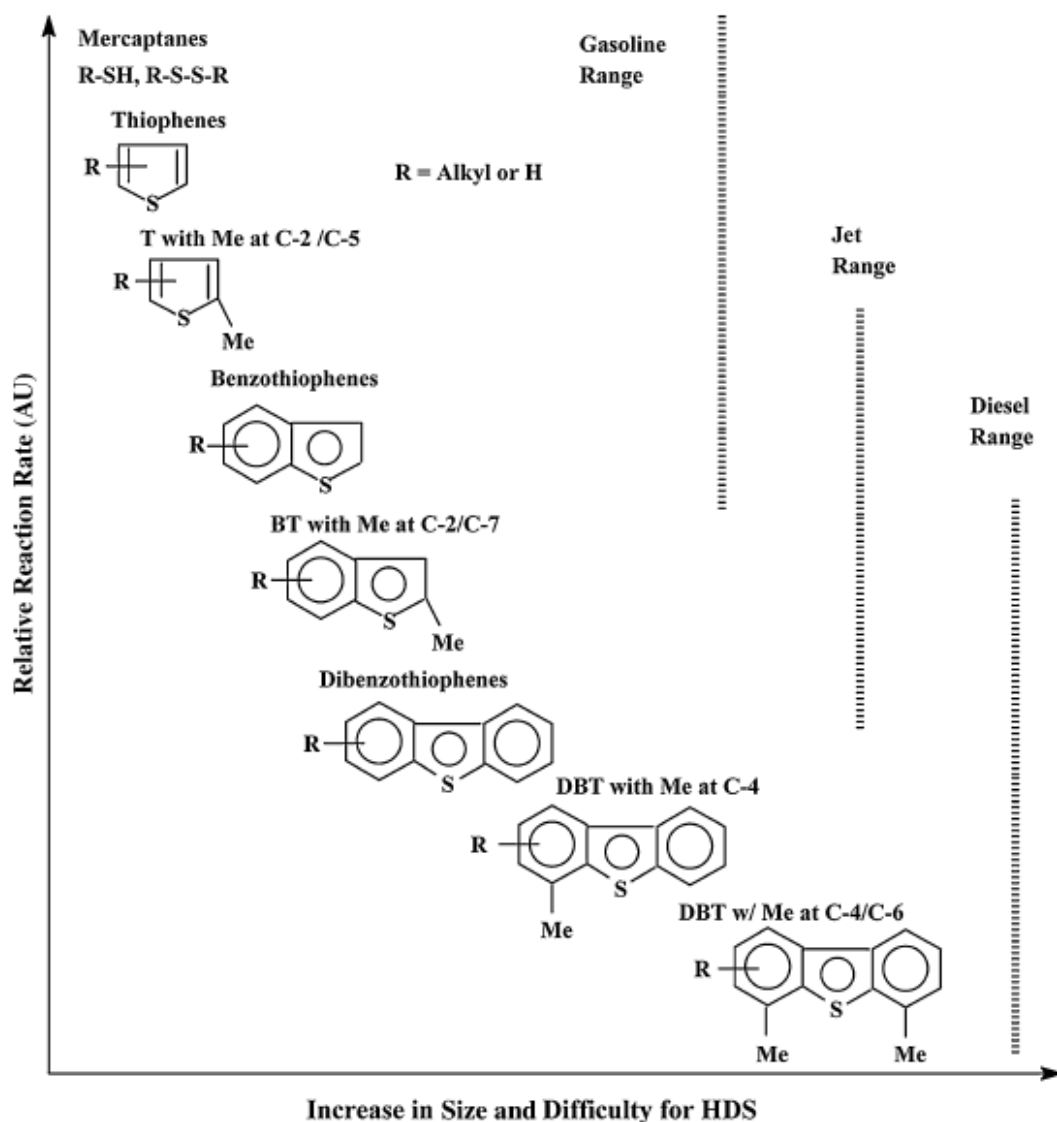
Figure 3.2: HDS reactivity of various organic sulfur compounds with respect to their ring sizes and alkyl substitutions; T: thiophene, BT: benzothiophene, DBT: dibenzothiophene, Me: methyl-group. Adapted from [12]

Among these methods, the adsorptive desulfurization seems to be a very promising alternative to be used either alone or in conjunction with other methods, as it is less energy intensive, it can be carried out under mild conditions of temperature and pressure, it doesn't require the consumption of H_2 or liquid solvents, and the adsorbents can be tailored for high selectivity of sulfur compounds [12, 13]. An example of adsorptive desulfurization used in the industrial scale is the S-Zorb process

introduced by Phillips Petroleum Co. in 2001 in which selective adsorption is combined with hydrotreatment [12, 13].

The desirable inherent properties of an adsorbent, that enhance the efficiency of an adsorptive desulfurization process, include:

a) Its high surface area [103].

b) Its high total pore volume [104].

c) Its high micropore volume [105].

d) The presence of oxygen-containing functional groups [106].

e) The presence of transition metals or metal oxides [107, 108].

f) Possible doping with heteroatoms [109].

g) Its selectivity over aromatic or aliphatic hydrocarbons [110].

h) Its regenerability [111,112].

i) Its thermal stability when the process is conducted at high T.

j) Its low cost.

Carbon-based adsorbents, in general, possess most of these properties, and the additional advantage that they can relatively easily be functionalized or modified to improve their performance. Their main disadvantage is probably the selectivity against aromatic components, while their regeneration is also an important factor to be considered.

3.3 CNFs for adsorptive desulfurization

Various researchers have focused on different adsorbents, including carbon nanomaterials, activated carbon, metal-organic frameworks, metal-oxide nanoparticles and zeolites. For the purpose of this review, the focus will be on carbon nanofibers that have been tested for the adsorption of various types of sulfur compounds.
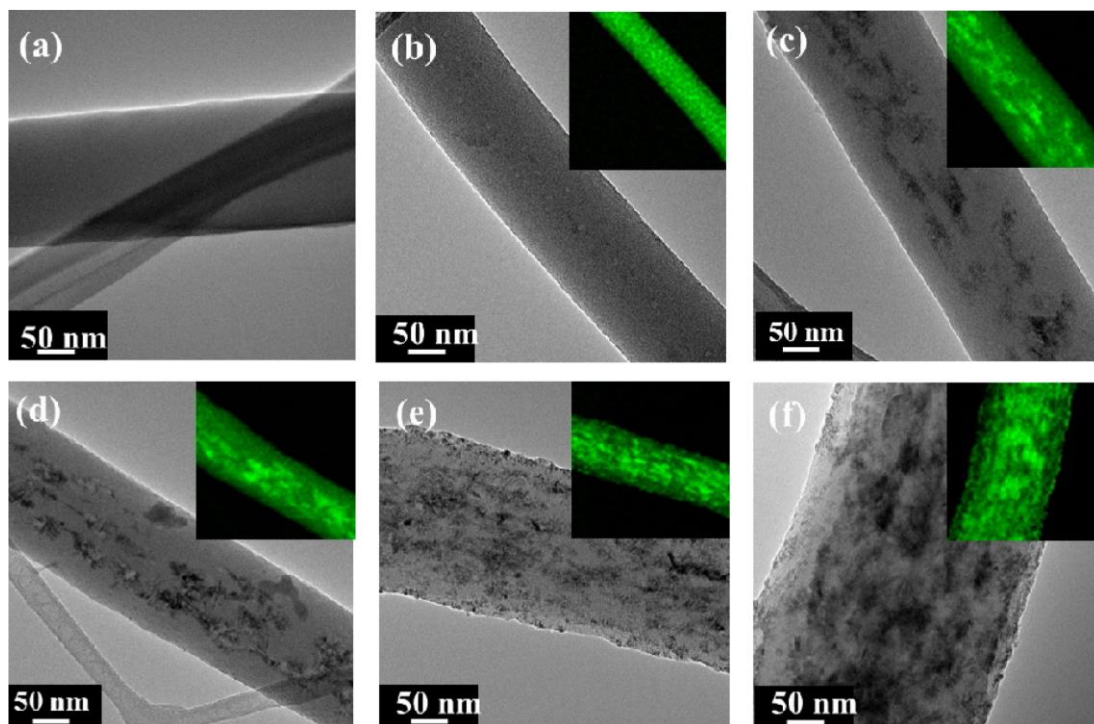
Figure 3.3: TEM images of CNFs containing different amount of ZnO nanoparticles; a) 0; b) 13.6; c) 19.0; d) 25.7; e) 29.5; f) 34.2 wt% [18]

Kim et al. [18] prepared carbon nanofibers decorated with ZnO nanoparticles for the adsorption of H_2S from a stream of nitrogen. CNFs were prepared from the thermal treatment of poly(acrylonitrile) (PAN) nanofibers, which had been fabricated using the electrospinning technique. The decoration was carried out by adding zinc acetate dihydrate in the spinning solutions and a subsequent thermal treatment; the nanoparticle content on the surface of CNFs amounted to 13.6-34.2 wt%. The average diameter of the various CNF samples was 152-304 nm, with the larger diameters appearing for the samples of higher ZnO content. Figure 3.3 shows TEM images of the CNFs containing different amounts of ZnO. It was found that when the ZnO content was increased, the average nanoparticle size also increased due to agglomeration; therefore, at 25.7 wt% ZnO content, the nanoparticles had an average diameter of ~10 nm, while at a higher content, their average diameter increased to 50-

80 nm, as more bulky clusters formed. Obviously, this is not desirable for the adsorption process, as a percentage of their surface is rendered inaccessible to the adsorbates and therefore useless. As a result, the maximum breakthrough time for a breakthrough concentration of 1 ppm was observed for CNFs containing 25.7 wt% ZnO (530 min/g-adsorbent) and it was significantly larger than the breakthrough time of undecorated CNFs (76 min/g-sorbent) or than that of pure ZnO (160 min/g-sorbent). In contrast, CNFs with a very high ZnO content of 34.2 wt% showed a breakthrough time of only 143 min/g-adsorbent.

Bajaj et al. [19] also utilized CNFs prepared from electrospun PAN, but their strategy was to decorate it with Cu/Cu_xO nanoparticles for the adsorption of H_2S. The term "Cu/Cu_xO" denotes that after activation of the nanofibers, it was found that Cu nanoparticles were present together with their oxides on the nanofiber surface. Here, in contrast to the breakthrough time for pure CNFs, which was 62 min/g-adsorbent, the CNFs with 10 wt% Cu/Cu_xO showed a breakthrough time of 791 min/g-adsorbent, while for those with 30 wt% Cu/Cu_xO it was 938 min/g-adsorbent, which is around 15 times higher than that of undecorated CNFs.

Karami et al. [113] used commercial CNFs for the adsorption of 1-butyl mercaptan (1-butanethiol) from hexane, after first activating them through treatment with acids (HNO_3, H_2SO_4, HCl) and decorating them with various amounts of Ni through electroless coating. The adsorption studies showed that the CNFs which were coated with the highest amount of Ni (around 800 ppm) exhibited the highest percent of removal from the model diesel (~70%). Moreover, investigation of the adsorption kinetics revealed that increasing the amount of Ni in CNFs caused an increase in the adsorption rate constants, denoting acceleration of the process. For first-order kinetics,

CNFs containing ~300 ppm Ni had a rate constant of 0.7 s^{-1}, while for those with ~800 ppm the rate constant was 2.3 s^{-1}.

Besides electrospinning, CNFs can be also synthesized via chemical vapor deposition (CVD). Bigdeli et al. [104] used CVD to grow CNFs from methane and ethane gases on the surface of activated carbon, attempting to increase its surface area. Here, Ni was used as a catalyst for CNF growth; therefore, activated carbon was first decorated with it. It was found that CNFs synthesized from methane gas were thinner (average diameters in the range of 45-55 nm) than those synthesized from ethane (120-190 nm). The presence of CNFs also significantly increased the specific surface area of the adsorbents, from the value of 529 m^2/g for the initial activated carbon, to 714 m^2/g for the sample containing CNFs synthesized from ethanol and 790 m^2/g for those synthesized from methane; the total pore volume was doubled, as well. These adsorbents were tested for the removal of thiophene or dibenzothiophene from n-octane. The results showed that the adsorption capacity of the CNF-containing samples was close to 13 mg/g for dibenzothiophene and close to 5 mg/g for thiophene; these numbers were almost double compared to the adsorption capacity of the initial activated carbon for both adsorbates. The higher adsorbed amount of DBT compared to thiophene can be attributed to its higher molecular weight, and to its plate shape, which allows more interactions with the adsorbent.

CVD-synthesized CNFs for the adsorption of thiophene from octane were also tested by Prajapati et al. [114]. Here Cu was used for the growth of CNFs and then they were thermally treated for increasing their surface area and also decorated with Ni. Thermally treated Ni/Cu-CNFs exhibited a specific surface area of 346 m^2/g, much higher than the simple Cu-grown CNFs (107 m^2/g). This was obviously reflected to their adsorption capacity, which was 0.5 mgS/g with a breakthrough time of 130 min;

in contrast, simple Cu-grown CNFs showed an adsorption capacity of 0.03 mgS/g and instant breakthrough. It was also found that increasing the temperature of adsorption from 30°C up to 200°C had an adverse effect on the process by decreasing the breakthrough time and adsorption capacity. It was, therefore, concluded that the adsorption of thiophene is exothermic and thus, favorable at low temperatures.

The presence of CNFs is not always favorable for adsorption, as the process also depends on other characteristics such as the adsorbate characteristics or the substrate. Prajapati et al. [115] synthesized Ni-doped activated carbon beads with CNFs grown on them through CVD using acetylene. CNFs were observed to be hollow, with average diameter close to 70 nm. While the starting activated carbon beads had a significantly large specific surface area (1159 m^2/g), when CNFs grew on them, their surface area dropped to around 500 m^2/g because many micropores were blocked. The authors used these adsorbents for the removal of thiophene from n-octane. The presence of Ni was proven to boost the adsorption in all cases. The results showed that for DBT the efficiency of the adsorbent containing CNFs was much smaller at all temperatures due to decreased surface area and total pore volume (8.2 mgS/g vs. 27.3 mgS/g for the case of activated carbon beads alone). In contrast, for the adsorption of thiophene there was no significant difference in absolute numbers (capacity close to 86 mgS/g for each of them). Considering, however, that the adsorbent containing CNFs had much smaller surface area and pore volume, the capacity of CNFs was larger in this case. The most probable explanation stated by the authors is the difference in the molecular size between thiophene and DBT; thiophene is much smaller, so its adsorption is mostly dependent on the pore filling.

Chapter 4: Experimental Part

4.1 Materials

Kraft lignin (low sulfonate content, Mw~10,000 g/mol) was purchased from Sigma-Aldrich (#471003) and it was used without further modification. Waste water-bottles were used as the source of PET. All of them came from the same bottling company in the U.A.E. (Masafi). Prior to the preparation of the spinnable solutions, the bottles were left to dry and then, they were cut into pieces. The Melt Flow Index (MFI) of the used PET was measured to be 72 g/10 min at 265°C with 2.16 kg load (measurement with a Chengde Jingmi (XRL-400) plastometer according to ASTM D1238). Similar MFI values for PET which has undergone thermal processing cycles, as it is expected for the raw PET used in this research, have been reported elsewhere [116, 117]. For pristine PET, an indicative MFI value found in the literature is 23 g/10 min [117, 118]. For comparison, PET with MFI 20 g/10 min has an indicative molecular weight (Mw) of 42100 g/mol [119]. Trifluoroacetic acid (TFA, 99%) purchased from Merck was used as the solvent for the electrospinning process.

High purity N_2 (99.999%) was used in all the carbonization experiments. High purity CO_2 (99.99%) was used in the activation experiments of Section 5.3. HNO_3 65%, HCl 37%, bromothymol blue, NaOH pellets and KOH pellets were purchased from Sigma-Aldrich. For the adsorption experiments (Section 5.4), dibenzothiophene (DBT, 98%) and 4,6-dimethyldibenzothiophene (DMDBT, 97%) purchased from Sigma-Aldrich were used. N-dodecane (99%) was used as a model diesel fuel, and it was purchased from Riedel de Haen. Commercial activated carbon (Merck 1.02186, BET surface area 775 m^2/g) was used for comparison in the adsorption experiments.

4.2 Preparation and characterization of precursor electrospun fibers from lignin/r-PET

In the following paragraphs, the methodology applied here for the preparation of the electrospun precursor nanofibers will be presented.

4.2.1 The electrospinning process and the experimental design
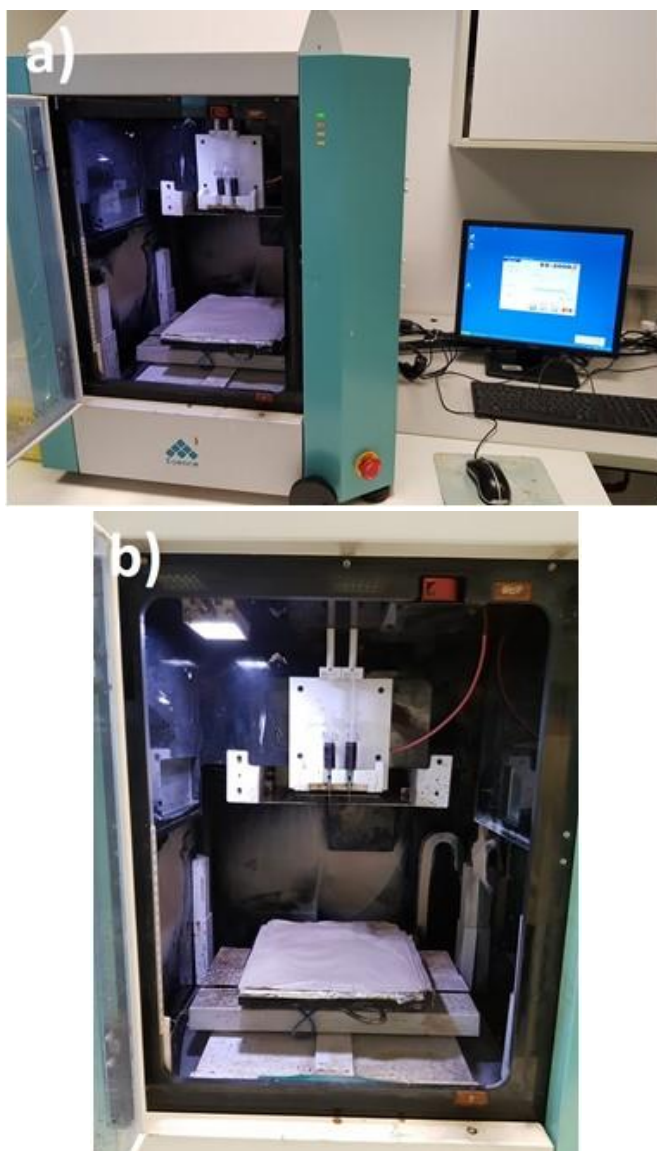
Figure 4.1: The electrospinning apparatus used in this research; a) general view; b) detailed view of the electrospinning chamber with the syringes and the collector

The electrospinning solutions were produced after certain quantities of lignin and r-PET (Table 4.1) were dissolved in TFA under magnetic stirring at room temperature. Then, each solution was transferred to two disposable 10 mL syringes (21G needle) which were placed inside the electrospinning apparatus. The electrospun mats were fabricated in a FUENCE E-sprayer (ES-2000S) apparatus in which the setup has vertical orientation similar to the one shown in Figure 2.2. The electrospinning apparatus used in this research is shown in Figure 4.1. The grounded collector was moving horizontally during the process in a controlled pattern, while there was continuous ventilation inside the closed electrospinning chamber.

In the first stage of this research, a Design-of-Experiments statistical methodology was applied in order to estimate which electrospinning factors influence the average fiber diameter and how (Section 5.1). The design factors of the electrospinning process were the distance between the needle and the collector, the applied voltage, the flow rate of the solution, the concentration of both polymers in the solution and the lignin mass ratio in the polymer blend. Two response variables were chosen: the average fiber diameter and the standard deviation of the fiber diameter.

The levels of the various factors were determined after some preliminary experiments, in which the limits of the experimental area were investigated. For reliably assessing the effect of each factor on the response, it is necessary that the experimental area is as wide as possible, so the range of each factor should be as wide as possible. The criterion for deciding on the range of each factor was the continuous formation of fibers without spray falling on the collector. In addition, the electrospinning apparatus used in this research has certain limits regarding the allowed values of each factor; the maximum voltage allowed is 30 kV, the maximum spinning distance 20 cm and the minimum flow rate 0.1 μL/min. Therefore, the design factors

and their value range, as it was decided after some preliminary experiments, are presented in Table 4.1. In the electrospinning apparatus used, the fiber spinning was taking place in a closed chamber with controlled ventilation; therefore, all the electrospinning experiments were conducted at room temperature (~23-25°C).

Table 4.1: Design factors and their respective levels

	Levels	
Factors	**Low**	**High**
Needle-collector distance (factor A)	7 cm	20 cm
Concentration of both polymers in the solution (factor B)	15% w/v[*]	25% w/v[*]
Lignin mass ratio in the polymer blend (factor C)	20%	50%
Voltage (factor D)	20 kV	30 kV
Flow rate (factor E)	0.1 μL/min	2 μL/min
[*]the unit w/v denotes weight of polymer (grams) per 100 mL volume of solvent		

Factorial designs are the standard methods of experimental design for screening purposes. Screening is an experimental methodology followed when many factors are involved in a process, and it is necessary to examine which of these factors actually influence the response and which don't. In order to avoid an excessive number of experimental runs, it is better to keep the number of factor levels low. Usually two factor levels are enough to characterize the process, and therefore, for each factor only the highest and the lowest value were chosen in order to construct a 2^k factorial design (where k is the number of factors). If more than two levels are chosen for each factor, the number of experiments increases exponentially; if five factors are to be examined, then a two-level full factorial design demands $2^5=32$ experimental runs, while a 3-level full factorial design demands $3^5=125$ experimental runs. Since a 2-level factorial

design can reliably indicate which factors are significant and which are not, it is the best option when many possible factors are involved. More details about the 2^k factorial designs can be found in [120].

For 5 factors, a 2^5 full factorial design demands 32 unreplicated experimental runs. In order to minimize the experimental runs, only the half fraction of the design was chosen. Therefore a 2^{5-1}, resolution V, fractional factorial design with 16 unreplicated randomized runs was constructed. When only a fraction of the factorial design is run, some information must be sacrificed. This information is the effect of the high-order interactions between the factors. The resolution is an indication of which factor interactions are sacrificed in order to obtain the maximum information under the specific conditions. Particularly, resolution V means that the main factors are aliased with the 4-way interactions and the 2-way interactions are aliased with the 3-way interactions. It is not possible to distinguish the different influence of two aliased effects on the response. However, the high-order interactions (e.g. 3-way, 4-way, etc.) are assumed negligible in most cases.

The experiments were conducted by two researchers. For estimating the possible influence of each operator on the responses, the runs were divided in two blocks. Moreover, two center points were added in each block, in order to add degrees of freedom to the process and estimate the errors more accurately; so, in total, 20 experimental runs were conducted. The experimental design was constructed and analyzed using the Minitab 17 software with 95% confidence interval (alpha value is 0.05). Figure 4.2 shows the experimental region and the experimental runs (the large dots at the edges of the cubes). The results of the analysis of the factorial design are presented in Section 5.1.
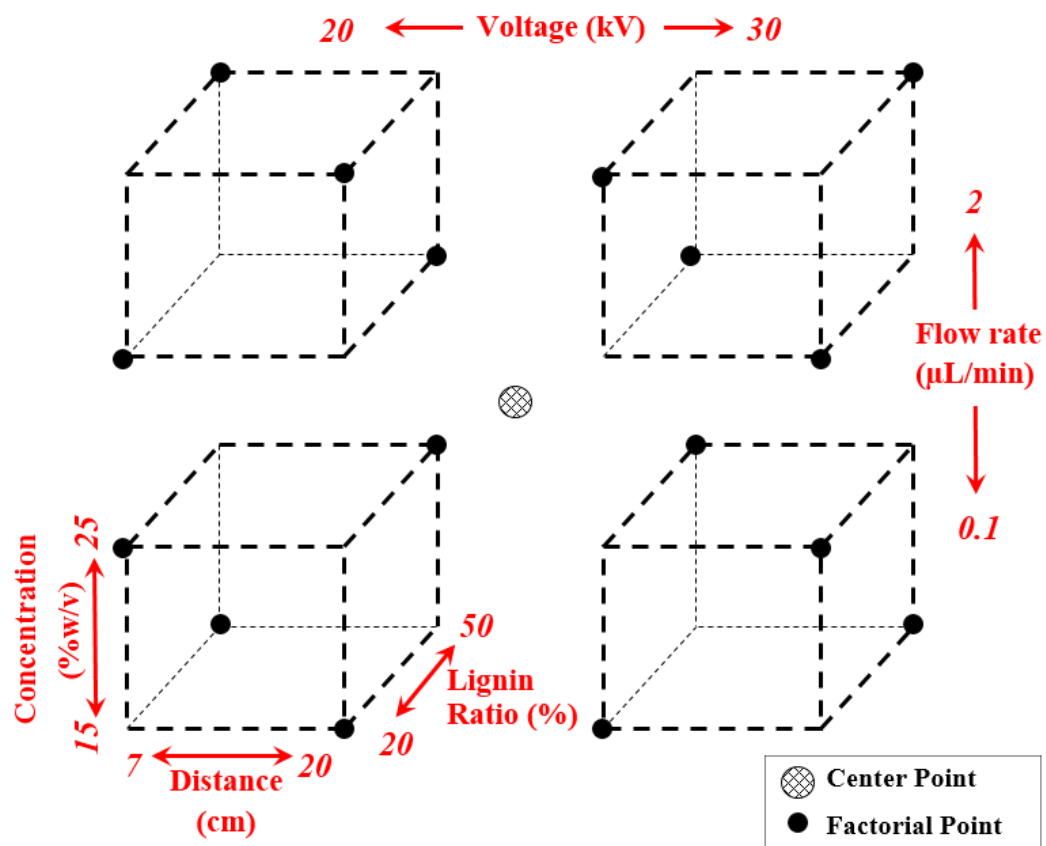
Figure 4.2: The 5-dimensional experimental space. Each dot represents an experimental run (the center point in the middle of the space is also included)

In Section 5.2, a set of electrospun samples consisting of different average fiber diameters and of varying lignin/r-PET mass ratios were fabricated and characterized. The electrospinning conditions for the preparation of each of these samples is presented in Tables 4.2-4.4.

Table 4.2: Electrospinning conditions for the preparation of samples used in Section 5.2.2

Sample No.	Lignin/r-PET mass ratio	Solution concentration (% w/v)	Voltage (kV)	Spinning Distance (cm)	Flow rate (μL/min)	Average fiber diameter (nm)
1	50/50	9	30	7.7	0.1	80 ± 21
2	50/50	10	30	7.7	0.1	121 ± 38
3	50/50	14	30	7.7	0.1	245 ± 79
4	50/50	25	30	7	0.1	387 ± 148
5	50/50	25	20	20	0.1	547 ± 205
6	50/50	32	30	7.7	1	781 ± 284
7	(pure r-PET)	15	30	10	5	204 ± 90

Table 4.3: Electrospinning conditions for the preparation of samples used in Sections 5.2.3 and 5.2.4

Sample No.	Lignin/r-PET mass ratio	Solution concentration (% w/v)	Voltage (kV)	Spinning Distance (cm)	Flow rate (μL/min)	Average fiber diameter (nm)
1	50/50	9	30	7.7	0.1	80 ± 21
2	50/50	14	30	7.7	0.1	230 ± 77
3	50/50	18	30	7.7	0.1	308 ± 88
4	50/50	25	30	7.7	0.1	387 ± 148
5	67/33	10	20	7.7	0.1	97 ± 20
6	67/33	15	30	7.7	0.1	176 ± 38
7	67/33	20	30	7.7	0.1	320 ± 94
8	80/20	10	30	7.7	0.1	95 ± 27
9	80/20	13	30	7.7	0.1	135 ± 49
10	80/20	15	30	7.7	0.1	168 ± 41
11	80/20	20	30	7.7	0.1	279 ± 74
12	90/10	11	30	7.7	0.1	95 ± 19
13	90/10	13	30	7.7	0.1	116 ± 32
14	90/10	13	30	7.7	0.1	125 ± 19
15	90/10	14	30	7.7	0.1	136 ± 41
16	90/10	17	30	7.7	0.1	171 ± 45
17	40/60	22	30	7.7	0.1	406 ± 141

Table 4.4: Electrospinning conditions for the preparation of samples used in Section 5.2.5

Sample No.	Lignin/r-PET mass ratio	Solution concentration (% w/v)	Voltage (kV)	Spinning Distance (cm)	Flow rate (μL/min)	Average fiber diameter (nm)
1	50/50	9	30	7.7	0.1	85 ± 27
2	50/50	14	30	7.7	0.1	230 ± 77
3	50/50	18	30	7.7	0.1	292 ± 76
4	50/50	25	30	7.7	0.1	395 ± 131
5	50/50	25	20	20	0.1	565 ± 189
6	80/20	20	30	7.7	0.1	252 ± 64
7	90/10	14	30	7.7	0.1	147 ± 48

For the preparation of the CNFs derived from 50/50 lignin/r-PET with ~400 nm average fiber diameter characterized in Section 5.3, for the ones used for the preparation of ACNFs-KOH and ACNFs-KOH-HNO$_3$ characterized in Section 5.3 and also for the ones used in all the adsorption experiments of Section 5.4, the following electrospinning conditions were used: 50/50 lignin/r-PET mass ratio, 21% w/v solution concentration, 30 kV voltage, 0.1 μL/min flow rate and 20 cm spinning distance. For these samples, it was decided to use the largest spinning distance (20 cm) so that the electrospun nanofibers would spread at a larger area on the collector and, so, they would dry more efficiently.

4.2.2 Lignin/r-PET mass ratio vs. molar ratio

Throughout this PhD dissertation research, the lignin/r-PET mass ratio was used in all the electrospinning experiments. PET consists of linear macromolecular chains, in which the repeating unit has the formula $C_{10}H_8O_4$ [121]. The molar mass of this repeating unit is 192 g/mol. In contrast, lignin has a more complicated branched structure, which is built after the radical polymerization of three phenylpropane units

(guaiacyl, syringyl and p-hydroxyphenyl units; G, S and H units respectively) (Figure 2.3) [38, 122]. The configuration of the lignin structure and the relative quantity of each of its three building monomers vary among plant species [29, 122]. Lignin derived from hardwoods mainly consists of S and G units, while lignin originating from softwoods primarily consists of G and small amounts of H units [29, 122]. For the same lignin that has been used in this research (alkali lignin with low sulfonate content purchased from Sigma-Aldrich, product number #471003), Zhang et al. have estimated that the relative proportion of the three monomers constituting the lignin structure is $H_{10.3}G_{35.8}S$ [122]. This means that the macromolecules of lignin contain around 3.5 times more G than H; therefore, G constitutes around 78% of its building monomers. The amount of S is negligible. The molecular formula of the predominant monomer G is $C_{10}H_{12}O_3$ with a molar mass of 180 g/mol. However, the various monomer units connect through linkages, e.g. ether bonds, carbon-carbon linkages, etc [123], so removing a hydrogen atom and adding an -O- bonding atom to the G group would give an approximate molecular formula of $C_{10}H_{11}O_4$, with a molar mass of 195 g/mol. Other studies using the same lignin that was used here indicate a similar relative ratio between C, O and H in its structure [124, 125]. This approximate formula and its calculated molar mass are very similar to those of the repeating unit of r-PET.

Therefore, it can be assumed that the lignin/r-PET mass ratio used for the preparation of each electrospinning solution throughout this research is fairly close to the corresponding molar ratio of their building blocks.

4.2.3 Characterization of the electrospun nanofibers

After the fabrication, all the electrospun samples were left to dry for 24 h at room temperature. The morphology of the fibrous mats was examined via Scanning

Electron Microscopy (SEM) (JEOL Neoscope JCM-5000) after gold coating them. The average fiber diameter was measured using an image analyzer (ImageJ, National Institutes of Health, U.S.A.). Around 100 measurements in each sample were used for the calculation of the fiber diameter and the standard deviation. Measurements at several different spots of each SEM image were taken in order to ensure a representative average fiber diameter for each different sample (mat).

In addition, Attenuated Total Reflection-Fourier Transform Infrared Spectroscopy (ATR-FTIR) analysis was performed to investigate the possible structural alterations of lignin under the effect of trifluoroacetic acid, as well as the structure of the lignin/r-PET electrospun fibers (Section 5.1). In the case of lignin, three different cases were examined: pristine, solvent-cast and electrospun (in reality "electrosprayed", see Section 5.1) lignin. In both solvent-cast and "electrosprayed" lignin, the concentration of lignin in TFA was 20% w/v. For the preparation of solvent-cast samples, pristine lignin was first dissolved in TFA and then, the solution was cast onto petri dishes and left to dry for 72 h. The spectra were obtained using an IRPrestige-21/Shimadzu spectrophotometer with a MIRacle ATR tool by PIKE Technologies.

The miscibility between lignin and r-PET was examined through Differential Scanning Calorimetry (DSC) using a Netzsch DSC 200 F3 instrument (Section 5.1). Five different compositions of the lignin/r-PET blend were investigated, namely 80/20, 65/35, 50/50, 35/65 and 20/80. Each blend was prepared by dissolving the appropriate quantities of polymers in TFA and then, following the electrospinning process they were spun into nanofibrous mats and left to dry for 72 h before monitoring their thermal behavior. For comparison, the thermogram of pristine untreated lignin as

well as that of the starting recycled PET were also recorded. For each measurement, a sample of 9-10 mg was tested in the range 40-300°C with a scan rate of 10°C/min.

In Section 5.2, the electrospun nanofibers were characterized with Thermogravimetry (TGA) using a TA Q500 instrument. Around 6-10 mg of each sample were heated under inert atmosphere with a rate of 7°C/min from 25 till 900°C. N$_2$ was used as a carrier gas with a flow rate of 40 mL/min. Moreover, the X-ray diffraction (XRD) patterns of the samples presented in Section 5.2 were recorded using a Philips X'Pert3 diffractometer with a Cu-Ka radiation source (1.54 Å). Differential Scanning Calorimetry (DSC) tests in Section 5.2 were performed at inert atmosphere (N$_2$) with a heating rate of 7°C/min, using a TA DSC25 instrument. Elemental analysis with Energy Dispersive X-Ray Spectroscopy (EDS) was performed using a JEOL JSM-6010PLUS scanning electron microscope.

4.3 Carbonization and activation: the experimental methodology and the characterization of the CNFs and of the ACNFs

For the experiments described in Section 5.2, the electrospun mats were carbonized in a temperature-programmed tubular furnace (Tube Furnace GSL-1500X-50, MTI). Each sample was heated under inert atmosphere (N$_2$) (flow rate ~300 cc/min) at a heating rate of 5°C/min until it reached 600°C, where it was held for 1 h; then, it was allowed to cool down at the same inert atmosphere. Initially, there was an attempt to thermally stabilize the fibers prior to carbonization, however, it was found out that this did not influence the fusion among them. Therefore, it was decided to omit the stabilization step in all experiments.

The morphology of the carbonized samples in Section 5.2 was examined with Scanning Electron Microscopy (SEM) (JEOL Neoscope JCM-5000) after they were

gold-coated. Their diameter distribution was measured using an image analyzer (ImageJ, National Institute of Health, U.S.A.).

For the investigation of the BET surface area with respect to the average fiber diameter of CNFs as this is described in Section 5.2.5, the following carbonization and activation procedure was applied: Each of these samples was carbonized in the tubular furnace under inert atmosphere (N_2) at a heating rate of $5^{\circ}C/min$ until it reached $800^{\circ}C$, where it was held for 1 h. Then the temperature was decreased to $600^{\circ}C$, the gas was switched to CO_2, and the sample was activated for 1 h at this temperature. Finally, the gas was switched again to N_2 and left to cool down at room temperature.

The textural characterization of these samples (Section 5.2.5) was studied through N_2 physisorption using a Micromeritics Tristar II Plus instrument. The surface area of each sample was calculated using the Brunauer-Emmet-Teller (BET) equation, the total pore volume was determined using the Gurvitch rule at $P/P^{o}=0.95$ and the micropore volume was estimated using the t-plot approach. In addition, exactly the same procedure was followed for pristine lignin powder; it was carbonized at $800^{\circ}C$ with N_2, activated at $600^{\circ}C$ with CO_2 and its textural characteristics were measured for comparison, as well.

The CNFs (from either 50/50 or 90/10 lignin/r-PET) used for characterization in Section 5.3 were carbonized either at $800^{\circ}C$ or at $1000^{\circ}C$ for 1 h under N_2 in the tubular furnace.

The activation of the CNFs that is described in Section 5.3 was carried out using either physical activation with CO_2 or chemical activation with KOH. For all cases, CNFs carbonized at $1000^{\circ}C$ were the starting material. For the physical activation, the CNFs were manually crashed by fingers into smaller pieces, they were placed into a combustion boat and they were transferred into the temperature-

programed tubular furnace (GSL-1500X-50, MTI). These smaller pieces consisted of clusters of CNFs with sizes of few tens of micrometers, as it was found out after their examination with SEM. They were heated under N_2 atmosphere at a rate of 5°C/min until they reached 700°C. Then, the atmosphere was switched to CO_2 at a flow rate of 200-300 cc/min and they were held at this temperature for 1 h. Finally, the gas was switched again to N_2 and they were left to cool down.

For the chemical activation, the CNFs (derived from 50/50 lignin/r-PET with ~400 nm average fiber diameter) were first crashed by fingers into powder. They were dispersed into a KOH 3M solution at a mass ratio of 4/1 KOH/CNFs, and they were left under stirring for 12 h at room temperature. Then, they were placed into a combustion boat and transferred into the tubular furnace, in which they were heated under N_2 at a rate of 5°C/min up to 800°C, where they were held for 1 h. Finally, they were left to cool down. Subsequently, they were dispersed in an excess of HCl 1M solution under stirring in order to neutralize the remaining KOH, and they were repeatedly washed with de-ionized water and filtered via membrane filtration (Millipore membrane filter 0.22 μm) until the filtrate had pH ~7. Finally, they were dried overnight at 130°C. This sample is denoted as "ACNFs-KOH".

Some of the ACNFs-KOH were further treated with HNO_3. First, they were dispersed into HNO_3 4M (0.8 g per 100 mL solution) and they were left under stirring at 90°C for 8 h. Then, they were repeatedly washed with deionized water and filtered through membrane filtration (Millipore membrane filter 0.22 μm) until the filtrate had pH ~7. Finally, they were dried overnight at 130°C. This sample is denoted as "ACNFs-KOH-HNO_3".

The morphology of each sample was examined using Scanning Electron Microscopy (SEM) (JEOL Neoscope JCM-5000 for all figures except for Figure 5.51

in which JEOL JSM-6010PLUS was used) after coating them with gold. The average fiber diameter of each sample was measured using an image analyzer (ImageJ, National Institute of Health, U.S.A.). The morphology of the samples was also characterized with Transmission Electron Microscopy (TEM) (Tecnai G2 Transmission Electron Microscope 200kV).

The textural characterization of the activated carbon nanofibers in Section 5.3 was studied through N_2 physisorption using a Micromeritics Tristar II Plus instrument. The surface area of each sample was calculated using the Brunauer-Emmet-Teller (BET) equation, the total pore volume was determined using the Gurvitch rule at $P/P^o=0.95$ and the micropore volume was estimated using the t-plot approach. Raman Spectroscopy analysis was performed using Raman-AFM combination Alpha300 RA (WITec, Germany) at 532 nm laser wavelength. The X-ray diffraction (XRD) patterns in Section 5.3 were recorded using a Philips X'Pert3 diffractometer with a Cu-Ka radiation source (1.54 Å). For both Raman and XRD, the peaks were deconvoluted by fitting Lorentzian functions with the aid of a data analysis software (OriginPro).

Elemental analysis with Energy Dispersive X-Ray Spectroscopy (EDS) for the samples in Section 5.3 was performed using a JEOL JSM-6010PLUS scanning electron microscope. Boehm titration was carried out according to the methodology described in [126, 127]. Briefly, 0.2 g of the sample were dispersed into 8mL NaOH 0.05 M and left under shaking for 24 h. The solution was filtered through syringe filters (0.22 μm), an aliquot of 5 mL was added to 10 mL HCL, and the solution was titrated with NaOH 0.05 M (titrator base). Bromothymol blue was used as an indicator to determine the equivalent point. The volume of titrator base consumed was measured and converted to mmol/g of surface acidic groups using the methodology described in [126].

4.4 Adsorption experiments

All adsorption experiments were conducted in a batch mode. The flasks containing the solutions were placed in a water bath, at a shaking speed of 105 rpm. In all of them, the adsorbent dose was 10 g/L. This was defined after some preliminary experiments in which different values of the adsorbent dose were tested, and also after an overview of the relevant literature. Particularly, 0.04 g of the adsorbent were added in each flask containing 4 mL of solution.

For the DMDBT, the adsorption equilibrium was investigated for initial concentrations in the range of ~100-2000 ppmw, using three different adsorbents: CNFs derived from 50/50 lignin/r-PET carbonized at 1000°C with average diameter close to 400 nm, ACNFs-KOH and ACNFs-KOH-HNO$_3$, as they are described in the previous section. These experiments were performed at 22°C, and they were left to equilibrate for 24 h. In order to analyze the results, different adsorption isotherms were used, namely Langmuir, Freundlich and the extended Langmuir-Freundlich (see Section 5.4). For ACNFs-KOH-HNO$_3$ the adsorption experiments were also conducted at 50°C.

For the investigation of the kinetics of adsorption of DMDBT on ACNFs-KOH-HNO$_3$, an initial concentration of 335 ppmw DMDBT was used. The adsorption capacity was then measured after certain time intervals, at 22°C and at 50°C. These experimental results were fitted to three kinetic models; the pseudo-first order (Lagergren model), the pseudo-second order (Ho model), and the intraparticle diffusion model (Weber and Morris model) (see Section 5.4).

All the adsorption experiments for the removal of DMDBT from n-dodecane were carried out using the same batch of ACNFs-KOH-HNO$_3$, and they are presented

in Sections 5.4.1-5.4.3 (Figures 5.53, 5.55-5.58). This specific batch of ACNFs-KOH-HNO$_3$ was also used for the characterization presented in Section 5.3.3. These adsorption results were validated after a second batch of ACNFs-KOH-HNO$_3$ was produced under the same conditions. Using this second batch, some of the adsorption desulfurization experiments were replicated and these results are presented in Section 5.4.4; the second batch (sample) used for validation is denoted as "sample 2", while the initial batch (sample) is denoted as "sample 1".

Some adsorption experiments of DMDBT were also performed using commercial activated carbon (Merck 1.02186, BET surface area 775 m^2/g) for comparison purposes.

For DBT, the adsorption equilibrium was investigated for initial concentrations in the range of 100-2000 ppmw, using only ACNFs-KOH-HNO$_3$, and particularly the same batch that was used for all the adsorption experiments of DMDBT (named as "sample 1"). These experiments were performed at 22°C, and they were left to equilibrate for 24 h. The same isotherms were used here, as well. For the investigation of adsorption kinetics, an initial concentration of 233 ppmw DBT was used; the adsorption capacity was then measured after certain time intervals, at 22°C. The results were fitted to the pseudo-first order and to the pseudo-second kinetic model. Again, the results for the adsorption of DBT were validated by replicating some of them using the second batch of ACNFs-KOH-HNO$_3$ (named as "sample 2") (see Section 5.4.5).

In all the adsorption experiments, the concentrations were measured according to the following methodology: the solution was filtered through a syringe filter (0.22 μm) after the adsorption process was finished and the filtrate was transferred to a quartz cuvette. Each solution concentration of DMDBT or DBT was measured using UV-Vis spectroscopy (Shimadzu UV 1800) at the wavelength of 313 nm, after a

calibration curve was built for each of these S-compounds. After measuring the quantity adsorbed in ppm (mg of solute/kg of solvent), the adsorption capacity was calculated using the formula q=(ppm adsorbed)*0.748/10, where 0.748 kg/L is the density of n-dodecane and 10 g/L the adsorbent dose. Thus, the adsorption capacity is measured in mg of solute per g of adsorbent (mg_{DMDBT}/g_C or mg_{DBT}/g_C for DMDBT and DBT respectively).

Chapter 5: Results and Discussion

5.1 Electrospun nanofibers made of lignin/r-PET: the experimental design and characterization

The first step of this research involved the preparation of electrospun nanofibers of lignin/r-PET, that will be used as CNF precursors. In this section, the electrospinning procedure is described, the influence of the electrospinning variables on the fiber morphology is analyzed, and the electrospun nanofibers are characterized in terms of their structure and their thermal properties.

5.1.1 Electrospinning of lignin alone

The choice of trifluoroacetic acid (TFA) as a solvent was made due to its suitability for the electrospinning of PET [128-130]. Generally, PET is insoluble in the common solvents used in the literature for the electrospinning of lignin (H_2O, N,N-dimethylformamide, acetonitrile, ethanol, etc.) [23, 24, 35, 46, 131, 132]. However, the behavior of lignin in TFA is rather ambiguous. TFA has been proposed as a solvent for the treatment and fractionation of plant biomass in order to separate and recover various useful components (cellulose, lignin, non-cellulosic polysaccharides) [133, 134]. In this context, Morrison and Steward [133] reported that most of the lignin of oat straw is insoluble to TFA, with Poirier et al. [135] presenting similar results for lignin derived from maize leaves and attributing this feature to some degree of cross-linking. In addition, Fanta et al. [136] stated that ~10% of lignin derived from wheat straw underwent degradation in TFA and gave water soluble fractions. Similar results were reported by Dong et al. [134]. Other researchers who used TFA for the electrospinning of lignocellulosic fibers [137, 138] report that the dissolution of lignin

in TFA includes the cleavage of some covalent bonds and the disruption of its 3D network. Moreover, the hydroxyl groups of lignin create ester bonds with TFA, a process which, however, is reversible in atmospheric conditions [137, 138]. In this research, kraft lignin was found totally soluble in TFA, and the solutions were stable. In general, the chemical properties of lignin depend on its plant source, the extraction process and possible post-treatment. Some of these variables defined this behavior here, probably the fact that it has some small degree of sulfonation, as it is specified by the supplier. However, even some degree of degradation is expected. The possible structural changes of lignin dissolved in TFA were studied with ATR-FTIR (Section 5.1.5).
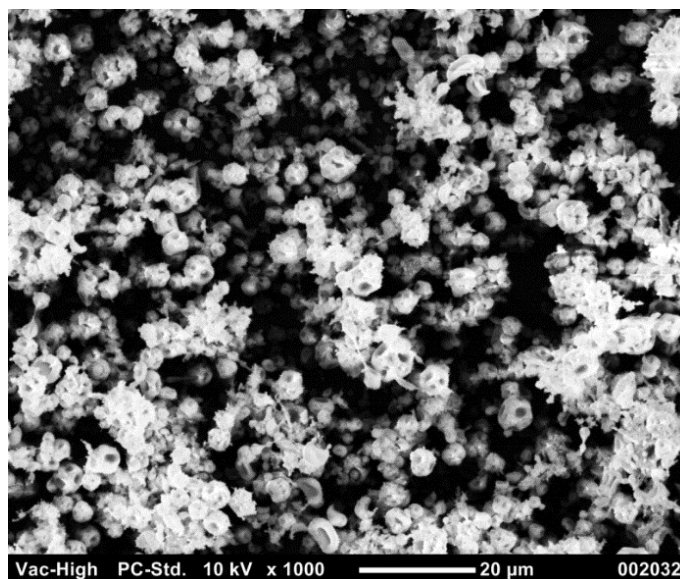
Figure 5.1: SEM image of electrospun (electrosprayed) lignin 30% w/v in TFA

The attempts to produce fibers of pure lignin were unsuccessful. Instead of electrospun fibrous mats, there was just electrospray (Figure 5.1). This has been observed previously with solutions of kraft lignin in water or N,N-dimethylformamide [23, 24, 46, 132]. This behavior is attributed to the relatively low molecular weight of

kraft lignin resulting in the absence of extensive chain structures and/or molecular entanglements [23]. Therefore, the presence of r-PET as a binder polymer is determinant for successful electrospinning. Dallmeyer et al. [132]. reported that the electrospinnability of lignin in the presence of a binder polymer (in their case poly(ethylene oxide)) is dependent on the viscoelastic properties of the solution, as an increase in shear modulus and strain hardening was observed. The interaction between lignin and r-PET is obviously important for the successful fiber formation. The nature of this interaction was studied by Kadla and Kubo [94]. Although both polymers possess functional groups capable of forming hydrogen bonds, they concluded that only a minor degree of such interaction existed between the two polymers. Instead, the fact that the glass transition temperature of the blend (T_g) exhibited negative deviation from a linear mixing rule was an indication of weak intermolecular interactions.
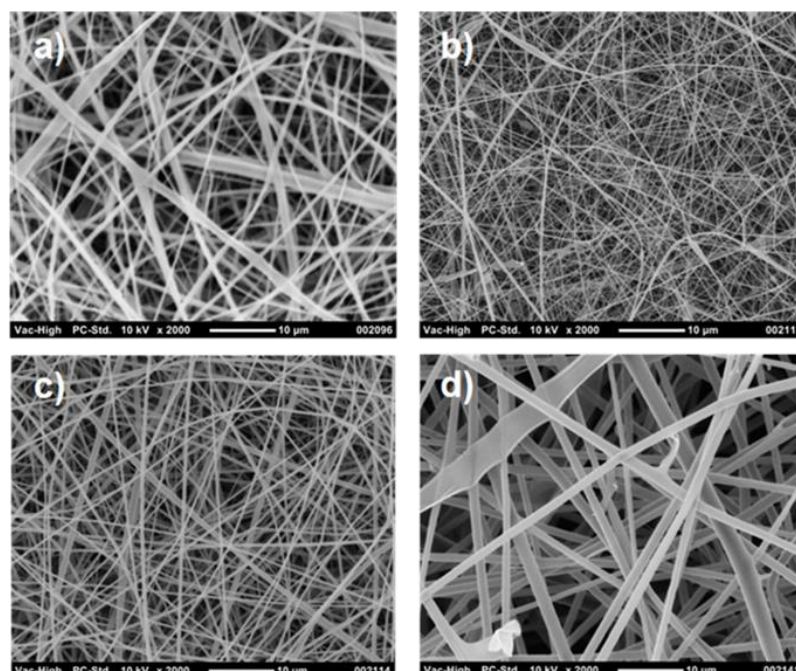
Figure 5.2: SEM micrographs of various representative fiber morphologies with varying average diameter; a) 733 ± 388 nm; b) 229 ± 84 nm; c) 462 ± 178 nm; d) 1473 ± 575 nm (see Table 5.1). Scale bar is 10 μm in all images

5.1.2 Electrospinning of the lignin/r-PET blend

Figure 5.2 shows SEM images of various representative electrospun lignin/r-PET fiber morphologies produced under different conditions (see Table 5.1). With the naked eye, the electrospun mats appear as flexible membranes of light brown color (Figure 5.3).
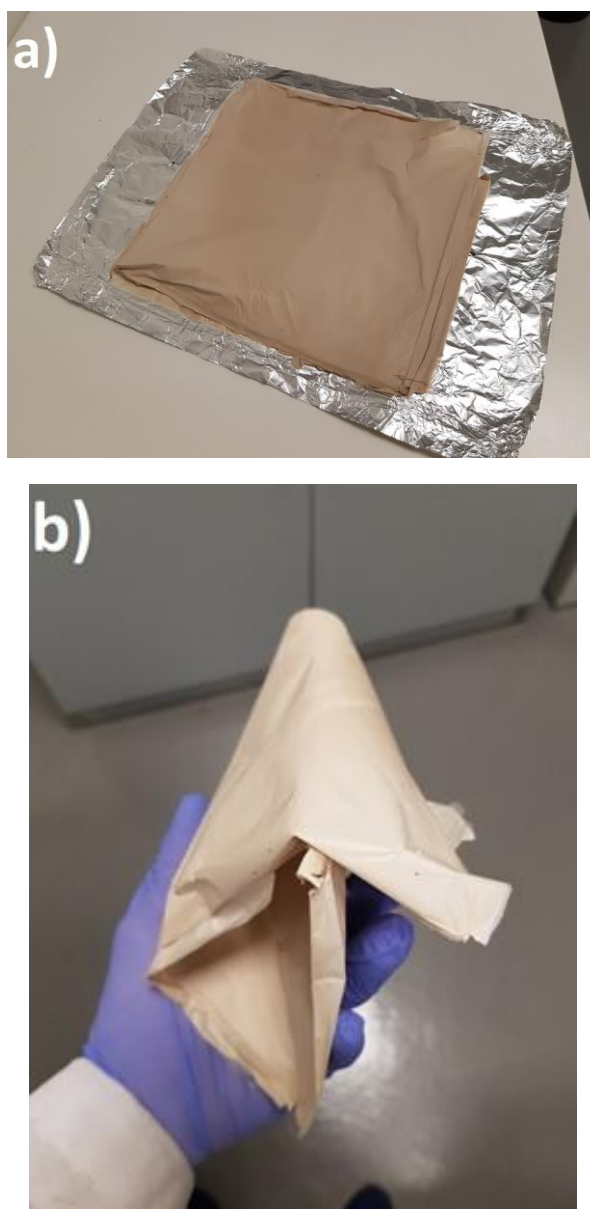
Figure 5.3: A representative electrospun mat as it appears with naked eye (sample 2 from Table 5.1)

After completing the experimental design as it was described in Section 4.2.1, the measured average fiber diameter and the standard deviation for each experimental run was measured, and they are presented in Table 5.1.

Table 5.1: Measured average fiber diameter and standard deviation for each experimental run

Exper. Run	Distance (cm)	Concentration (% w/v)	Lignin (%)	Voltage (kV)	Flow Rate (μL/min)	Average Fiber Diameter (nm)	Standard Deviation (nm)
1	7.0	25	20	30	2.00	733	388
2	7.0	25	50	30	0.10	455	181
3	20.0	15	50	20	2.00	368	111
4	20.0	15	20	30	2.00	255	68
5	20.0	15	20	20	0.10	325	99
6	13.5	20	35	25	1.05	504	173
7	13.5	20	35	25	1.05	423	246
8	7.0	25	50	20	2.00	670	267
9	20.0	15	50	30	0.10	229	84
10	7.0	25	20	20	0.10	462	178
11	7.0	15	20	30	0.10	328	84
12	7.0	15	20	20	2.00	365	98
13	7.0	15	50	30	2.00	278	71
14	7.0	15	50	20	0.10	278	88
15	13.5	20	35	25	1.05	450	108
16	13.5	20	35	25	1.05	508	168
17	20.0	25	20	20	2.00	639	180
18	20.0	25	20	30	0.10	1145	560
19	20.0	25	50	30	2.00	969	385
20	20.0	25	50	20	0.10	1473	575

5.1.3 Average fiber diameter: statistical analysis of the factorial design

For the average diameter, the initial analysis of variance gave the results presented in the Pareto chart of Figure 5.4a.

This chart presents the magnitude and relative importance of the standardized effects by displaying their absolute value. Effects lying beyond the reference line are statistically significant. The plot reveals that the only main factors that influence the fiber diameter are the concentration of the solution and the distance between the needle tip and the collector (factors B and A respectively). The lignin ratio, the voltage and the flow rate were found insignificant to the response. Generally, these factors are known to influence the morphology of electrospun fibers [17]. In this research, if a wider range of values had been examined, it is possible that some additional factors would also be significant. However, this specific range of values was based on the demand of acceptable spinnability and was also limited by the apparatus' allowable limits in voltage and spinning distance. In the case of lignin mass ratio, there were spinnability issues at very high percentages of lignin.

Therefore, it was not possible to examine a wider range of these three factors. Even so, all factors influence the response through their interactions. The design was constructed in such way that the 2-way interactions are aliased with the effect of the 3-way interactions. Most probably, however, the high-order effects are a result of the 2-way interactions. The Pareto chart indicated that the factors BD, AD and CE were not important for the procedure. So, they could be eliminated from the model, together with their aliased ones. Factors C (% lignin), D (voltage) and E (flow rate) couldn't be eliminated, because they participated in significant 2-way interactions. The blocking factor was also found insignificant (p-value=0.785) and it was removed from the model, as well. This was an indication that the two operators who conducted the experiments did not influence the results.
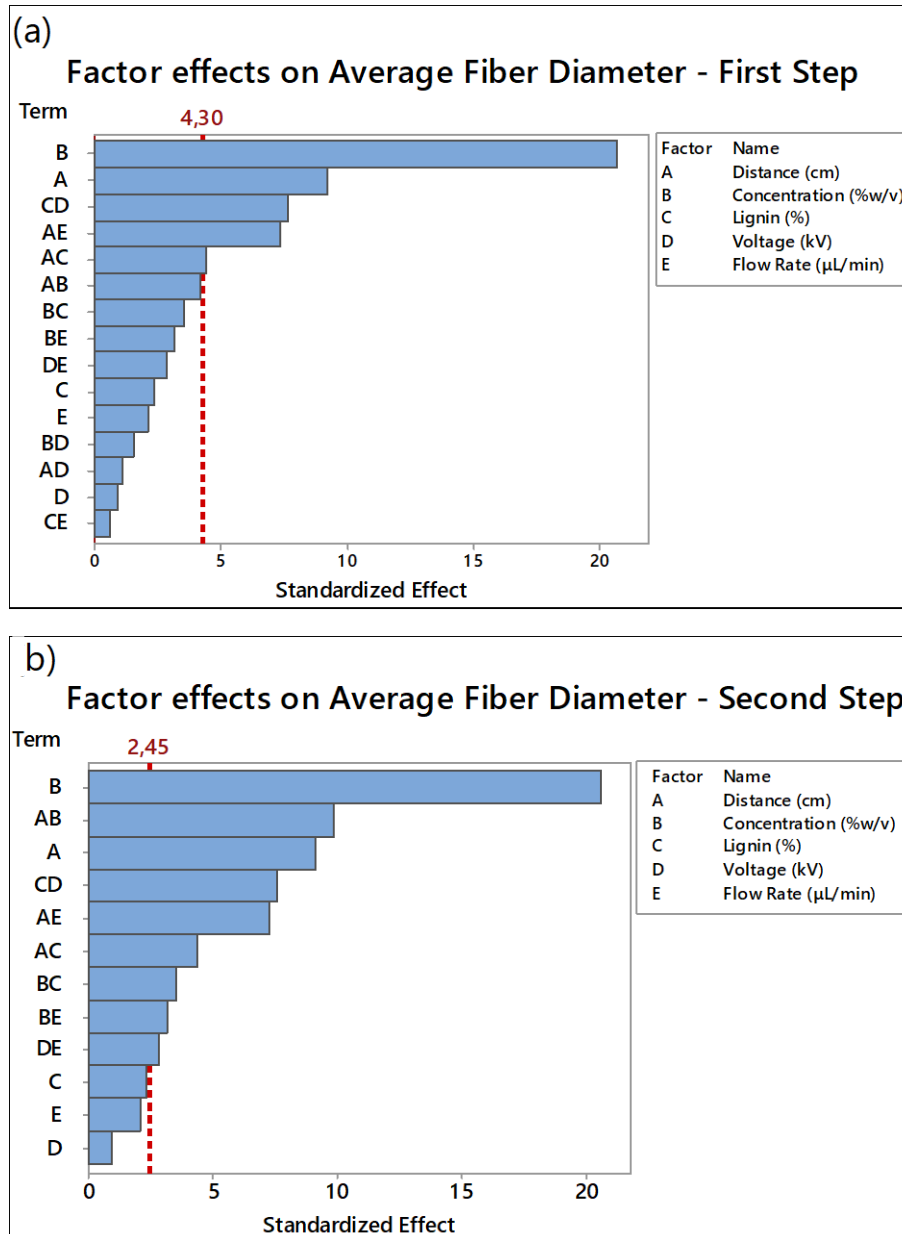
Figure 5.4: The standardized effects of electrospinning factors on the average fiber diameter; a) in the first step of analysis; b) after eliminating the insignificant interactions

After elimination of the insignificant factors, the second step of the analysis

revealed a similar situation (Figure 5.4b). It is important to note here that, now (after

the removal of the blocking effect), the AB interaction has a relatively higher effect

compared to that in the first step. The reason is that the model was initially designed

in such way that the blocking factor was confounded with the AB interaction. Thus,

the large AB effect was initially concealed by the very small effect of the blocking factor, and its true effect was revealed after removing the latter.

Table 5.2: Factor effects on the average fiber diameter

Factor	Effect
Concentration	+0.5150
(Distance)*(Concentration)	+0.2472
Distance	+0.2292
(Lignin%)*(Voltage)	-0.1910
(Distance)*(Flow Rate)	-0.1830
(Distance)*(Lignin%)	+0.1103
(Concentration)*(Lignin%)	+0.0885
(Concentration)*(Flow Rate)	-0.0788
(Voltage)*(Flow Rate)	+0.0718
Lignin%	+0.0585
Flow Rate	-0.0523
Voltage	-0.0235

The actual effect of each factor is concisely presented with its algebraic sign in Table 5.2. Here, the effects are ranked in a descending order of absolute values. It must be mentioned here that the actual effect values presented in Table 5.2 are different from the values shown in the Pareto chart of Figure 5.4, because the Pareto chart uses standardized effects based on the t-values of the ANOVA.

The line above lignin% in Table 5.2 indicates the limit below which the effects are insignificant to the response. The variability attributed to the insignificant factors has been eliminated, so now all interactions appear significant. The three main effects C, D and E (lignin mass ratio, voltage and flow rate respectively) still remain

insignificant to the response. Interestingly, the product (lignin%)*(voltage) of two insignificant factors appears to have a relatively large effect. However, the model was constructed in such a way that this interaction is aliased with the (concentration)*(distance)*(flow rate) interaction, so, it is possible that this significant effect derives from its aliased factor, where two significant factors participate.

The p-value for the model was found to be 0.000, a strong indication that the model adequately describes the data. A further support to this were the values of R^2 and R^2(pred). R^2 measures the proportion of the total variability explained by the model and in this case it was 99.24%. The prediction R^2 was found 85.46%, indicating a model expected to explain around 85% of the variability in new data. The p-value for the lack-of-fit was 0.307, a proof that the removal of the insignificant factors didn't influence the validity of the model (if the p-value of the lack-of-fit was below 0.05 which is the alpha value, it would mean that the model would not be able to describe the data reliably). Finally, the p-value for curvature was found 0.019, a sign that in some areas inside the experimental topography, a quadratic model would most accurately fit the data.

The model includes three basic assumptions: that the errors are normally distributed, that they are independently distributed and that their variance is constant. The standardized residual plots of the second step of the analysis (Figure 5.5) are useful for testing these assumptions. More information on the residual plots can be found in [123]. The normal probability plot confirms that the first assumption is satisfied. Moreover, the plot of the residuals versus observation order follows no obvious pattern, confirming the second assumption.
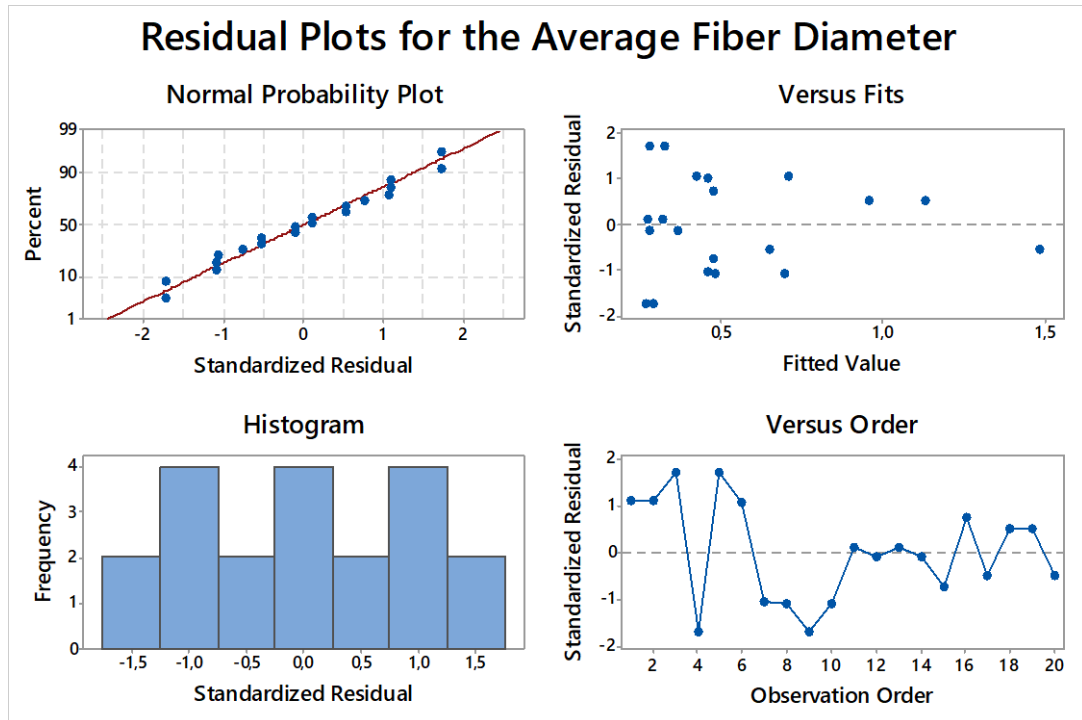
Figure 5.5: Standardized residual plots for the average fiber diameter

The plot of standardized residuals versus fitted value is useful for testing the third assumption. This graph shows that all residuals are included in the [-2,2] range, which is desirable. However, there is much more scatter in the smaller values of response, a sign of higher variability in diameters below 0.5 μm. The explanation for this pattern is that the measurements of fiber diameter through the analysis of SEM images had a higher degree of uncertainty, when measuring narrower fibers. This is rational, because in the SEM images the larger fibers are measured with higher accuracy than the smaller ones. Usually, when patterns like this appear in the residual plots, a transformation of the response is applied. However, in this case the transformation did not alter the situation. Since the source of variability can be recognized, it is valid to assume that it does not influence the adequacy of the model, especially when all other indicators give acceptable results.
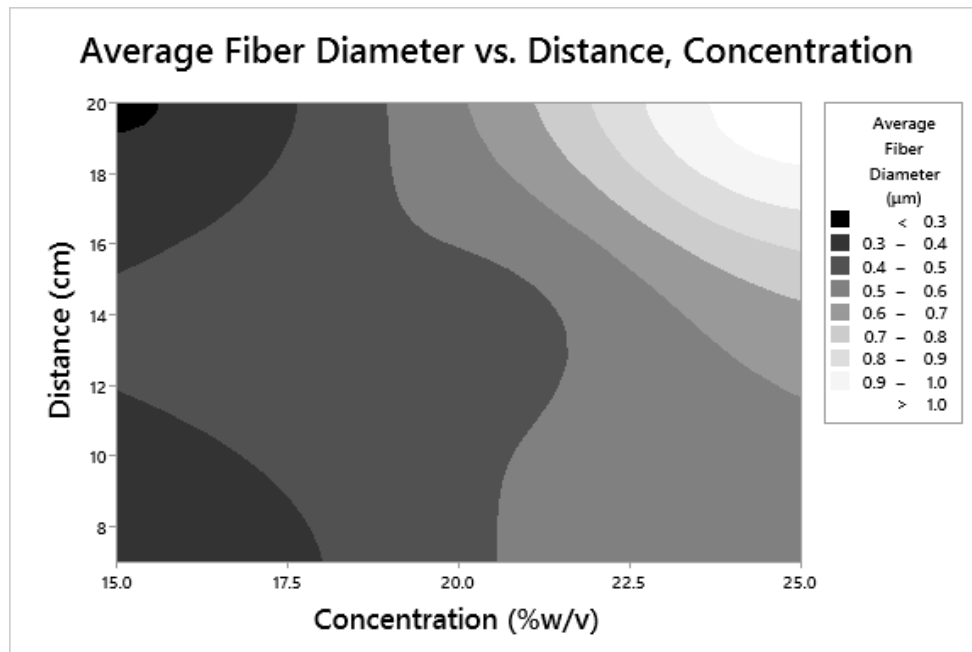
Figure 5.6: Minitab-generated contour plot of average fiber diameter vs. distance and concentration, based on the results of the factorial design

The contour plot of average fiber diameter as a function of the two most significant factors (concentration and spinning distance) is presented in Figure 5.6 (excluding the least significant factors for the range of input values in this factorial design, i.e. voltage, flow rate and lignin/r-PET mass ratio). Here, each shaded area on the plot, corresponds to an experimental region where the fiber diameters have similar values. So, the smallest fiber diameters are found in the darkest areas (diameters < 0.4 μm), while the largest diameters appear in the areas of whiter shade (diameters > 1.0 μm). The contour plot reveals that the diameter is minimized as the concentration is decreased. However, the contour plot exhibits two areas of minimization (saddle point): in the lowest distance and in the maximum distance. This behavior is reflected in the algebraic values of the effects of concentration, distance and (distance)*(concentration) on the response. It was mentioned earlier that concentration has an effect of +0.5150, distance has an effect of +0.2292 and

(distance)*(concentration) has an effect of +0.2472. The two latter effects are very close. The positive sign practically means that an increase in their value tends to increase the diameter. To minimize the response, all three factors [concentration, distance and (distance)*(concentration)] should be set to their lowest values, in order to counteract their positive effect. However, when both distance and concentration are set to their lowest values, then their interaction has its highest value [in coded units this is (-1)*(-1)=(+1)], so it results in increasing the response. When concentration is set to its lowest value and distance to its highest value, their interaction has its lowest value [in coded units (-1)*(+1)=(-1)], but then the adverse effect is caused by the high value of distance. It is not possible to simultaneously minimize all three effects. In each case, a suitable combination of the other factors should be chosen.

It is well described in the literature that decreasing the concentration of the spinning solution decreases the fiber diameter [17, 130, 132, 139, 140]. The reason is that the solutions of lower concentration have lower viscosity. As the jet travels towards the collector, the low viscosity facilitates the extension of the jet, resulting in thinner fibers [139]. Theoretically, if the concentration and the viscosity are too low, then the surface tension prevails and the jet breaks up into droplets, resulting in bead formation [139]. The literature gives various possible relationships between the concentration and the fiber diameter (power law, linear, quadratic or cubic relationship) [17, 139].

The effect of spinning distance on fiber diameter is sometimes more complicated. In many cases it has been reported that a larger distance results in thinner fibers [17, 140-142]. When the distance is long enough, the fibers have more time to stretch and elongate under the electrostatic forces before they reach the collector [17, 142]. The solvent evaporation is facilitated and the charged fluid has more time to split

into smaller portions [140, 143]. However, different observations have been reported for various systems and there seems to be a more complex relationship [143-146]. In some systems, the increase of distance initially decreases the fiber diameter, but gradually the diameter increases again [144-146]. In these cases, the results are explained by focusing on the strength of the electric field, which is the ratio of voltage over spinning distance [143-146]. At constant voltage, the field is stronger when the distance is small, and it gradually weakens with increasing distance. At small spinning distance, the field exerts higher electrostatic force on the jet leading to the formation of thinner fibers [143]. At the same time, a strong field causes higher mass flow, tending to increase the fiber diameter [143]. These antagonistic effects can result in a complex relationship similar to the one observed here.

After identification of the important factors that influence the electrospinning process, a further elaboration of the electrospinning conditions at the experimental regions of lower average fiber diameter (as indicated from the contour plot of Figure 5.6) enabled the fabrication of nanofibrous mats with average fiber diameter lower than 100 nm. Particularly, it was found that using a concentration of 9% w/v enabled the fabrication of electrospun mats with average fiber diameter of around 80-90 nm from 50/50 lignin/r-PET (see the experimental part, Section 4.2.1) (Figure 5.7). These very fine nanofibers are two orders of magnitude thinner than lignin/PET fibers manufactured with other methods [93, 95]. This very important finding has significant implications, because the minimization of the fiber diameter at such low levels maximizes the specific external surface area of the fibers (not taking into account any porosity as these fibers are non-porous), and it enhances their suitability in any application in which the nano-sized dimension is significant. In addition, these values

of the average fiber diameter are among the lowest that have been reported for lignin-based electrospun nanofibers (see Table 2.1).
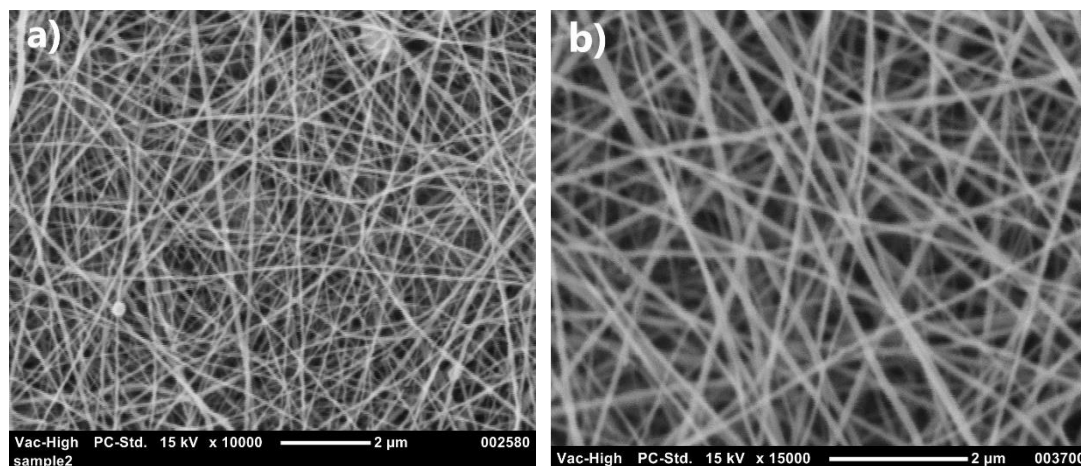
Figure 5.7: Electrospun nanofibers of 50/50 lignin/r-PET with very small diameters; a) 80 ± 21 nm; b) 91 ± 27 nm

5.1.4 Standard deviation: statistical analysis of the factorial design

The selection of the standard deviation of fiber diameter as the second response serves the purpose of investigating in which electrospinning conditions there is a narrower distribution of diameters. The analysis of variance revealed the experimental conditions that induce higher degree of diameter variation. After eliminating the insignificant factors, the final results are presented in Figure 5.8. This plot reveals a situation similar to the average fiber diameter. The only main factors having significant influence on the standard deviation are the concentration and spinning distance (factors B and A respectively), while the other three factors are important only through their interactions. The algebraic signs of the important effects (B, AE, CD, A and AB) were found to be the same as in the case of the average fiber diameter. The p-values of the model (0.001) and the lack-of-fit (0.938) and, in addition, the values of R^2 (97.65%) and R^2(pred) (88.71%) confirm the validity of the model.
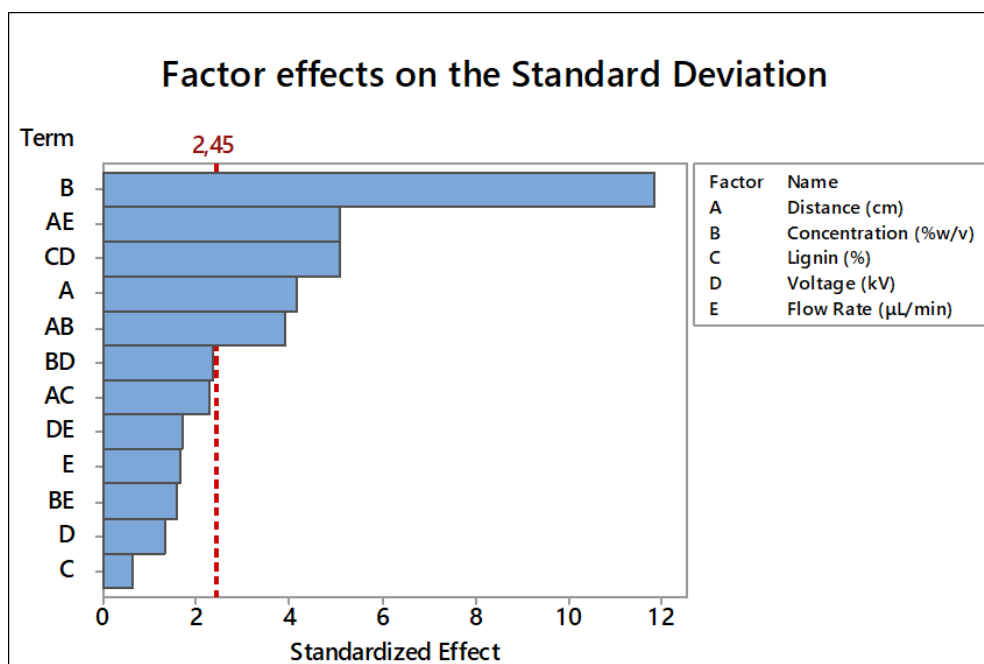
Figure 5.8: The standardized factor effects on the standard deviation of fiber diameter

The contour plot of standard deviation versus concentration and distance follows the same pattern with the average fiber diameter (Figure 5.9), revealing that the two responses have similar behavior (as in Figure 5.6, excluding the voltage, the flow rate and the lignin/r-PET mass ratio).

The lowest values appear in low levels of concentration, in either the highest or the lowest levels of distance. This seems rational, because when the average diameter has a certain value, the range of similar diameters must be of the same magnitude; for instance, when the average diameter is 1473 nm the standard deviation is 575 nm, while for average diameter of 255 nm the standard deviation is 68 nm. Therefore, in order to estimate more thoroughly in which conditions the narrowest distribution appears, it was more appropriate to use the relative standard deviation, RSD (or coefficient of variation), which is the standard deviation expressed as a percentage of the average fiber diameter. This measure has been used in the literature

[143, 147] to estimate the width of the diameter distribution regardless of the diameter

magnitude. The RSD for each experimental run is presented in Table 5.3.
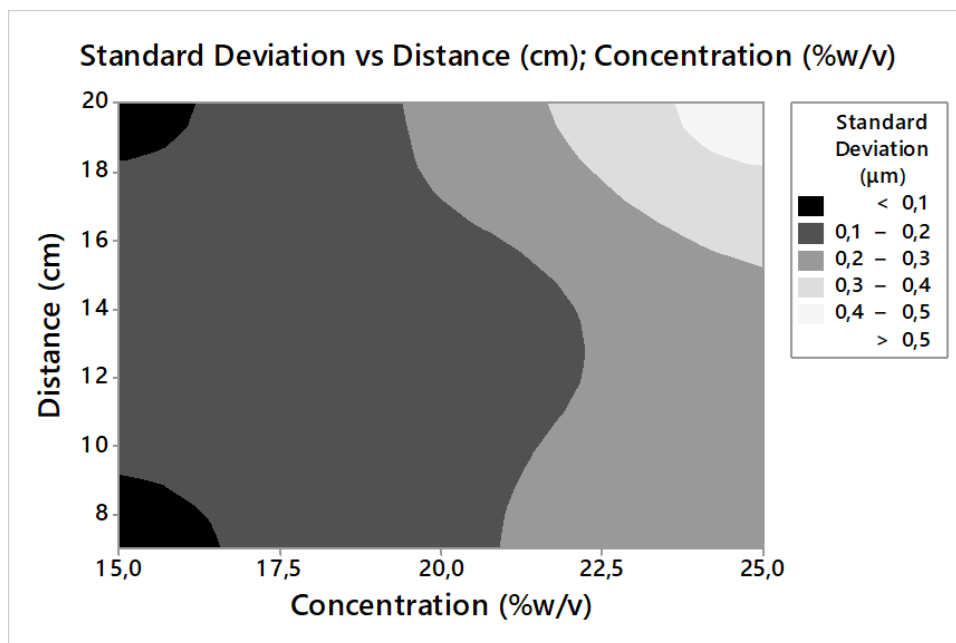
Figure 5.9: Contour plot of standard deviation vs. concentration and spinning distance based on the results of the factorial design
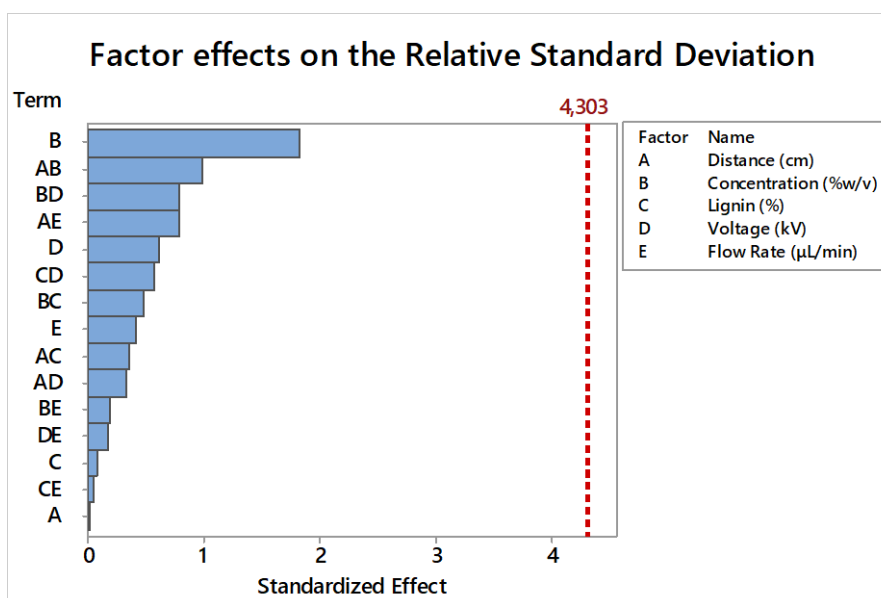
Figure 5.10: Effect of the electrospinning factors on Relative Standard Deviation (RSD)

Analysis of variance was performed again considering the RSD as a response and the results are presented in Figure 5.10. The results reveal a totally different situation; none of the controllable factors has a significant effect on RSD. The variability of the RSD seems to be a random phenomenon, or at least not depending on the factors examined here. Therefore, it was concluded that the fibrous mats exhibit diameter distribution of similar order of magnitude, regardless of the specific electrospinning conditions.

Table 5.3: Relative standard deviation (RSD%) for each experimental run

Run Order	Average fiber diameter (nm)	RSD%	Run Order	Average fiber diameter (nm)	RSD%
1	733	52.9	11	328	25.6
2	455	39.8	12	365	26.8
3	368	30.2	13	278	25.5
4	255	26.7	14	278	31.6
5	325	30.4	15	450	24.0
6	504	34.3	16	508	33.1
7	423	58.1	17	630	28.2
8	670	39.8	18	1145	48.9
9	229	36.7	19	969	39.7
10	462	38.5	20	1473	39.0

5.1.5 Characterization with ATR-FTIR
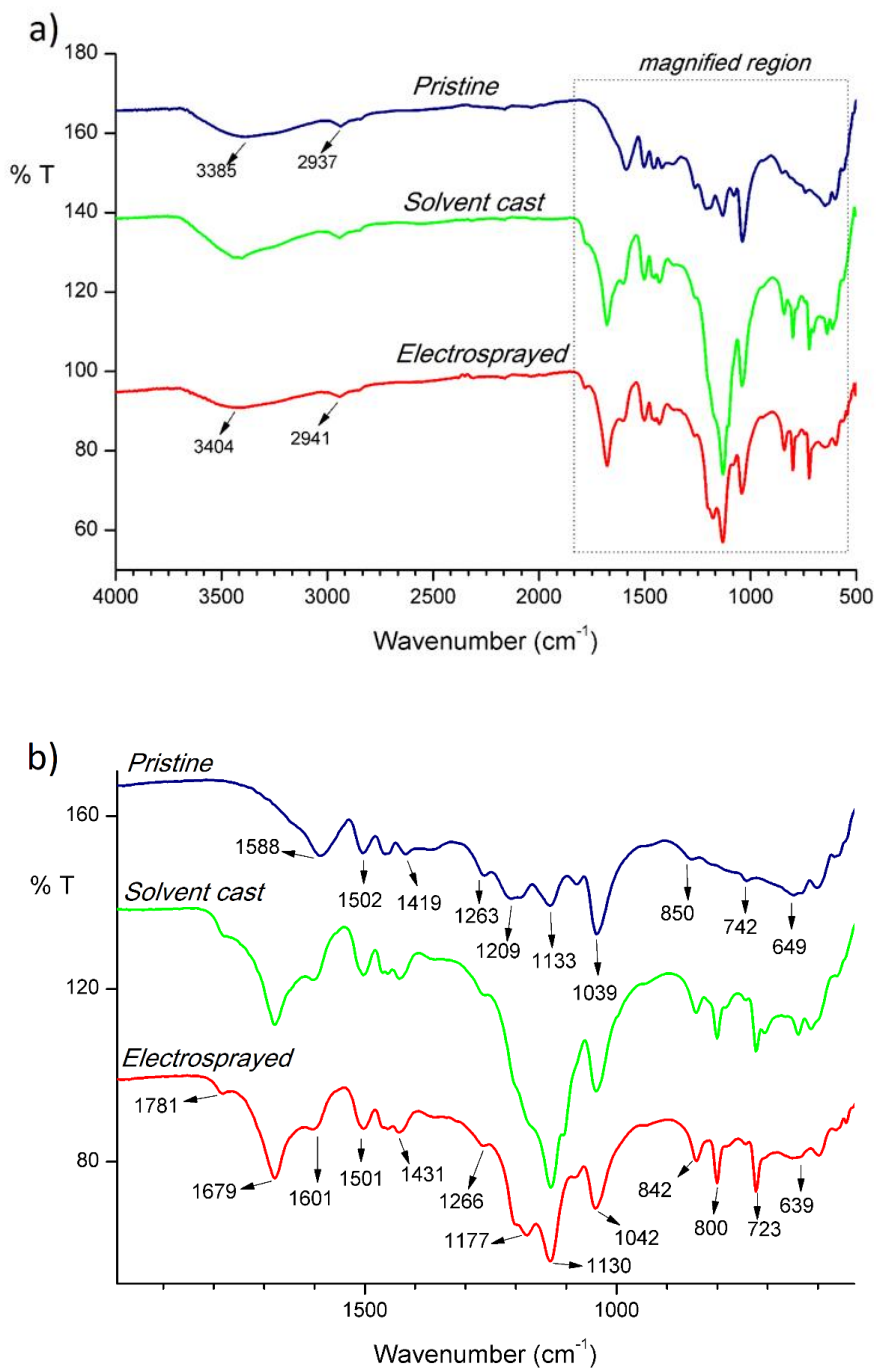
Figure 5.11: ATR-FTIR spectra of the lignin samples; a) wavenumber from 4000 to 500 cm^{-1}; b) magnified region of IR spectra (1900-500 cm^{-1})

Table 5.4: Absorption peaks and types of vibrations in the pristine lignin sample

Peak location (cm^{-1})	Type of vibration
3385	Stretching vibrations of alcoholic and phenolic -OH groups involved in hydrogen bonds [148]
2937	CH stretching (-CH$_3$ or -CH$_2$-) [149, 150]
1588	Aromatic ring vibrations [148]
1502	Aromatic ring vibrations [148]
1458	Aromatic ring vibrations / asymmetric deformation of C-H stretching [150, 151]
1419	Aromatic ring skeletal vibrations combined with C-H in-plane deformation [131, 148, 149]
1263	Vibrations of guaiacyl rings and stretching vibrations of C-O bonds [148, 149]
1209	Vibrations of guaiacyl rings and stretching vibrations of C-O bonds [148, 152]
1133	Deformation vibrations of C-H bonds in the aromatic rings-syringyl units [131, 148, 149]
1039	Vibrations of C-H bonds in guaiacyl rings/C-O stretching in O-CH$_3$, C-OH groups [148-151, 153]
850	Deformation vibrations of C-H bonds associated to guaiacyl [148, 150]
742	Deformation vibrations of C-H bonds associated to aromatic rings [148]
649	Out-of-plane -OH bend [151]

i) Lignin

In order to assess the possible influence of TFA in the structure of lignin, the ATR-FTIR spectra of pristine, solvent-cast and electrospun (electrosprayed) lignin were examined and are shown in Figure 5.11. This Figure presents the absorption bands (a) in the region 4000-500 cm^{-1} and (b) in the magnified region 1900-500 cm^{-1}.

The spectra contain the typical peaks found in the literature for lignin samples [148-151, 153].

Table 5.4 summarizes the peaks detected in the pristine lignin sample and their assigned types of vibration. The solvent-cast and the electrospun (electrosprayed) lignin samples exhibited differences in their spectra compared to pristine lignin. Due to the similarity between the spectra of solvent-cast and electrosprayed lignin, in Figure 5.11 only the peaks of the latter are marked.

The most important differences between the spectrum of the electrospun (electrosprayed) lignin and that of the pristine lignin are:

- Solvent-cast and electrosprayed lignin exhibit a large absorption band in the area 1650-1800 cm^{-1}. This band probably corresponds to vibrations of C=O groups either in conjunction or not with the aromatic ring [148-151, 153], probably associated with guaiacyl units [149]. The appearance of these bands could be an indication of cleavage of ester linkages [149]. The peak in the region of 1781 cm^{-1} may signify the presence of trifluoroacetyl groups, since TFA can act as esterifying agent of hydroxyl groups present in lignin [137, 138].

- The most significant difference between pristine and electrosprayed lignin is the huge increase in absorption in the area 1100-1200 cm^{-1}. This area is associated with deformation vibrations of C-H bonds in the aromatic rings [131, 148, 149] probably in syringyl units [148, 149] and is also associated with some possible overlapping of stretching vibrations of C-O bonds [148, 153]. This could signify a higher number of un-substituted positions in the aromatic ring or rearrangement of peripheral groups attached to it [154]. The mechanism of this effect, induced by the strong acid, is not clear. Similar

observations are found elsewhere [150, 154, 155]. In [155] some possible mechanisms of rearrangement in the lignin structure are speculated. However, the large absorption in these wavelengths perhaps also signifies that there is still TFA remaining in the samples, although they were left to dry before FTIR was performed. TFA has an intense absorption band at 1000-1200 cm^{-1} [156]. In this case, the fact that this peak is less intense in the electrosprayed sample than in the solvent-cast sample, could indicate that TFA evaporated more easily from the electrosprayed lignin because it consists of fine microgranules. If this is the case, then any other structural changes in the lignin structure would be concealed.

- Solvent-cast and electrosprayed lignin have intense absorption peaks in the region 640-850 cm^{-1}. These peaks are attributed to deformation vibrations of C-H bonds in aromatic rings [148] or C-H out-of-plane vibrations in guaiacyl units [150]; perhaps another indication of un-substituted positions in the aromatic ring or rearrangement of peripheral groups.

- Generally, in most peaks there is a shift towards higher or lower wavenumber values between pristine and electrosprayed lignin, indicating small structural differences between them. However, the ATR-FTIR spectra don't provide strong evidence of major structural changes in lignin after its dissolution in TFA. Instead, it is possible that some quantity of TFA doesn't evaporate due to intermolecular interactions with the lignin macromolecules.
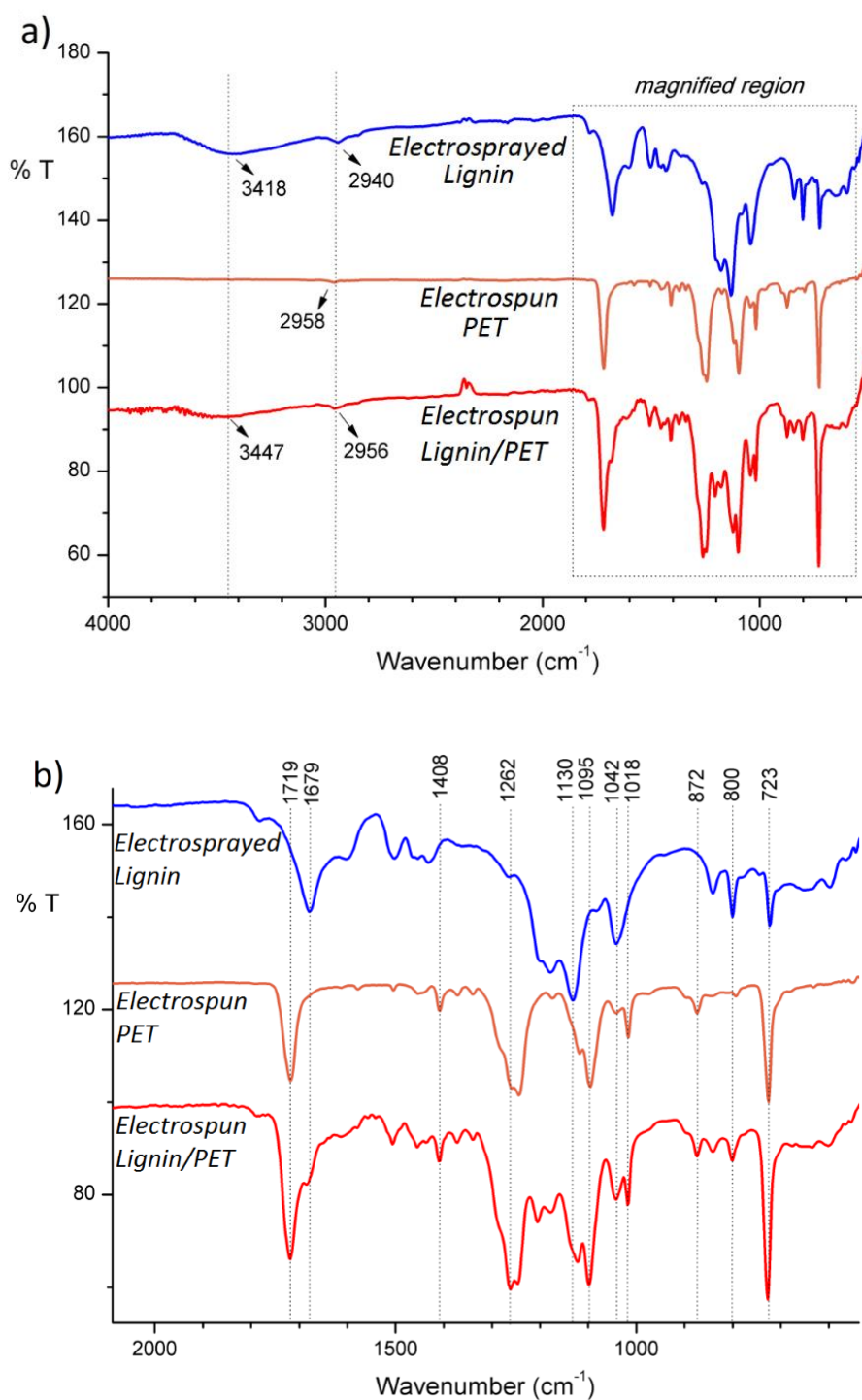
Figure 5.12: ATR-FTIR spectrum of electrospun lignin/r-PET mat in comparison
with the spectra of electrospun (electrosprayed) lignin and electrospun PET;
a) presenting the whole region (wavenumber from 4000 to 500 cm^{-1}); b) presenting
the magnified region

ii) lignin/r-PET blend

Figure 5.12 unveils the ATR-FTIR spectrum of electrospun lignin/r-PET mats in comparison with the spectra of electrospun (electrosprayed) lignin and of the raw r-PET that was used in the experiments. The electrospun r-PET had identical spectrum with the raw PET, so only the former is presented here. The electrospun lignin/r-PET mat, the spectrum of which is presented here, consisted of a 50-50 lignin-PET blend. Spectra of different lignin-PET ratios exhibited absorption peaks at the same wavenumbers.

Table 5.5 summarizes the absorption peaks of electrospun r-PET and their respective types of vibrations as described in the literature. Here, the most distinctive peaks of the r-PET spectrum appear in 1719, 1408, 1242, 1095, 1018, 872 and 723 cm^{-1}. These peaks appear in the electrospun lignin/r-PET mat almost at the same wavenumbers. The same happens with the main lignin absorption peaks (see Table 5.4). The fact that most of the peaks in the blend appear unchanged compared to those of the pure polymers, is an indication of weak intermolecular interactions between them.

Kadla and Kubo [94] reported that in the blend of lignin with PET, the intermolecular bonds consisted mainly of weak intermolecular interactions rather than hydrogen bonding. In the area around 3300-3500 cm^{-1}, which corresponds to hydroxyl stretching due to hydrogen bonding, there is a shift in the peak shown in Figure 5.12a (from 3418 to 3447 cm^{-1}). This is a possible indication of some hydrogen bonding development between the two polymers. However, the peak at 1719 cm^{-1}, which shows the C=O stretching in the r-PET molecules, appears almost unchanged in the blend;

therefore, it can be assumed that there is only a small degree of hydrogen bonding, in accordance with the observations by Kadla and Kubo.

Table 5.5: Absorption peaks and types of vibrations in the electrospun r-PET sample

Peak location (cm^{-1})	Type of vibration
1719	C=O stretching [152]
1408	Para-substituted benzene ring, ring C-H in-plane deformation, ring C-C stretching [152]
1242	(C=O)-C stretching of ester, ring-ester in-plane mode, amorphous phase [152, 157]
1095	Ester C=O stretching / O-CH$_2$ stretching, in-plane ring mode, amorphous phase [152, 157]
1042	Gauche O-CH$_2$ stretching, amorphous phase, gauche conformation [152]
1018	Para-substituted benzene ring, ring C-H in-plane deformation, gauche conformation [152, 157]
872	Para-substituted benzene ring, ring C-H out-of-plane vibration, crystalline phase [152, 157]
723	Ring C-C bending and ring C-H out-of-plane [152, 157]

5.1.6 Elemental analysis

Elemental analysis of the electrospun nanofibers was performed through EDS in order to investigate how the lignin/r-PET mass ratio influences the carbon and oxygen content in the fibers. Particularly, two mass ratios were investigated: 50/50 and 90/10. The samples examined in this case were the samples 4 and 13 respectively from Table 4.3. It was decided to focus on this region of mass ratios, as it was found that mass ratios between 50/50-90/10 yield much better carbonization results than the mass ratios which are less than 50/50. This is explained and analyzed in Section 5.2.
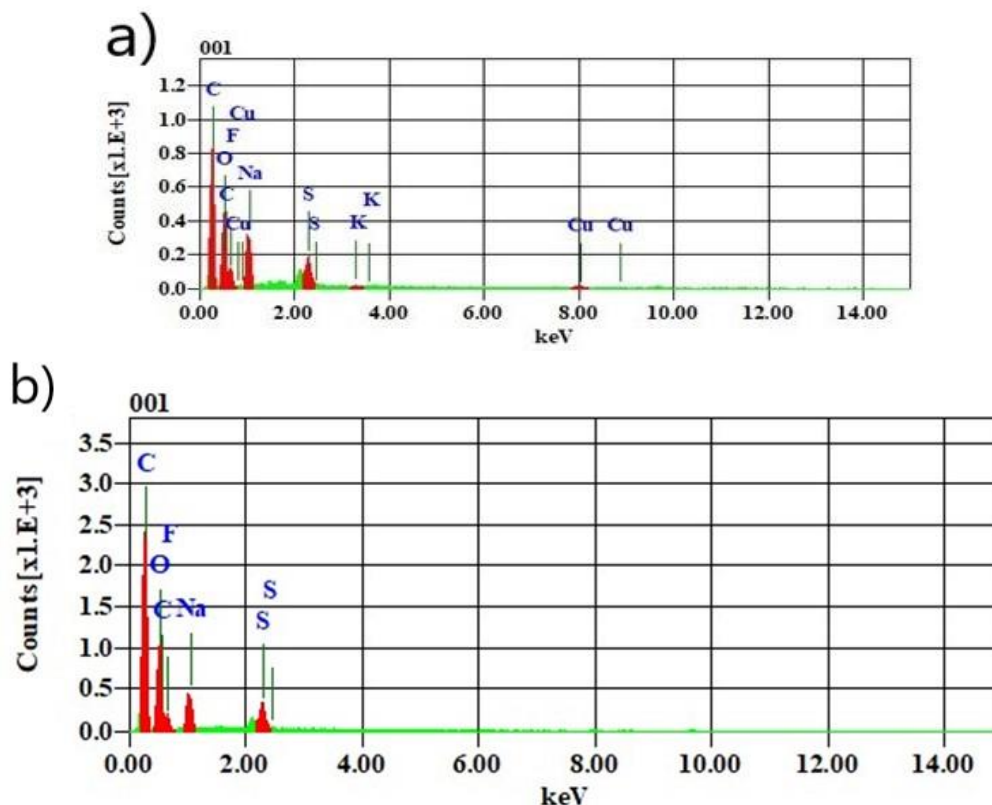
Figure 5.13: EDS spectra of the electrospun nanofibers with different lignin/r-PET mass ratio; a) 90/10; b) 50/50

The results showed that the 90/10 sample consists of $54.67 \pm 1.07\%$ C, $29.16 \pm 2.08\%$ O and the balance ($16.17 \pm 1.12\%$) of other elements (F, Na, K, S, Cu) per unit mass (Figure 5.13b) (average of two measurements). EDS doesn't detect H, therefore this analysis is based on unit mass without H. The 50/50 sample consists of $57.36 \pm 1.95\%$ C, $32 \pm 2.33\%$ O on average and the balance ($10.64 \pm 1.4\%$) of other elements (Figure 5.13a) (average of two measurements). Therefore, the starting kraft lignin contains less C and O than r-PET and a significant amount of impurities (ash). However, it was decided not to purify the starting kraft lignin for three reasons. First, in order to avoid one additional step of treatment; second, in order to demonstrate the feasibility of producing the desirable CNFs from untreated lignin; and third because impurities of alkali and transition metals catalyze the gasification reactions and assist

the development of porosity during carbonization [158]. The detection of F in the electrospun samples denotes the presence of TFA which hasn't evaporated from the samples, in connection to the results from ATR-FTIR presented in Figure 5.11.

5.1.7 Thermal behavior and miscibility of the lignin/r-PET blend

A common way of assessing the miscibility of polymers is by monitoring the thermal behavior of their blends in various compositions. The appearance in the blends of a single glass transition temperature (T_g), which is dependent on the blend composition, signifies full miscibility at a dimensional scale between 5-15 nm [94]. The appearance of two distinct glass transition temperatures, however, is an indication of immiscible polymers.

Figure 5.14 presents the DSC curves of the electrospun mats prepared from lignin/r-PET blends of various compositions. In addition, the thermograms of the pristine untreated lignin (100/0) and the starting r-PET (0/100) are presented. In order to reveal more details about the thermal behavior of PET, its thermogram in the region 60-130°C is magnified.
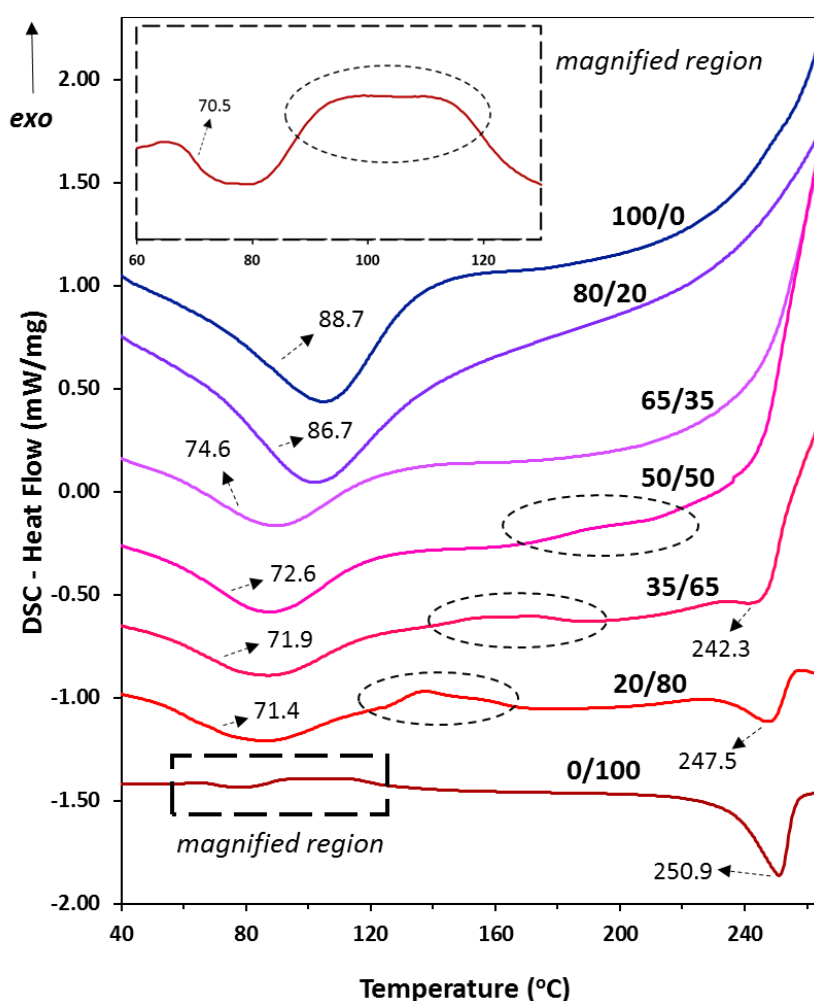
Figure 5.14: DSC thermograms of electrospun mats prepared from various lignin/r-PET blends (80/20, 65/35, 50/50, 35/65, 20/80), the pristine untreated lignin (100/0) and the starting r-PET (0/100). The dashed ellipses indicate the regions of cold crystallization

The r-PET has T_g at 70.5^{o}C as indicated by the respective slope appearing at that region. The large endothermic peak at 250.9 indicates its melting temperature (T_m), while the broad exothermic plateau in the region 95-120°C is associated with its cold crystallization temperature (T_{cc}). The T_{cc} of pure PET generally appears in the region between 100-160°C, while its T_g is generally between 70-80°C [116-118, 159].

On the other hand, the T_g of lignin generally varies depending on its source, while it doesn't exhibit any melting temperature since it is amorphous due to its

complex structure [160-162]. Here, the T_g of lignin appears at approximately 88.7°C. One can observe that each lignin/r-PET blend has one single T_g which depends on the blend composition. Increasing the mass fraction of lignin, there is a slight gradual increase in the T_g of the blend from the curve of pure r-PET (0/100) towards the curve of pristine lignin (100/0). It can be deduced that the incorporated amorphous lignin interacts with r-PET at molecular level and restricts the motion of the polyester macromolecules, raising its T_g. Therefore, there is evidence that the two polymers are miscible.

Due to the close proximity of the glass transition temperature between pristine lignin and raw PET, as well as the moderate inclination that the DSC curves exhibit at that region, there could be a possibility of overlapping between two separate peaks; this scenario would conceal the possible immiscibility between lignin and r-PET. Nevertheless, this case should be rejected since the T_{cc} and T_m peaks provide a collateral evidence for the good miscibility of the two polymers. It is clear that the cold crystallization region in the raw r-PET shifts gradually towards higher temperatures with increasing lignin content, until it disappears for lignin mass fraction higher than 65 wt% (the trend is highlighted with the dashed ellipses in Figure 5.14).

In addition, the melting temperature of r-PET gradually decreases with increasing lignin content (from 250.9°C at 0 wt% lignin to 242.3°C at 35 wt% lignin) until it practically vanishes for more than 50 wt% lignin content. This is an indication of amorphous structure, or perhaps only minor regions in the blend are crystalline, which are undetectable in the thermograms here. It can be inferred from the observations regarding T_g, T_{cc} and T_m, that lignin interacts with the polyester macromolecules, restricts their mobility and impedes their crystallization. The lignin-PET interactions disrupt the integrity and purity of r-PET spherulites and induce a drop

in the melting temperature of the polyester. Similar behavior has been reported for the blend of lignin with poly(lactic acid) [162, 163]. These results provide therefore strong support to the hypothesis that lignin and r-PET exhibit good miscibility, and agree with previous observations for the same polymers [94].

5.1.8 Section summary

In this Section it was demonstrated how a designed experimental approach enabled the modeling of the electrospinning process, the investigation of the influence of the process variables on the morphology of the electrospun fibers and the identification of the conditions that decrease the average fiber diameter. For the electrospinning process, only the solution concentration and the spinning distance were found to influence the fiber diameter. In contrast, the applied voltage, the flow rate and the lignin ratio in the polymer blend were insignificant to the fiber diameter and to its standard deviation for the range of factor values examined in this experimental design. Hence, it was found that decreasing the solution concentration induces a decrease in the average fiber diameter of the electrospun mats. A further experimentation under these conditions enabled the preparation of electrospun nanofibers with average diameter as low as 80 nm. This is a very important result as this value represents a scaling down of lignin/PET fiber diameters by two orders of magnitude compared to lignin/PET fibers produced by other methods reported in the literature. This scaling down in the average fiber diameter maximizes the external surface area of the fibers, a property which is crucial for a variety of applications. Furthermore, examination of the electrospun mats with ATR-FTIR indicated the blending of the two polymers via weak intermolecular interactions. Evidence of the good miscibility between lignin and r-PET was also provided by DSC measurements.

Moreover, elemental analysis with EDS highlighted how the carbon content in the fibers changes with the lignin/r-PET mass ratio, and revealed the presence of impurities mainly in the starting kraft lignin.

5.2 Carbonization of the precursor electrospun nanofibers: the synergy between the mass ratio and the average fiber diameter

After producing electrospun nanofibers of desired morphology at certain lignin/r-PET mass ratios, the next step of this research was to carbonize them for their transformation into CNFs. Some preliminary experiments suggested that the carbonization yield is much better when the percentage of lignin in the blend is higher than 50%. Therefore, it was decided to focus on lignin/r-PET mass ratios between 50/50-90/10, as there were spinnability problems beyond 90/10. Moreover, it was found that in this whole range of mass ratios it is feasible to produce electrospun nanofibers with average diameters lower than 100 nm, when a solution concentration of 10% w/v was used. The electrospinning conditions for producing the mats that were used in the experiments included in this Section are presented in Chapter 4.

Furthermore, it was repeatedly observed that the production of CNFs with a well-formed filamentous structure is only possible under certain conditions regarding the mass ratio between lignin and r-PET and the average diameter of the precursor electrospun nanofibers. In this section, the conditions leading to the successful fabrication of CNFs are described, while the reasons leading to the collapse of the fibrous structure when these conditions are not met are illuminated. First, the nano-diameter effect will be analyzed for fibers prepared from 50/50 lignin/r-PET (Section 5.2.2), and the discussion will be extended for different mass ratios, in which the combined effect of the mass ratio with the nano-diameter will be explained.

5.2.1 The decomposition profiles of lignin and of r-PET

Figure 5.15 shows the decomposition of pristine lignin in comparison with that of the electrosprayed lignin. Pristine lignin undergoes a multiple-stage decomposition, the first stage of which is located between 154-400°C (after the removal of moisture at T<100°C). At this wide stage, the cleavage of weaker bonds (e.g. C-O) takes place with the maximum rate of decomposition appearing at 295°C. The asymmetrical shape of this peak indicates the diversity of the decomposition reactions taking place, which is due to the irregular structure of lignin. The evolution of medium-volatile constituents continues until around 600°C, above which the final stage of lignin decomposition takes place, with the cleavage of stronger bonds (e.g. C-H) [164, 165]. This profile is in accordance with similar curves for commercial lignin found in the literature [43, 166].

Inspection of Figure 5.15 shows clearly that the first stage of decomposition of electrosprayed lignin is much different than that of the pristine one. Between 185-267°C there is a significant weight loss, followed by a smaller weight loss between 267-400°C. In the first of these two regimes, the rate of weight loss reaches the peak value of 0.56%/^{o}C at 237°C, which is much higher (more than double) than that at the peak of pristine lignin (0.25%/^{o}C at 295°C). These differences in the two profiles, indicate that electrosprayed lignin decomposes faster compared to the pristine one, and a larger amount of volatile gases evolve from its bulk. The second regime reaches its highest value of decomposition rate (0.17%/^{o}C) at 307°C. At 400°C, the residual weight is 51.5% and 65% for the electrosprayed and the pristine lignin respectively. Above this temperature, there is no significant change in DTG curve between these

two materials, but electrosprayed lignin keeps decomposing at a slightly higher rate. The final yield at 900°C is 8.6% and 29% respectively.
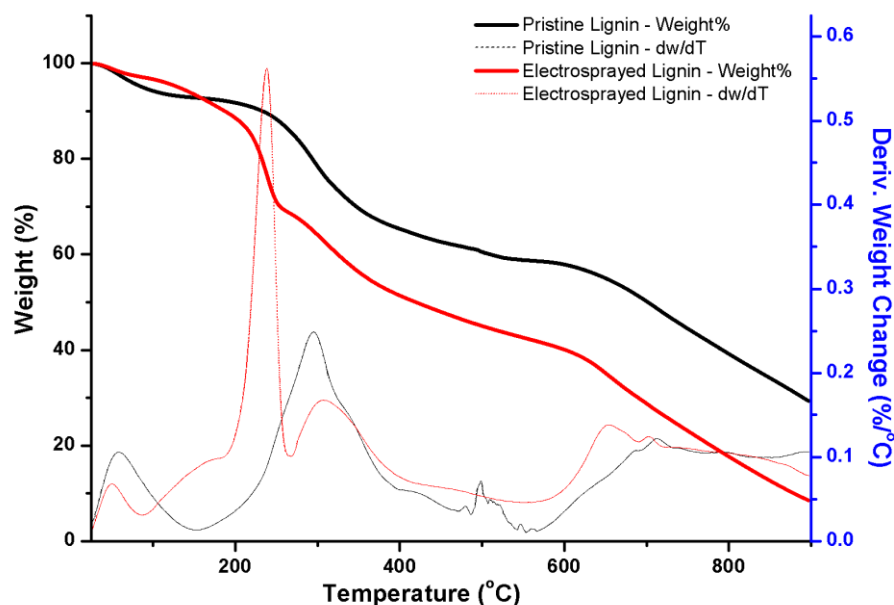
Figure 5.15: Weight loss as a function of temperature for the pristine lignin (black) and for the electrosprayed lignin (red). The dotted lines display the first derivative of the weight loss

It has been reported that trifluoroacetic acid, the electrospinning solvent used in this study, induces changes in the lignin molecular structure [155], which are associated with oxidation of aryl-carbon atoms or attachment of fluoride ions on them, and possibly with some rearrangement of their peripheral groups. Obviously, these changes have an impact on the carbonization profile of lignin.

In addition, the most important reason for the difference in the decomposition profiles between the two samples, is most probably the large size difference between their granules. Figure 5.16 shows that pristine commercial lignin consists of large granules with an average size that was measured to be 56.4 ± 24 μm.
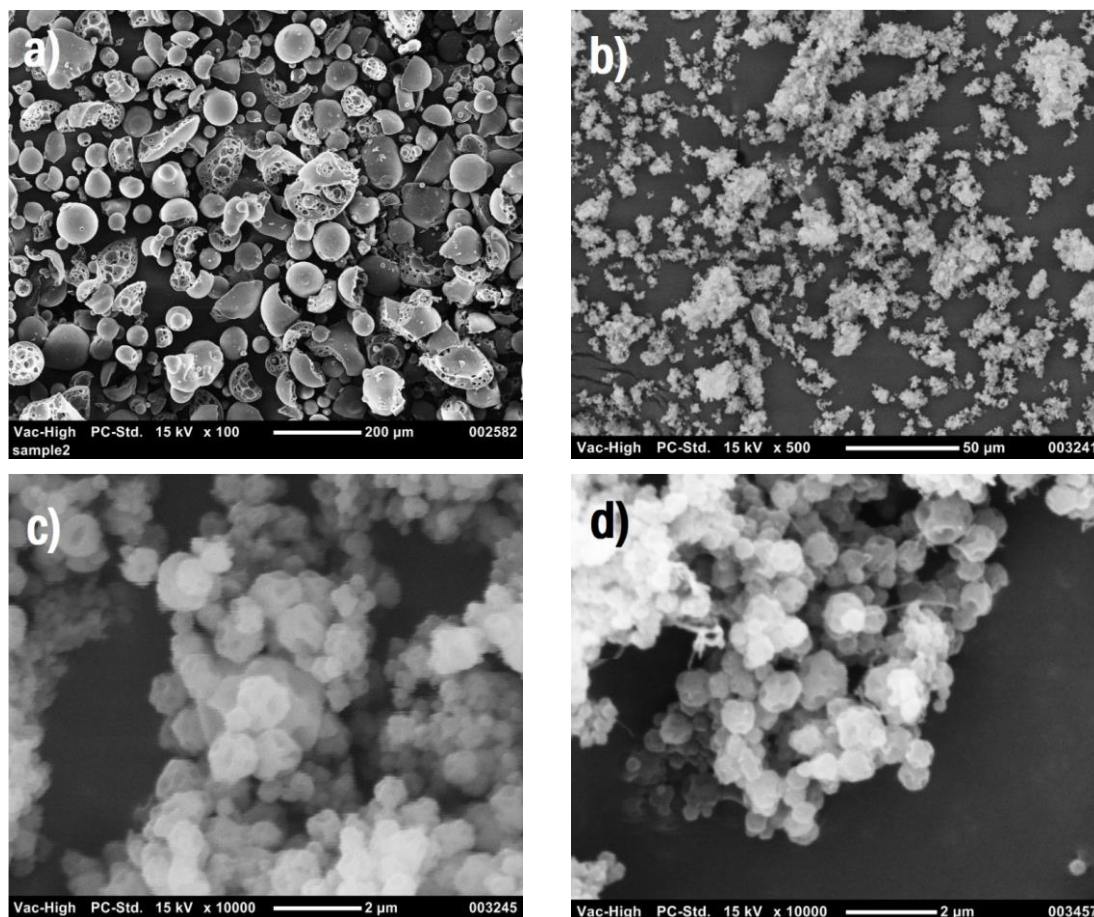
Figure 5.16: SEM images of pristine, electrosprayed and carbonized lignin;
a) granules of pristine lignin (magnification x100); b) electrosprayed lignin (x500);
c) electrosprayed lignin (x10,000), d) carbonized electrosprayed lignin (x10,000)

In contrast, the electrospinning process produces spray of very small droplets, which after deposition on the collector and evaporation of the solvent, results in the formation of submicron-sized rough granules of electrosprayed lignin (Figure 5.15b-c). The average diameter of these granules was measured to be 669 ± 228 nm. This almost hundred-fold decrease in the average size of lignin particles results in a vast increase in the total surface area per unit mass. More precisely, and assuming spherical granules and by simple geometrical calculations, decreasing their average diameter by 84.3 times, increases their specific surface area by around 7,106 times. Since the decomposition process is dependent on heat transfer towards the interior of the

particles and mass transfer from their interior to the atmosphere, such a massive increase in the surface area of the granules is expected to speed up the whole process. The reason is that more molecules are on the surface or near the surface of the granules, and the volatile gases can escape faster through diffusion from their core. Indeed, the TGA profiles of these two samples demonstrate this effect.

Moreover, the complex irregular structure of lignin results in the absence of melting temperature as it was shown in the previous section. In the case of the carbonization of lignin/r-PET fibers, this property of lignin is desirable, since it allows the preservation of the fibrous structure, as the fibers are slowly carbonized without melting. Figure 5.16d shows the electrosprayed lignin after having been carbonized at 800°C under inert atmosphere. The granules retain their shape, while their size distribution remains at the same levels as of the starting electrosprayed ones (622 ± 213 nm).

Using lignin alone, it was not feasible to produce electrospun fibers. This is attributed to the relatively low molecular weight of the lignin used here, which results in the absence of extensive chain structures and molecular entanglements [23]. This in turn results in lignin solutions of relatively low viscosities, or at least lower than the values required for the successful formation of fibers. For the electrospinning technique, it is well known that if the viscosity of the solution is relatively low then the jet breaks into droplets under the influence of the electrostatic field [17]. Therefore, it was not possible to produce lignin nanofibrous mats of different average fiber diameters and to compare their decomposition rates.

Figure 5.17 presents the TGA curve of the starting r-PET as well as that of the electrospun r-PET. The fibrous mat of electrospun r-PET consisted of fine fibers with average fiber diameter of 204 ± 90 nm (sample 7, Table 4.2) (see Figure 5.18). Here

the behavior is totally different than in the case of lignin. Both samples exhibit an almost identical TGA profile, with a main decomposition step taking place at 340-476°C, and a maximum decomposition rate of 2%/°C appearing at 409°C. This peak temperature is in accordance with the decomposition profiles of PET found in the literature [167, 168]. Although the r-PET electrospun mat consisted of very fine fibers with much larger surface area than the small pieces of the starting r-PET, it seems that the nanoscale dimension plays no role in its decomposition profile. The reason is that r-PET melts at 250.9°C, much earlier than the onset of decomposition. Therefore, by the time the material reaches 340°C, the nanofibers have been transformed into a shapeless melt (see Figure 5.18b-c).
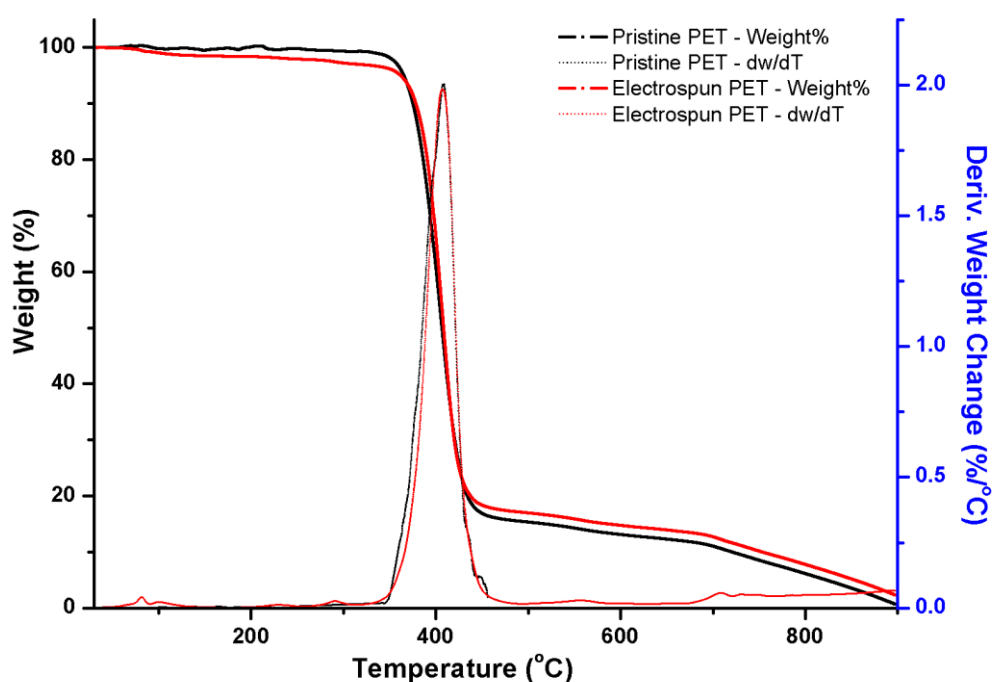
Figure 5.17: TGA curves of the starting r-PET and of the electrospun r-PET nanofibers
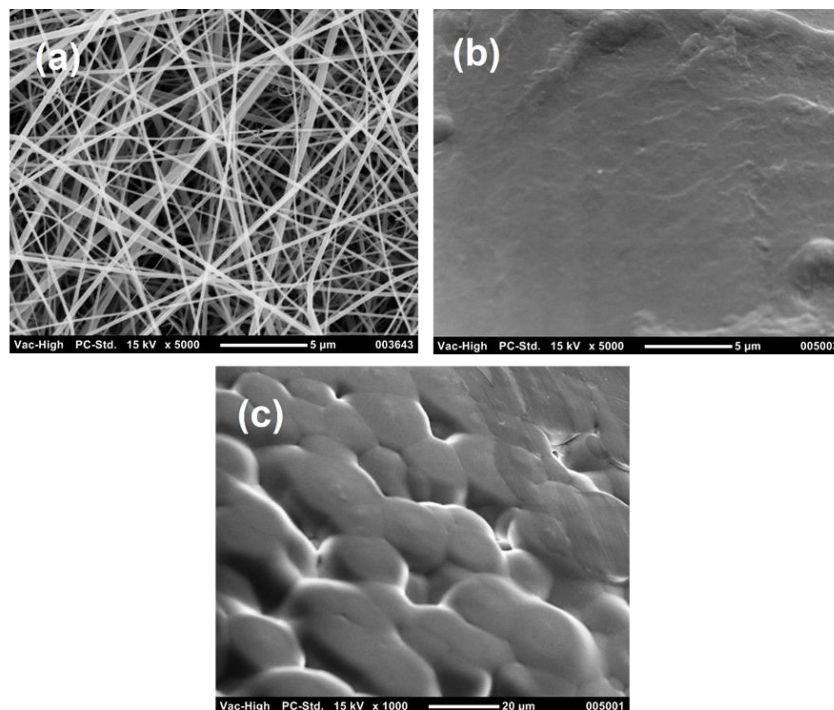
Figure 5.18: SEM images of electrospun r-PET nanofibers; a) average fiber diameter of 204 ± 90 nm; b) and c) the same nanofibers after being heated at 300°C under N_2

The decomposition continues at higher temperatures until the residual weight reaches almost 0% at 900°C. In the case of r-PET it is feasible to produce electrospun mats of varying average fiber diameter using r-PET alone. Nevertheless, due to the melting of these mats at 250.9°C, they all lose their filamentous structure and they decompose at a similar rate at 409°C.

5.2.2 The effect of the nanoscale dimension

Understanding the carbonization of electrospun lignin/r-PET fibers is crucial for the preparation of tailor-made carbon nanofibers with a well-formed structure. In order to examine the effect of lowering the diameter to the nanoscale, electrospun samples of varying average fiber diameter were prepared and their TGA curves are presented in Figures 5.19 and 5.20.
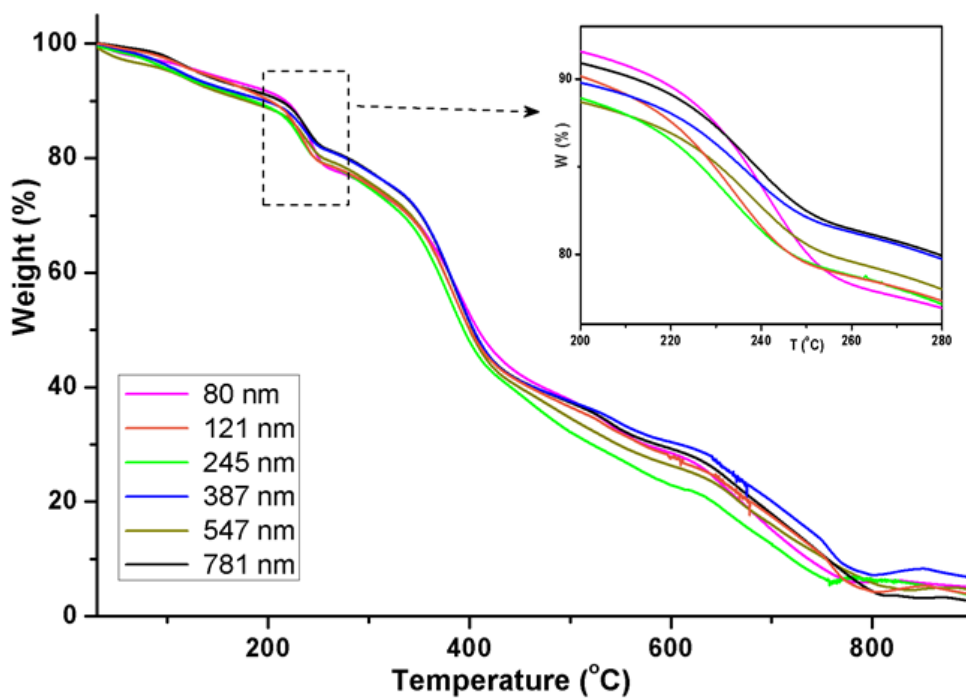
Figure 5.19: Weight loss as a function of temperature for electrospun 50/50 lignin/r-PET fibrous samples of varying average fiber diameter
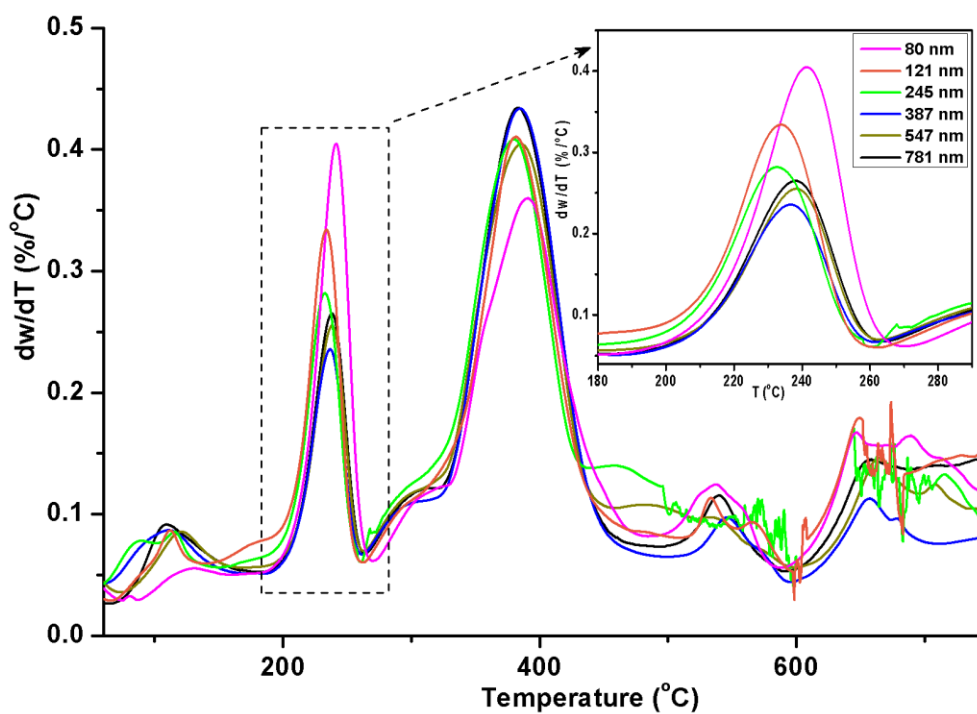
Figure 5.20: DTG curves of the electrospun 50/50 lignin/r-PET fibrous mats

In the figures, the TGA profiles of six electrospun samples consisting of fibers with average diameter of 80, 121, 245, 387, 547 and 781 nm respectively are displayed (see Table 4.2 for the electrospinning conditions). All samples were prepared using a lignin/r-PET mass ratio of 50/50. Here, it is apparent that the fibers decompose in distinctive steps, which correspond to the regimes found in pristine lignin and in r-PET. The first major step is located between 180-260°C and is attributed to the decomposition of lignin; this is followed by a smaller regime around 300°C, similar to the one appearing in electrosprayed lignin. In the region between 325-460°C, the major decomposition of the r-PET chains take place. Finally, there are two more decomposition regimes, one located between 500-600°C and another one at higher temperatures; both are mainly attributed to lignin.

The effect of lowering the average fiber diameter to the nanoscale is explicit in the first decomposition regime of lignin (180-260°C). The relatively thicker fibers (387-781 nm) exhibit a peak of maximum decomposition rate of 0.24-0.26%/^{o}C (Figure 5.20). However, a higher peak is observed as the diameter decreases. For the fibers of 245 nm the decomposition rate reaches a peak value of 0.28%/^{o}C, and for those of 121 nm their decomposition rate reaches a peak of 0.33%/^{o}C. Furthermore, the thinnest fibers (80 nm) exhibit the highest peak in this region, as their decomposition rate reaches a maximum of 0.40%/^{o}C. This is around 60% higher than the maximum decomposition rate of thicker fibers (>387 nm). These values refer to the peak in the decomposition rate exhibited by the samples in this region, not to the average rate. However, if a comparison based on the average rate is performed, then the thinnest fibers will again have the highest value, as it is reflected in the weight loss measured in this region. For fibers of 387-781 nm, the weight loss between 180-260°C is around 8.5-9.3%. Fibers of 245 nm exhibit a weight loss of 10.3%, those of 121 nm

exhibit a weight loss of 11.3%, and the maximum weight loss in this region is found for the minimum fibers of 80 nm, and it is measured 14.5%. These numbers are concisely presented in Figure 5.21.
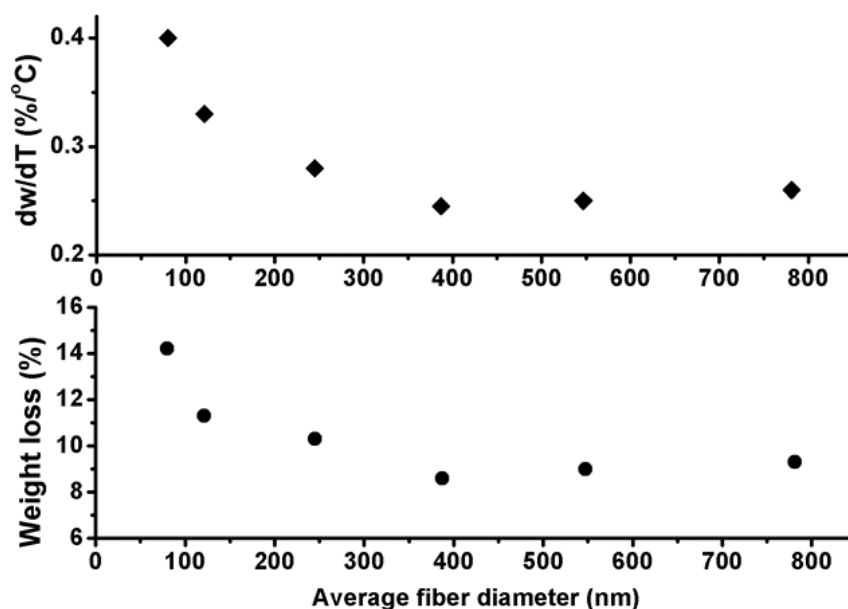
Figure 5.21: The influence of the average fiber diameter in the maximum decomposition rate (%/°C) and in the weight loss (%) of the precursor fibers in the region 180-260°C

As already mentioned, the carbonization of the electrospun fibers is a process involving restrictions due to heat and mass transfer. From the previous observations, it can be concluded that these restrictions are dominant in fibers of relatively larger diameter (>387 nm). The transfer of heat towards the interior of the fiber and the evolution of volatiles from its core due to diffusion obviously limit the rate of decomposition, to a value that is almost constant over a wide range of diameters (387-781 nm). However, as the average diameter is reduced to less than 245 nm, it seems that these restrictions diminish. Reaching the minimum diameter of 80 nm, these limitations play a minimum role, and here it seems that the overall rate of the process is mainly controlled by the decomposition reactions taking place inside and on the

surface of the nanofibers, as the volatile products can be transported more easily to the atmosphere. This effect for the decomposition of nanofibers, although rational, has scarcely been reported. J.S. Ye et al. [169] have presented a higher weight loss for PAN-based electrospun nanofibers of 39 nm average diameter compared to thicker nanofibers, although their study was focused on different aspects.

During carbonization, a higher specific surface area is expected to facilitate the heat transfer towards the interior of the fibers and the mass transfer of the decomposition products to the atmosphere through molecular diffusion. Moreover, a sample of higher surface area will have more molecules exposed on its surface, which can more easily undergo decomposition. Assuming nanofibrous mats of equal mass, prepared from the same raw material, with fibers of a uniform cylindrical shape, and using simple calculations based on their geometry, one can calculate that a relatively small decrease in the average fiber diameter will have a large impact on their total length and specific surface area. Specifically, the electrospun nanofibers with average diameter of 80 nm are 128% longer than those of 121 nm, 838% longer than those of 245 nm and 2240% longer that those of 387 nm. Moreover, the sample having average diameter of 80 nm will theoretically have 51% higher external surface area than the sample of 121 nm, 206% higher external surface area than the one of 245 nm, and 383% higher than the one of 387 nm (external surface without taking into account any porosity, as the assumption that the electrospun nanofibers are not porous is valid here). Finally, considering the ratio of surface to volume, which shows the number of molecules exposed on the surface compared to those confined in the bulk, the sample of 80 nm will also have 50%, 206% and 383% higher ratio compared to the samples of 121, 245 and 387 nm respectively. Comparisons with the samples which are made of thicker fibers, reveal a much larger difference. The fact that the samples consist of

fibers, which have a distribution of diameters over a wider range, doesn't influence so much these calculations, as the samples exhibit a similar fiber distribution with standard deviation around 30-40% of the average diameter.

Regarding the decomposition regime of r-PET, which appears between 325-470°C, having a peak at around 383°C, it seems in Figure 5.20 that the sample of 80 nm shows a lower decomposition rate than the rest. However, its peak is broader to the right, and calculations regarding the % weight loss show that it is similar for all samples in this region, around 31-33%. This amount is lower than the total% of r-PET mass present in each sample (50%). This means that due to the presence of lignin and the intermolecular interactions between these polymers, not all the r-PET decomposes in this region. Instead, a part of it decomposes at higher temperatures.

The differences in the decomposition noticed among the samples with respect to their average fiber diameter, can be observed by examining their SEM images after their carbonization at 600°C under N_2. Figures 5.22a-f present these results, comparing between the precursor electrospun (on the left) and the same sample after carbonization (on the right), for all the samples of different diameters. In the experiments conducted here, carbonizing at even higher temperature (e.g. at 800°C) didn't change the morphology of the fibrous mat.

As the SEM images suggest, the effect of the average fiber diameter, which was observed in the TGA, has an impact on the shape of the carbonized fibers. The samples of relatively larger average diameter (>387 nm) retain their fibrous structure during carbonization. There is no obvious melting or perhaps only at a minor degree, which doesn't destroy the original cylindrical form of the fibers. The final carbon fibers have average diameter at the same levels as the precursors. However, as the diameter is lowered to the nanoscale, there seems to be melting and fusion of the fibers.
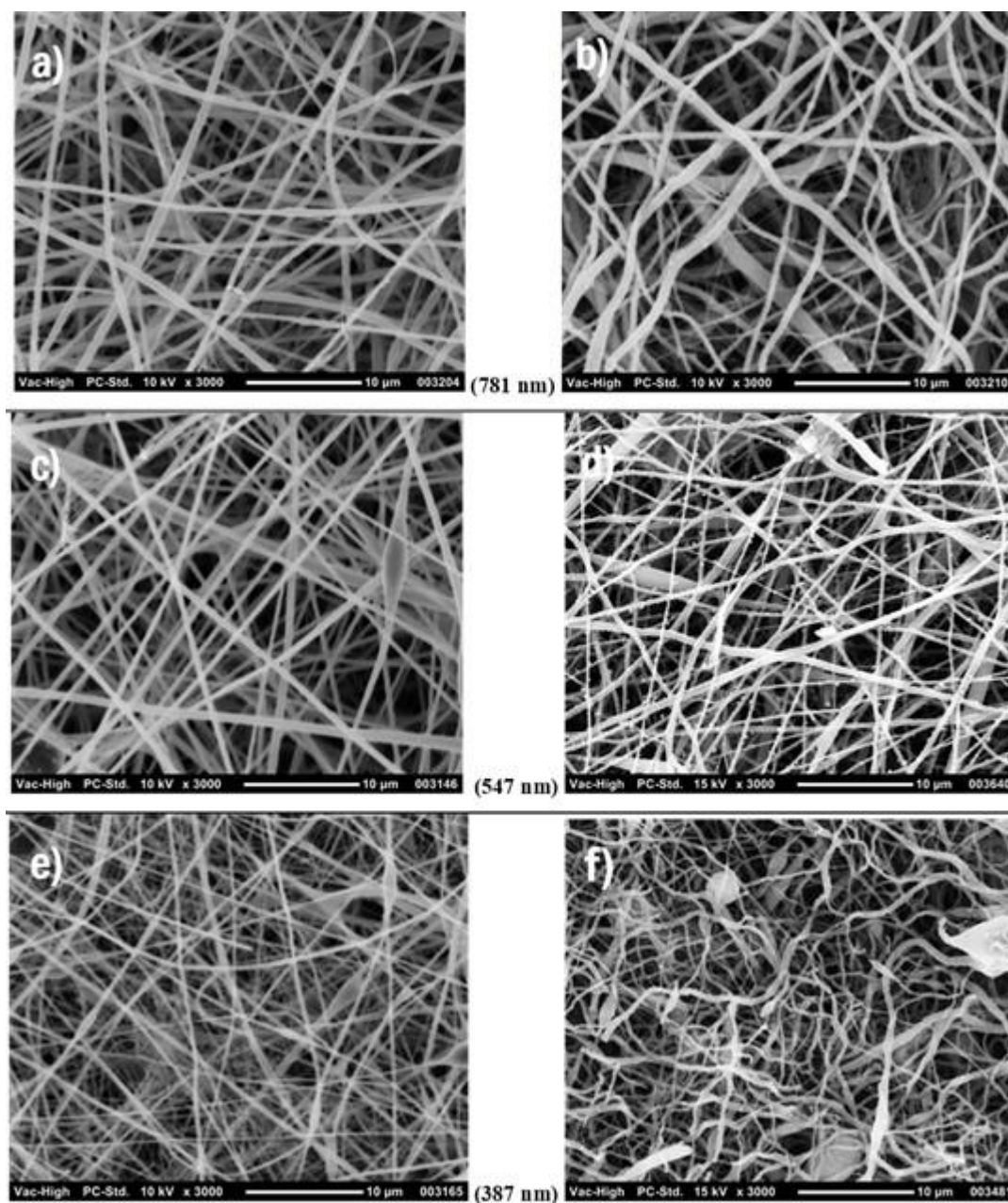
Figure 5.22: Carbonization results for the electrospun 50/50 lignin/r-PET fibrous mats of different average fiber diameter. The precursor mats are presented on the left, and the corresponding carbonized ones on the right; a)-b) 781 nm, c)-d) 547 nm, e)-f) 387, g)-h) 245 nm, i)-j) 121 nm, k)-l) 80 nm. Magnification: images a)-f): x3000, images g)-h): x5000, images i)-l): x10000
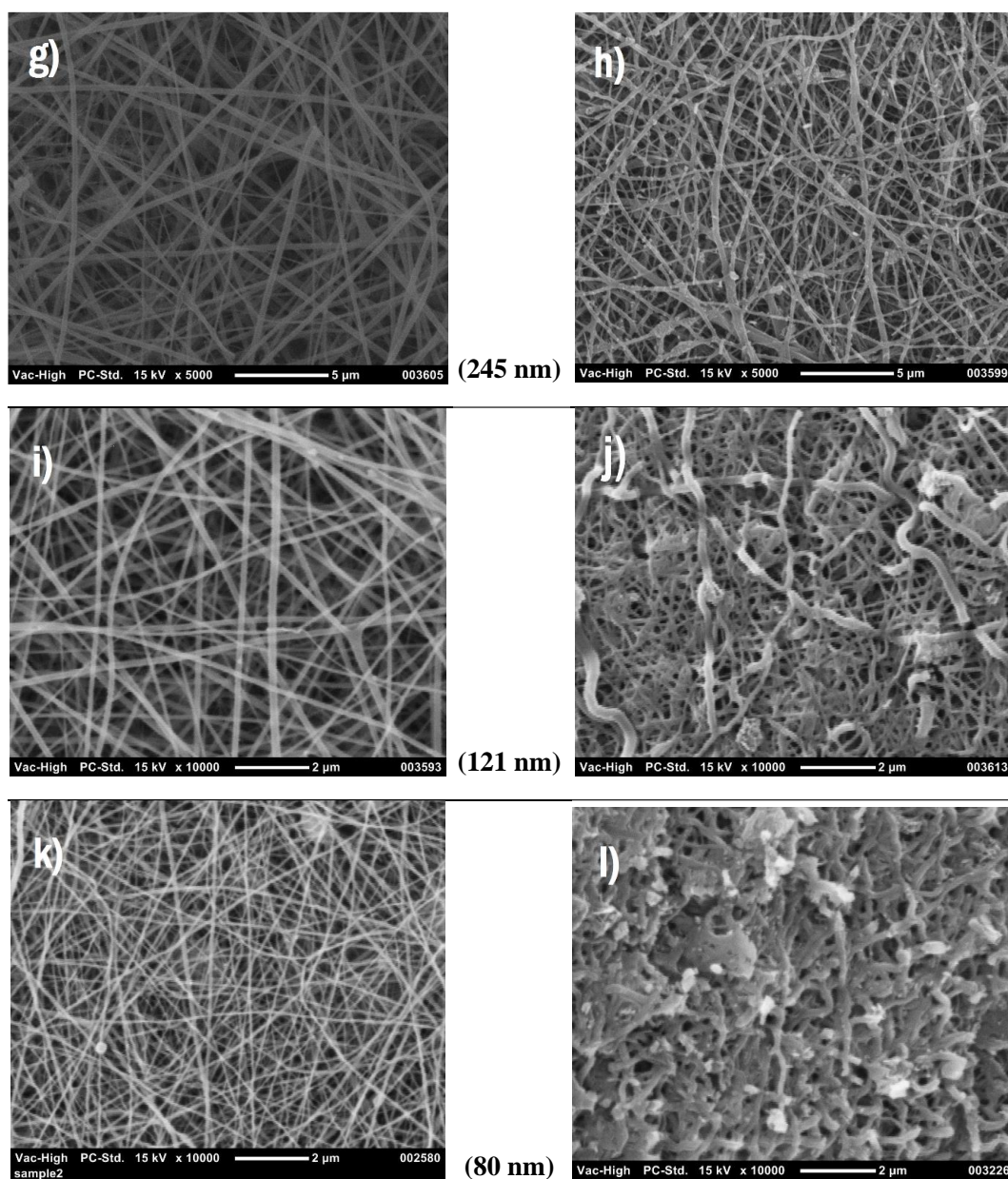
Figure 5.22: Carbonization results for the electrospun 50/50 lignin/r-PET fibrous mats of different average fiber diameter. The precursor mats are presented on the left, and the corresponding carbonized ones on the right; a)-b) 781 nm, c)-d) 547 nm, e)-f) 387, g)-h) 245 nm, i)-j) 121 nm, k)-l) 80 nm. Magnification: images a)-f): x3000, images g)-h): x5000, images i)-l): x10000 (continued)

The sample of 121 nm shows a considerable degree of melting, while in the sample of the minimum diameter (80 nm) the melting and fusing is so extensive that the structure cannot be characterized as "fibrous". This melting is expected to have an

impact on the surface area of the fibers and to compromise their applicability in relevant applications. It must be mentioned here, that the addition of a "stabilization" step of heating in air before carbonizing them under inert atmosphere, did not prevent the fibers from fusing, although it has been reported effective in other types of lignin-based fibers [29, 35].

In the previous section it was shown that lignin and r-PET are fully miscible. R-PET itself is a semicrystalline polymer with melting point at 250.9^{o}C, while lignin is amorphous. When the two polymers are mixed, lignin disrupts the integrity of the r-PET spherulites as it is intercalated among the r-PET chains and restricts their movement. However, and based on the results from the TGA studies, it seems that the decomposition of the lignin macromolecules occurring at 180-260°C gives the chance to r-PET chains to gain some mobility. This result is more pronounced in the nanofibers of 80 nm, where the decomposition rate is much higher. Therefore, a visible melting behavior appears to some extent, and it results in the fusion among the nanofibers of the minimum average diameter. Heating these nanofibers under N_2 with the same heating rate until just 300°C reveals that the melting has already occurred at that temperature and that it has destroyed the fibrous network (see Figure 5.23). This means that the fusion of the nanofibers is manifested at the region of lignin decomposition for the above-mentioned reasons. In contrast, there is no visible melting and fusion in the samples of thicker fibers.

The hypothesis, that the decomposition of lignin up to 300°C results in an increased mobility of the PET chains and therefore in the melting of the nanofibers, was tested using DSC. Four of the samples were heated one after the other inside the tubular furnace at standard heating rate (5°C/min) up to 300°C, without holding them at that temperature, and then they were left to cool down. The whole process was

carried out under N_2 atmosphere. The four samples were those with average fiber diameter of 80, 121, 387 and 781 nm respectively. After they cooled down, their DSC curves were recorded and are presented in Figure 5.24.
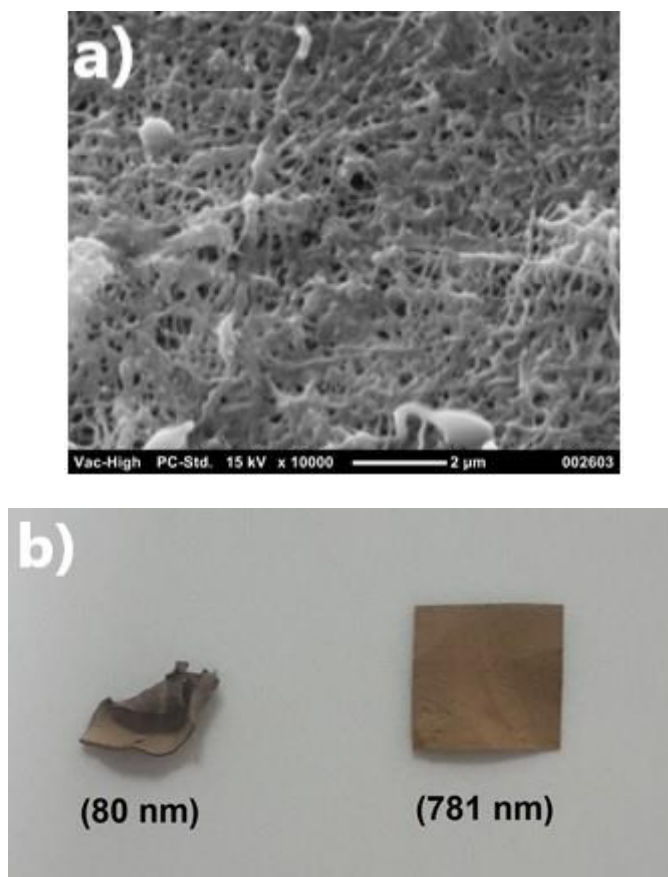
Figure 5.23: The effect of heating on lignin/r-PET electrospun nanofibers; a) lignin/r-PET electrospun nanofibers heated under N_2 up to 300°C; b) comparison of shrinkage and warp between mats of different average fiber diameter. The samples are: 80 nm vs. 781 nm, heated under N_2 at 300°C. Lignin/r-PET is 50/50 in both images
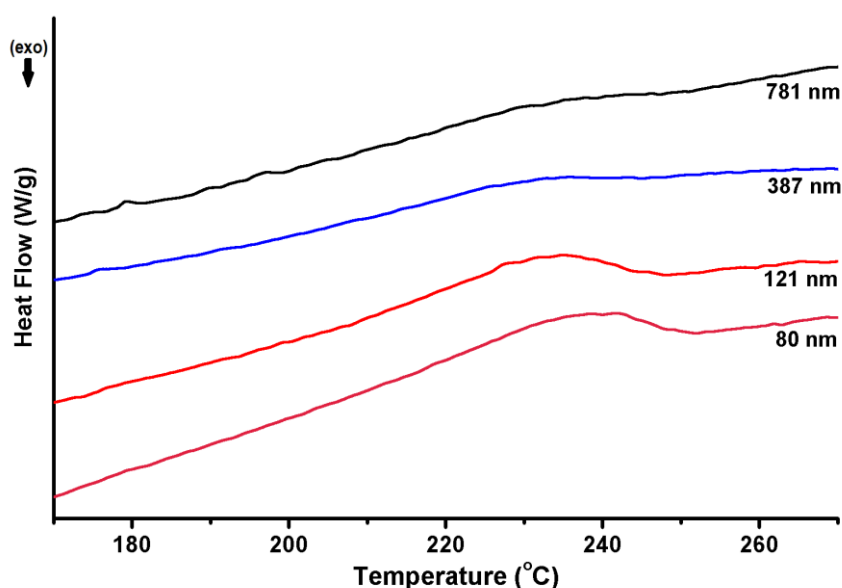
Figure 5.24: DSC curves of the samples with average fiber diameter of 80, 121, 387 and 781 nm, after they were heated up to 300°C. Lignin/r-PET is 50/50

The DSC curves illuminate the differences in the carbonization behavior of the samples based on their diameter. It seems that the samples of small diameter (80 and 121 nm) exhibit clear melting peaks in the region of 230-240°C. Both peaks are very broad, indicating a non-uniformity of the melting regions. The enthalpy of melting for both samples was measured to be around 1.1-1.2 J/g. In contrast, for the samples of large diameter, the melting peak is much less pronounced, and almost undetectable. For both samples, integration of the curve at this region gave an enthalpy of melting of around 0.4 J/g. This value is much lower than that of the samples of small diameter. Hence, there are much fewer regions inside the material that melt. This observation confirms the hypothesis that the increased decomposition of lignin up to 300°C in the minimum-diameter nanofibers is responsible for their more pronounced melting, compared to the thicker fibers.

In addition, besides the melting of fibers observed microscopically in the nanofibrous mats of minimum diameter when they are heated, macroscopically these

samples show a larger shrinkage and warp compared to those consisting of thicker fibers, and they become more brittle during carbonization (see Figure 5.23, for the samples heated up to 300ºC). This behavior denotes that during their heating more volatiles are evolved, their hydrogen and oxygen content is reduced more rapidly, and in the end, they yield a stiffer material consisting of a higher percentage of carbon.

This assumption was validated and confirmed by performing elemental analysis using EDS for the samples of 80 nm and 781 nm, after they were heated at 320, 490 and 800ºC under inert atmosphere (Figure 5.25). This analysis reveals that as these samples are heated, the carbon content in the sample of minimum diameter becomes gradually higher than that of the sample of maximum diameter at the same temperature, while the oxygen content becomes progressively lower.
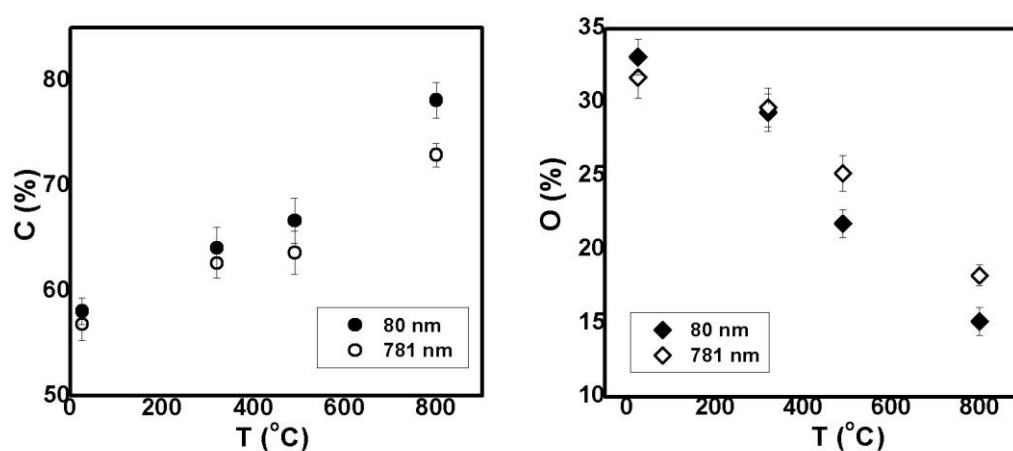
Figure 5.25: C% and O% per unit mass of the samples of minimum and maximum average diameter, as they are heated under N_2 atmosphere up to 800ºC

It should be pointed out that when the average diameter of fibers is reduced to the nanoscale, their surface energy has been reported to increase [170]. Hence, an additional reason here could contribute to the melting of nanofibers, as the excessive surface energy could provide the potential for an increased degree of melting. Even if

this phenomenon occurs here, this is an additional, indirect effect of the nano-dimension.

5.2.3 The effect of the lignin/r-PET mass ratio

In this section, a more detailed description of the melting of nanofibers will be attempted, as it has been repeatedly observed during this research that at certain conditions the fibers melt to a smaller or larger extent, therefore, the filamentous structure collapses. When the degree of melting is extensive, then these electrospun samples yield a rigid, brittle chunk of char, which has lost its fibrous structure. In contrast, when there is only minor or negligible melting among the fibers, then these samples yield carbon nanofibrous mats which have some degree of flexibility and they retain their filamentous structure. Quantifying the degree of melting is not easy; thus, it was decided to use a simple qualitative description by distinguishing three categories for the extent of melting; namely, "extensive", "moderate" and "minor". It is termed as "extensive" the degree of melting which results in the total collapse of the filamentous structure; in this case, most of the fibers have lost their shape and it is not possible to distinguish them. Typical examples of this behavior are presented in Figure 5.22l and in Figure 5.23a.

In "moderate" melting, there is an existing yet relatively limited extent of fusion, especially at the spots where many fibers form "knots". Here, there is a significant degree of interconnection among the fibers, but their shape is distinguishable. Typical examples of moderate melting are presented in Figure 5.26.
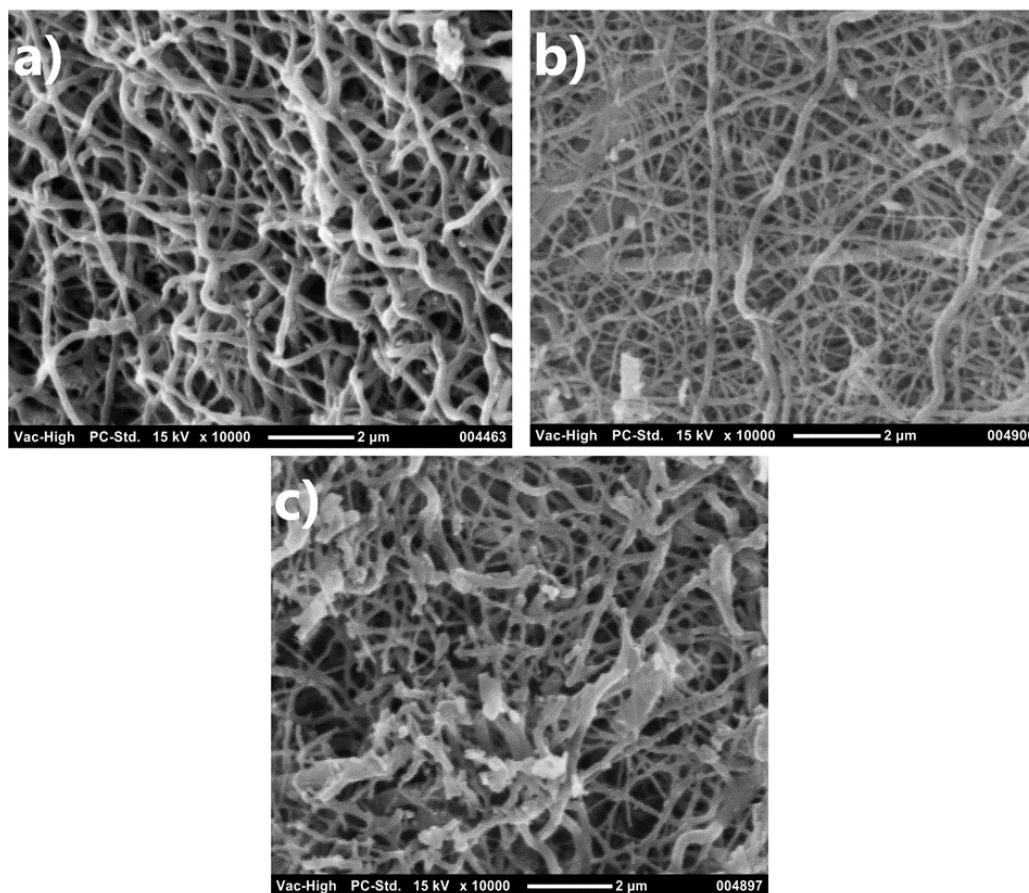
Figure 5.26: Typical examples of samples which presented a moderate degree of melting during carbonization; a) sample derived from electrospun nanofibers of 50/50 lignin/r-PET with average fiber diameter of 230 nm; b) sample derived from electrospun nanofibers of 80/20 lignin/r-PET with average fiber diameter of 135 nm; c) sample derived from electrospun nanofibers of 67/33 lignin/r-PET with average fiber diameter of 176 nm (see Table 4.3). Scale bar is 2 μm in all images

Finally, when the degree of melting is very limited or hard to distinguish, the term "minor" is used. There are signs of fusion at some spots where the fibers touch each other, but the degree of interconnection is very limited. Typical examples of minor melting are presented in Figure 5.27. Although this is a subjective description and the limits between these categories are not well-defined, it offers a relatively precise overview of the behavior of the electrospun nanofibers upon heating, as it is apparent in the SEM images of Figure 5.28.
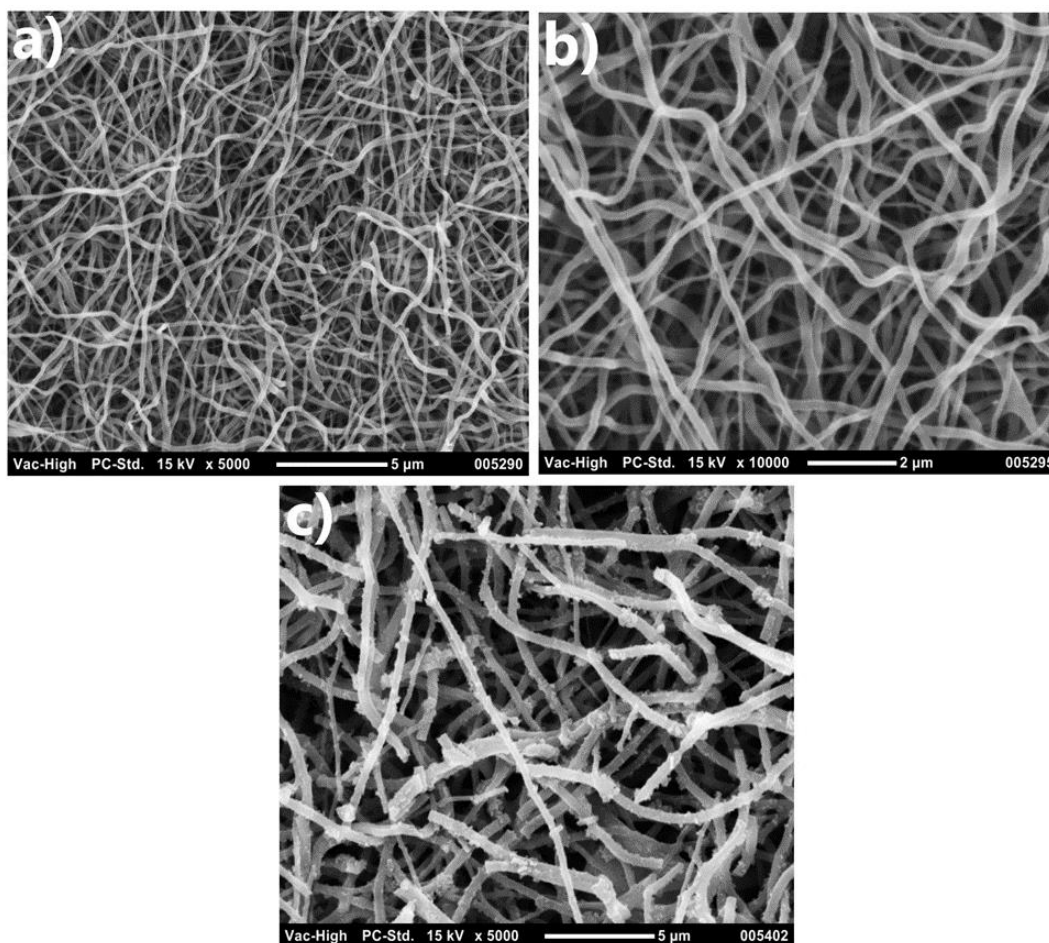
Figure 5.27: Typical examples of samples which presented a minor degree of melting during carbonization; a) and b) sample derived from electrospun nanofibers of 90/10 lignin/r-PET with average fiber diameter of 171 nm; c) sample derived from electrospun samples of 50/50 lignin/r-PET with average fiber diameter of 395 nm (see Tables 4.3 and 4.4). Scale bar is 5 μm in a) and in c); scale bar is 2 μm in b)
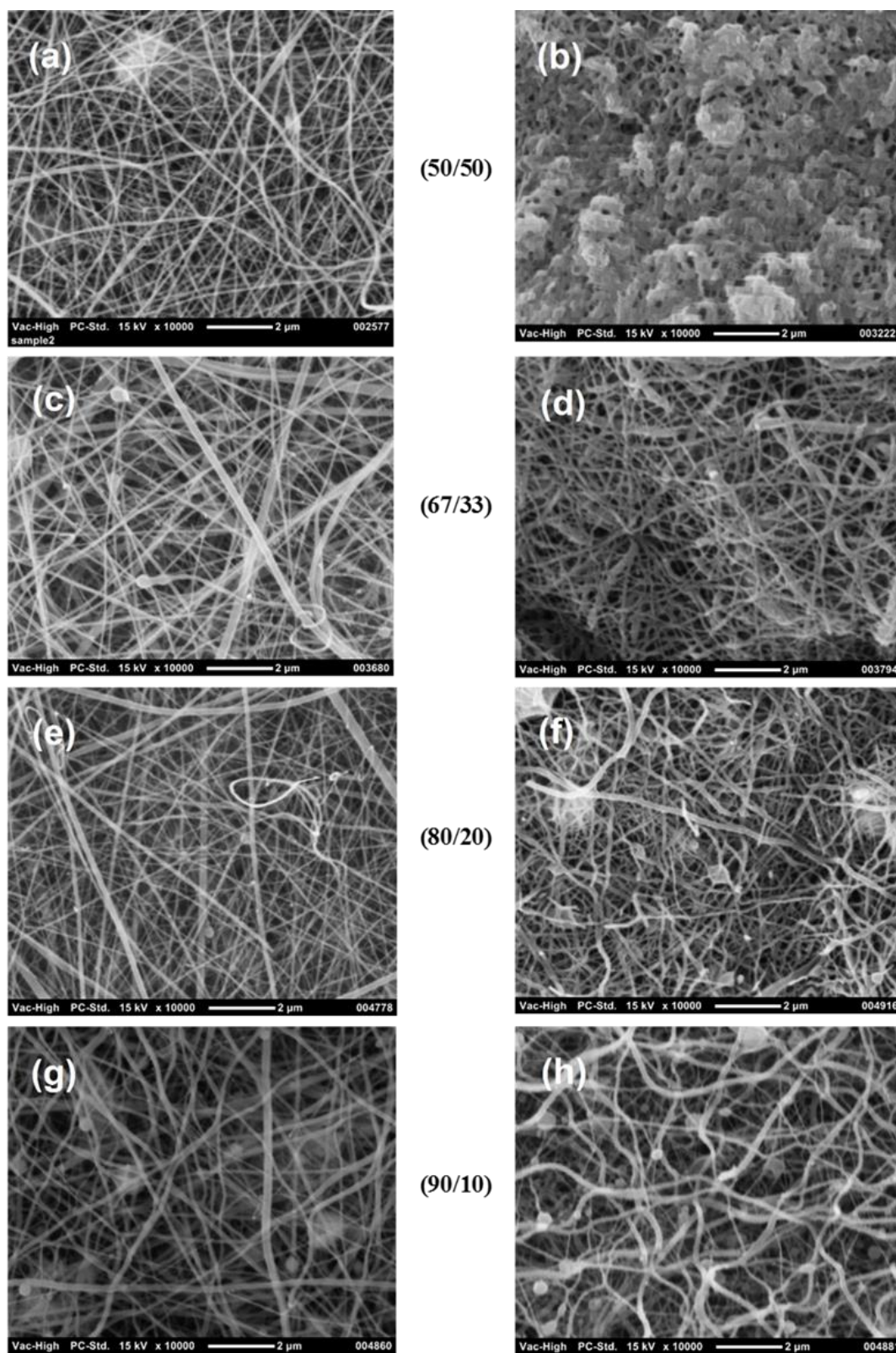
Figure 5.28: The morphology of the electrospun (left) and of the carbonized (right) nanofibers of minimum average diameter (<100 nm). The brackets show the varying lignin/r-PET mass ratio. Scale bar in all SEM images is 2 μm

Figure 5.28 presents the effect of the lignin/r-PET mass ratio in the carbonization of electrospun mats, in which the average fiber diameter is in the range of 80-100 nm, the lowest average fiber diameters produced successfully (see Table 4.3 for the electrospinning conditions). The images on the left side correspond to the electrospun samples, while these on the right to the carbonized ones. Apparently, when the lignin/r-PET mass ratio is 50/50, which means that the percentage of r-PET in the fibers is relatively high, then there is an extensive degree of melting (Figures 5.27a-b). The fibers have almost completely fused with each other, and the filamentous structure has collapsed. In contrast, at higher lignin/r-PET mass ratios, when the percentage of r-PET becomes progressively less, the degree of melting wanes. Thus, at 67/33 there is an extensive to moderate melting (Figures 5.28c-d), at 80/20 a minor to moderate melting (Figures 5.28e-f) and at 90/10 only a minor degree (Figures 5.28g-h).

This behavior is justified by the differences in the macromolecular structure and in the thermal properties between these two polymers as PET is a linear, semicrystalline polymer with a melting point of around 250°C, while the lignin used here is highly branched, amorphous and infusible when heated. Therefore, it is expected that samples which contain a larger amount of r-PET will exhibit more extensive melting. In the samples of minor melting, the resulting carbon nanofibers have average diameters similar to the precursor ones.

5.2.4 The synergy between the mass ratio and the average fiber diameter

The behavior described in the previous section is not uniform for the whole range of average fiber diameters at the sub-micron scale. As the average fiber diameter of the electrospun sample becomes larger, then the degree of melting becomes much

less pronounced, even for samples that contain a large proportion of r-PET. Hence the

nano-diameter effect wanes for increasing lignin/r-PET mass ratios.
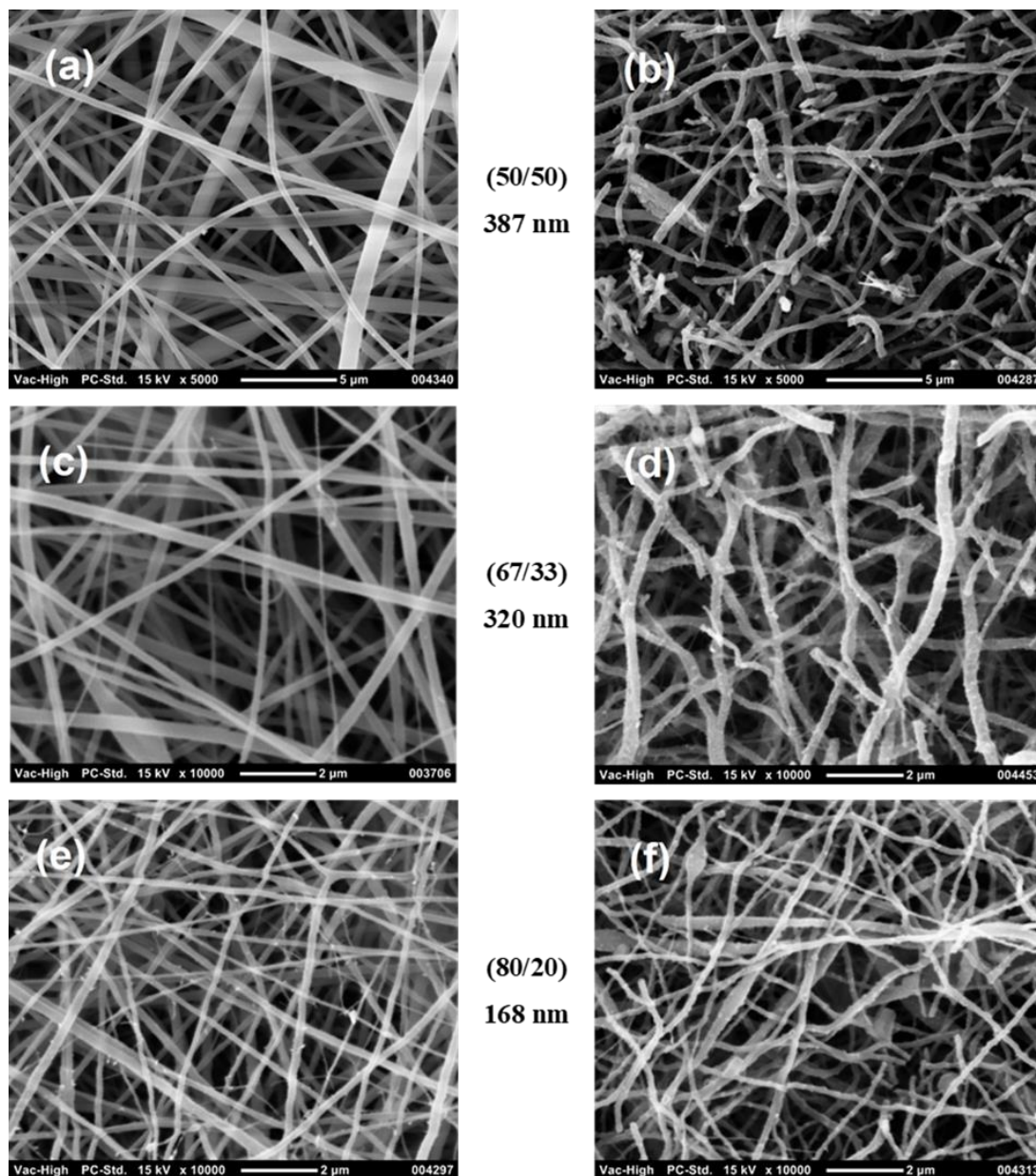
Figure 5.29: SEM images showing the morphology of the electrospun (left) and of the carbonized (right) samples consisting of relatively thicker fibers. Scale bar in a) and b) is 5 μm; scale bar in the c), d), e) and f) is 2 μm

Figure 5.29 shows the carbonization results for the four mass ratios examined

here, but for relatively thicker fibers. In Figures 5.29a and 5.29b, it is apparent that the

electrospun sample consisting of 50/50 lignin/r-PET with average fiber diameter of 387 nm exhibits a minor degree of fusion. So, the fibrous structure is retained and carbon submicron fibers are produced successfully. For electrospun samples consisting of 67/33 lignin/r-PET with an average diameter of 320 nm (Figures 5.29c-d), it is obvious that there is only a moderate to minor melting, and definitely to a less extent compared to the thinner nanofibers shown in Figure 5.29d. Similarly, fibers consisting of 80/20 lignin/r-PET with average diameter of 168 nm exhibit a rather minor degree of melting (Figures 5.29e-f), while for fibers of 90/10 mass ratio the extent of melting is minor even for the thinnest fibers as shown in Figure 5.28h and the same occurs for thicker fibers.

As the SEM images in Figures 5.28 and 5.29 indicate and as it was repeatedly observed when samples of varying average fiber diameters and mass ratios were carbonized, the samples consisting of the thinnest fibers tend to melt more extensively, and this degree of melting wanes as the average fiber diameter is increased and as the lignin/r-PET mass ratio is higher. Concisely, these observations are visualized in Figure 5.30. Here, the darkest regions correspond to a higher degree of melting, while the lighter ones to a lower degree. The purpose of this figure is to provide a rough estimation and a better understanding, but not to set distinct and rigor limits between the regions. This figure was drawn based on the carbonization results of the samples given in Table 4.3, and after additional replication experiments. Here, it must be mentioned that it has been repeatedly noticed that the melting in each sample is manifested even when it is heated under N_2 up to just 250-300°C. Further heating to higher temperatures doesn't contribute to the extent of melting, but rather it only serves as the route to transform the samples into carbon fibers. In other studies where carbon fibers are produced from the carbonization of lignin, it is commonly suggested that

including a stabilization step of heating in air at around 250°C can help in preserving the filamentous structure [35]. However, adding a stabilization step here didn't make any difference in the degree of fusion between the fibers, probably because this is caused by the presence of r-PET.
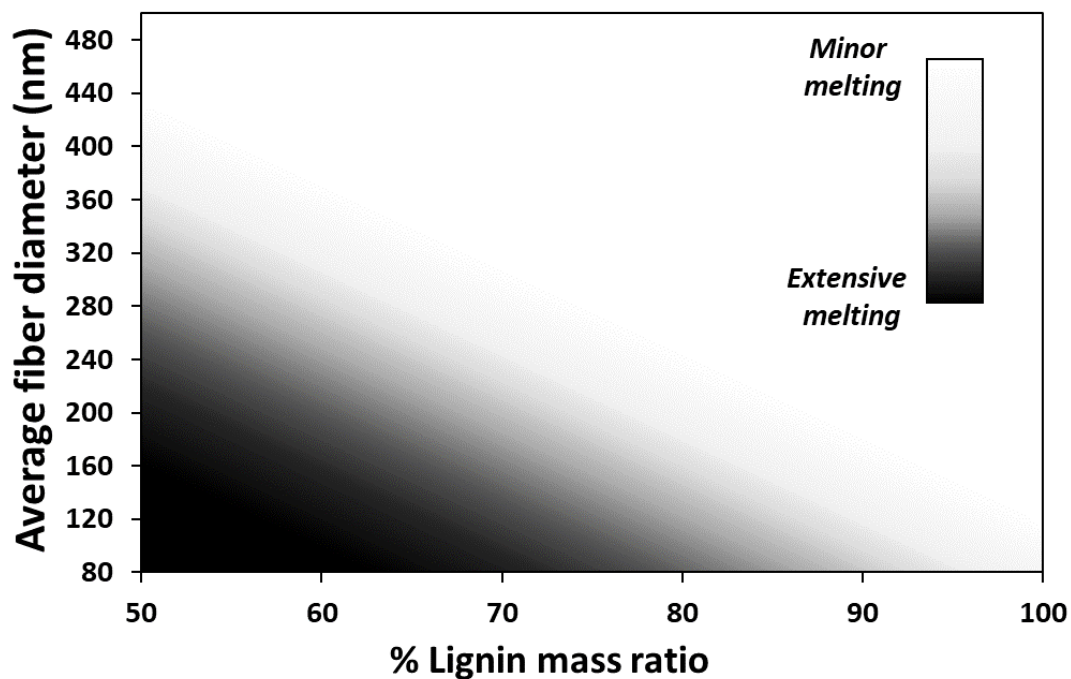
Figure 5.30: The approximate degree of melting with regards to the lignin/r-PET mass ratio and to the average fiber diameter of the electrospun samples
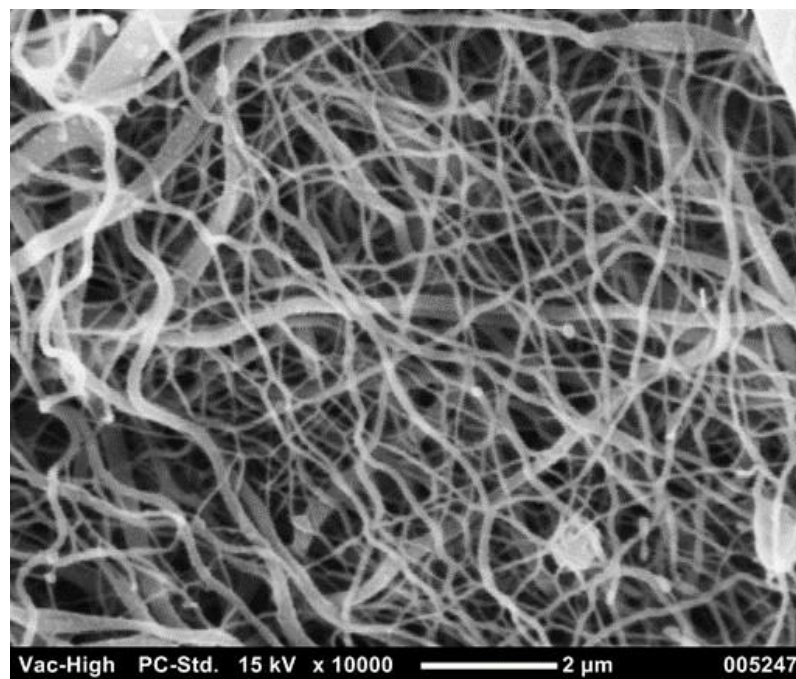
Figure 5.31: CNFs with average fiber diameter of 116 nm fabricated from 90/10 lignin/r-PET (see Table 4.3)
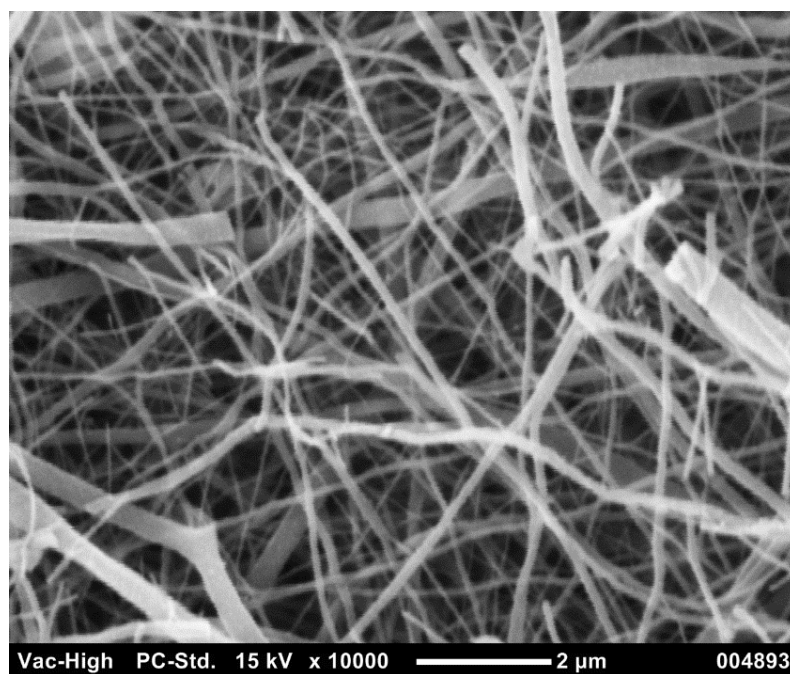
Figure 5.32: CNFs with average fiber diameter of 125 nm fabricated from 90/10 lignin/r-PET (see Table 4.3)

Hence, confirming the conditions mapped in Figure 5.30 that lead to successful fabrication of infusible CNFs with an average diameter close to 100 nm, a few more SEM images of these CNFs are provided in Figures 5.31 and 5.32. These samples were fabricated from 90/10 lignin/r-PET (see Table 4.3 for the electrospinning conditions). Such a small average fiber diameter for lignin-based CNFs has rarely been reported.

Moreover, it is necessary to mention that there was an attempt to fabricate CNFs from lower lignin/r-PET mass ratios (that is <50/50). When electrospun fibers with average diameter of around 400 nm consisting of a 40/60 lignin/r-PET ratio were prepared, it was observed that during carbonization there was a moderate to extensive melting (Figure 5.33). This is attributed to the high content of r-PET. So, for 40/60 mass ratio, samples of different average fiber diameter were not prepared to study their behavior. Instead, it was chosen to focus on samples containing less r-PET, from which there is evidence that thinner carbon nanofibers can be produced. Thus, it was decided to focus only on lignin/r-PET ratios between 50/50-90/10.
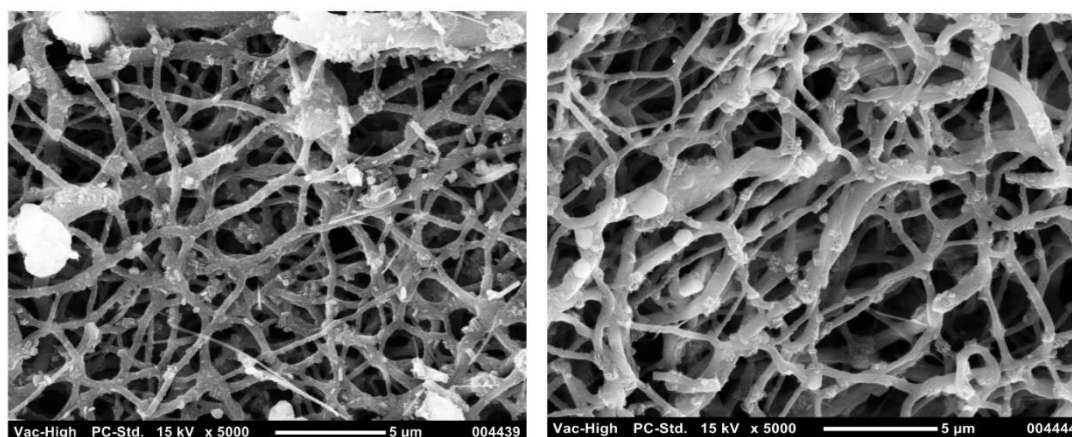
Figure 5.33: SEM images of the carbonized sample derived from lignin/r-PET 40/60 mass ratio with average fiber diameter of 406 nm

In Figure 5.34, the weight loss and the decomposition rates of lignin/r-PET electrospun samples prepared from different mass ratios (50/50-90/10) can be seen, as they were monitored through thermogravimetry in the region between 50-800°C. All of the samples presented here consist of nanofibers with similar average diameters (80-100 nm), the minimum range of average diameters produced successfully (see Table 4.3 for the electrospinning conditions).
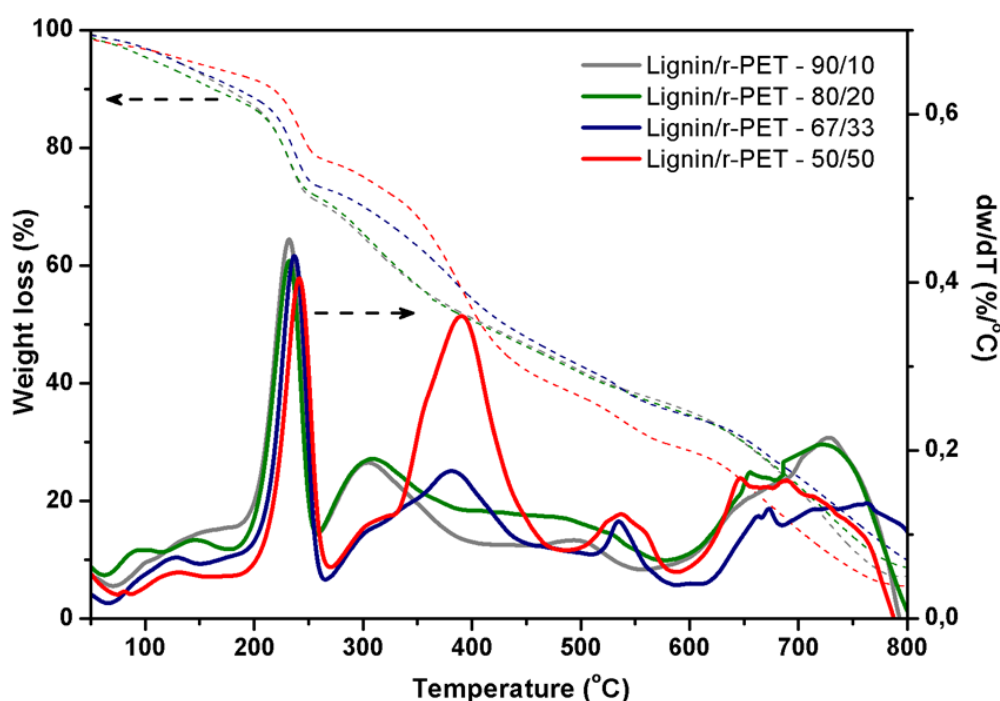
Figure 5.34: The decomposition profiles of the lignin/r-PET electrospun nanofibers of minimum average diameter

The results indicate that in the region between 180-260°C (the first decomposition regime of lignin), the samples which contain a larger amount of lignin exhibit a higher weight loss and a slightly higher decomposition rate (see Table 5.6). In this region, the percent of weight loss for the sample of 50/50 is measured 14.5%, for the sample of 67/33 it is 17.2%, for the one of 80/20 it is 17.4% and for that of 90/10 it reaches the value of 19.2%. Similarly, the maximum decomposition rate

(peak) in this region appears in the sample which contains the highest amount of lignin (90/10), and it is measured to be 0.45%/°C. The sample of 50/50 reaches a maximum rate of 0.40%/°C. Furthermore, in the region where the r-PET decomposes (330-470°C), the sample containing the highest amount of r-PET shows the highest peak of decomposition (0.36%/°C) and the highest weight loss, while the other samples decompose at a significantly lower rate here.

Table 5.6: Thermogravimetric features in the region 180-260°C for different mass ratios (Figure 5.34)

	Lignin/r-PET mass ratio			
	50/50	**67/33**	**80/20**	**90/10**
Weight loss (%)	14.5	17.2	17.4	19.2
Maximum decomposition rate (peak) (%/°C)	0.40	0.43	0.43	0.45

Focusing on the samples with mass ratios 50/50 and 67/33, which melt to a larger extent when their average fiber diameter is minimum, a comparison of the thermogravimetric curves between samples of different average diameters illuminates the cause of this phenomenon. Figure 5.35 presents a comparison of the decomposition rates between samples of the minimum average fiber diameter (which melt to a larger extent) and samples of relatively larger average fiber diameter (which show a minor degree of melting) for these two mass ratios (see Table 4.3 for the electrospinning conditions of each sample). This Figure reveals that the samples of minimum average fiber diameter decompose at a significantly higher rate compared to those consisting of a larger average fiber diameter in the first region of lignin decomposition, i.e.

between 180-260°C. The features measured for these 4 samples are concisely presented in Table 5.7.
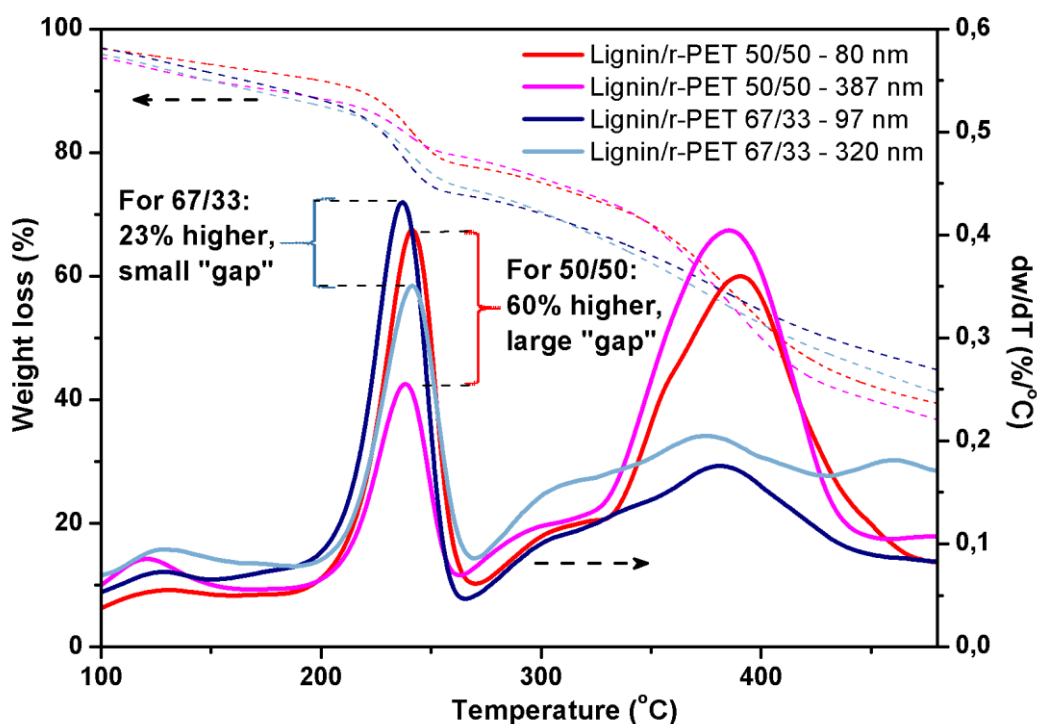
Figure 5.35: The combined effect between the mass ratio and the average fiber diameter in the decomposition of lignin/r-PET electrospun nanofibers

For the samples consisting of 50/50 lignin/r-PET, the nanofibers of 80 nm reach a maximum decomposition rate (peak) of 0.40%/°C, while those of 387 nm reach a peak of only 0.25%/°C. Similarly, for 67/33 lignin/r-PET the nanofibers of 97 nm reach a maximum rate of 0.43%/°C, while those of 320 nm reach a maximum rate of just 0.35%/°C (Table 5.7). It seems that as the lignin/r-PET mass ratio increases, the "gap" in the decomposition rate between the thinnest and the thicker fibers closes. Thus, for 50/50 lignin/r-PET the maximum rate reached by the thinnest fibers is 60% higher than the peak of the larger fibers, while for 67/33 the peak of the thinnest fibers is just 23% higher of the thicker ones (as noted on Figure 5.35). This means that as the

lignin/r-PET ratio increases, the difference in the decomposition rates between fibers of different diameters decreases, and the effect of the diameter becomes less significant. This observation explains why at high lignin/r-PET ratios the degree of melting doesn't vary much among fibers of different diameters (Figure 5.30).

Table 5.7: Thermodynamic features in the region 180-260°C: the synergy of the mass ratio with the average fiber diameter

	Mass ratio 50/50		Mass ratio 67/33	
	387 nm	80 nm	320 nm	97 nm
Maximum decomposition rate (peak) (%/°C)	0.25	0.40	0.35	0.43

At high lignin/r-PET mass ratios, there is a higher percentage of lignin macromolecules on the surface and inside the fibers. As the nanofibers are heated, they reach the region of 180-260°C, and lignin starts to decompose. When the fibers contain a higher percentage of lignin, it seems that the lignin decomposition reactions themselves are more significant than the heat and mass transfer for the overall rate of the process, because less r-PET macromolecules are present and, so, they hinder to a lesser extent the decomposition of lignin. The hindering effect of the r-PET is based on the fact that they occupy parts of the fiber surface, and also by the fact that they absorb energy in this region (180-260°C) without decomposing. Therefore, at higher lignin/r-PET mass ratios, the mass ratio itself becomes more important than the fiber diameter, as it is shown in the thermogravimetric results of Figure 5.35 and also in the morphologies of Figure 5.29. Here, this is the first time that the combining effect between the mass ratio and the average fiber diameter has been reported to determine

the morphology of the carbonized fibers, when a blend of polymers is used as feedstock.

The differences in the decomposition of lignin between 180-260°C are crucial for understanding the distinct melting behavior of each sample, as it will be shown in the following results from XRD and DSC. As r-PET consists of linear macromolecular chains, when lignin and r-PET are mixed then the branched macromolecules of lignin restrict the movement of r-PET chains and they hinder its crystallization, as it was shown in Section 5.1.7. The extent of this hindrance depends on the mass ratio of lignin.

When pure r-PET is used, the r-PET nanofibers prepared from the electrospinning process are amorphous, as it is revealed when they are examined with XRD (Figure 5.36, for an electrospun r-PET nanofibrous mat of 204 nm average fiber diameter, see Table 4.2 for the electrospinning conditions). This is not unexpected; instead, this has been reported in the literature in several occasions [171, 172] not only for PET but for other polymers as well [17]. This absence of crystallinity in the as-prepared r-PET nanofibers can be explained by the rapid solidification process during electrospinning [17]. However, when these r-PET nanofibers are heated, they totally melt at around 250°C, because they pass through a crystallization phase at around 150-190°C [172]. As a certain amount of lignin is mixed with r-PET (e.g. 30-40%), the crystallinity being developed in this region is compromised. When the percentage of lignin is increased, then the crystallization shifts towards higher temperatures and it becomes less apparent in the DSC thermograms until it is practically undetected when the lignin/r-PET mass ratio is higher than 67/33 (Section 5.1.7, Figure 5.14).
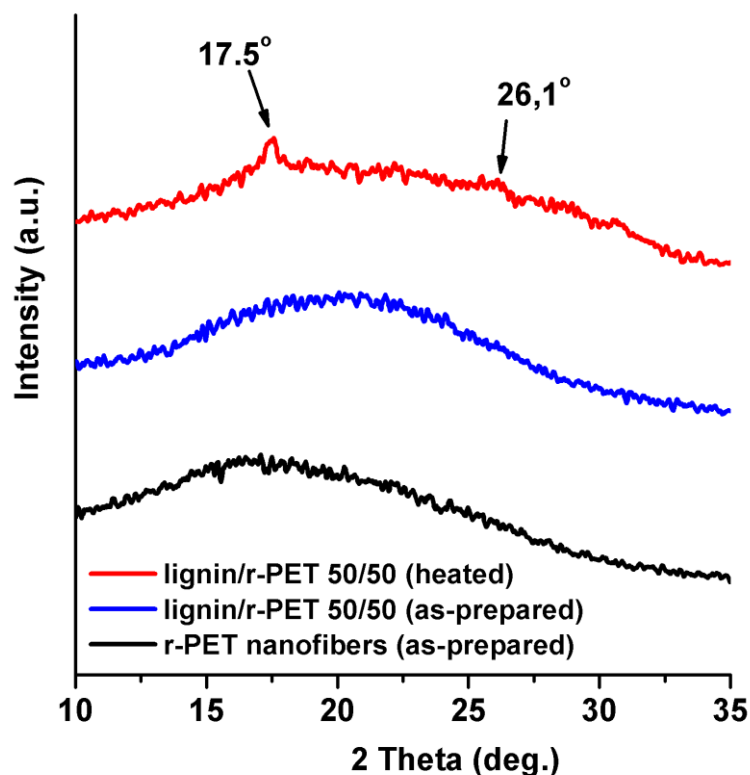
Figure 5.36: X-Ray diffraction patterns of electrospun nanofibers prepared from pure r-PET, from 50/50 lignin/r-PET (as-prepared) and from 50/50 lignin/r-PET after heating them at 300°C. The curves have been displaced on the y-axis

However, the fact that lignin starts to decompose above 180°C probably gives the chance to r-PET chains to gain some mobility and to re-organize to a small extent at some regions, especially when the fiber diameter is minimum and the lignin decomposition rate becomes maximum. Therefore, when the electrospun samples reach temperatures between 220-250°C, there is some extent of melting. The fact that more lignin decomposes when the sample consists of thin nanofibers (~80-100 nm) compared to samples consisting of thicker fibers (Figure 5.20), probably means that the r-PET chains gain more space to re-organize, therefore, these samples exhibit a higher degree of melting compared to the samples which contain thicker submicron

fibers. This behavior is more pronounced for samples consisting of lignin/r-PET mass ratio of 50/50, but it also occurs for samples of 67/33 even to a smaller extent.

This phenomenon can be better understood when an electrospun sample is heated to 300°C under N_2 and then left to cool down at room temperature. In this case, a portion of lignin has decomposed, while the r-PET chains have not. Therefore, there can be a detectable difference in the crystallinity between the as-prepared electrospun sample and the sample heated at 300°C. This difference can be seen in Figure 5.36 for a sample consisting of 50/50 lignin/r-PET, with average fiber diameter of 80 nm. The as-prepared sample doesn't contain any peaks. However, when it is heated at 300°C and then left to cool down, two peaks emerge: a larger one at 2θ=17.5° and a broad smaller one at 2θ=26.1°. These peaks correspond to characteristic patterns of the crystal planes of PET (the first peak to (010) and second one to (100) respectively) [173, 174]. This implies that the sample undergoes some small extent of crystallization as it is heated, which is obviously enhanced by the decomposition of lignin above 180°C.

Investigation with DSC can contribute to a further understanding of these phenomena. Again, these measurements were conducted for the electrospun samples which were heated at 300°C under N_2, then left to cool down and afterwards they were examined with DSC. In Figure 5.37, the DSC thermograms are presented for four samples in the region of 170-270°C, the region where the melting peak is expected to appear. The samples shown here are two samples of lignin/r-PET with mass ratio 50/50 and average fiber diameter of 80 nm and of 387 nm, one sample of 67/33 lignin/r-PET with average fiber diameter of 97 nm and one sample consisting of 80/20 lignin/r-PET with average fiber diameter of 95 nm (see Table 4.3 for the electrospinning conditions). The curves corresponding to the two 50/50 lignin/r-PET samples were

also presented in Figure 5.24, and here they are included in the graph for comparison. The sample of 67/33, which consists of thin nanofibers, shows a very broad and small melting peak between 210-240°C. This indicates that even when the amount of lignin is twice as large as the amount of r-PET in the sample, there is some minor rearrangement of some parts of the r-PET chains and some degree of melting as it is shown in Figure 5.29, due to the higher decomposition rate of lignin appearing when the sample consists of thin nanofibers. The enthalpy of melting here was measured to be around 0.1 J/g. In contrast, when the percentage of lignin is even higher (80%) which means that the sample contains four times more lignin than PET, there is no detectable melting peak.
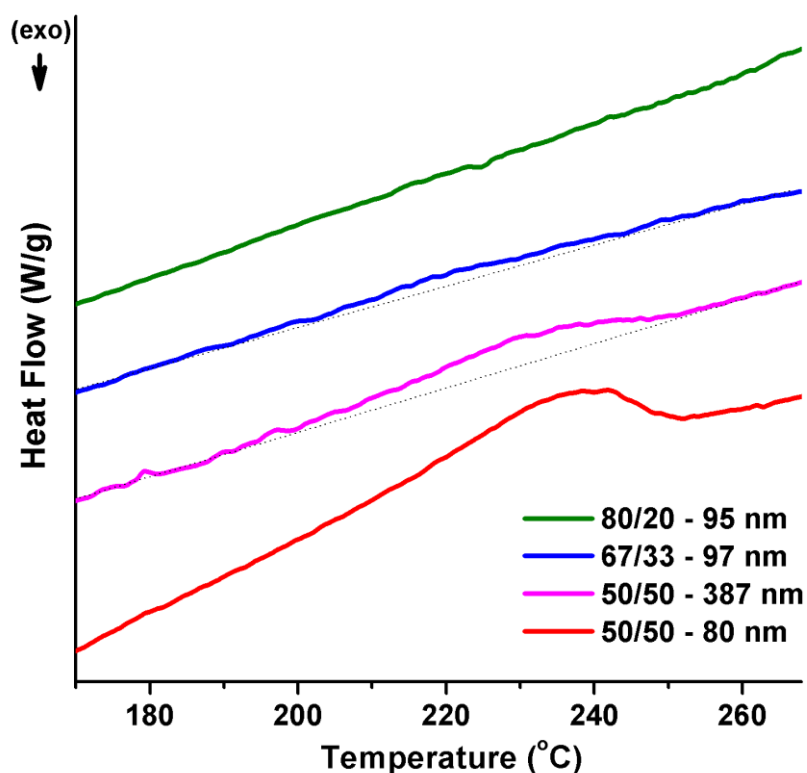
Figure 5.37: DSC curves of electrospun samples after they were heated up to 300°C under N_2. The dotted straight lines were added for the ease of comparison. See Table 4.3 for the electrospinning conditions. The curves have been displaced on the y-axis

Here it should be underlined that the emergence of some degree of melting is not necessarily a drawback. As it was mentioned in the literature review of Section 2.4, in many cases the fused CNFs exhibit higher electrical conductivity and enhanced tensile strength. These properties were not measured here as this is outside of the scope of this research, which is the production of desulfurization adsorbents.

5.2.5 The impact of melting on the porosity of activated CNFs

Table 5.8: Textural characterization of the activated carbon nanofibers carbonized at 800ºC and activated at 600ºC

Sample ID		Results		
Lignin/r-PET mass ratio	Average fiber diameter (nm)	BET surface area (m²/g)	Total pore volume (cm³/g)	Micropore volume (cm³/g)
50/50	85	72	0.060	0.028
50/50	230	123	0.112	0.046
50/50	292	132	0.109	0.052
50/50	395	288	0.194	0.116
50/50	565	276	0.182	0.108
80/20	252	210	0.136	0.079
90/10	147	216	0.133	0.089
100/0 (pure Lignin)	-	176	0.091	0.079

After mapping the conditions that are necessary for the avoidance of melting, it was necessary to investigate if the melting influences the porosity of the carbon nanofibrous mats. For this purpose, seven samples were prepared, carbonized and activated as described in Chapter 4 (Table 4.4) and their porosity and BET surface area

were measured. For comparison, the same procedure was followed for pristine lignin powder, as well. The results are displayed in Table 5.8.

The two samples consisting of 80/20 and of 90/10 lignin/r-PET were fabricated with such average fiber diameters, in order to avoid melting and to assess how the lignin/r-PET mass ratio affects the porosity. All the N_2 physisorption isotherms are presented in Figures 5.38 and 5.39, while representative SEM images of the samples derived from 80/20 and of 90/10 lignin/r-PET are shown in Figures 5.40 and 5.41.
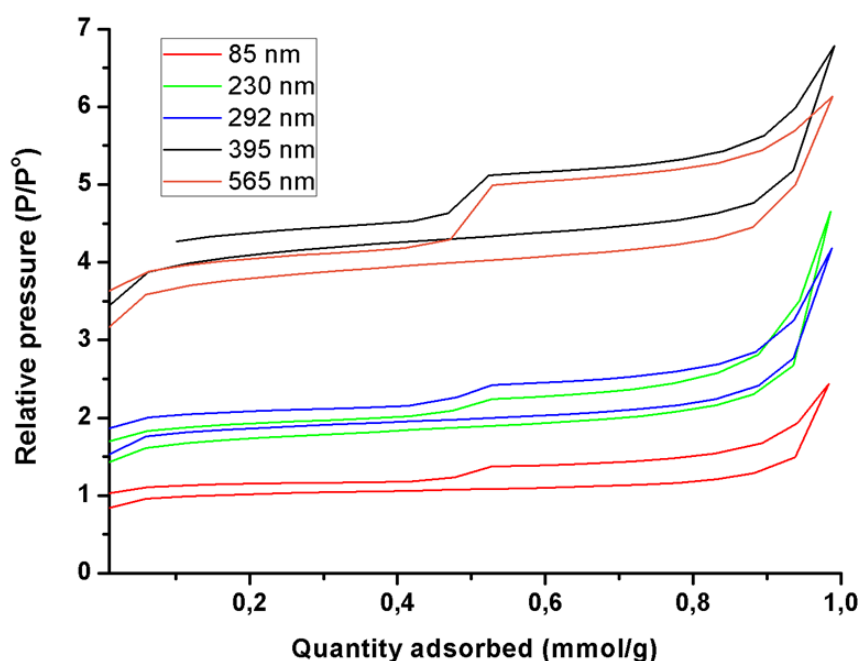
Figure 5.38: N_2 physisorption isotherms of activated carbon nanofibers prepared from lignin/r-PET 50/50 with different average fiber diameters

The results clearly indicate that in the samples consisting of 50/50 mass ratio the degree of melting influences the development of porosity. The highest values of BET surface area and of total pore volume appear for the samples that remain infusible (average fiber diameter >395 nm). Moreover, it seems that increasing the average fiber diameter from 395 to 565 nm doesn't affect the porosity significantly, as the BET

surface area ranges between 276-288 m^2/g and the total pore volume between 0.182-0.194 cm^3/g. In contrast, when the nanofibrous mats consist of thinner fibers that melt (<292 nm) the BET surface area doesn't increase more than 132 m^2/g.

In addition, the lowest porosity and BET surface area appears for the sample that exhibits the most extensive melting. After such a sample is carbonized, it appears as a solid chunk of carbon; since the lignin and the r-PET decompose anyway during carbonization, obviously closed pores are created which are inaccessible to N_2. On the contrary, when the samples remain infusible the different nanofibrous horizontal layers can be separated by friction and they are more flexible. For the samples which remain infusible, the average fiber diameters of the CNFs remain at similar levels as the precursor electrospun nanofibers.
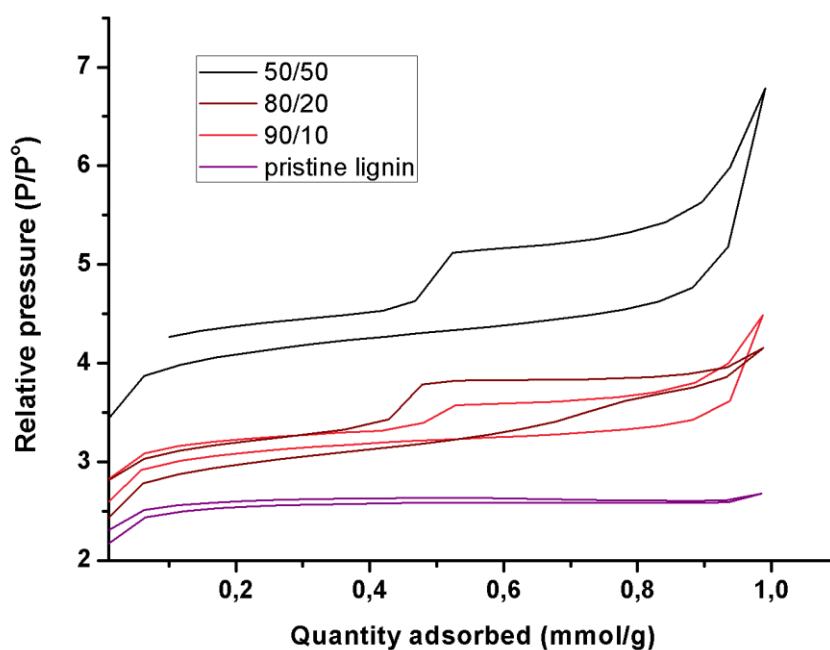
Figure 5.39: N_2 physisorption isotherms of activated carbon nanofibers prepared from different lignin/r-PET mass ratios, consisting of nanofibers that were infusible during carbonization. The average fiber diameter of each sample is given in Table 5.8 (for the 50/50 sample it is 395 nm). For comparison, the N_2 isotherm of the activated carbon produced from pristine lignin is displayed

Furthermore, although the samples of higher lignin content (80/20 and 90/10) consist of almost infusible thin nanofibers, their porosity lies in the range between 0.133-0.136 cm^3/g which is much less compared to the infusible 50/50 samples. Based on these measurements, it seems that the r-PET functions as a sacrificial, porosity-generating template. The r-PET macromolecules decompose to a larger extent than lignin, as it was shown previously. Measurements with thermogravimetric analysis showed that the starting recycled PET leaves a residue of less than 10 wt% at 800°C, while the residue of pristine lignin powder is close to 35 wt% (Section 5.2.1). In the case of lignin/r-PET nanofibers, the decomposition of the r-PET macromolecules leaves voids which translate into porosity, hence, when the r-PET content is larger the porosity is higher. This has also been reported for other lignin-based electrospun-derived carbon nanofibers, in which lignin was combined with poly(vinyl alcohol) [62,68] or polyvinylpyrrolidone [86]. In these cases, the binder polymer acted sacrificially for porosity development, as well.
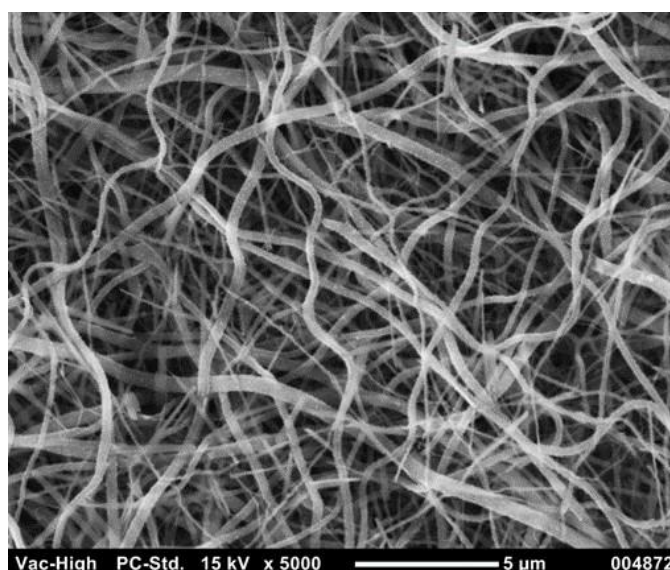
Figure 5.40: Activated CNFs prepared from a lignin/r-PET sample of 80/20 mass ratio and 252 nm average fiber diameter. The preparation conditions are described in Table 5.8 and in Section 4.3
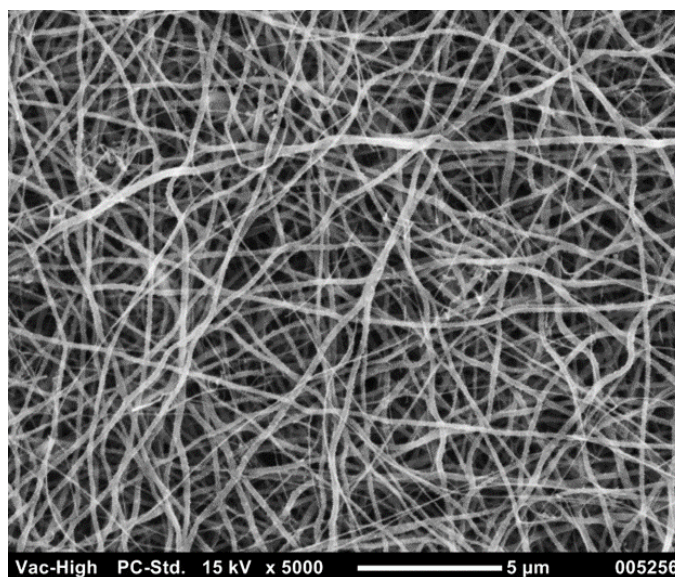
Figure 5.41: Activated CNFs prepared from a lignin/r-PET sample of 90/10 mass ratio and 147 nm average fiber diameter. The preparation conditions are described in Table 5.8 and in Section 4.3

5.2.6 Section summary

In this section, it has been demonstrated that when carbon nanofibers from a blend of lignin with r-PET are produced, their fibrous morphology can be customized by properly adjusting the lignin/r-PET mass ratio and the average diameter of the precursor nanofibers. Particularly, precursor electrospun nanofibers having a relatively high mass ratio of r-PET (>33 wt%) and low average fiber diameters (~100 nm) exhibit extensive melting and the fibrous structure collapses. In contrast, samples of the same high mass ratio of r-PET but large average fiber diameters (>300-400 nm) yield infusible filamentous carbon structures. This nano-dimension phenomenon declines when the r-PET content is low enough (~10 wt%). In this case, the nanofibers are practically almost infusible and carbon nanofibers with average diameters close to 100 nm and a well-formed filamentous structure are produced. Moreover, BET surface area

measurements indicate that the melting of nanofibrous mats compromises the porosity of the activated carbon nanofibers produced from them, while the presence of r-PET has a positive impact on the development of porosity. Finally, it has to be highlighted that very fine CNFs with average diameters close to 100 nm are among the lowest reported when lignin is used as precursor.

5.3 Characterization of the CNFs and of the ACNFs

In the previous section, the conditions leading to the successful preparation of carbon nanofibers starting from different lignin/r-PET mass ratios were described. Consequently, it was decided to investigate the structure and properties of these carbon nanofibers more thoroughly. Particularly, it was decided to focus on two specific samples; CNFs prepared from 50/50 lignin/r-PET with ~400 nm average fiber diameter, and CNFs prepared from 90/10 lignin/r-PET with ~110-150 nm average fiber diameter. As it was described in the previous section, the former can yield the highest BET surface area and the latter consists of the minimum average fiber diameters produced successfully. For these two mass ratios, only the carbonized fibers without any activation were initially investigated, in order to examine the features of the produced carbon structures starting from different lignin/r-PET mass ratios. Moreover, two carbonization temperatures were considered, namely 800 and 1000ºC, in order to estimate the impact of the carbonization temperature on the properties of the prepared CNFs. The carbonization at higher temperatures was avoided, so that the process doesn't become too energy-intensive.

5.3.1 Porosity and BET surface area of CNFs

As the primary target of this research is to develop efficient adsorbents, the surface area and the porosity of the CNFs is considered their most important feature. Table 5.9 presents the BET surface area and the porosity characteristics of the CNFs prepared either from 50/50 lignin/r-PET mass ratio (average fiber diameter ~400 nm) or from 90/10 lignin/r-PET mass ratio (average fiber diameter ~110-150 nm), after carbonization at 800 or at 1000°C. Tables 4.3 and 4.4 present the electrospinning conditions that were used for the preparation of these samples.

In this chapter, no specific average fiber diameter is mentioned, but a range of diameters is given; the reason is that the CNFs derived from 50/50 lignin/r-PET consisting of ~400 nm were produced by mixing various 50/50 lignin/r-PET samples with average diameters in this range. Similarly, the CNFs derived from 90/10 lignin/r-PET was prepared after mixing various 90/10 lignin/r-PET samples with average diameters in the range of 110-150 nm.

Table 5.9: Textural characteristics of the CNFs carbonized at 800°C or at 1000°C

Lignin/r-PET mass ratio (%)	Temperature (°C)	BET surface area (m²/g)	Total pore volume (cm³/g)	Micropore volume (cm³/g)	% Microporous	Average pore width (nm)
50/50	800	45	0.058	0.017	29.3	26.1
50/50	1000	353	0.223	0.139	62.3	6.3
90/10	800	47	0.052	0.010	19.2	8.7
90/10	1000	115	0.093	0.032	34.4	6.1

As the results presented in Table 5.9 clearly demonstrate, an increase in the carbonization temperature from 800 to 1000°C enhances the porosity of the CNFs.

Particularly, the BET surface area for the 90/10 sample increases from 47 to 115 m^2/g, while for the 50/50 sample it rises to 353 m^2/g. Similar increase is observed for their respective total pore volume. This observation agrees with numerous other studies for carbon fibers and for granular carbon [35, 70]. Porosity is defined as the space inside a (porous) solid which is accessible to molecules from a gas or a liquid phase (adsorbates) [15]. This space is created as the precursor progressively decomposes at elevated temperatures. Therefore, increasing the carbonization temperature results in a more extensive decomposition which translates into the evolution of low molecular weight molecules from the carbon material and into the development of a porous network [15]. According to IUPAC, the pores are classified according to their width as micropores when their width is smaller than 2 nm, mesopores when their width is between 2 and 50 nm and macropores when their width is larger than 50 nm [16].

Another important result found here is the difference in the pore volume and in the BET surface area between the 50/50 and the 90/10 sample at 1000°C, which is around 3 times higher (353 vs. 115 m^2/g). Obviously, this is due to the presence of the r-PET in the precursor nanofibers. As it was also shown in the previous Section 5.2.5 for the activated CNFs prepared from different lignin/r-PET mass ratios, the r-PET macromolecules decompose to a larger extent, leaving voids inside the carbon material. Therefore, it acts as a template for the development of porosity and especially microporosity, as it is inferred from the higher microporosity percentage of the 50/50 samples. In addition, it should be noted that the yield of carbonization provides further evidence for the more extensive development of porosity when the percentage of PET is larger. It was observed that precursor electrospun nanofibers consisting of 50/50 lignin/r-PET have a carbonization yield of ~24-26% mass at 1000°C, while those

consisting of 90/10 give a yield of ~35-38%. Hence, when the former are used, a much higher fraction of their mass decomposes, leaving voids into the carbon structure.

Furthermore, the higher carbonization temperature seems to favor the development of microporosity for both samples, which is also accompanied by a reduction in the average pore width. All four samples contain significant mesoporosity, as indicated by the differences between the total pore volume and the micropore volume. The average pore width of 26.1 nm exhibited by the 50/50 sample carbonized at 800°C seems as a discrepancy. However, it should be considered that this sample consists of nanofibers with average diameter close to 400 nm, therefore, the inter-fiber voids are significantly larger than the voids between the thin fibers constituting the 90/10 sample. Thus, these voids (macropores) probably drag the average pore width towards larger values; this result was validated after replicating the measurement. Finally, it should be pointed out that the oxygen which is present in the macromolecules of both lignin and PET has been suggested as an agent which promotes the development in porosity during carbonization [35, 50].

Figure 5.42 presents the N_2 physisorption isotherms of the four samples studied here. All of them are type IV isotherms according to the IUPAC classification [175], the most common type encountered in granular carbon and in carbon fibers. All of them contain hysteresis loops, which indicate the presence of mesoporosity, in accordance with the results presented in Table 5.9 [175]. The rise in the extent of adsorption above $P/P^o=0.9$ appearing in the sample of 50/50-800°C denotes the presence of macropores [175] and it justifies the large value of its average pore width shown in Table 5.9.
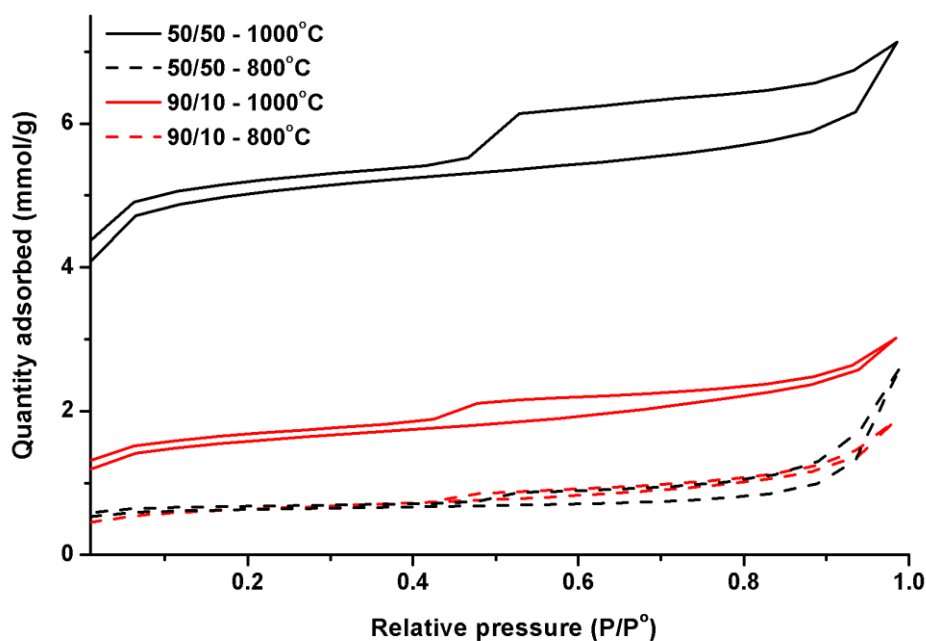
Figure 5.42: N_2 physisorption isotherms of the CNFs prepared from different lignin/r-PET mass ratios (50/50 and 90/10) at different carbonization temperatures (800 and 1000°C)

5.3.2 The structure of CNFs: Raman spectroscopy, XRD and EDS

Raman spectroscopy is a very useful experimental technique for characterizing the structure of carbon samples. The Raman spectra of the four samples described in Section 5.3.1 were recorded and they are presented in Figures 5.43 and 5.44. Each spectrum was deconvoluted using Lorentzian functions with the aid of a data analysis software (OriginPro). This procedure is commonly followed for the analysis of Raman spectra [35, 176, 177] as it reveals the presence of peaks associated with different structural components of the carbon material. Four peaks were identified in the samples examined here.
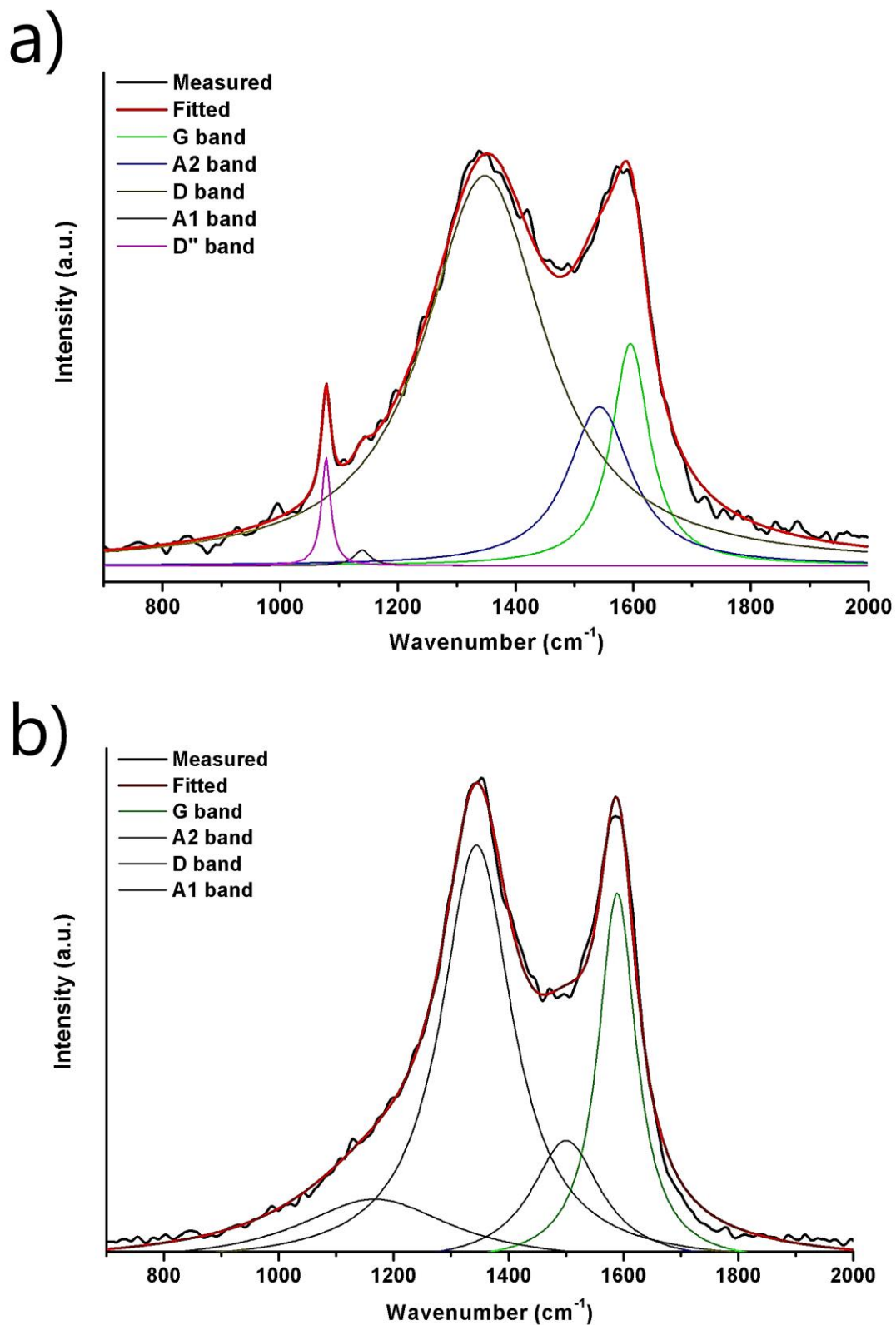
Figure 5.43: Raman spectra of the four CNF samples; a) lignin/r-PET 50/50 carbonized at 800°C; b) lignin/r-PET 50/50 carbonized at 1000°C; c) lignin/r-PET 90/10 carbonized at 800°C; d) lignin/r-PET 90/10 carbonized at 1000°C

Figure 5.43: Raman spectra of the four CNF samples; a) lignin/r-PET 50/50 carbonized at 800ºC; b) lignin/r-PET 50/50 carbonized at 1000ºC; c) lignin/r-PET 90/10 carbonized at 800ºC; d) lignin/r-PET 90/10 carbonized at 1000ºC (continued)

The peak appearing around 1590 cm^{-1}, termed as the G band, is associated with the vibration modes of the graphitic lattice and especially with the in-plane stretching vibrations of the aromatic rings [176, 178]. The D band appears at around 1344-1348 cm^{-1} and corresponds to disordered carbon structure, namely to imperfect graphitic domains in which defect-induced breathing modes of hexagonal carbon lattices appear [36, 69, 176]. Two more bands related to amorphous carbon appear: the A1 band near 1139-1167 cm^{-1} and the A2 band around 1500-1543 cm^{-1}. Although there is no standard name for these two bands, here they are named A1 and A2, following the terminology of Ghosh et al. [176]. These two bands are related to amorphous sp^2-forms of carbon, to pentagonal or heptagonal rings in the hexagonal carbon network, to the presence of impurities or functional groups and also to sp^3 bonds [35, 176]. Only in the sample derived from 50/50 lignin/r-PET carbonized at 800°C (Figure 5.43a) one additional peak appears at 1078 cm^{-1} (D'' band [176]), while the A1 peak here appears insignificant. This peak is related to the disordered regions of the carbon structure, as well. This difference is obviously related to the presence of PET in this sample, as it perhaps contributes to a larger extent of disordered graphitic structure. However, this peak disappears if the carbonization temperature is 1000°C; instead, an A1 band related to amorphous carbon is present in this case.

Table 5.10 concisely presents the peak positions, as well as the I_D/I_G ratio, the relative intensity ratio between D and G band which is commonly used to assess the degree of structural order in the carbon materials. The results here suggest that when the carbonization temperature increases, the CNFs exhibit a more ordered graphitic structure, as it is apparent from the decreasing I_D/I_G ratio (Table 5.10), as well as from the increasing intensity and sharpness of the G band appearing in Figures 5.43b and 5.43d.
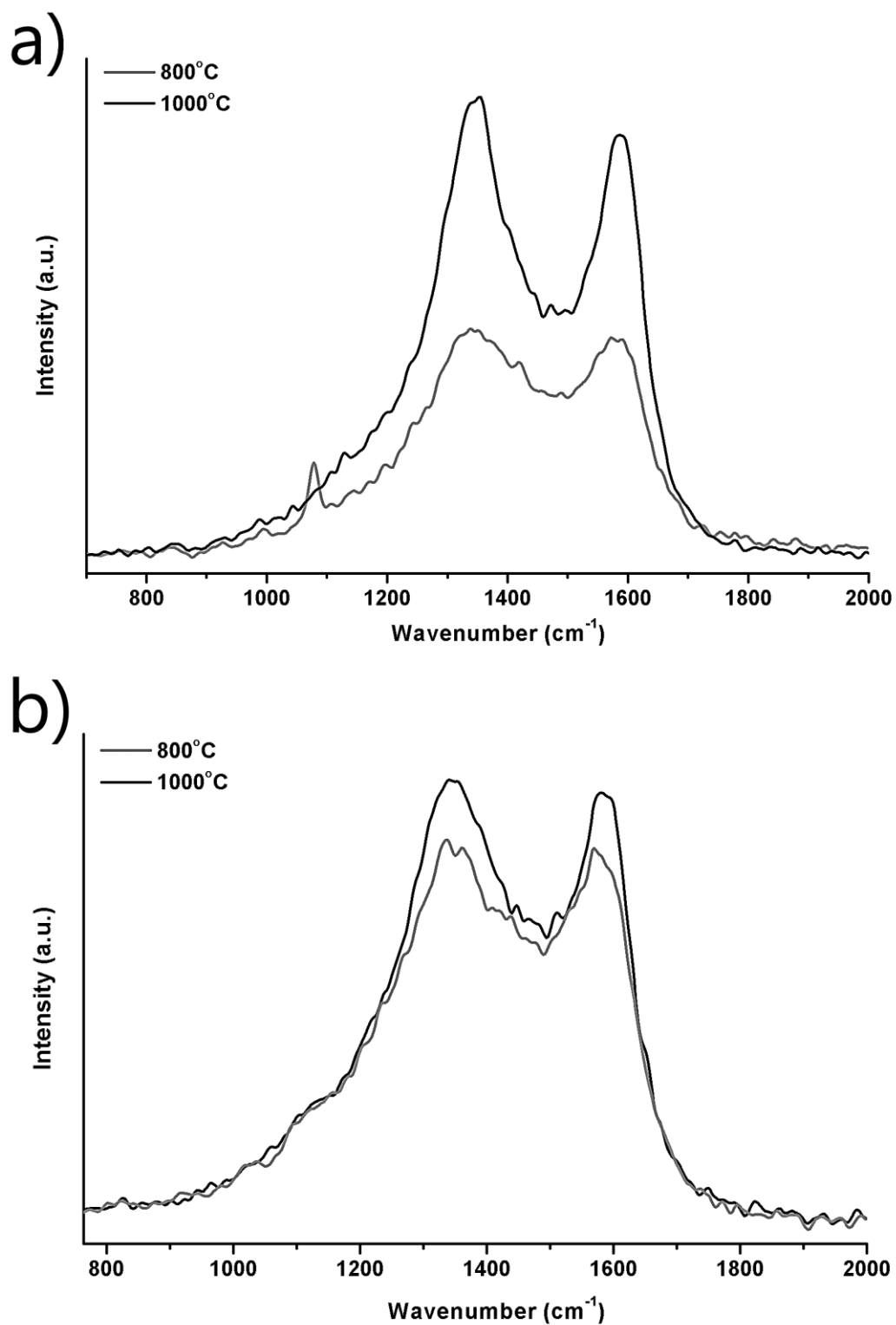
Figure 5.44: Raman spectra of the four CNF samples presented with respect to the lignin/r-PET mass ratio of their precursors; a) lignin/r-PET 50/50; b) lignin/r-PET 90/10. Grey line: 800°C; black line: 1000°C

Table 5.10: Features of the Raman spectra of CNFs

Lignin/r-PET mass ratio (%)	Carbonization temperature (°C)	D'' band position (cm⁻¹)	A1 band position (cm⁻¹)	A2 band position (cm⁻¹)	D band position (cm⁻¹)	G band position (cm⁻¹)	I_D/I_G
50/50	800	1078	1139	1543	1348	1595	1.75
50/50	1000	-	1167	1500	1344	1589	1.13
90/10	800	-	1166	1517	1348	1590	1.27
90/10	1000	-	1155	1503	1347	1590	1.16

Particularly, a large decrease in the I_D/I_G intensity ratio is measured for the CNFs derived from 50/50 mass ratio when the carbonization temperature rises from 800 to 1000°C (from 1.75 to 1.13). This reflects a vast increase in the degree of structural order of the carbon structure due to higher graphitization [36]. As the material progressively decomposes during carbonization and low molecular weight molecules evolve, especially those containing O and H, this breakage of bonds can lead to rearrangement of C atoms, which can move to positions of higher stability and form hexagonal rings [15]. Therefore, the degree of graphitic structure is increased. In this sample, the extensive decomposition of PET probably promotes a more extensive rearrangement of the aromatic rings existing in lignin, and the formation of graphitic domains. This trend has also been reported for other lignin-based or PAN-based CNFs [36, 69]. However, the disordered structure is still predominant in all samples. Furthermore, a decrease in the I_D/I_G ratio is also measured in the sample derived from 90/10 mass ratio, indicating an increase in the graphitic structure, although here the difference is not very large (from 1.27 to 1.16). The smaller decrease here can be attributed to the much smaller PET content of the precursor nanofibers. The sample consisting of 90/10 lignin/r-PET is more homogeneous and lignin decomposes to a smaller extent than PET. Therefore, its aromatic rings can rearrange to a smaller

degree. This can also be noted from the Raman spectra as they are shown in Figure 5.44. The transformation in the spectrum of the CNFs derived from 50/50 lignin/r-PET between 800 and 1000°C is very apparent (Figure 5.44a), while in the CNFs derived from 90/10 mass ratio the two spectra are similar (Figure 5.44b). This observation is in accordance with the BET surface area measurements of the 90/10 sample, in which the increasing carbonization temperature doesn't enhance its porosity dramatically. Here, it should be mentioned that this trend of increasing structural order with increasing the carbonization temperature is not ubiquitous; instead, for various types of lignin-based and also for cellulose-based carbon fibers the opposite may occur [69].
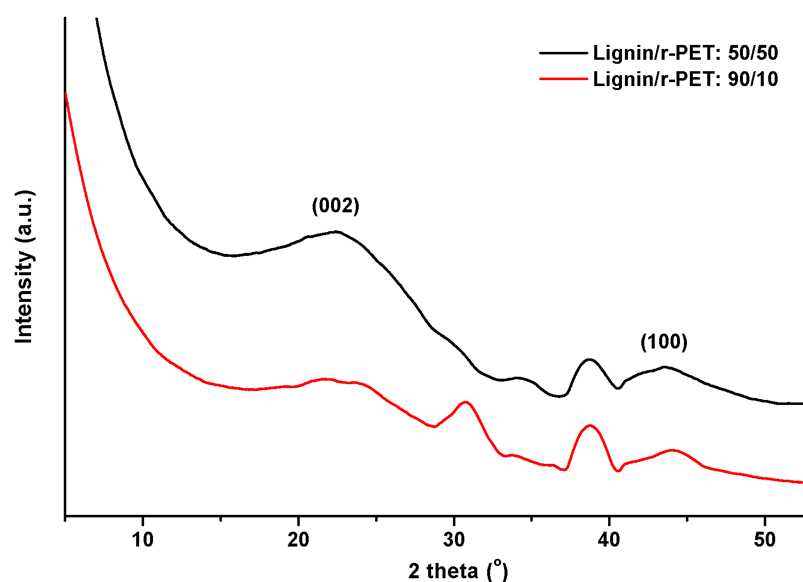
Figure 5.45: XRD diffractograms of the CNFs prepared from 50/50 and from 90/10 lignin/r-PET mass ratio carbonized at 1000°C

XRD measurements can contribute significantly to the more thorough characterization of the structure of CNFs. The diffractograms of the 50/50 and of the 90/10 sample carbonized at 1000°C are presented in Figure 5.45. In each graph, two broad peaks which are characteristic of carbon materials are apparent. The peak centered at around 23° corresponds to the (002) plane of the graphitic nanocrystalline

lattice, while the peak at around 44° is associated with its (100) plane [48, 69, 176]. The emergence of these peaks suggests that there are small crystalline graphitic domains inside the CNFs. The diffraction patterns of the two samples contain other peaks centered at 32°, 35° and 38°, as well. These peaks correspond to impurities deriving from the ash which is present in the starting lignin, and they are more intense in the 90/10 sample because its precursor contains a higher amount of lignin, as it was shown in Section 5.1. These impurities contain alkali metals, mainly Na; the peak centered at ~38° was identified as $KNa(SO_4)$ using the database installed in the XRD software.

The average size of the graphitic domains of each sample is possible to be calculated through analysis of their respective diffractograms. After subtracting the baseline and fitting a gaussian curve in each of their peaks, these features were calculated and they are presented in Table 5.11. The average interlayer spacing $d_{(002)}$ between consecutive graphene layers was calculated using Bragg's equation [176, 179]:

$$d_{(002)} = \frac{\lambda}{2 * \sin\theta}$$

Where λ is the wavelength (0.154 nm) and θ is the diffraction angle (°). The crystallite size L_c along the c axis and the size of ab planes L_a was calculated using Scherrer's equation [176, 179]:

$$L_c = \frac{0.91 * \lambda}{(FWHM)_{(002)} * \cos\theta_{(002)}}$$

$$L_c = \frac{1.84 * \lambda}{(FWHM)_{(100)} * \cos\theta_{(100)}}$$

FWHM is the full width at half maximum of each peak measured in rad, and it is used for the calculation of L_a and L_c. N_c is the average number of graphene layers in each crystallite [176]. The results suggest that the CNFs derived from 90/10 lignin/r-PET have a more ordered structure, as it is revealed by the average size of their graphitic domains, which is clearly larger than those existing in the CNFs prepared from 50/50 lignin/r-PET. The smaller interlayer spacing $d_{(002)}$ of the 90/10 sample indicates its higher level of organization, as well. The interlayer spacing of a perfect graphitic crystal is 0.335 nm [61] and a larger deviation from this number shows a higher degree of disorder [61, 176]. These results agree with the porosity measurements presented in Table 5.9. CNFs prepared from 50/50 lignin/r-PET mass ratio have a higher degree of disorder, therefore, their structure includes more defects which induce a higher degree of porosity. In contrast, CNFs prepared from 90/10 lignin/r-PET have a more ordered structure which translates into lower porosity.

Table 5.11: Crystallite features of carbon nanofibers prepared from different lignin/r-PET mass ratios

Lignin/r-PET mass ratio (%)	$2\theta_{(002)}$ (º)	$d_{(002)}$ (nm)	FWHM$_{(200)}$ (rad)	L_c (nm)	$2\theta_{(100)}$ (º)	FWHM$_{(100)}$ (rad)	L_a (nm)	N_c
50/50	23.2	0.383	0.147	0.97	43.5	0.106	2.87	2.53
90/10	23.7	0.375	0.111	1.29	43.7	0.091	3.35	3.44

The carbon and oxygen content in these CNFs produced from 50/50 and from 90/10 lignin/r-PET mass ratio was measured using EDS. It was measured that the 90/10-CNFs consist of 77.65 ± 2.06% C and 10.04 ± 1.12% O with the balance representing the impurities (Na, F, S, K, Cu, Ca) (percentage per unit mass) (Figure 5.46a). On the other hand, 50/50-CNFs consist of 78.7 ± 1.84% C and 12.5 ± 0.9% O

(Figure 5.46b). Thus, the C content in both these CNFs is similar, but there is a significant difference in the O content. This result agrees, as well, with the previous remarks, as the O molecules represent defects in the graphitic structure of CNFs.
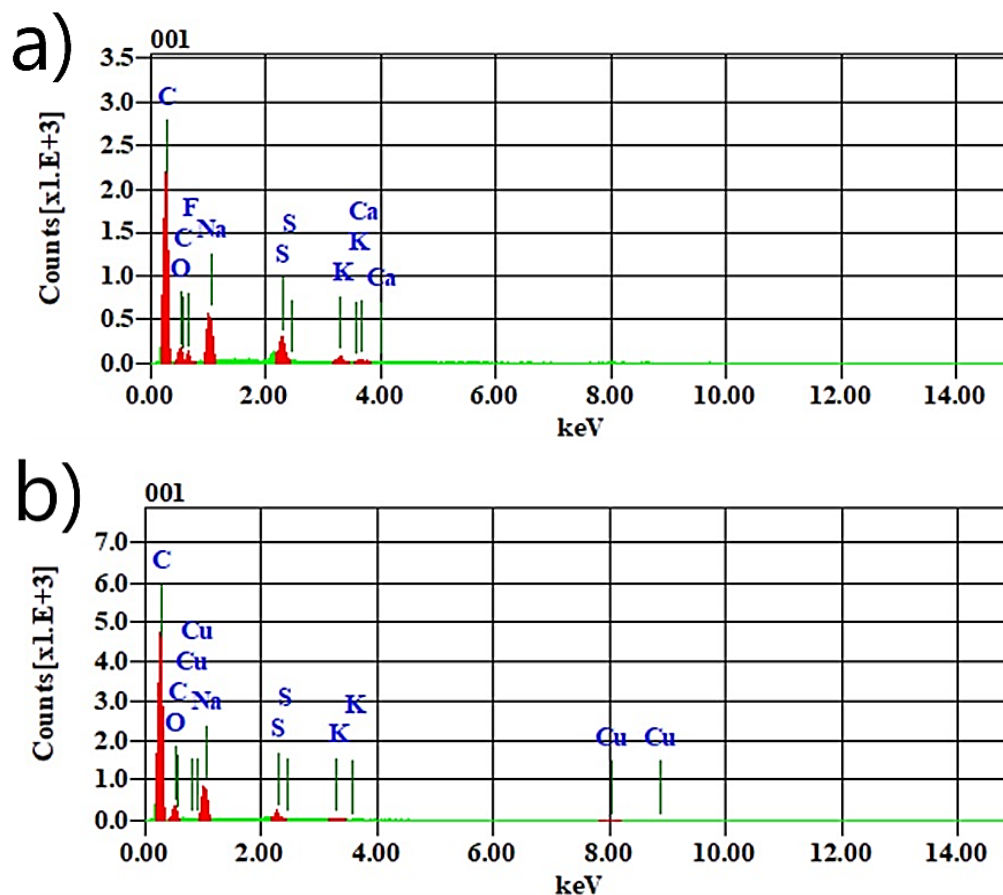
Figure 5.46: EDS spectra of the CNFs prepared from different lignin/r-PET mass ratio and carbonized at 1000°C; a) 90/10; b) 50/50

5.3.3 Preparation and characterization of activated ACNFs

The next step after the preparation of the CNFs was their activation and the investigation of the properties of the activated CNFs (ACNFs). Particularly, it was decided to apply two different methods of activation; physical activation using CO_2 and chemical activation using KOH (as it was described in Chapter 4). The physical activation was applied in the CNFs prepared from 50/50 and from 90/10 lignin/r-PET

carbonized at 1000°C (from average fiber diameter of ~400 nm and of 110-150 nm respectively, as previously). These samples are denoted here as "ACNFs-50/50-CO_2" and "ACNFs-90/10-CO_2". The activation with KOH was applied only to the CNFs prepared from 50/50 carbonized at 1000°C, because it was described in the previous section that this sample possesses much higher porosity. This sample is denoted here as "ACNFs-KOH". In all cases of activation, the final yield of the ACNFs was ~45-50% with respect to the mass of the starting CNFs. Finally, the ACNFs-KOH were further treated with HNO_3 according to the methodology described in Chapter 4. This treatment is usually applied in order to oxidize the carbon structure and to introduce O-containing functional groups which augment the adsorption capacity of the adsorbent [180-182]. This sample is here denoted as "ACNFs-KOH-HNO_3". The yield of the HNO_3-treatment process was ~90-95% with respect to the mass of the starting ACNFs-KOH.

After preparing these four samples, their porosity characteristics were measured through N_2 physisorption, and the results are presented in Table 5.12 and in Figure 5.47. All the isotherms are type IV with hysteresis loops. The results suggest that the activation raised the porosity of all samples significantly. For the ACNFs-90/10-CO_2 it is obvious that although its BET surface area almost tripled compared to that of the starting CNFs (299 vs. 115 m^2/g), the value of 299 m^2/g is much lower than the other 3 samples. Therefore, it was decided that this sample would not be used in the adsorption experiments. For the CNFs derived from 50/50 lignin/r-PET, physical activation with CO_2 increased their BET surface area to 686 m^2/g, but the chemical activation with KOH boosted their BET surface area to 1413 m^2/g. This value was validated through replication. Furthermore, the physical activation produces ACNFs which are mostly mesoporous with only a small percentage of microporosity. For both

these samples, their microporous fraction is around 11%, their average pore width is around 7 nm, and their isotherms contain hysteresis loops and show elevated adsorption at high values of relative pressure, therefore, they contain large mesopores and macropores. The adsorption of adsorbates in the pores of an adsorbent takes place mainly inside the micropores, as the dispersion forces are stronger there [175]. The main role of mesoporosity is to promote the faster mass transfer of the adsorbates to the active sites of the carbon surface. Therefore, it is desirable that an adsorbent contains both micro- and mesopores. However, the microporosity developed after activation with CO_2 is rather low. During this process, selective gasification takes place on the surface of carbon, especially where the carbon structure is defective, during which C atoms are extracted in the form of CO [158]. More ordered graphitic structure renders the extraction of carbon atoms harder, and probably this is the reason why the porosity of CNFs-90/10 doesn't increase to a larger extent. In both cases of activation with CO_2, there was an extensive burn-off which promoted the widening of pores and yielded a mostly mesoporous carbon structure.

Table 5.12: Textural characteristics of the activated CNFs (ACNFs)

Sample	BET surface area (m^2/g)	Total pore volume (cm^3/g)	Micropore volume (cm^3/g)	% Microporous	Average pore width (nm)
ACNFs-50/50-CO_2	686	0.853	0.095	11.1	7
ACNFs-90/10-CO_2	299	0.381	0.043	11.3	6.9
ACNFs-KOH	1413	1.010	0.138	13.7	3.7
ACNFs-KOH-HNO_3	1267	0.811	0.261	32.2	3.6

In contrast, activation with KOH yielded ACNFs with much larger BET surface area and total pore volume, while their porosity contains a higher microporous fraction and narrower average pore width. The KOH activation proceeds mainly through the intercalation of K atoms among the various graphene layers which causes their expansion, while gasification occurs as well [183]. Similar values of BET surface area have been reported for other lignin-based ACNFs after treatment with KOH (see Table 2.1). Furthermore, after treating these ACNFs with HNO_3, the BET surface area and the total pore volume decrease (1267 m^2/g and 0.811 cm^3/g respectively). The reason is the attachment of functional groups on the carbon surface, which narrows or closes some pores. However, this sample contains a higher percentage of microporosity, perhaps due to the narrowing of small mesopores.
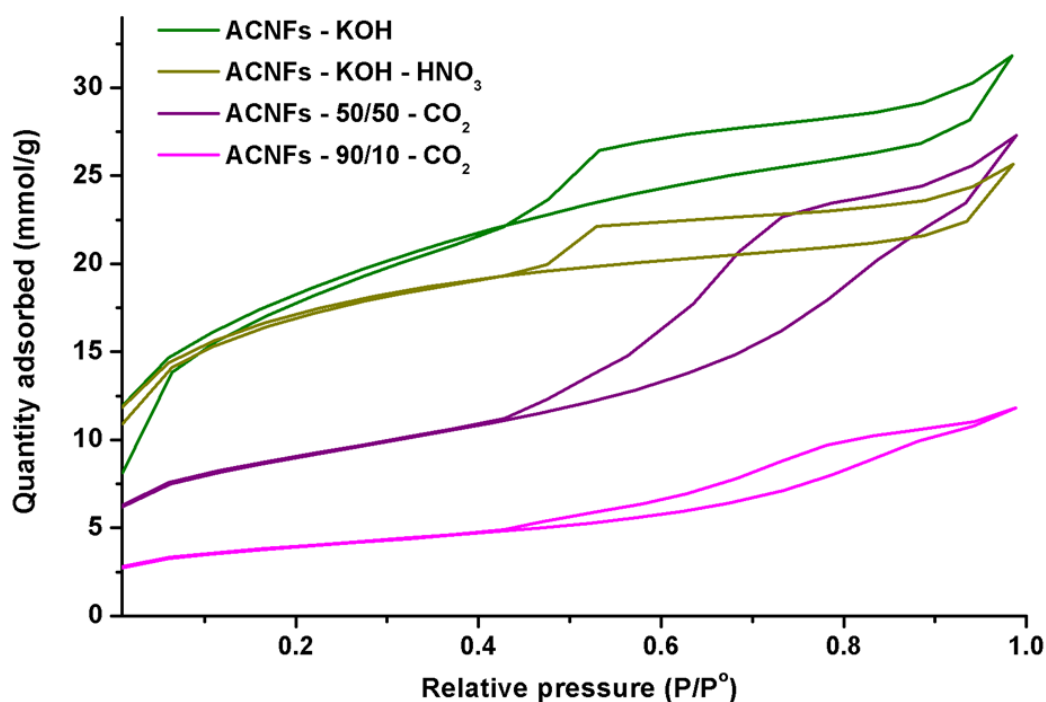
Figure 5.47: N_2 physisorption isotherms of the ACNFs

The presence of O on the surface of carbon materials can be determined through Boehm titration. Following the methodology described elsewhere [126,127] and that is briefly summarized in Chapter 4, it was estimated that the total acidic groups in ACNFs-KOH amount to 1.06 ± 0.06 mmol/g while in the ACNFs-KOH-HNO$_3$ they amount to 1.78 ± 0.13 mmol/g (average of two measurements). A more detailed measurement of the relative quantities of each type of acidic group was not carried out.
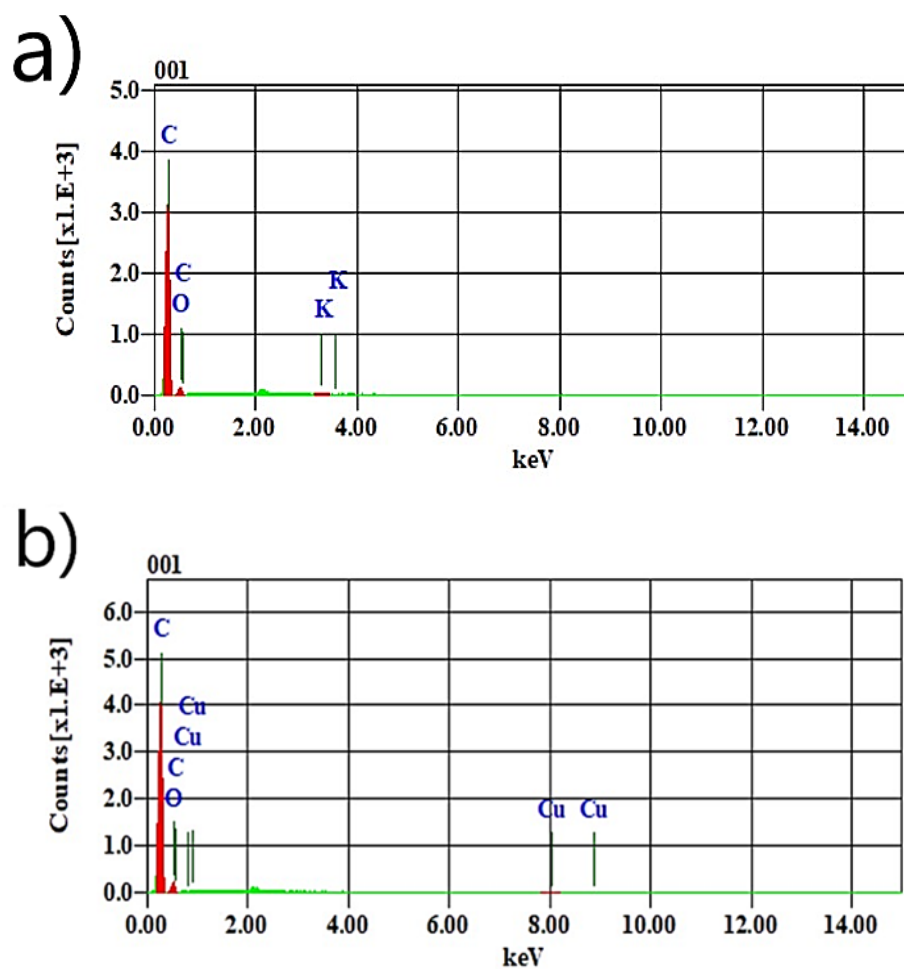
Figure 5.48: EDS spectra of the chemically activated CNFs; a) ACNFs-KOH; b) ACNFs-KOH-HNO$_3$

Furthermore, these samples were examined using EDS in order to measure their C and O content. The measurements revealed that ACNFs-KOH contain $86.86 \pm 1.4\%$ C and $13.12 \pm 1.4\%$ O, while ACNFs-KOH-HNO$_3$ contain $84.07 \pm 1.19\%$ C and 15.22

± 0.9% O (percentages per unit mass, average of two measurements) (Figure 5.48). Interestingly, other impurities in these two samples were almost undetected, although it was previously mentioned that the starting CNFs contain ~ 9% of other atoms. It seems that these impurities were washed away during the activation process.Figure 5.49 presents the C and O content after each stage of the preparation of ACNFs; starting from the precursor electrospun nanofibers from 50/50 lignin/r-PET, moving to CNFs, then ACNFs-KOH and finally to ACNFs-KOH-HNO$_3$. The CNFs presented in this figure are those prepared at 1000°C.
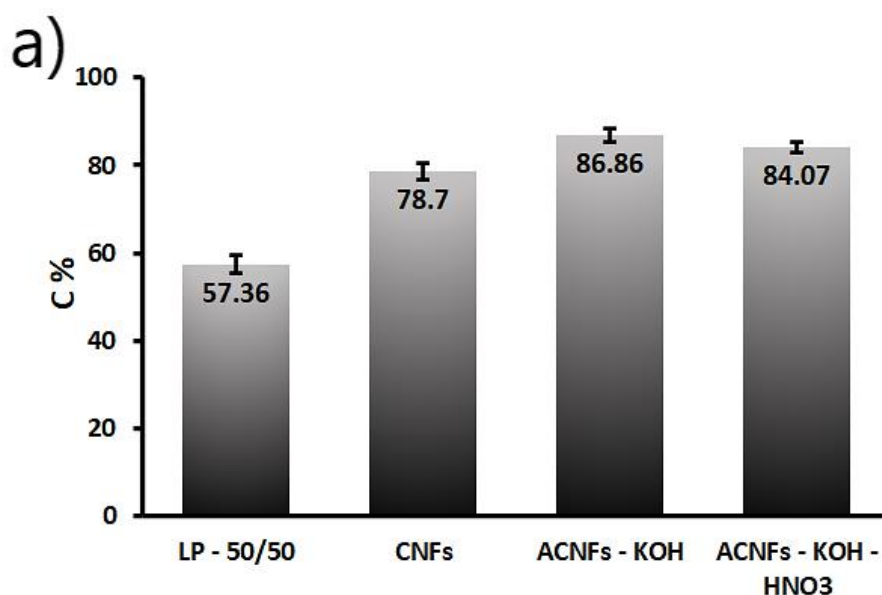
Figure 5.49: Evolution of the C% and the O% mass ratio from the precursor 50/50 lignin/r-PET electrospun nanofibers to the ACNFs-KOH-HNO$_3$; a) C%; b) O%. The error bars are denoted on top of each bar
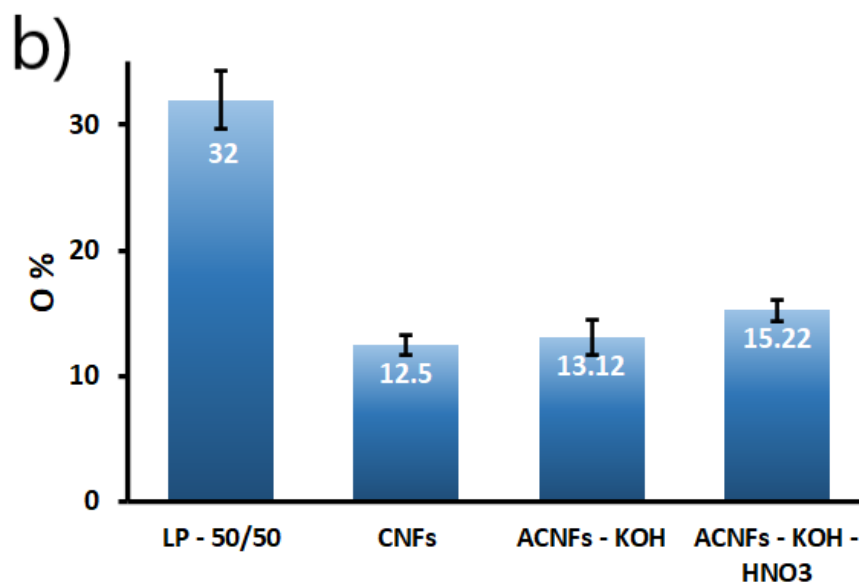
Figure 5.49: Evolution of the C% and the O% mass ratio from the precursor 50/50 lignin/r-PET electrospun nanofibers to the ACNFs-KOH-HNO$_3$; a) C%; b) O%. The error bars are denoted on top of each bar (continued)

SEM images of the ACNFs-KOH and of the ACNFs-KOH-HNO$_3$ are presented in Figures 5.50 and 5.51. These samples consist of fibers with average diameter close to 350-400 nm, which is of similar magnitude to that of the precursor electrospun nanofibers from which they were produced. Prior to activation, the CNFs were manually crashed in order to be dispersed in the KOH solution, as it is described in Chapter 4. The ACNFs-KOH-HNO$_3$ in the images shown here are, therefore, fractured, and their final form resembles the shape of nano-cylinders of finite length (SEM images in Figure 5.51).
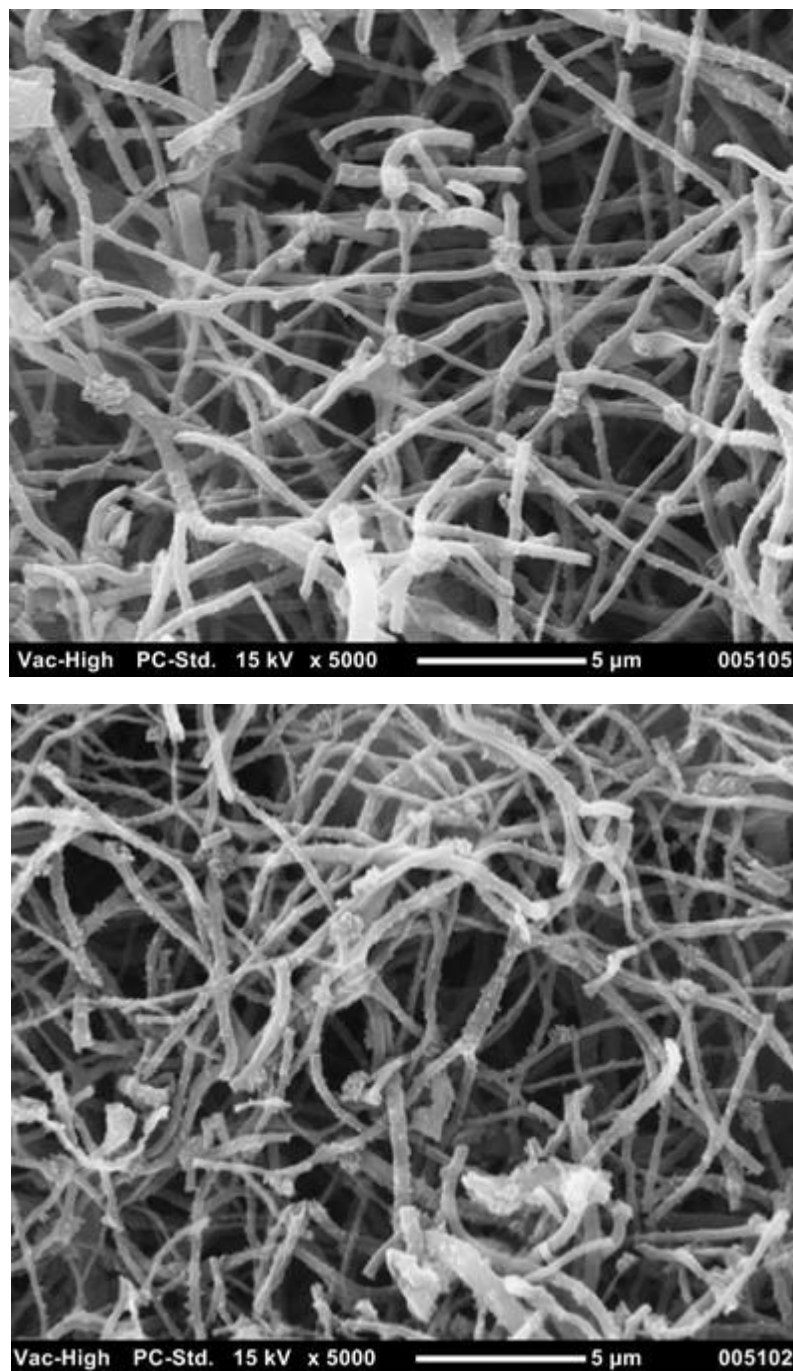
Figure 5.50: SEM images of the ACNFs-KOH. The average fiber diameter is measured to be 378 nm. The images are taken on different regions of the same sample. The scale bar is 5 μm
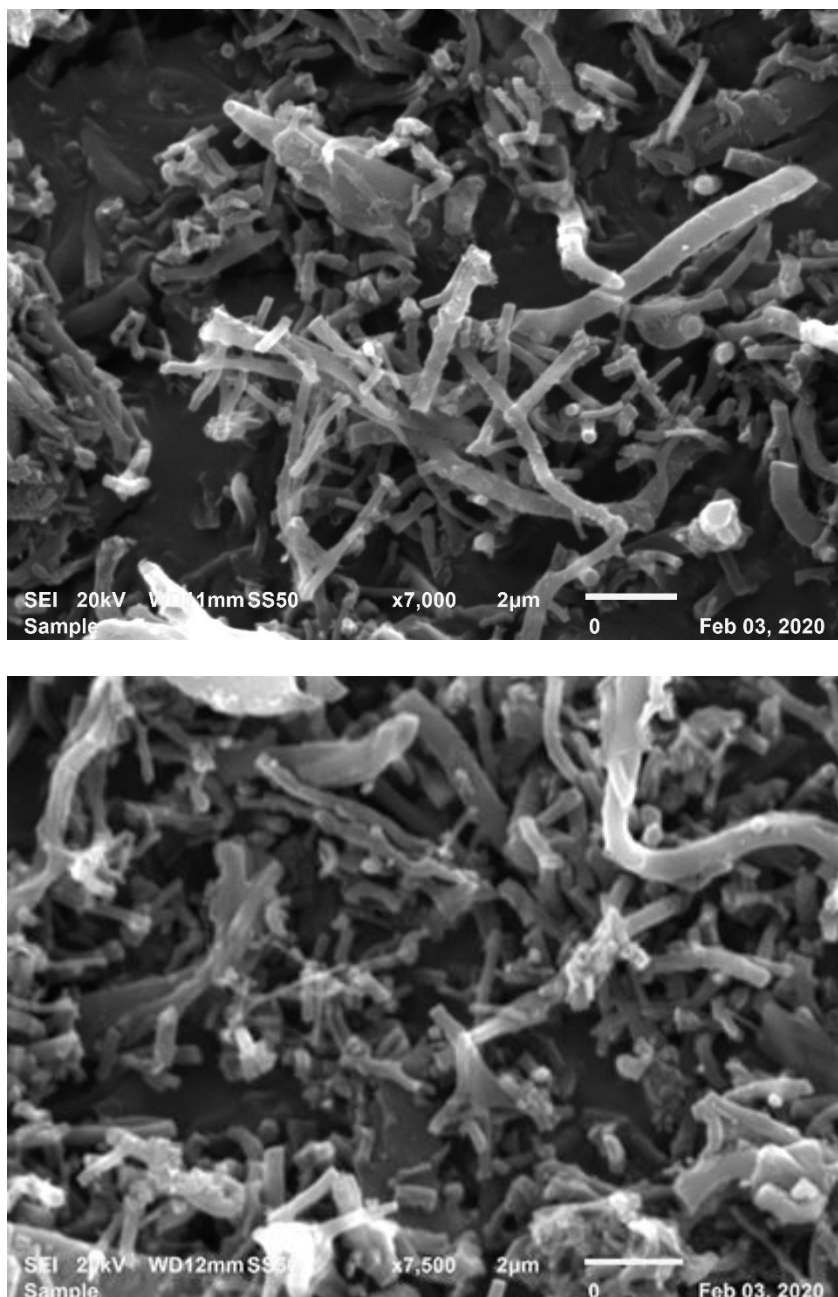
Figure 5.51: SEM images of the ACNFs-KOH-HNO$_3$. The average fiber diameter is measured to be 356 nm. The images are taken on different regions of the same sample. The scale bar is 2 μm

With naked eye, the material appears as a very fine powder. In this form they were used for the adsorption experiments. Furthermore, as the CNFs lose weight during the activation process, which results into the development of porous channels into their structure, their density is reduced. Hence, after activation and after the

subsequent treatment with HNO_3, the ACNFs exhibit a very low bulk density, that is, a small amount of ACNFs occupies much space if it is not compacted. Particularly, the bulk density of ACNFs-KOH and of ACNFs-KOH-HNO_3 was measured to be ~0.075 g/mL, hence 1 g of ACNFs occupies ~13.3 mL. The bulk density of CNFs manually crashed into powder amounts to ~0.133 g/mL. For comparison, the bulk density of commercial activated carbon (Merck 1.02186) was measured to be 0.16 g/mL.

Figure 5.52 presents the TEM micrographs of the CNFs prepared from 50/50 lignin/r-PET carbonized at 1000°C (Figures 5.52a-c), and of the ACNFs-KOH derived after the chemical activation (Figures 5.52d-f). The images show that the surface of the fibers is rough and it contains protuberances, as it was also denoted from the images presented in Figure 5.50. The randomly oriented, corrugated layers of carbon indicate that the CNFs mainly consist of amorphous and disordered structure, although careful examination reveals the existence of spots in which there is parallel stacking of a few graphene layers (as indicated by the arrows in 5.52b and 5.52c). These graphitic domains are, however, very small. The diffused concentric circles in the electron diffraction pattern shown as an inset in Figure 5.52a confirms that the structure of CNFs has a low degree of order, and it corroborates the results of the XRD and of the Raman spectroscopy. In addition, the porous network constituting the structure of the ACNFs is apparent in Figure 5.52f.
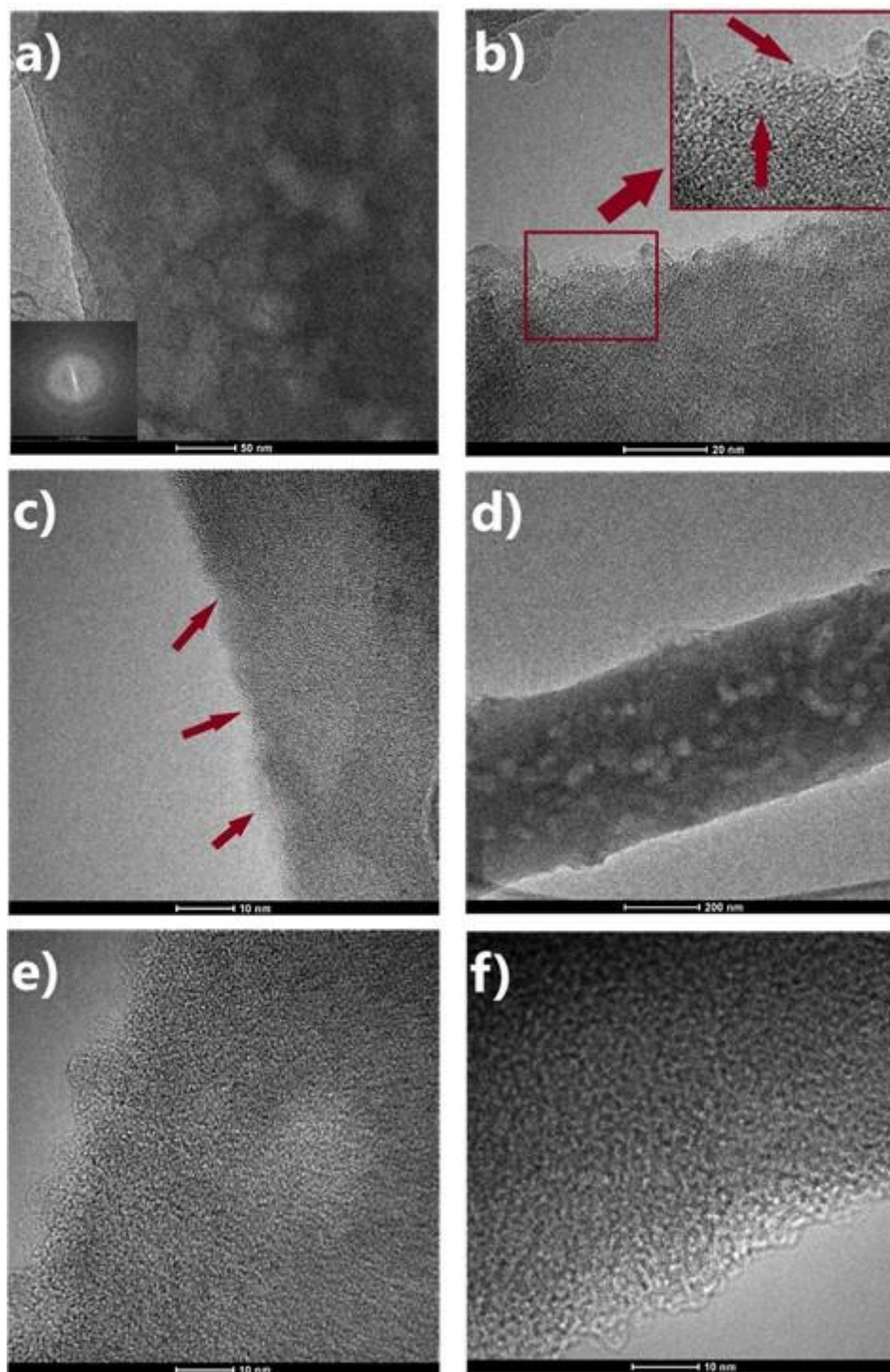
Figure 5.52: TEM images of CNFs and of ACNFs; a), b) and c) the starting CNFs derived from 50/50 lignin/r-PET carbonized at 1000°C; d), e) and f) the ACNFs-KOH produced after chemical activation

Based on the results presented in this section, the CNFs exhibiting the highest

porosity are the ones derived from 50/50 lignin/r-PET with average fiber diameters

close to 400 nm. These CNFs are mostly microporous with a disordered carbon structure, and after chemical activation with KOH they yield ACNFs with a BET surface area of 1413 m^2/g, the highest BET surface area achieved for these materials. Further treatment with HNO_3 yields ACNFs which contain more functional groups in their structure. These functional groups are expected to act as active sites for adsorption.

Moreover, these characteristics (very high external surface area due to their nanosized diameter, very high porosity, a combination of microporosity with mesoporosity, the presence of functional groups) are promising not only for adsorption, but also for other applications such as for energy storage, as it was mentioned in Section 2.4. As the adsorptive desulfurization is the application of interest of this research, the results will be presented in the following section.

5.3.4 Section summary

In this section, a detailed characterization of the structure and of the porosity characteristics of the CNFs and of the ACNFs was presented. In the case of CNFs, increasing the carbonization temperature to 1000°C and the lignin/r-PET mass ratio to 90/10 raises the degree of order in their carbon structure. Nevertheless, the structure of all of them is mostly disordered, with only small nano-regions of graphitic domains. CNFs prepared from 50/50 lignin/r-PET and carbonized at 1000°C exhibit the largest BET surface area which amounts to 353 m^2/g. Moreover, it was found that chemical activation with KOH boosts their BET surface area to 1413 m^2/g, while a further treatment with HNO_3 decreases this value to 1267 m^2/g, but it functionalizes the carbon surface through the anchoring of O-functional groups.

5.4 The adsorption of refractory S-compounds from a model fuel using ACNFs: equilibria, kinetics and thermodynamics of adsorption

The results presented in the previous Section indicate that ACNFs-KOH and ACNFs-HNO$_3$ possess the highest BET surface area and porosity by far. Hence, these materials were selected to be used for the adsorptive desulfurization experiments. For comparison, the adsorption capacity of the non-activated CNFs prepared from 50/50 lignin/r-PET at 1000°C was investigated, as well. For the adsorption experiments reported in this chapter, the same samples that were characterized in Section 5.3 were used. All experiments were performed in a batch mode, according to the methodology described in Chapter 4.

As it is analyzed in Chapter 3, aromatic S-compounds, especially dibenzothiophene and alkylated dibenzothiophenes are the hardest to remove through the traditional hydrodesulfurization process (refractory S-compounds). Based on the need to develop alternative methods for the removal of these compounds from middle distillates of petroleum, it was decided to focus on the adsorption of 4,6-dimethyldibenzothiophene (DMDBT) from a model diesel fuel (n-dodecane, C$_{12}$). Thus, the adsorption equilibria, the adsorption thermodynamics and the adsorption kinetics were thoroughly investigated for the adsorption of DMDBT on ACNFs. In addition, the suitability of ACNFs for the adsorption of dibenzothiophene (DBT) was tested, as well. The structure of DBT and of DMDBT are presented in Figure 3.1.

5.4.1 The adsorption of DMDBT: adsorption equilibria

The results of the equilibrium adsorption of DMDBT on the three adsorbents studied here at room temperature are presented in Figure 5.53.
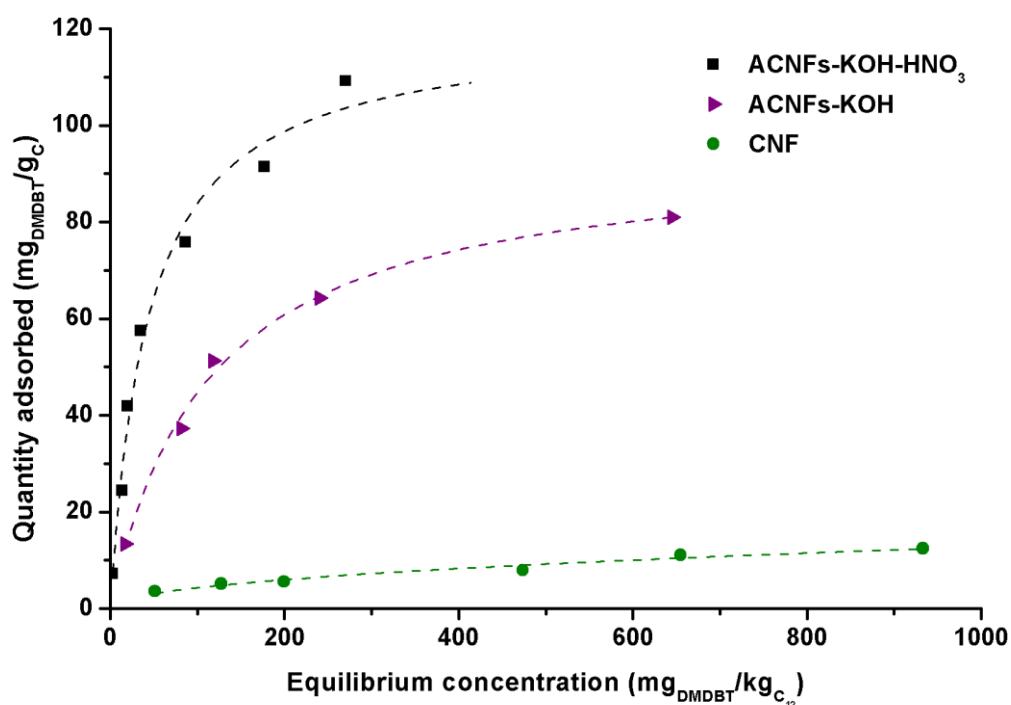
Figure 5.53: Adsorption isotherms of DMDBT on CNFs, ACNFs-KOH and ACNFs-KOH-HNO$_3$ at T=22°C. The dashed lines in the ACNFs present the fitted Langmuir isotherms, while the dashed line in CNFs present the Freundlich isotherm

The Figure suggests that ACNFs-KOH-HNO$_3$ exhibit the highest adsorption capacity, while the adsorption capacity of CNFs is very low, as it is expected based on their relatively lower BET surface area. The data were fitted to three different adsorption isotherms, namely Langmuir, Freundlich, and the modified Langmuir-Freundlich model, using non-linear regression with the aid of a data analysis software (OriginPro) (equations 5.1, 5.2 and 5.3).

$$\text{Langmuir isotherm: } q_e = q_{m-L} * \frac{K_L * C_e}{1 + K_L * C_e} \quad (5.1)$$

Where q_e (mg$_{DMDBT}$/g$_C$) is the equilibrium adsorption capacity, Ce (mg$_{DMDBT}$/kg$_{C12}$) is the equilibrium concentration, q_{m-L} (mg$_{DMDBT}$/g$_C$) is the maximum adsorption capacity predicted from the Langmuir isotherm and K$_L$ is the Langmuir constant [184-186].

$$\text{Freundlich isotherm: } q_e = K_F C_e^{1/n_F} \quad (5.2)$$

Where q_e (mg_{DMDBT}/g_C) is the equilibrium adsorption capacity, Ce (mg_{DMDBT}/kg_{C12}) is the equilibrium concentration, K_F [(mg_{DMDBT}/g_C)/(mg_{DMDBT}/kg_{C12})$^{1/n}$] is the Freundlich constant related to the adsorption capacity and n_F (dimensionless) is the Freundlich constant related to the adsorption intensity [179, 184].

$$\text{Langmuir-Freundlich isotherm: } q_e = q_{m-LF} * \frac{(K_{LF}*C_e)^{1/n_{LF}}}{1+(K_{LF}*C_e)^{1/n_{LF}}} \quad (5.3)$$

Where q_e (mg_{DMDBT}/g_C) is the equilibrium adsorption capacity, Ce (mg_{DMDBT}/kg_{C12}) is the equilibrium concentration, K_{LF} [(mg_{DMDBT}/g_C)/(mg_{DMDBT}/kg_{C12})$^{1/n}$] is the Langmuir-Freundlich constant related to the adsorption capacity and the exponent n_{LF} (dimensionless) is related to the surface heterogeneity [187-189].

Langmuir isotherm assumes monolayer adsorption on a surface of identical sites [190, 191]. Freundlich isotherm is an empirical model applicable for heterogeneous surfaces or multilayer adsorption, in which $n_F>1$ indicates favorable adsorption [179, 191]. In the Langmuir-Freundlich model, the exponent n_{LF} accounts for the heterogeneity of the site energies, with a large deviation from the value of 1 indicating a higher degree of heterogeneity [186].

The results of the model fitting for each adsorbent are shown in Table 5.13. With the exception of CNFs, in which the Freundlich model gave the best fitting, the adsorption experimental data of the ACNFs were best fitted to the Langmuir model. However, the R^2 values of the Freundlich model are also high, therefore, it cannot be disregarded.

Table 5.13: Equilibrium adsorption of DMDBT: parameters of the Langmuir, Freundlich and Langmuir-Freundlich model

Sample	Temperature (ºC)	Langmuir			Freundlich			Langmuir-Freundlich			
		q_{m-L}	K_L	R^2	K_F	n_F	R^2	q_{m-LF}	K_{LF}	n_{LF}	R^2
CNFs	22	15.73	0.0032	0.8891	0.493	2.12	0.9618	-[*]	-[*]	-[*]	-[*]
ACNFs-KOH	22	95.40	0.0088	0.9835	3.77	1.91	0.9526	98.65	0.0082	1.035	0.9673
ACNFs-KOH-HNO$_3$	22	120.3	0.0230	0.9800	11.18	2.43	0.9507	128.6	0.0191	1.11	0.9761
ACNFs-KOH-HNO$_3$	50	113.9	0.0160	0.9894	7.093	2.08	0.9706	130.2	0.0110	1.168	0.9598
Units: q_{m-L}: mg_{DMDBT}/g_C; K_L: kg_{C12}/mg_{DMDBT} ; K_F: $[(mg_{DMDBT}/g_C)/(mg_{DMDBT}/kg_{C12})^{1/n}]$; n_F: dimensionless; q_{m-LF}: mg_{DMDBT}/g_C; K_{LF}: kg_{C12}/mg_{DMDBT}; n_{LF}: dimensionless											
[*]The fitting of the model did not converge											

The modified Langmuir-Freundlich model fitted the data less accurately than the other two models, as it is indicated by the values of R^2. Even so, the values of n_{LF} are close to 1, which shows a good approximation of the Langmuir model.

Therefore, the results suggest that there is homogeneous monolayer adsorption, although a heterogeneous mechanism may also be involved, especially at low surface coverage, when the DMDBT molecules first adsorb on the sites of higher energy [186, 192]. A larger K_F of the Freundlich isotherm indicates higher adsorption capacity, while a smaller n_F denotes a more homogeneous adsorbent with a narrower site energy distribution [193]. In this case, ACNFs-KOH-HNO$_3$ seems to have a more heterogeneous surface energy, due to the anchoring of more O-functional groups on the carbon surface.

The calculated parameters of the Langmuir isotherm presented in Table 5.13 show that the ACNFs-KOH-HNO$_3$ exhibit a maximum adsorption capacity of 120.3 mg$_{DMDBT}$/g$_C$, which corresponds to 18.2 mgS/g$_C$. This value is among the highest found in the literature for the adsorption of DMDBT on activated carbon or related materials. Table 5.14 presents a literature overview of the highest values reported for the adsorption of DMDBT on carbon-based adsorbents, as they are calculated from the Langmuir isotherm (q_{m-L} values). It should be noticed, however, that a direct comparison with the values reported in other studies is not always reliable, as there are various factors which influence the adsorption capacity, such as the dose of adsorbent, the presence of other solutes and the solvent itself. Very high adsorption capacity values have been reported for the adsorption of DMDBT from hexane, heptane and octane; however, the solubility of DMDBT in these relatively light hydrocarbons is significantly smaller than its solubility in dodecane and hexadecane. Therefore, the

removal of DMDBT from the lighter hydrocarbons is more favorable, just as it happens

with other refractory S-compounds [194].

Table 5.14: Comparison of maximum adsorption capacities calculated through
Langmuir isotherm for DMDBT on carbon-based adsorbents

Adsorbent	Solvent	Adsorption Capacity	Reference
Activated carbon nanofibers	Dodecane	120.3 mg$_{DMDBT}$/g	This work
Activated carbon	Hexadecane	26.85 mgS/g= 177.7 mg$_{DMDBT}$/g	[188]
Activated carbon cloth	Heptane	49 mgS/g= 324.4 mg$_{DMDBT}$/g	[192]
Activated carbon	Hexadecane	19.5 mgS/g= 128.7 mg$_{DMDBT}$/g	[190]
Activated carbon doped with boron	Isooctane	30.2 mgS/g= 199 mg$_{DMDBT}$/g	[195]
Activated carbon	n-Octane	385 mg$_{DMDBT}$/g	[196]
Activated carbon doped with metals	Decane/hexadecane	0.391 mmol/g= 82.9 mg$_{DMDBT}$/g	[197]
Activated carbon	Decane/hexadecane	84 *mg$_{DMDBT}$/g*	[198]
Activated carbon	Hexadecane	31.88 mgS/g= 211 mg$_{DMDBT}$/g	[199]
Activated carbon	Hexadecane	11.3 mg$_{DMDBT}$/g	[182]
Activated carbon	Dodecane	0.41 mmol/g= 86.7 mg$_{DMDBT}$/g	[200]
Activated carbon and carbon fibers doped with metals	Hexane	23.5 mgS/g= 155.6 mg$_{DMDBT}$/g	[201]
Activated carbon doped with metals	Hexadecane	0.77 mmolS/g= 163.1 mg$_{DMDBT}$/gC	[202]

As an example, for the case of DBT, it has been reported that changing the solvent from n-hexane to n-decane can decrease the maximum adsorption capacity by more than 40% [194]. Taking this into consideration, a comparison of the adsorption capacity found here with the values found in the literature (Table 5.14) suggest that ACNFs exhibit a high capacity for the adsorption of DMDBT.
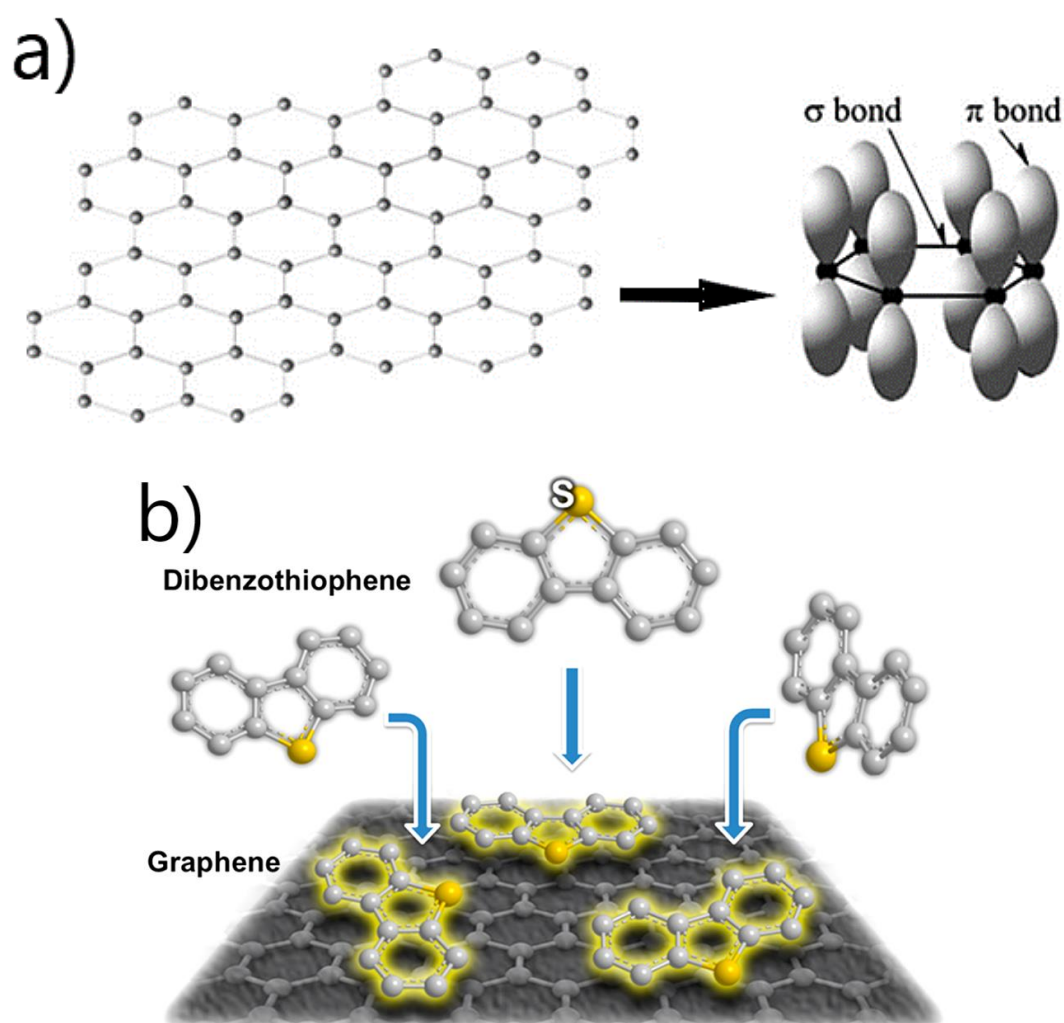
Figure 5.54: The structure of graphene and its adsorption of sulfur-compounds; a) the conjugated π orbitals on a graphene layer [203]; b) the mechanism of π-π interactions between aromatic S-compounds and sp^2-hybridized carbon substrates [204]

In general, carbon materials have demonstrated a very good adsorption capacity for aromatic S-compounds. These adsorbents are mainly built of carbon atoms

connected through sp^2-hybridized bonds; hence, they contain conjugated π-orbitals lying perpendicular to the plane (Figure 5.54a). These out-of-plane conjugated π-orbitals can generate interactions with other aromatic molecules. On the other hand, thiophenes and benzothiophenes contain aromatic rings, hence, they form π-π interactions with graphitic substrates. The interaction between the delocalized π-electrons of the aromatic S-compounds and the electron-rich regions of the carbon substrate is based on dispersion forces [181]. This mechanism is schematically demonstrated in Figure 5.54b.

Moreover, the adsorption capacity of ACNFs-KOH is clearly lower than that of the ACNFs-KOH-HNO$_3$ (95.4 vs. 120.3 mg$_{DMDBT}$/g$_C$), although its BET surface area and porosity are higher as it was described in the previous section. The reason is that ACNFs-KOH-HNO$_3$ contain much more O-functional groups, which are known to enhance the adsorption of S-compounds. The various types of thiophenes and benzothiophenes have a basic character as the S-atom acts as an electron donor [181, 205]. Thus, they interact with the acidic O-groups through Lewis acid-base interactions [181, 206]. Hence, the treatment with HNO$_3$ enhances the adsorption capacity of the adsorbent [106, 207].

5.4.2 The adsorption of DMDBT: adsorption thermodynamics

Investigation of the adsorption equilibrium at a higher temperature can provide information about the enthalpy of adsorption and the spontaneity of the process. Using the ACNFs-KOH-HNO$_3$ which gave the highest adsorption capacity, the adsorption of DMDBT was carried out at 50°C and the results are presented in Figure 5.55. For comparison, the adsorption isotherm at 22°C is presented in this figure, as well. The

calculated parameters of the Langmuir, the Freundlich and the Langmuir-Freundlich model are provided in Table 5.13.
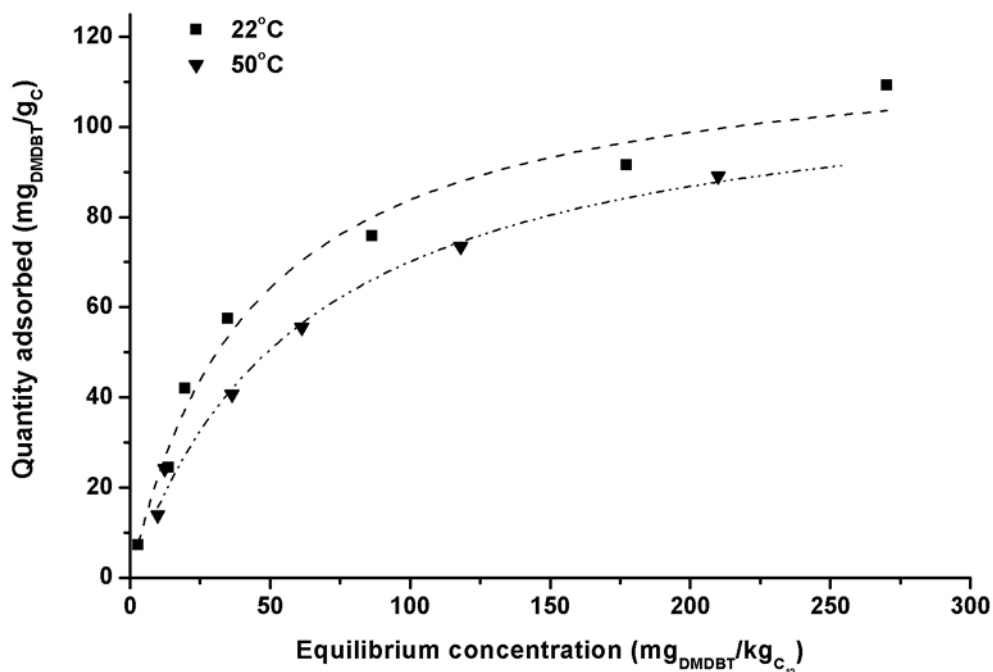
Figure 5.55: Adsorption isotherms of DMDBT on ACNFs-KOH-HNO$_3$ at 22°C and at 50°C

Again, it was found that the Langmuir model fits the data more accurately. The calculated maximum adsorption capacity is 113.9 mg$_{DMDBT}$/g$_C$, which is slightly lower that the adsorption capacity of ACNFs-KOH-HNO$_3$ at room temperature. Hence, the process is exothermic and more favorable at lower temperatures for the range of temperatures studied here. The thermodynamic parameters of the process were calculated using the fundamental equations:

$$\Delta G^o = \Delta H^o - T\Delta S^o \quad (4.4) \text{ and } \Delta G^o = -RT\ln K_e \quad (5.5)$$

$$\text{which give } \ln K_e = -\frac{\Delta H^o}{RT} + \frac{\Delta S^o}{R} \quad (5.6)$$

Where R is the ideal gas constant, ΔG^o is the standard Gibbs free energy change, ΔH^o is the standard enthalpy change and ΔS^o is the standard entropy change. The dimensionless equilibrium constant K_e was calculated following the methodology described in [208]. Briefly, the adsorption can be represented as the following reversible process:

Adsorbate in the solution $\Leftrightarrow$ Adsorbate on the adsorbent
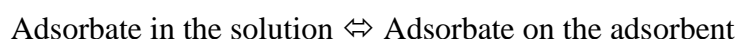
Therefore, K_e was determined based on the equation $K_e=q_e/C_e$ at different initial concentrations of adsorbate and extrapolating to zero. Then, $\ln K_e$ was plotted against $1/T$ and after a simple linear regression it was calculated that $\Delta H^o=-8.423$ kJ/mol and $\Delta S^o=0.677$ J/molK. This value of adsorption enthalpy is lower in absolute value than -20 kJ/mol, and this is an indication that the DMDBT molecules are physisorbed on the surface through dispersion forces [209]. Gibbs energy ΔG^o was also calculated for these two temperatures and it was found negative (see Table 5.15). Therefore, the process is spontaneous and exothermic. The positive entropy indicates an increased randomness at the solid/solution interface after the adsorption of DMDBT.

Table 5.15: Thermodynamic parameters for the adsorption of DMDBT on ACNFs-KOH-HNO$_3$

Temperature (ºC)	K_e	ΔG^o (kJ/mol)	ΔH^o (kJ/mol)	ΔS^o (J/mol*K)
22	33.644	-8.623	-8.423	0.677
50	24.981	-8.642		

5.4.3 The adsorption of DMDBT: adsorption kinetics

Investigation of the adsorption kinetics is very important as this is closely connected to the feasibility of the process at an industrial scale. The adsorption kinetics were studied at 22°C and at 50°C, at an initial DMDBT concentration of 335 ppm, following the methodology described in Chapter 4. At certain time intervals the solution concentration was measured, and the results are presented in Figures 5.56 and 5.57 for the temperatures of 22°C and of 50°C respectively.
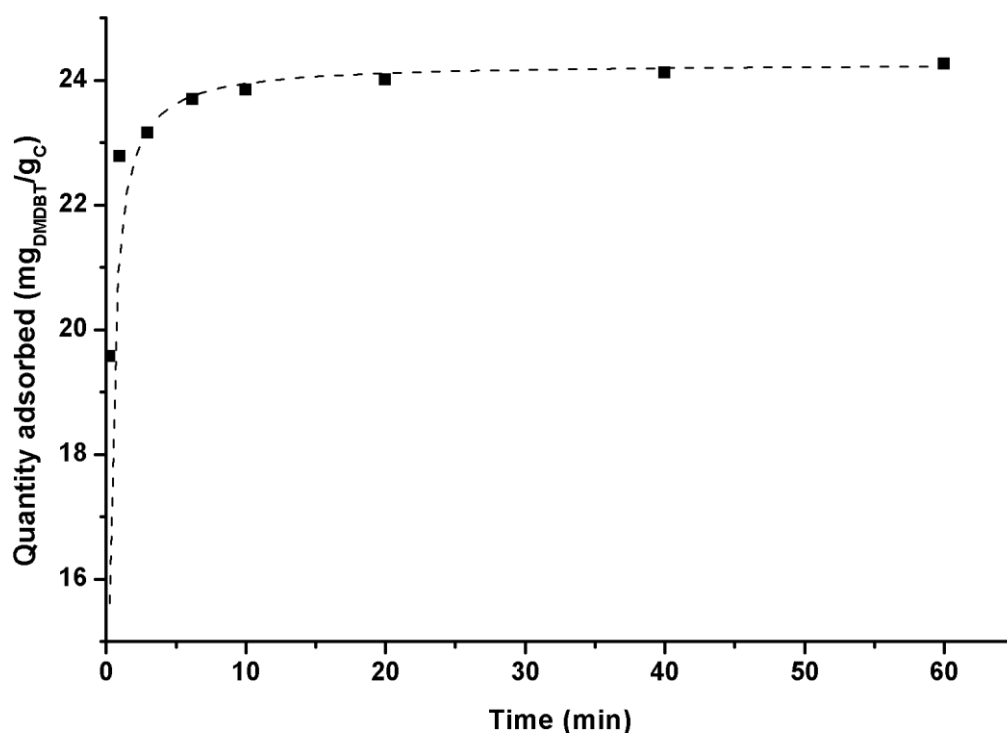
Figure 5.56: Adsorption kinetics for DMDBT on ACNFs-KOH-HNO$_3$ at 22°C. The dashed line shows the fitting of the pseudo-second order model
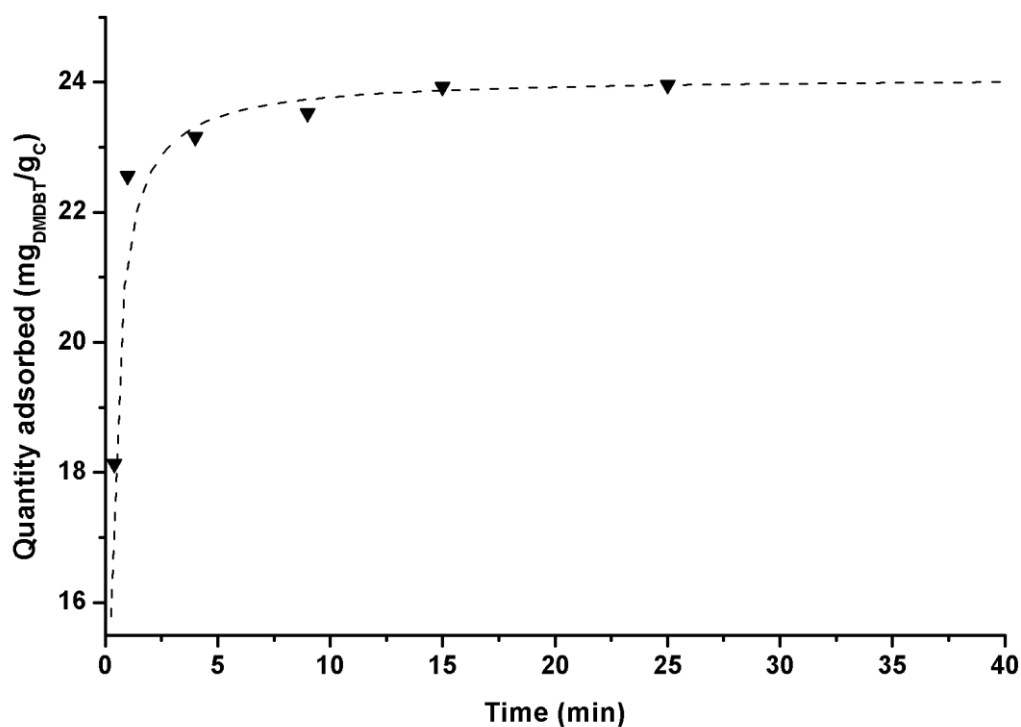
Figure 5.57: Adsorption kinetics for DMDBT on ACNFs-KOH-HNO$_3$ at 50$^{\text{o}}$C. The dashed line shows the fitting of the pseudo-second order model

Two models were investigated according to their accuracy to describe the data [184, 186]:

The pseudo-first order model:

$$\frac{dq_t}{dt} = k_1(q_e - q_t) \iff q_t = q_e(1 - e^{-k1*t}) \quad (5.7)$$

Where q_t (mg$_{\text{DMDBT}}$/g$_{\text{C}}$) is the adsorbed quantity at time t, q_e (mg$_{\text{DMDBT}}$/g$_{\text{C}}$) is the equilibrium adsorption and k_1 (min^{-1}) is the rate constant of the pseudo-first order model.

The pseudo-second order model:

$$\frac{dq_t}{t} = k_2(q_e - q_t)^2 \iff q_t = \frac{k_2 q_e^2 t}{1 + k_2 q_e t} \iff \frac{t}{q_t} = \frac{1}{k_2 q_e^2} + \frac{t}{q_e} \quad (4.8)$$

Where q_t (mg$_{\text{DMDBT}}$/g$_{\text{C}}$) is the adsorbed quantity at time t, q_e (mg$_{\text{DMDBT}}$/g$_{\text{C}}$) is the equilibrium adsorption and k_2 [g$_{\text{C}}$/(mg$_{\text{DMDBT}}$*min)] is the rate constant of the pseudo-

second order model. The pseudo-first order model is used to describe the initial stages of the adsorption, while the pseudo-second order describes much better the whole process and assumes the sharing of electrons or the electron exchange between the adsorbate and the adsorbent [181].

An overview of the results presented in Figures 5.56 and 5.57 indicates that the adsorption is remarkably fast. Particularly for room temperature, around 94% of the final equilibrium adsorption is reached after just 1 min, and 98% after 10 min. Similarly, at 50°C 99% of the final equilibrium adsorption is reached after just 15 min. A further proof of the very fast kinetics is provided by the rate constants calculated by fitting the above-mentioned kinetic models. While the pseudo-first order model doesn't fit the data well as indicated by R^2, the pseudo-second order model is very accurate with R^2 reaching 0.999 for both temperatures. For 22°C the rate constant is 0.297 $g_C/(mg_{DMDBT}*min)$, while for 50°C the rate constant is 0.316 $g_C/(mg_{DMDBT}*min)$, which translates to faster kinetics at higher temperature (Table 5.16). Table 5.17 compares the rate constants calculated here with the highest values found in the literature using the pseudo-second order kinetic model for the adsorption of DMDBT on carbon-based adsorbents.

Table 5.16: Kinetic parameters for the adsorption of DMDBT on ACNFs-KOH-HNO$_3$

Temperature (°C)	q$_e$-experimental	Pseudo-1st order			Pseudo-2nd order		
		q$_e$	k$_1$	R^2	q$_e$	k$_2$	R^2
22	24.25	23.7	6.97	0.8792	24.28	0.297	0.9998
50	24.13	23.64	3.08	0.5768	24.08	0.316	0.9995
Units: q$_e$: mg$_{DMDBT}$/g$_C$; k$_1$: (min^{-1}); k$_2$: [g$_C$/(mg$_{DMDBT}$*min)]							

Table 5.17: Comparison of the adsorption kinetics measured here for the adsorption of DMDBT with the highest values found in the literature

Adsorbent	Solvent	Adsorbent dose [(adsorbent mass)/(solution mass or volume)]	Initial concentration of DMDBT	k_2 [g/(mg*min)]	Shaking speed	Ref.
Activated carbon nanofibers	Dodecane	10 g/L	335 ppm	0.297 (94% of equilibrium after just 1 min)	105 rpm	This work
Activated carbon cloth	Heptane	0.02 g/3.5 g	200 ppm (total concentration, in the presence of other S-compounds)	0.029 (90% of equilibrium after >40 min)	150 rpm	[192]
Activated carbon cloth	Heptane	0.025 g/4 g	0.632 mmol/kg (in the presence of other S-compounds)	0.12 (90% of equilibrium after >25 min)	N/A	[186]
Activated carbon	Dodecane	1 g/50 g	23.8 μmol/g (total S concentration, in the presence of other compounds)	0.3021 mmol/g/min (90% of equilibrium after >30 min)	N/A	[208]
Activated carbon doped with metals	Hexane/ toluene	(not stated clearly)	50 ppm (in the presence of other S-compounds)	0.0406 (90% of equilibrium after >20 min)	N/A	[210]
Activated carbon doped with metals	Hexane/ toluene	(not stated clearly)	50 ppm (in the presence of other S-compounds)	0.0311 (90% of equilibrium after 20 min)	N/A	[211]
Activated carbon doped with metals	Decane/ hexadecane	0.05 g/10 mL	100 mgS/L	(not calculated) 90% of equilibrium after >10 h	110 rpm	[197]
Activated carbon	Hexadecane	0.01 g/L	20 ppmS	0.153	N/A	[182]
Activated carbon doped with boron	Isooctane	(not clearly stated)	5-150 ppmS	0.514	300 rpm	[195]

Ganiyu et al. [195] have reported very fast kinetics for the adsorption of DMDBT on activated carbon, however, they report that the experiments were conducted at an

extreme shaking speed of 300 rpm, while isooctane was used as a solvent. Thus, under these conditions it is expected to measure very fast kinetics. Furthermore, shorter-chain hydrocarbons lead to much faster adsorption rates due to a combined influence of their viscosity with the surface tension [194]. In contrast, the experiments in the present study were contacted at a low speed of 105 rpm. Therefore, based on the information presented in Table 5.16, the results presented here correspond to comparatively the fastest kinetics that have been reported for the adsorption of DMDBT on a carbon-based adsorbent.

Based on the adsorption kinetics at the two distinct temperatures, it is possible to calculate the activation energy of the adsorption. The adsorption rate constant k_2 calculated from the pseudo-second order model is a function of temperature according to Arrhenius equation [184]:

$$k_2 = A * e^{-\frac{Ea}{RT}} \Leftrightarrow \ln k_2 = \ln A - \frac{E_a}{RT}$$

Where E_a (kJ/mol) is the activation energy, A [g_C/(mg_{DMDBT}*min]) is the collision frequency factor and R is the ideal gas constant. By plotting $\ln k_2$ vs. T at 295 K and at 323 K and fitting a linear relationship, it is calculated that E_a=1.76 kJ/mol and A=0.607 [g_C/(mg_{DMDBT}*min]). Values of E_a<4 kJ/mol denote physisorption, while E_a>8 kJ/mol is an indication of chemisorption [184]. Thus, this rather small value of E_a calculated here provides a further proof that the adsorption of DMDBT on the ACNFs proceeds through dispersion forces.

The claim, that ACNFs present the fastest kinetics compared to the values at various conditions encountered in the literature, is corroborated by fitting the intraparticle diffusion model to the data presented here for the adsorption of DMDBT on ACNFs-KOH-HNO$_3$. This model gives an insight into the mechanisms involved

during the process, and it is expressed as an empirical formula according to the following equation:

$$q_t = k_{id} * t^{\frac{1}{2}} + C_{id} \quad (5.9)$$

Where t is the time (min), q_t (mg_{DMDBT}/g_C) is the amount of solute adsorbed at time t, C_{id} (mg_{DMDBT}/g_C) is the intercept, which is related to the size of the boundary layer, and k_{id} [$mg_{DMDBT}/(g_C*(min^0.5))$] is the rate constant of each separate stage of the adsorption [212, 213]. The model assumes that the adsorption proceeds through separate stages, the first of which is the external surface adsorption through the boundary layer, the second one is the intraparticle adsorption to the micropores and the third one is the surface adsorption at equilibrium [212]. If the plot of q_t vs. $t^{1/2}$ is linear, then the process is only controlled by intraparticle diffusion [213]. However, the usual case is a multi-linear plot consisting of two or three stages; hence, more than one mechanisms are controlling the adsorption process [213].

Figure 5.58 shows the plot of q_t vs. $t^{1/2}$ for the adsorption data of DMDBT on ACNFs-KOH-HNO$_3$ at 22°C and at 50°C. Both plots clearly consist of three stages, and each one is highlighted with a dashed straight line. For each stage, the intraparticle diffusion constant k_{id} and the intercept C_{id} was calculated through linear regression of equation 5.9 and the results are presented in Table 5.18.

Table 5.18: Calculated parameters of the intraparticle diffusion model

Temperature (^{o}C)	First stage		Second stage		Third stage	
	k_{id1}	C_{id1}	k_{id2}	C_{id2}	k_{id3}	C_{id3}
22	6.4178	16.359	0.5205	22.277	0.0876	23.584
50	12.045	10.507	0.5984	21.954	0.0265	23.826
Units: k_{id}: [$mg_{DMDBT}/(g_C*(min^0.5))$]; C: mg_{DMDBT}/g_C						
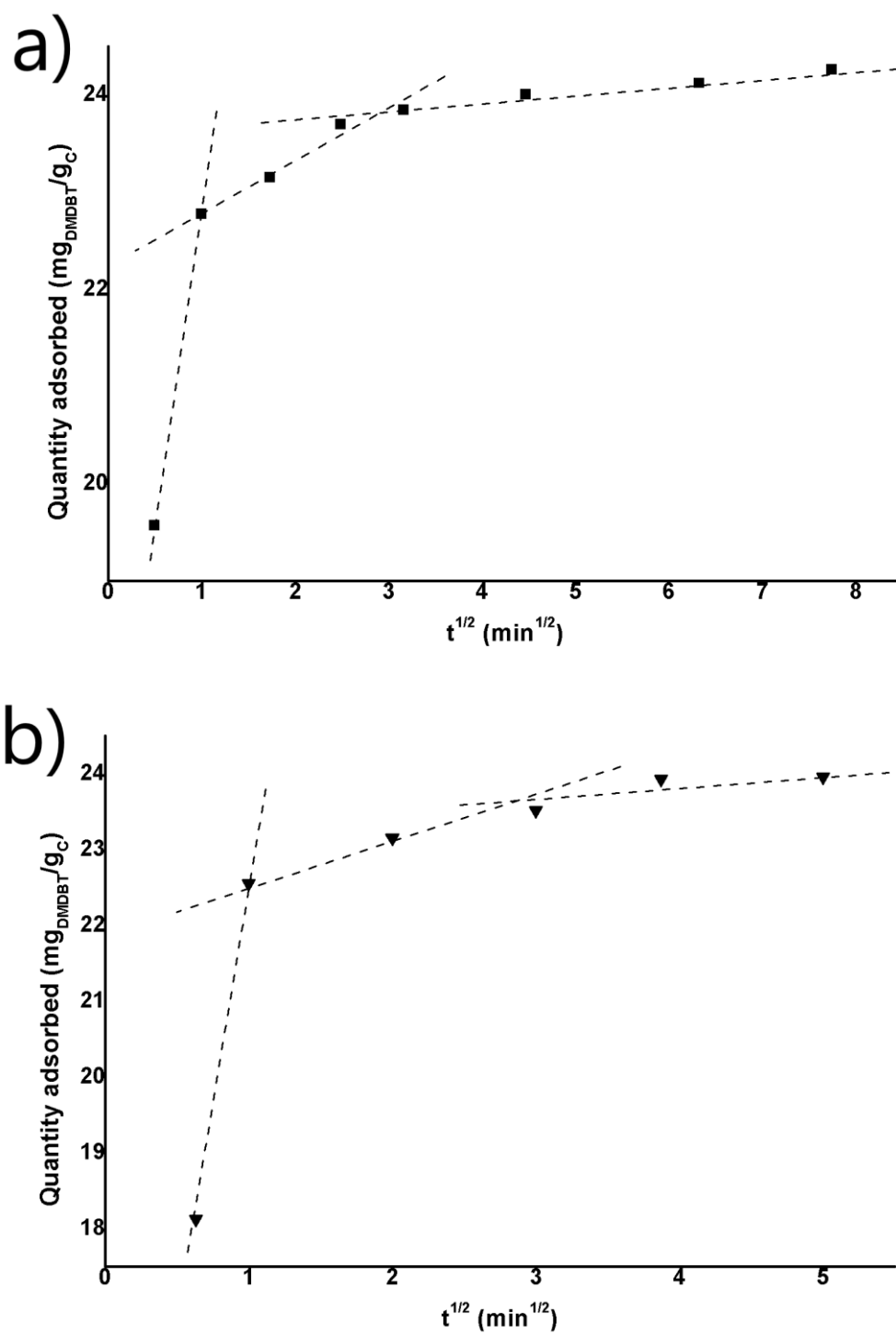
Figure 5.58: Fitting of the DMDBT adsorption kinetics data to the intraparticle diffusion model; a) T=22°C; b) T=50°C

In both cases, the first stage of adsorption is remarkably fast with a very high rate constant of 6.4178 [$mg_{DMDBT}/(g_C*(min^{0.5}))$] at 22°C and almost double at 50°C

(12.045 [$mg_{DMDBT}/(g_C*(min\char`^0.5))$]). Thus, the external diffusion through the boundary layer proceeds extremely fast, especially at higher temperatures. The rate then drops as the adsorbate molecules diffuse into the micropores and finally they reach the equilibrium, as indicated by the final almost horizontal plateau. Therefore, the data suggest that the process involves a multi-stage mechanism, and it is mainly controlled by intraparticle diffusion into the micropores as the external diffusion is extremely fast.

For the adsorption of DMDBT on activated carbon-based adsorbents, values found in the literature for the fitting of the interparticle diffusion model have calculated k_{id1} to be 0.641 ($mg/g*min^{1/2}$) for the first stage of external diffusion [210] and up to 0.0657 for the second and third stage of adsorption [195]; these values are orders of magnitude lower than the calculated values reported here. Therefore, the parameters calculated from fitting the intraparticle model further support that the activated carbon nanofibers exhibit the fastest kinetics for the adsorption of DMDBT, with 94% of the final equilibrium adsorption reached after just 1 min, and 98% after 10 min at room temperature at a low shaking speed of 105 rpm. Moreover, the results suggest that these fast kinetics are based on the extremely fast initial external diffusion of the adsorbates to the adsorbent surface through the boundary layer. This is justified by the morphology and structure of the ACNFs. As it was demonstrated in Section 5.3, this material actually consists mostly of nano-sized cylinders or clusters of them with large voids (macropores and large mesopores), therefore, it has a remarkably high external surface area (the external surface area of the fibers) which translates into a very large interface between the adsorbent and the solution. In contrast, the common activated carbon mainly consists of microparticles, hence the total interface between the adsorbate and the solution is considerably smaller.

5.4.4 Replication of the adsorption measurements

As it is described in the experimental part (Section 4.4) all the adsorption desulfurization experiments for the removal of DMDBT were carried out using the same batch of ACNFs-KOH-HNO$_3$, the properties of which were also characterized in Section 5.3. For validation purposes, a second batch of ACNFs-KOH-HNO$_3$ was produced under the same conditions and it was used to replicate a limited number of the adsorption experiments. The replication results are presented in the four graphs of Figure 5.59 for the equilibrium adsorption and for the adsorption kinetics at room temperature and at 50°C. In these graphs, the results obtained using the second batch of ACNFs are represented by the red dots (denoted as "sample 2"). The blue dots ("sample 1") signify the initial results presented in Sections 5.4.1-5.4.3. In all cases, the adsorption measurements showed very good reproducibility. The equilibrium results obtained from the second sample differed less than 10% compared to the initial sample, while the adsorption kinetics differed less than 5%.
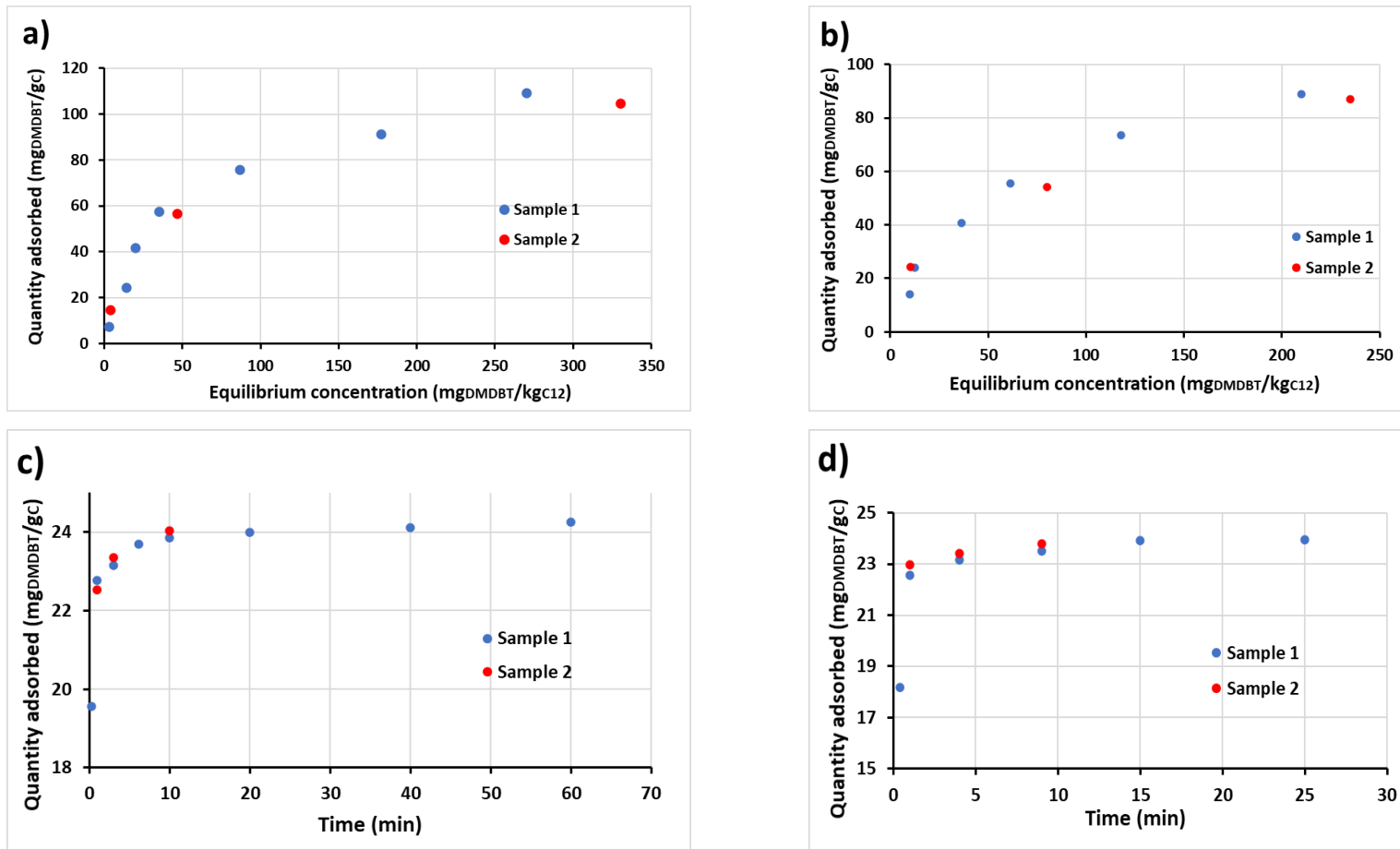
Figure 5.59: Replication of the measurements for the adsorption of DMDBT on ACNFs-KOH-HNO$_3$; a) adsorption isotherms at room temperature; b) adsorption isotherms at 50°C; c) adsorption kinetics at room temperature; d) adsorption kinetics at 50°C. "Sample 2" is the second batch of ACNFs used for validation (red dots), while "sample 1" is the initial batch (blue dots)

5.4.5 The adsorption of DBT: equilibria and kinetics

As a further proof of the potential of ACNFs-KOH-HNO$_3$ to be used for adsorptive desulfurization, the adsorption of dibenzothiophene (DBT) from n-dodecane (C$_{12}$) at room temperature was also studied, following the methodology described in Chapter 4. Prior to these experiments, preliminary experiments for the comparison of the adsorption capacity of ACNFs-KOH-HNO$_3$ with ACNFs-KOH and with commercial activated carbon (Merck 1.02186, BET surface area of 775 m^2/g) were conducted. It was found that the adsorption capacity of ACNFs-KOH-HNO$_3$ was almost 35-45% larger compared to commercial activated carbon and around 20-30% larger compared to ACNFs-KOH (results not shown here). Hence, the presence of acidic O-functional groups favors the adsorption of DBT, as it was also shown for DMDBT. Therefore, it was decided to proceed with using only the ACNFs-KOH-HNO$_3$ for the adsorption experiments.

The adsorption results are presented in Figure 5.59, while the fitting parameters of the Langmuir and Freundlich isotherms are shown in Table 5.19. The fitting of the Langmuir-Freundlich isotherm was less accurate and it is not presented here.

Table 5.19: Fitting parameters for the adsorption equilibrium of DBT

Sample	Temperature (ºC)	Langmuir			Freundlich		
		q_{m-L}	K_L	R^2	K_F	n_F	R^2
ACNFs-KOH-HNO$_3$	22	77.82	0.0217	0.9680	9.62	2.97	0.9602
Units: q_{m-L}: mg$_{DBT}$/g$_C$; K_L: kg$_{C12}$/mg$_{DBT}$; K_F:(mg$_{DMDBT}$/g$_C$)/(mg$_{DBT}$/kg$_{C12}$)$^{1/n}$]; n_F: dimensionless							
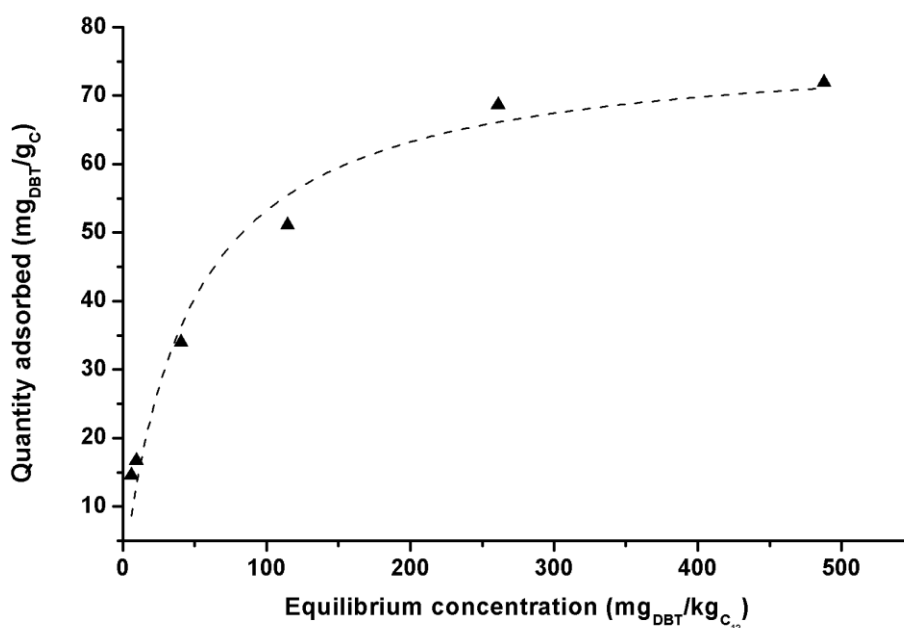
Figure 5.60: Adsorption isotherm of DBT on ACNFs-KOH-HNO$_3$ at room temperature. The dashed line shows the fitted Langmuir isotherm

Similarly to DMDBT, the adsorption results of DBT best fitted to the Langmuir isotherm; however, Freundlich gives also an adequately large R^2. Thus, there is homogeneous monolayer adsorption, although a heterogeneous mechanism is also involved, especially at low surface coverage, when the DBT molecules first adsorb on the sites of higher energy [192]. From the Langmuir model, it is calculated that the maximum adsorption capacity amounts to 77.82 mg$_{DBT}$/g$_C$, which corresponds to 13.5 mgS/g$_C$.

As in the case of DMDBT, comparison with the values found in the literature for the adsorption of DBT on carbon adsorbents can be misleading, as the different solvent, adsorbent dose and the presence of other solutes renders the comparison difficult. Values of maximum adsorption capacity in the range of 300-500 mg$_{DBT}$/g have been reported for the adsorption of DBT from shorter-chain hydrocarbons (hexane, heptane) [214, 215]. However, the removal of refractory sulfur compounds

from lighter hydrocarbons is easier; it has been reported that changing the solvent from n-hexane to n-decane can decrease the maximum adsorption capacity by more than 40% [194]. While hydrocarbons ranging from C6-C8 are used in the majority of studies, there are a few reports in which decane and/or hexadecane have been used; these results are summarized in Table 5.20. Based on these results, it can be concluded that ACNFs-KOH-HNO$_3$ exhibit a remarkable adsorption capacity for DBT, as well.

In addition, a comparison with the adsorption capacity calculated for DMDBT on ACNFs-KOH-HNO$_3$ in terms of mgS/g$_C$ unveils that the adsorption capacity of DBT on ACNFs is comparatively lower (18.2 mgS/g$_C$ vs. 13.5 mgS/g$_C$). The reason is that DMDBT is a larger molecule which creates stronger dispersion forces with the carbon surface. Since the adsorption is based on these dispersion forces, it is expected that the adsorption of DMDBT will be higher compared to DBT, as it has been elsewhere observed [216].

Furthermore, the adsorption kinetics of DBT on ACNFs-KOH-HNO$_3$ at room temperature were studied, following the methodology described in Chapter 4. The results are presented in Figure 5.60 and in Table 5.21. The pseudo-second order model was found to best fit the data, with a rate constant of 0.588 [g$_C$/(mg$_{DBT}$*min)]. Similarly to DMDBT, the kinetics here are also remarkably fast; almost 95% of the final equilibrium capacity is reached after 1.5 min, and 98% after 10 min. These results were compared to reported values in the literature for the fitting of the pseudo-second order model to the adsorption of DBT on carbon adsorbents, and they are summarized in Table 5.22.

Table 5.20: Comparison with values found in the literature for the adsorption of DBT on carbon-based adsorbents. Fitting with Langmuir.

Adsorbent	Solvent	Adsorption Capacity	Ref.
Activated carbon nanofibers	Dodecane	77.82 mg$_{DBT}$/g	This work
Activated carbon	Hexadecane	555.6 μmol/g= 102.3 mg$_{DBT}$/g (in the presence of other solutes)	[217]
Activated carbon	Decane/hexadecane	61.3 μmolS/g= 11.3 mgDBT/g (in the presence of other solutes)	[218]
Activated carbon doped with metals	Diesel	8.1 mgS/g= 46.57 mg$_{DBT}$/g (in the presence of other solutes)	[114]
Carbon aerogel	Hexadecane	15.1 mgS/g= 86.8 mg$_{DBT}$/g	[115]
Activated carbon	n-Decane	152 mg$_{DBT}$/g	[194]
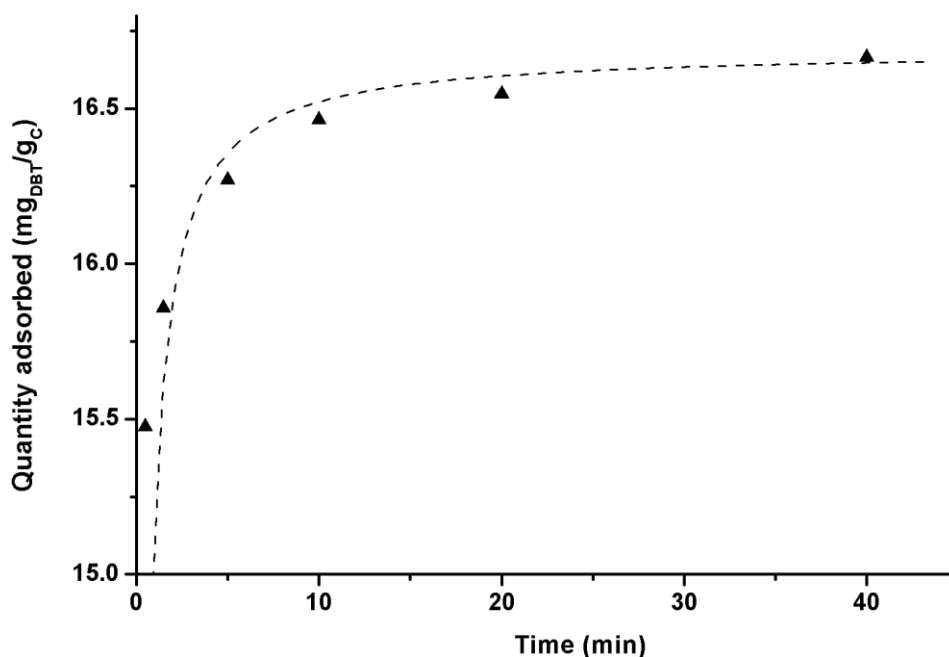
Figure 5.61: Adsorption kinetics of DBT on ACNFs-KOH-HNO$_3$ at room temperature. The dashed line shows the fitted pseudo-second order model

Table 5.21: Kinetic parameters for the adsorption of DBT on ACNFs-KOH-HNO$_3$

Temperature (ºC)	q$_e$-Experimental	Pseudo-1st order			Pseudo-2nd order		
		q$_e$	k$_1$	R^2	q$_e$	k$_2$	R^2
22	16.73	16.36	5.82	0.5282	16.69	0.588	0.9999
Units: q$_e$: mg$_{DBT}$/g$_C$; k$_1$: (min^{-1}); k$_2$: [g$_C$/(mg$_{DBT}$*min)]							

Based on the results exhibited in Table 5.22, it is obvious that the adsorption rates reported here for DBT are much faster than the adsorption rates found in the literature, considering the solvent used in this research (n-dodecane) compared to shorter-chain hydrocarbons. This result, as in the case of DMDBT, is based on the nano-structured morphology of the ACNFs which comprises a very large external surface area (the external surface of the fibers) and a significant number of macro- and

mesopores which render the mass transport of solutes on the carbon surface remarkably fast.

Table 5.22: Kinetics of DBT adsorption: comparison with literature values

Adsorbent	Solvent	Adsorbent dose [(adsorbent mass)/(solution mass or volume)]	Initial concentration of DBT	k_2 [g/(mg*min)]	Shaking speed	Ref.
Activated carbon nanofibers	Dodecane	10 g/L	335 ppm	0.588 (95% of equilibrium after 1.5 min)	105 rpm	This work
Activated carbon	Decane	0.2 g/20 g	7.3 mg$_{DBT}$/L	2.74 [g/(mg*h)]= 0.046 [g/mg*min)]	N/A	[194]
Activated carbon doped with metals	Hexane/ toluene	(not stated clearly)	50 ppm in the presence of benzothiophene	0.394	150	[219]
Activated carbon doped with metals	Petroleum ether	0.75 g/20 mL	500 ppm	(90% of equilibrium in >10 h)	N/A	[220]
Activated carbon	Commercial diesel + acids	50 g/1000 cm^3	593 mg$_{DBT}$/kg	0.06 (total S-compounds)	250	[221]
Carbon microsphere	n-Hexane	5 g/L	200 ppmS= 1150 ppm DBT	0.27-2.02	N/A	[180]
Activated carbon	n-Octane	40 mg/10 mL	(not stated clearly)	0.0180	N/A	[222]
Activated carbon	Hexane/ toluene	0.5 g/20 mL	51 ppm (in the presence of other solutes)	95% removal after 5 min	N/A	[181]
Activated carbons doped with metals	n-Octane	0.5 g/100 mL	300 mg/L	0.001062	N/A	[223]
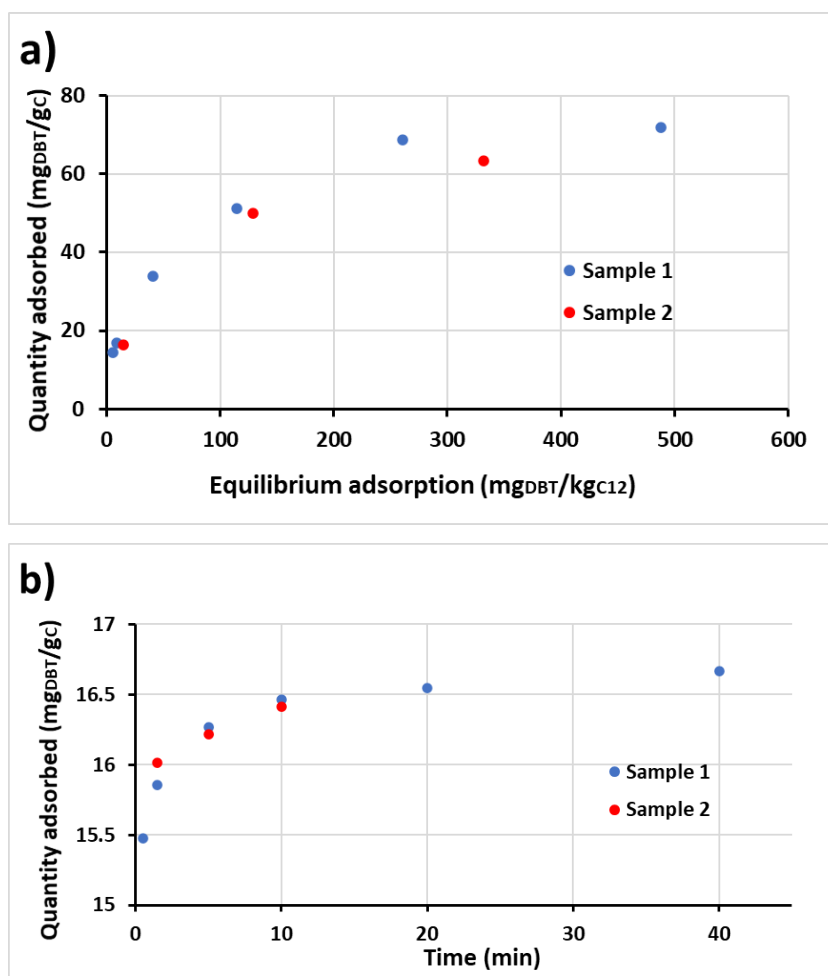
Figure 5.62: Replication of the measurements for the adsorption of DBT on ACNFs-KOH-HNO$_3$ at room temperature; a) equilibrium adsorption and b) adsorption kinetics. "Sample 2" is the second batch of ACNFs used for validation (red dots), while "sample 1" is the initial batch (blue dots)

The experiments for the adsorption of DBT on ACNFs-KOH-HNO$_3$ were validated by replicating some of them using the second sample of carbon nanofibers, according to the procedure described in Section 4.4 and in similar manned as in Section 5.4.4 for DMDBT. The validation results are presented in the two graphs of Figure 5.62 for the equilibria and for the kinetics of adsorption. The reproducibility was satisfactory, as the replication results were lying within a 6% margin compared to the results obtained for the initial sample of ACNFs-KOH-HNO$_3$.

5.4.6 Section summary

In this section, the CNFs and the ACNFs were tested for the adsorptive desulfurization of a model fuel (n-dodecane). Focusing on the adsorption of DMDBT, a chemical compound which can hardly be removed through the traditional hydrodesulfurization process, it was found that ACNFs-KOH-HNO$_3$ exhibit a very high adsorption capacity, accompanied by remarkably fast adsorption kinetics, which are comparatively the fastest kinetics reported in the literature for this process. The process is exothermic and the dominant mechanism is physisorption of DMDBT through π-π interactions with the carbon surface and through acid-base interactions with the acidic O-functional groups. Furthermore, ACNFs-KOH-HNO$_3$ exhibit a high adsorption capacity for DBT, and comparatively the fastest adsorption kinetics that have been reported for the removal of DBT from fossil fuels using carbon-based adsorbents. These results point out the suitability of ACNFs for adsorptive desulfurization, as an alternative method to the current industrial practice.

Chapter 6: Conclusions and Recommendations

The aim of this PhD dissertation research was to successfully produce activated carbon nanofibers (ACNFs) from a blend of a renewable with a waste resource (lignin with recycled PET) that can potentially be used for the adsorptive desulfurization of fossil fuels. First, using a well-established nano-manufacturing method, the electrospinning technique, electrospun nanofibers of varying average diameters were prepared from different lignin/r-PET mass ratios. Then, they were carbonized and activated with different methods for their transformation into ACNFs of very high porosity. Finally, these ACNFs exhibited a very high adsorption capacity for the removal of 4,6-dimethyldibenzothiophene (DMDBT) and dibenzothiophene (DBT) from a model diesel fuel (n-dodecane), combined with remarkably fast kinetics. These results provide a very promising perspective for the development of next-generation adsorbents and for the upgrade of current industrial practice. They also serve as a road-map for the manufacture of high added-value products from widely-available inexpensive resources.

6.1 Preparation and characterization of activated carbon nanofibers from a blend of lignin with r-PET

The first step of this PhD dissertation research focused on the preparation of electrospun nanofibers from a blend of lignin with r-PET (Section 5.1). The electrospinning of lignin alone was not possible due to its relatively low molecular weight; thus, the presence of r-PET was crucial for the formation of nanofibers. Different nanofibrous morphologies of varying average fiber diameter were systematically prepared under different experimental conditions (varying spinning

distance, voltage, flow rate, solution concentration, lignin/r-PET mass ratio). Following a Design-of-Experiments statistical methodology, the effect of each experimental factor on the average fiber diameter was investigated, and it was found that the solution concentration and the spinning distance are the most significant ones. Particularly, it was found that the average fiber diameter decreases when low solution concentration is used (<15%) either at the maximum (20 cm) or at the minimum (~7cm) spinning distance. Low solution concentration translates into low solution viscosity; therefore, the electrospinning jet can elongate more easily and form thinner nanofibers. A more elaborate experimentation under these conditions enabled the preparation of electrospun nanofibers of 50/50 lignin/r-PET with average fiber diameter of 80 nm. This is a significant result as it proves the feasibility to manufacture very thin lignin/r-PET nanofibers. This value is among the lowest reported in the literature for lignin-based electrospun nanofibers, and it is also lower by two orders of magnitude compared to lignin/PET fibers manufactured with other methods. In addition, it is a very important result because such thin nanofibers have a very high external surface area, a property which is crucial in applications such as adsorption, filtration, catalysis and energy storage, in which the nano-dimension plays a key role. Furthermore, although lignin has been combined with other polymers (PAN, PEO, PVA) for the manufacture of nanofibers, this is the first time that it is combined with PET, a very common commodity plastic. Hence, the way of upgrading the value of this major compound of municipal waste through the manufacture of a high added-value product is demonstrated.

Examination of the electrospun nanofibers with ATR-FTIR indicated that the two polymers are blended through weak intermolecular interactions. This observation was corroborated by DSC, through which the miscibility of the lignin with r-PET was

proven by monitoring the differences in their T_g, T_{cc} and T_m at different mass ratios. Furthermore, EDS revealed that the electrospun nanofibers consist of ~54.67%-57.36% C per unit mass depending on the lignin/r-PET mass ratio (90/10-50/50 respectively), while it detected the presence of impurities (ash) derived from the starting lignin.

After the successful preparation and the characterization of electrospun nanofibers, the next step was their carbonization, in order to prepare CNFs of desired morphologies (Section 5.2). Here, it was discovered that the production of CNFs with a well-formed filamentous structure is only possible under certain conditions regarding the lignin/r-PET mass ratio and the average diameter of the precursor electrospun nanofibers. The impact of the nano-dimension on the carbonization process has scarcely been reported in the relevant literature and it is usually overlooked. In this PhD dissertation research it was diligently investigated, by fabricating electrospun fibrous mats of different average fiber diameters ranging from 80 nm to 781 nm from 50/50 lignin/r-PET, and by monitoring their decomposition profiles via thermogravimetry. It was discovered that precursor fibers with average diameter larger than 387 nm show an almost stable decomposition rate (0.24-0.26%/^{o}C) between 180-260°C, the region of lignin decomposition, and yield well-formed carbon fibers. In contrast, minimizing the average diameter of the precursor nanofibrous mats to 80 nm results in the maximum thermal degradation rate (0.40%/^{o}C) and the maximum weight loss between 180-260°C, and in the fusion of nanofibers. The reason is that the heat and mass transfer limitations are not determinant of the process at such low nano-dimensions, as many more macromolecules are located on the surface of the fibers. Therefore, lignin decomposes faster, and as a consequence the mobility of PET macromolecules becomes less restricted and the nanofibers merge with each other.

Furthermore, these observations were extended to higher lignin/r-PET mass ratios up to 90/10. Here it was discovered that there is a synergy between the average fiber diameter and the lignin/r-PET mass ratio. Particularly, when the mass ratio is roughly between 50/50-67/33, there is a considerable degree of melting during the carbonization of precursor nanofibrous mats with low average diameters (lower than 200 nm), due to the differences in the thermal properties between these two polymers. For this range of mass ratios, the fusion of fibers is minimized when the average fiber diameter of the mats is increased above 300-400 nm. In contrast, when the lignin/mass ratio approaches the value of 90/10, then the precursor nanofibers tend to retain their filamentous morphology even when the average fiber diameter is low, therefore, it is feasible to produce lignin-based carbon nanofibrous mats with average diameter close to 100 nm. At such lignin/r-PET mass ratios, the amount of lignin is so high that it prevents the r-PET chains from crystallizing, and thus, the melting can be avoided. These results were confirmed through DSC and XRD. This is the first time that the synergy between the mass ratio and the average fiber diameter has been described as a crucial factor, when carbon nanofibers are prepared from a blend of two polymers. Therefore, these results can serve as a road-map for the manufacture of CNFs with a desired morphology. Controlling the degree of fusion among the CNFs can enhance their mechanical properties and electrical conductivity, although excessive fusion compromises their BET surface area. Moreover, lignin-derived CNFs with average diameter as low as 100 nm have scarcely been reported.

A more detailed characterization of the structure and properties of the produced CNFs was conducted through N_2 physisorption, Raman spectroscopy, XRD and EDS (Section 5.3). CNFs prepared from 90/10 (average fiber diameter ~100-150 nm) and 50/50 lignin/r-PET (average fiber diameter ~400 nm) were compared, while the role

of carbonization temperature was also investigated. The porosity measurements showed that increasing the carbonization temperature to 1000°C enhances the BET surface area of CNFs and also it is desirable to have a high r-PET content. R-PET acts as a template for the promotion of microporosity through its decomposition during carbonization. Hence, CNFs derived from 50/50 mass ratio are mostly microporous and they exhibit the highest BET surface area of 353 m^2/g. Generally, the CNFs have a disordered carbon structure as it was revealed using XRD, Raman spectroscopy and TEM. However, CNFs derived from 90/10 lignin/r-PET mass ratio have more ordered structure than those produced from 50/50. Increasing the carbonization temperature has a positive impact in the development of a higher degree or graphitic order.

In addition, the CNFs were activated using either physical activation through heating with CO_2 or chemical activation through treatment with KOH. Physical activation raises their BET surface area to 686 m^2/g creating a mostly mesoporous structure. In contrast, starting from CNFs derived from 50/50 lignin/r-PET with ~400 nm average fiber diameter, the chemical activation transforms them into ACNFs with BET surface area of 1413 m^2/g, which is a value comparable to that of commercial activated carbon (sample "ACNFs-KOH"). Furthermore, these ACNFs were treated with HNO_3. Although their BET surface area dropped slightly to 1267 m^2/g, their carbon structure was functionalized with acidic oxygen-functional groups as it was confirmed through Boehm titration and through EDS (sample "ACNFs-KOH-HNO$_3$"). Moreover, after the treatment with KOH and then with HNO_3, the activated carbon nanofibers become a very lightweight material with a bulk density of 0.075 g/mL, which is less than half compared to that of commercial activated carbon.

These values of porosity, as well as their nanostructure which translates into a very high specific surface area, render ACNFs potential candidates not only for

adsorption applications, but also for any process in which the high surface area plays an important role in eliminating mass transfer limitations, such as for catalysis and for energy storage.

6.2 Adsorption of S-compounds using ACNFs

One of the goals of this PhD dissertation research was to demonstrate that ACNFs have the potential to be used as efficient adsorbents, especially for the removal of refractory S-compounds from commercial fuels. ACNFs, which were derived from 50/50 lignin/r-PET with ~400 nm average fiber diameter, were tested for the adsorption of DMDBT and DBT from a model diesel fuel (n-dodecane) (Section 5.4). The experiments focused more on the removal of DMDBT, as it is one of the refractory S-compounds for which the traditional industrial practice of hydrodesulfurization is not efficient. After investigation of the equilibrium adsorption at room temperature and the fitting of three different isotherms (Langmuir, Freundlich and Langmuir-Freundlich), it was found that ACNFs-KOH-HNO$_3$ have a very high adsorption capacity of 120.3 mg$_{DMDBT}$/g$_C$, while ACNFs-KOH perform also very well with an adsorption capacity of 95.4 mg$_{DMDBT}$/g$_C$. In contrast, CNFs without activation exhibited very low adsorption capacity (15.73 mg$_{DMDBT}$/g$_C$), as they possess much lower porosity than the other adsorbents. ACNFs-KOH-HNO$_3$ exhibit higher adsorption capacity than ACNFs-KOH despite their relatively lower BET surface area, due to the presence of O-functionalities which interact with the S-compounds through acid-base interactions. Besides the very high adsorption capacity, ACNFs-KOH-HNO$_3$ show remarkably fast adsorption kinetics, as the system reaches 94% of the equilibrium adsorption capacity after only 1 min and 98% after 10 min. These kinetics for the adsorption of DMDBT are comparatively the fastest that have been reported

when a carbon-based adsorbent is used, and they are justified by the nano-structured morphology of ACNFs, which comprises a very large external surface area (the external surface of the fibers) and includes a significant volume of meso- and macro-porosity. These characteristics render the mass transport of solutes on the carbon surface very fast. Besides the adsorption process, this very fast mass transfer is crucial for energy storage applications, for which ACNFs would be a very promising candidate, as well as for catalytic applications. In addition, investigation of the adsorption at higher temperature (50°C) showed that the process is exothermic and its ΔH^{o} value (-8.423 kJ/mol) indicates that the dominant mechanism is physisorption.

ACNFs-KOH-HNO$_3$ were further tested for the adsorption of DBT from n-dodecane at room temperature. In this case they also exhibited a high adsorption capacity of 77.82 mg$_{DBT}$/g$_C$, and again remarkably fast kinetics as the system reaches 95% of the equilibrium adsorption after only 1.5 min and 98% after 10 min. Such fast kinetics would be desirable at an industrial level as they would allow the processing of a large volume of fuels at a shorter time.

These results practically denote that ACNFs are capable of treating fuels with a very high content of S-compounds (~150 ppm S) and of lowering it to less than 15 ppm as most regulations demand. Considering these results, it has been proven that ACNFs are an excellent desulfurization adsorbent. In addition, they are a promising candidate for a variety of other applications in the general field of adsorption, as well as in catalysis and in energy storage.

6.3 Recommendations for further research

Established benchmark materials or long-standing processes can only be replaced when the new ones can be translated into processes that are competitive

enough to justify the cost and disruption of replacing existing industrial practice. In this framework, there is still a lot to be done towards the direction of preparing a material that is ready to be used industrially.

In the first part of this research, the electrospinning method was used for the preparation of electrospun nanofibers using TFA as a solvent. Generally, the electrospinning method offers a low production rate, while TFA is a rather expensive solvent and it should be handled carefully due to its acidic nature. Therefore, there are limitations in the commercial viability of the whole process, and a further assessment of this issue should be carried out. Many electrospinning setups working in parallel and a recycling of the solvent could be possible solutions.

In terms of the production of ACNFs, different activation methods could be investigated, e.g. with other chemical agents such as $ZnCl_2$, or physical activation with H_2O. Different activation methods could give rise to different textural properties, which would add to the versatility of the ACNFs. Moreover, doping with metals would be a very interesting modification, which would provide the ACNFs with catalytic properties and possibly even better performance in desulfurization. Finally, the ACNFs produced here could probably be a promising material for the manufacture of electrodes for energy storage devices. Their large surface area which minimizes mass transfer limitations, would probably make a difference in such devices.

Regarding the adsorptive desulfurization, an important issue is always the selectivity of S-compounds against other molecules such as aromatics. Generally, the O-functional groups of the carbon surface improve their selectivity, but this should be tested, and possibly improved with methods that have been proposed elsewhere, for example through doping with transition metals. Besides batch adsorption, adsorption at dynamic conditions should also be investigated for the determination of

breakthrough curves, as this is closer to practical industrial applications. Here, it was proven that ACNFs show excellent adsorption capacity for the adsorption of S-compounds from a model diesel fuel. However, experimentation with commercial diesel is necessary, as this is a complex mixture of hydrocarbons and other compounds. Finally, the regeneration of the adsorbent is another important issue that needs further investigation.

References

[1]   L. Zhang, A. Aboagye, A. Kelkar, C. Lai, H. Fong, A review: Carbon nanofibers from electrospun polyacrylonitrile and their applications, J. Mater. Sci. 49 (2014) 463-480. https://doi.org/10.1007/s10853-013-7705-y.

[2]   W. Li, M. Li, K.R. Adair, X. Sun, Y. Yu, Carbon nanofiber-based nanostructures for lithium-ion and sodium-ion batteries, J. Mater. Chem. A. 5 (2017) 13882-13906. https://doi.org/10.1039/c7ta02153d.

[3]   B. Zhang, F. Kang, J.M. Tarascon, J.K. Kim, Recent advances in electrospun carbon nanofibers and their application in electrochemical energy storage, Prog. Mater. Sci. 76 (2016) 319-380. https://doi.org/10.1016/j.pmatsci.2015.08.002.

[4]   J.F. Vivo-Vilches, A. Celzard, V. Fierro, I. Devin-Ziegler, N. Brosse, A. Dufour, M. Etienne, Lignin-based carbon nanofibers as electrodes for vanadium redox couple electrochemistry, Nanomaterials. 9 (2019) 1-13. https://doi.org/10.3390/nano9010106.

[5]   P. Figueiredo, K. Lintinen, J.T. Hirvonen, M.A. Kostiainen, H.A. Santos, Properties and chemical modifications of lignin: Towards lignin-based nanomaterials for biomedical applications, Prog. Mater. Sci. 93 (2018) 233-269. https://doi.org/10.1016/j.pmatsci.2017.12.001.

[6]   S. Laurichesse, L. Avérous, Chemical modification of lignins: Towards biobased polymers, Prog. Polym. Sci. 39 (2014) 1266-1290. https://doi.org/10.1016/j.progpolymsci.2013.11.004.

[7]   D. Kai, M.J. Tan, P.L. Chee, Y.K. Chua, Y.L. Yap, X.J. Loh, Towards lignin-based functional materials in a sustainable world, Green Chem. 18 (2016) 1175-1200. https://doi.org/10.1039/c5gc02616d.

[8]   C.-Q. Wang, H. Wang, Y.-N. Liu, Separation of polyethylene terephthalate from municipal waste plastics by froth flotation for recycling industry., Waste Manag. 35 (2015) 42-47. https://doi.org/10.1016/j.wasman.2014.09.025.

[9]   USA Environmental Protection Agency. https://www.epa.gov/diesel-fuel-standards/diesel-fuel-standards-and-rulemakings, (accessed on 28/05/2020).

[10]   Transport Policy. https://www.transportpolicy.net/standard/eu-fuels-diesel-and-gasoline/, (accessed on 28/05/2020).

[11]   Emirates Authority for Standardization and Metrology. https://www.esma.gov.ae/ar-ae/Pages/default.aspx, (accessed on 28/05/2020).

[12]   C. Song, U. Turaga, X. Ma, Desulfurization, in: S. Lee (1st Ed.), Encyclopedia of Chemical Processing, Taylor & Francis, New York, 2006.

[13] W. Ahmad, Sulfur in Petroleum, in: T.A. Saleh 1st Ed., Appying Nanotechnology to Desulfurization Process in Petroleum Engineering, Engineering Science Reference (IGI Global), Hershey, 2016.

[14] A. Ogale, J. Zhang Meng, J. Jin, Recent advances in carbon fibers derived from biobased precursors, J. Appl. Polym. Sci. 133 (2016) 44212. https://doi.org/10.1002/app.44212.

[15] H. Marsh, F. Rodríguez-Reinoso, Section 2.3, in: Activated Carbon, 1st ed., Elsevier, 2006, pp. 17-22. https://doi.org/https://doi.org/10.1016/B978-008044463-5/50016-9.

[16] H. Marsh, F. Rodríguez-Reinoso, Chapter 3, in: Activated Carbon, 1st ed., Elsevier, 2006, pp. 87-142. https://doi.org/10.1016/B978-0-08-044463-5.50017-0.

[17] F. Ko, Y. Wan, Chapter 3, in: Introduction to Nanofiber Materials, 1st ed., Cambridge University Press, Cambridge, 2014, pp. 45-64.

[18] S. Kim, B. Bajaj, C.K. Byun, S.J. Kwon, H.I. Joh, K.B. Yi, S. Lee, Preparation of flexible zinc oxide/carbon nanofiber webs for mid-temperature desulfurization, Appl. Surf. Sci. 320 (2014) 218-224. https://doi.org/10.1016/j.apsusc.2014.09.093.

[19] B. Bajaj, H.I. Joh, S.M. Jo, J.H. Park, K.B. Yi, S. Lee, Enhanced reactive H_2S adsorption using carbon nanofibers supported with Cu/Cu_xO nanoparticles, Appl. Surf. Sci. 429 (2018) 253-257. https://doi.org/10.1016/j.apsusc.2017.06.280.

[20] B. Scrosati, J. Hassoun, Y.K. Sun, Lithium-ion batteries. A look into the future, Energy Environ. Sci. 4 (2011) 3287-3295. https://doi.org/10.1039/c1ee01388b.

[21] L. Borchardt, M. Oschatz, S. Kaskel, Tailoring porosity in carbon materials for supercapacitor applications, Mater. Horizons. 1 (2014) 157-168. https://doi.org/10.1039/c3mh00112a.

[22] M. Inagaki, Y. Yang, F. Kang, Carbon nanofibers prepared via electrospinning, Adv. Mater. 24 (2012) 2547-2566. https://doi.org/10.1002/adma.201104940.

[23] I. Dallmeyer, F. Ko, J.F. Kadla, Electrospinning of technical lignins for the production of fibrous networks, J. Wood Chem. Technol. 30 (2010) 315-329. https://doi.org/10.1080/02773813.2010.527782.

[24] C. Lai, Z. Zhou, L. Zhang, X. Wang, Q. Zhou, Y. Zhao, Y. Wang, X.F. Wu, Z. Zhu, H. Fong, Free-standing and mechanically flexible mats consisting of electrospun carbon nanofibers made from a natural product of alkali lignin as binder-free electrodes for high-performance supercapacitors, J. Power Sources. 247 (2014) 134-141. https://doi.org/10.1016/j.jpowsour.2013.08.082.

[25] H.G. Wang, S. Yuan, D.L. Ma, X.B. Zhang, J.M. Yan, Electrospun materials for lithium and sodium rechargeable batteries: From structure evolution to electrochemical performance, Energy Environ. Sci. 8 (2015) 1660-1681. https://doi.org/10.1039/c4ee03912b.

[26] C.L. Zhang, S.H. Yu, Nanoparticles meet electrospinning: Recent advances and future prospects, Chem. Soc. Rev. 43 (2014) 4423-4448. https://doi.org/10.1039/c3cs60426h.

[27] Q. Fan, C. Ma, L. Wu, C. Wei, H. Wang, Y. Song, J. Shi, Preparation of cellulose acetate derived carbon nanofibers by $ZnCl_2$ activation as a supercapacitor electrode, RSC Adv. 9 (2019) 6419-6428. https://doi.org/10.1039/c8ra07587e.

[28] J. Cai, H. Niu, H. Wang, H. Shao, J. Fang, J. He, H. Xiong, C. Ma, T. Lin, High-performance supercapacitor electrode from cellulose-derived, inter-bonded carbon nanofibers, J. Power Sources. 324 (2016) 302-308. https://doi.org/10.1016/j.jpowsour.2016.05.070.

[29] E. Frank, L.M. Steudle, D. Ingildeev, J.M. Spörl, M.R. Buchmeiser, Carbon fibers: precursor systems, processing, structure, and properties, Angew. Chemie Int. Ed. 53 (2014) 5262-5298. https://doi.org/10.1002/anie.201306129.

[30] M. Lallave, J. Bedia, R. Ruiz-Rosas, J. Rodríguez-Mirasol, T. Cordero, J.C. Otero, M. Marquez, A. Barrero, I.G. Loscertales, Filled and hollow carbon nanofibers by coaxial electrospinning of Alcell lignin without binder polymers, Adv. Mater. 19 (2007) 4292-4296. https://doi.org/10.1002/adma.200700963.

[31] P. Schlee, O. Hosseinaei, D. Baker, A. Landmer, P. Tomani, M. Mostazo-Lopez, D. Cazorla-Amoros, S. Herou, M.-M. Titirici, From waste to wealth-from kraft lignin to free-standing supercapacitors, Carbon 145 (2019) 470-480. https://doi.org/https://doi.org/10.1016/j.carbon.2019.01.035.

[32] F.J. García-Mateos, T. Cordero-Lanzac, R. Berenguer, E. Morallón, D. Cazorla-Amorós, J. Rodríguez-Mirasol, T. Cordero, Lignin-derived Pt supported carbon (submicron)fiber electrocatalysts for alcohol electro-oxidation, Appl. Catal. B Environ. 211 (2017) 18-30. https://doi.org/10.1016/j.apcatb.2017.04.008.

[33] F.J. García-Mateos, R. Berenguer, M.J. Valero-Romero, J. Rodríguez-Mirasol, T. Cordero, Phosphorus functionalization for the rapid preparation of highly nanoporous submicron-diameter carbon fibers by electrospinning of lignin solutions, J. Mater. Chem. A. 6 (2018) 1219-1233. https://doi.org/10.1039/c7ta08788h.

[34] X. You, J. Duan, K. Koda, T. Yamada, Y. Uraki, Preparation of electric double layer capacitors (EDLCs) from two types of electrospun lignin fibers, Holzforschung. 70 (2016) 661-671. https://doi.org/10.1515/hf-2015-0175.

[35] R. Ruiz-Rosas, J. Bedia, M. Lallave, I.G. Loscertales, A. Barrero, J. Rodriguez-Mirasol, T. Cordero, J. Rodríguez-Mirasol, T. Cordero, The production of submicron diameter carbon fibers by the electrospinning of lignin, Carbon 48 (2010) 696-705. https://doi.org/doi:10.1016/j.carbon.2009.10.014.

[36] N. Dalton, R.P. Lynch, M.N. Collins, M. Culebras, Thermoelectric properties of electrospun carbon nanofibres derived from lignin, Int. J. Biol. Macromol. 121 (2019) 472-479. https://doi.org/10.1016/j.ijbiomac.2018.10.051.

[37] M. Cho, M. Karaaslan, H. Wang, S. Renneckar, Greener transformation of lignin into ultralight multifunctional materials, J. Mater. Chem. A. 6 (2018) 20973-20981. https://doi.org/10.1039/C8TA07802E.

[38] A. Duval, M. Lawoko, A review on lignin-based polymeric, micro- and nano-structured materials, React. Funct. Polym. 85 (2014) 78-96. https://doi.org/10.1016/j.reactfunctpolym.2014.09.017.

[39] E.P. Feofilova, I.S. Mysyakina, Lignin: Chemical structure, biodegradation, and practical application (a review), Appl. Biochem. Microbiol. 52 (2016) 573-581. https://doi.org/10.1134/S0003683816060053.

[40] S. Hu, Y.-L. Hsieh, Ultrafine microporous and mesoporous activated carbon fibers from alkali lignin.pdf, J. Mater. Chem. A. 1 (2013) 11279. https://doi.org/10.1039/c3ta12538f.

[41] D.A. Baker, T.G. Rials, Recent advances in low-cost carbon fiber manufacture from lignin, J. Appl. Polym. Sci. 130 (2013) 713-728. https://doi.org/10.1002/app.39273.

[42] X. Wang, W. Zhang, M. Chen, X. Zhou, Electrospun enzymatic hydrolysis lignin-based carbon nanofibers as binder-free supercapacitor electrodes with high performance, Polymers 10 (2018) 1306. https://doi.org/10.3390/polym10121306.

[43] C. Rodríguez Correa, M. Stollovsky, T. Hehr, Y. Rauscher, B. Rolli, A. Kruse, Influence of the carbonization process on activated carbon properties from lignin and lignin-rich biomasses, ACS Sustain. Chem. Eng. 5 (2017) 8222-8233. https://doi.org/10.1021/acssuschemeng.7b01895.

[44] C. Mohabeer, L. Abdelouahed, S. Marcotte, B. Taouk, Comparative analysis of pyrolytic liquid products of beech wood, flax shives and woody biomass components, J. Anal. Appl. Pyrolysis. 127 (2017) 269-277. https://doi.org/10.1016/j.jaap.2017.07.025.

[45] X. You, K. Koda, T. Yamada, Y. Uraki, Preparation of electrode for electric double layer capacitor from electrospun lignin fibers, Holzforschung 69 (2015) 1097-1106. https://doi.org/10.1515/hf-2014-0262.

[46] D.I. Choi, J.-N. Lee, J. Song, P.-H. Kang, J.-K. Park, Y.M. Lee, Fabrication of polyacrylonitrile/lignin-based carbon nanofibers for high-power lithium ion battery anodes, J. Solid State Electrochem. 17 (2013) 2471-2475. https://doi.org/10.1007/s10008-013-2112-5.

[47] J. Jin, B.J. Yu, Z.Q. Shi, C.Y. Wang, C. Bin Chong, Lignin-based electrospun carbon nanofibrous webs as free-standing and binder-free electrodes for sodium ion batteries, J. Power Sources. 272 (2014) 800-807. https://doi.org/10.1016/j.jpowsour.2014.08.119.

[48] Z. Shi, G. Jin, J. Wang, J. Zhang, Free-standing, welded mesoporous carbon nanofibers as anode for high-rate performance Li-ion batteries, J. Electroanal. Chem. 795 (2017) 26-31. https://doi.org/10.1016/j.jelechem.2017.03.047.

[49] R.A. Perera Jayawickramage, K.J. Balkus, J.P. Ferraris, Binder free carbon nanofiber electrodes derived from polyacrylonitrile-lignin blends for high performance supercapacitors, Nanotechnology 30 (2019) 355402 https://doi.org/10.1088/1361-6528/ab2274.

[50] S.I. Yun, S.H. Kim, D.W. Kim, Y.A. Kim, B.H. Kim, Facile preparation and capacitive properties of low-cost carbon nanofibers with ZnO derived from lignin and pitch as supercapacitor electrodes, Carbon 149 (2019) 637-645. https://doi.org/10.1016/j.carbon.2019.04.105.

[51] D. Lei, X.D. Li, M.K. Seo, M.S. Khil, H.Y. Kim, B.S. Kim, $NiCo_2O_4$ nanostructure-decorated PAN/lignin based carbon nanofiber electrodes with excellent cyclability for flexible hybrid supercapacitors, Polymer 132 (2017) 31-40. https://doi.org/10.1016/j.polymer.2017.10.051.

[52]   Z. Dai, P.G. Ren, Y.L. Jin, H. Zhang, F. Ren, Q. Zhang, Nitrogen-sulphur Co-doped graphenes modified electrospun lignin/polyacrylonitrile-based carbon nanofiber as high performance supercapacitor, J. Power Sources 437 (2019) 226937. https://doi.org/10.1016/j.jpowsour.2019.226937.

[53]   S. Demiroğlu Mustafov, A.K. Mohanty, M. Misra, M.Ö. Seydibeyoğlu, Fabrication of conductive Lignin/PAN carbon nanofiber with enhanced graphene for the modified electrode, Carbon 147 (2019) 262-275. https://doi.org/10.1016/j.carbon.2019.02.058.

[54]   C.W. Park, W.J. Youe, S.Y. Han, Y.S. Kim, S.H. Lee, Characteristics of carbon nanofibers produced from lignin/polyacrylonitrile (PAN)/kraft lignin-g-PAN copolymer blends electrospun nanofibers, Holzforschung 71 (2017) 743-750. https://doi.org/10.1515/hf-2017-0024.

[55]   A. Ma, L. Zhou, J. Chang, Conversion of lignin-nanofibers to CNFs, Nano 10 (2015) 1-9. https://doi.org/10.1142/S1793292015500927.

[56]   X. Xu, J. Zhou, L. Jiang, G. Lubineau, Y. Chen, X.F. Wu, R. Piere, Porous core-shell carbon fibers derived from lignin and cellulose nanofibrils, Mater. Lett. 109 (2013) 175-178. https://doi.org/10.1016/j.matlet.2013.07.082.

[57]   X. Xu, J. Zhou, L. Jiang, G. Lubineau, S.A. Payne, D. Gutschmidt, Lignin-based carbon fibers: Carbon nanotube decoration and superior thermal stability, Carbon 80 (2014) 91-102. https://doi.org/10.1016/j.carbon.2014.08.042.

[58]   W.J. Youe, S.M. Lee, S.S. Lee, S.H. Lee, Y.S. Kim, Characterization of carbon nanofiber mats produced from electrospun lignin-g-polyacrylonitrile copolymer, Int. J. Biol. Macromol. 82 (2016) 497-504. https://doi.org/10.1016/j.ijbiomac.2015.10.022.

[59]   Z. Dai, X. Shi, H. Liu, H. Li, Y. Han, J. Zhou, High-strength lignin-based carbon fibers via a low-energy method, RSC Adv. 8 (2018) 1218-1224. https://doi.org/10.1039/c7ra10821d.

[60]   R. Ding, H. Wu, M. Thunga, N. Bowler, M.R. Kessler, Processing and characterization of low-cost electrospun carbon fibers from organosolv lignin/polyacrylonitrile blends, Carbon 100 (2016) 126-136. https://doi.org/10.1016/j.carbon.2015.12.078.

[61]   R. Zhang, Q. Du, L. Wang, Z. Zheng, L. Guo, X. Zhang, X. Yang, H. Yu, Unlocking the response of lignin structure for improved carbon fiber production and mechanical strength, Green Chem. 21 (2019) 4981-4987. https://doi.org/10.1039/c9gc01632e.

[62] R.J. Beck, Y. Zhao, H. Fong, T.J. Menkhaus, Electrospun lignin carbon nanofiber membranes with large pores for highly efficient adsorptive water treatment applications, J. Water Process Eng. 16 (2017) 240-248. https://doi.org/10.1016/j.jwpe.2017.02.002.

[63] X. Ma, P. Kolla, Y. Zhao, A.L. Smirnova, H. Fong, Electrospun lignin-derived carbon nanofiber mats surface-decorated with MnO_2 nanowhiskers as binder-free supercapacitor electrodes with high performance, J. Power Sources. 325 (2016) 541-548. https://doi.org/10.1016/j.jpowsour.2016.06.073.

[64] X. Ma, A.L. Smirnova, H. Fong, Flexible lignin-derived carbon nanofiber substrates functionalized with iron (III) oxide nanoparticles as lithium-ion battery anodes, Mater. Sci. Eng. B Solid-State Mater. Adv. Technol. 241 (2019) 100-104. https://doi.org/10.1016/j.mseb.2019.02.013.

[65] C. Lai, P. Kolla, Y. Zhao, H. Fong, A.L. Smirnova, Lignin-derived electrospun carbon nanofiber mats with supercritically deposited Ag nanoparticles for oxygen reduction reaction in alkaline fuel cells, Electrochim. Acta. 130 (2014) 431-438. https://doi.org/10.1016/j.electacta.2014.03.006.

[66] E. Stojanovska, E.S. Pampal, A. Kilic, M. Quddus, Z. Candan, Developing and characterization of lignin-based fibrous nanocarbon electrodes for energy storage devices, Compos. Part B Eng. 158 (2019) 239-248. https://doi.org/10.1016/j.compositesb.2018.09.072.

[67] R.A. Perera Jayawickramage, J.P. Ferraris, High performance supercapacitors using lignin based electrospun carbon nanofiber electrodes in ionic liquid electrolytes, Nanotechnology 30 (2019) 155402. https://doi.org/https://doi.org/10.1088/1361-6528/aafe95.

[68] M. Ago, M. Borghei, J.S. Haataja, O.J. Rojas, Mesoporous carbon soft-templated from lignin nanofiber networks: Microphase separation boosts supercapacitance in conductive electrodes, RSC Adv. 6 (2016) 85802-85810. https://doi.org/10.1039/c6ra17536h.

[69] J. Roman, W. Neri, A. Derré, P. Poulin, Electrospun lignin-based twisted carbon nanofibers for potential microelectrodes applications, Carbon 145 (2019) 556-564. https://doi.org/10.1016/j.carbon.2019.01.036.

[70] Y. Zhao, Y. Liu, C. Tong, J. Ru, B. Geng, Z. Ma, H. Liu, L. Wang, Flexible lignin-derived electrospun carbon nanofiber mats as a highly efficient and binder-free counter electrode for dye-sensitized solar cells, J Mater Sci. 53 (2018) 7637-7647. https://doi.org/https://doi.org/10.1007/s10853-018-2059-0.

[71] M. Song, L. Yu, B. Song, F. Meng, X. Tang, Alkali promoted the adsorption of toluene by adjusting the surface properties of lignin-derived carbon fibers, Environ. Sci. Pollut. Res. 26 (2019) 22284-22294. https://doi.org/10.1007/s11356-019-05456-9.

[72] F. Meng, M. Song, Y. Wei, Y. Wang, The contribution of oxygen-containing functional groups, Environ. Sci. Pollut. Reseach. 26 (2019) 7195-7204. https://doi.org/https://doi.org/10.1007/s11356-019-04190-6.

[73] M. Song, W. Zhang, Y. Chen, J. Luo, J. Crittenden, The preparation and performance of lignin-based activated carbon fiber adsorbents for treating gaseous streams, Front. Chem. Sci. Eng. 11 (2017) 328-337. https://doi.org/https://doi.org/10.1007/s11705-017-1646-y.

[74] Y. Wei, M. Song, L. Yu, X. Tang, Preparation of ZnO-loaded lignin-based carbon fiber for the electrocatalytic oxidation of hydroquinone, Catalysts. 7 (2017) 180. https://doi.org/10.3390/catal7060180.

[75] B. Yu, A. Gele, L. Wang, Iron oxide/lignin-based hollow carbon nanofibers nanocomposite as an application electrode materials for supercapacitors, Int. J. Biol. Macromol. 118 (2018) 478-484. https://doi.org/10.1016/j.ijbiomac.2018.06.088.

[76] I. Dallmeyer, L.T. Lin, Y. Li, F. Ko, J.F. Kadla, Preparation and characterization of interconnected, kraft lignin-based carbon fibrous materials by electrospinning, Macromol. Mater. Eng. 299 (2014) 540-551. https://doi.org/10.1002/mame.201300148.

[77] S. Hu, F. Jiang, Y.-L. Hsieh, 1D lignin-based solid acid catalysts for cellulose hydrolysis to glucose and nanocellulose, ACS Sustain. Chem. Eng. 3 (2015) 2566-2574. https://doi.org/DOI: 10.1021/acssuschemeng.5b00780.

[78] S. Aslanzadeh, B. Ahvazi, Y. Boluk, C. Ayranci, Carbon fiber production from electrospun sulfur free softwood lignin precursors, J. Eng. Fiber. Fabr. 12 (2017) 33-43. https://doi.org/10.1177/155892501701200405.

[79] J. Choi, H. Yang, F. Ko, S. Chan, W. Chung, S.S. Kim, Fabrication and characterization of palladium nanoparticle reinforced multifunctional lignin nanofiber mat, J. Nanosci. Nanotechnol. 16 (2016) 11046-11051. https://doi.org/10.1166/jnn.2016.13287.

[80] P. Schlee, S. Herou, R. Jervis, P.R. Shearing, D.J.L. Brett, D. Baker, O. Hosseinaei, P. Tomani, M.M. Murshed, Y. Li, M.J. Mostazo-López, D. Cazorla-Amorós, A.B. Jorge Sobrido, M.M. Titirici, Free-standing supercapacitors from Kraft lignin nanofibers with remarkable volumetric energy density, Chem. Sci. 10 (2019) 2980-2988. https://doi.org/10.1039/c8sc04936j.

[81] X. Shi, X. Wang, B. Tang, Z. Dai, K. Chen, J. Zhou, Impact of lignin extraction methods on microstructure and mechanical properties of lignin-based carbon fibers, J. Appl. Polym. Sci. 135 (2018) 1-7. https://doi.org/10.1002/app.45580.

[82] S.X. Wang, L. Yang, L.P. Stubbs, X. Li, C. He, Lignin-derived fused electrospun carbon fibrous mats as high performance anode materials for lithium ion batteries, ACS Appl. Mater. Interfaces. 5 (2013) 12275-12282. https://doi.org/10.1021/am4043867.

[83] L. Wang, A. Gele, Y. Sun, Preparation of iron oxide particle-decorated lignin-based carbon nanofibers as electrode material for pseudocapacitor, J. Wood Chem. Technol. 37 (2017) 423-432. https://doi.org/10.1080/02773813.2017.1310900.

[84] M. Cho, M. Karaaslan, S. Chowdhury, F. Ko, S. Renneckar, Skipping oxidative thermal stabilization for lignin-based carbon nanofibers, ACS Sustain. Chem. Eng. 6 (2018) 6434-6444. https://doi.org/10.1021/acssuschemeng.8b00209.

[85] S. Hu, S. Zhang, N. Pan, Y. Lo Hsieh, High energy density supercapacitors from lignin derived submicron activated carbon fibers in aqueous electrolytes, J. Power Sources. 270 (2014) 106-112. https://doi.org/10.1016/j.jpowsour.2014.07.063.

[86] C. Ma, Z. Li, J. Li, Q. Fan, L. Wu, J. Shi, Y. Song, Lignin-based hierarchical porous carbon nanofiber films with superior performance in supercapacitors, Appl. Surf. Sci. 456 (2018) 568-576. https://doi.org/10.1016/j.apsusc.2018.06.189.

[87] Z. Guo, Z. Liu, L. Ye, K. Ge, T. Zhao, The production of lignin-phenol-formaldehyde resin derived carbon fibers stabilized by BN preceramic polymer, Mater. Lett. 142 (2015) 49-51. https://doi.org/10.1016/j.matlet.2014.11.068.

[88] H. Jia, N. Sun, M. Dirican, Y. Li, C. Chen, P. Zhu, C. Yan, J. Zang, Electrospun kraft lignin-cellulose acetate derived a nano carbon network as an anode for high-performance sodium-ion batteries, ACS Appl. Mater. Interfaces. 10 (2018) 44368-44375. https://doi.org/https://doi.org/10.1021/acsami.8b13033.

[89] M. Schreiber, S. Vivekanandhan, A.K. Mohanty, M. Misra, Iodine treatment of lignin−cellulose acetate electrospun fibers: enhancement of green fiber carbonization, ACS Sustain. Chem. Eng. 3 (2015) 33-41. https://doi.org/https://doi.org/10.1021/sc500481k.

[90] S. Kubo, J.F. Kadla, Kraft lignin/poly(ethylene oxide) blends: Effect of lignin structure on miscibility and hydrogen bonding, J. Appl. Polym. Sci. 98 (2005) 1437-1444. https://doi.org/10.1002/app.22245.

[91] L. Deng, R.J. Young, I.A. Kinloch, Y. Zhu, S.J. Eichhorn, Carbon nanofibres produced from electrospun cellulose nanofibres, Carbon 58 (2013) 66-75. https://doi.org/10.1016/j.carbon.2013.02.032.

[92] J.F. Kadla, S. Kubo, R.D. Gilbert, R.A. Venditti, Lignin-based Carbon Fibers, in: T.Q. Hu 1st Ed., Chemical Modification and Proper Usage of Lignin, Kluwer Academic/Plenum Publishers, Philadelphia, 2002.

[93] S. Kubo, J.F. Kadla, Lignin-based carbon fibers: Effect of synthetic polymer blending on fiber properties, J. Polym. Environ. 13 (2005) 97-105. https://doi.org/10.1007/s10924-005-2941-0.

[94] J.F. Kadla, S. Kubo, Lignin-based polymer blends: analysis of intermolecular interactions in lignin-synthetic polymer blends, Compos. Part A Appl. Sci. Manuf. 35 (2004) 395-400. https://doi.org/10.1016/j.compositesa.2003.09.019.

[95] A.L. Compere, W.L. Griffith, C.F. Leitten, J.M. Pickel, Evaluation of lignin from alkaline-pulped hardwood black liquor, 2005. http://citeseerx.ist.psu.edu/viewdoc/download?doi=10.1.1.576.5845&rep=rep1&type=pdf, (accessed on 28/05/2020)

[96] NAPCOR-National Association for PET Container Resources (USA). http://www.napcor.com/PET/landing_petrecycling.html (accessed on 28/05/2020).

[97] M. Fahim, T. Al-Sahhaf, A. Elkilani, Chapter 3, in: Fundamentals of Petroleum Refining, 1st ed., Elsevier, 2010, pp. 33-67. https://doi.org/10.1016/C2009-0-16348-1.

[98] European Union Legislation. https://eur-lex.europa.eu/legal-content/EN/TXT/?uri=CELEX:32009L0030, (accessed on 28/05/2020).

[99] USA Environmental Protection Agency. https://www.epa.gov/gasoline-standards/gasoline-sulfur, (accessed on 28/05/2020).

[100] Y. Sano, T. Karasawa, M. Inomata, I. Mochida, J. Miyawaki, S.H. Yoon, Ultra-deep desulfurization process of diesel fuel with adsorption treatment, J. Japan Pet. Inst. 62 (2019) 61-66. https://doi.org/10.1627/jpi.62.61.

[101] J. Jing Li, H. Lu, X. dong Tang, M. Zhou, N. Hu, A novel method of preparation-adsorption desulfurization process for dibenzothiophene over sawdust-derived nickel/activated carbon, Pet. Sci. Technol. 36 (2018) 456-462. https://doi.org/10.1080/10916466.2018.1430152.

[102] International Maritime Organization. http://www.imo.org/en/MediaCentre/HotTopics/Pages/Sulphur-2020.aspx, (accessed on 28/05/2020).

[103] M.K. Nazal, M. Khaled, M.A. Atieh, I.H. Aljundi, G.A. Oweimreen, A.M. Abulkibash, The nature and kinetics of the adsorption of dibenzothiophene in model diesel fuel on carbonaceous materials loaded with aluminum oxide particles, Arab. J. Chem. (2015). https://doi.org/10.1016/j.arabjc.2015.12.003.

[104] S. Bigdeli, S. Fatemi, Fast carbon nanofiber growth on the surface of activated carbon by microwave irradiation: A modified nano-adsorbent for deep desulfurization of liquid fuels, Chem. Eng. J. 269 (2015) 306-315. https://doi.org/10.1016/j.cej.2015.01.059.

[105] M. Khaled, Adsorption performance of multiwall carbon nanotubes and graphene oxide for removal of thiophene and dibenzothiophene from model diesel fuel, Res. Chem. Intermed. 41 (2015) 9817-9833. https://doi.org/10.1007/s11164-015-1986-5.

[106] A. Zhou, X. Ma, C. Song, Effects of oxidative modification of carbon surface on the adsorption of sulfur compounds in diesel fuel, Appl. Catal. B Environ. 87 (2009) 190-199. https://doi.org/10.1016/j.apcatb.2008.09.024.

[107] S.P. Hernandez, D. Fino, N. Russo, High performance sorbents for diesel oil desulfurization, Chem. Eng. Sci. 65 (2010) 603-609. https://doi.org/10.1016/j.ces.2009.06.050.

[108] S.P. Lonkar, V. V. Pillai, S. Stephen, A. Abdala, V. Mittal, Facile In Situ Fabrication of Nanostructured Graphene-CuO Hybrid with Hydrogen Sulfide Removal Capacity, Nano-Micro Lett. 8 (2016) 312-319. https://doi.org/10.1007/s40820-016-0090-8.

[109] S.S. Meshkat, A. Rashidi, O. Tavakoli, Removal of mercaptan from natural gas condensate using N-doped carbon nanotube adsorbents: Kinetic and DFT study, J. Nat. Gas Sci. Eng. 55 (2018) 288-297. https://doi.org/10.1016/j.jngse.2018.04.036.

[110] R. Menzel, D. Iruretagoyena, Y. Wang, S.M. Bawaked, M. Mokhtar, S.A. Al-Thabaiti, S.N. Basahel, M.S.P. Shaffer, Graphene oxide/mixed metal oxide hybrid materials for enhanced adsorption desulfurization of liquid hydrocarbon fuels, Fuel. 181 (2016) 531-536. https://doi.org/10.1016/j.fuel.2016.04.125.

[111] K. Yang, Y. Yan, W. Chen, H. Kang, Y. Han, W. Zhang, Y. Fan, Z. Li, Nut-like MOF/hydroxylated graphene hybrid materials for adsorptive desulfurization of thiophene, RSC Adv. 8 (2018) 23671-23678. https://doi.org/10.1039/c8ra03834a.

[112] H. Ma, X. Sun, M. Wang, J. Zhang, Regenerable CuO/γ-Al$_2$O$_3$-reduced graphene oxide adsorbent with a high adsorption capacity for dibenzothiophene from model diesel oil, Ind. Eng. Chem. Res. (2018) acs.iecr.8b00407. https://doi.org/10.1021/acs.iecr.8b00407.

[113] F. Karami, M. Khanmohammadi, A.B. Garmarudi, ATR-FTIR spectroscopy and chemometrics application for analytical and kinetics characterization of adsorption of 1-butyl mercaptan (1-butanethiol) on nickel coated carbon nanofibers (CNFs), 48 (2016) 51-56.

[114] Y.N. Prajapati, N. Verma, Fixed bed adsorptive desulfurization of thiophene over Cu/Ni-dispersed carbon nanofiber, Fuel. 216 (2018) 381-389. https://doi.org/10.1016/j.fuel.2017.11.132.

[115] Y.N. Prajapati, N. Verma, Adsorptive desulfurization of diesel oil using nickel nanoparticle-doped activated carbon beads with/without carbon nanofibers: Effects of adsorbate size and adsorbent texture, Fuel. 189 (2017) 186-194. https://doi.org/10.1016/j.fuel.2016.10.044.

[116] Y. Srithep, A. Javadi, S. Pilla, L. Turng, S. Gong, C. Clemons, J. Peng, Processing and characterization of recycled poly(ethylene terephthalate) blends with chain extenders, thermoplastic elastomer and/or poly(butylene adipate- co -terephthalate), Polym. Eng. Sci. 51 (2011) 1023-1032. DOI 10.1002/pen.21916

[117] M.A.S. Spinace, M.A. De Paoli, Characterization of poly(ethylene terephtalate) after multiple processing sycles, J. Appl. Polym. Sci. 80 (2001) 20-25. https://doi.org/10.1002/1097-4628(20010404)80:1<20::AID-APP1069>3.0.CO;2-S

[118] S.S. Pesetskii, B. Jurkowski, O. V Filimonov, V.N. Koval, V. V Golubovich, PET/PC blends : effect of chain extender and impact strength modifier on their structure and properties, J. Appl. Polym. Sci. 119 (2010) 225-234. https://doi.org/10.1002/app.32532.

[119] F. Khoffi, N. Khenoussi, O. Harzallah, J. Drean, Mechanical behavior of polyethylene terephthalate/copper composite filament, Physics Procedia 21 (2011) 240-245. https://doi.org/10.1016/j.phpro.2011.11.001.

[120] D. Montgomery, Chapter 5, in: Design and Analysis of Experiments, 8th ed., Wiley, Hoboken NJ, 2013, pp. 183-232.

[121] B. Mishra, M. Kumar Gupta, Use of randomly oriented polyethylene terephthalate (PET) fiber in combination with fly ash in subgrade of flexible pavement, Constr. Build. Mater. 190 (2018) 95-107. https://doi.org/10.1016/j.conbuildmat.2018.09.074.

[122] M. Zhang, F.L.P. Resende, A. Moutsoglou, D.E. Raynie, Pyrolysis of lignin extracted from prairie cordgrass, aspen, and Kraft lignin by Py-GC/MS and TGA/FTIR, J. Anal. Appl. Pyrolysis. 98 (2012) 65-71. https://doi.org/10.1016/j.jaap.2012.05.009.

[123] R.P. Wool, X.S. Sun, Lignin polymers and composites, in: Bio-Based Polymers and Composites, AP Academic Press, 2005. https://doi.org/10.1016/B978-012763952-9/50017-4.

[124] C. Mohabeer, L. Reyes, L. Abdelouahed, S. Marcotte, B. Taouk, Investigating catalytic de-oxygenation of cellulose , xylan and lignin bio-oils using HZSM-5 and Fe-HZSM-5, J. Anal. Appl. Pyrolysis. 137 (2019) 118-127.

[125] P. Jönsson, P. Evangelopoulos, H. Persson, T. Han, N. Sophonrat, W. Yang, Evolution of sulfur during fast pyrolysis of sulfonated Kraft lignin, J. Anal. Appl. Pyrolysis. 133 (2018) 162-168. https://doi.org/10.1016/j.jaap.2018.04.006.

[126] S.L. Goertzen, K.D. Thériault, A.M. Oickle, A.C. Tarasuk, H.A. Andreas, Standardization of the Boehm titration. Part I. CO_2 expulsion and endpoint determination, Carbon 48 (2010) 1252-1261. https://doi.org/10.1016/j.carbon.2009.11.050.

[127] A.M. Oickle, S.L. Goertzen, K.R. Hopper, Y.O. Abdalla, H.A. Andreas, Standardization of the Boehm titration: Part II. Method of agitation, effect of filtering and dilute titrant, Carbon 48 (2010) 3313-3322. https://doi.org/10.1016/j.carbon.2010.05.004.

[128] C. Chen, L. Wang, Y. Huang, Ultrafine electrospun fibers based on stearyl stearate/polyethylene terephthalate composite as form stable phase change materials, Chem. Eng. J. 150 (2009) 269-274. https://doi.org/10.1016/j.cej.2009.03.007.

[129] J. Hao, G. Lei, Z. Li, L. Wu, Q. Xiao, L. Wang, A novel polyethylene terephthalate nonwoven separator based on electrospinning technique for lithium ion battery, J. Memb. Sci. 428 (2013) 11-16. https://doi.org/10.1016/j.memsci.2012.09.058.

[130] A. Hadjizadeh, A. Ajji, M.N. Bureau, Nano/micro electro-spun polyethylene terephthalate fibrous mat preparation and characterization, J. Mech. Behav. Biomed. Mater. 4 (2011) 340-351. https://doi.org/10.1016/j.jmbbm.2010.10.014.

[131] C. Salas, M. Ago, L. a. Lucia, O.J. Rojas, Synthesis of soy protein-lignin nanofibers by solution electrospinning, React. Funct. Polym. 85 (2014) 221-227. https://doi.org/10.1016/j.reactfunctpolym.2014.09.022.

[132] I. Dallmeyer, F. Ko, J.F. Kadla, Correlation of elongational fluid properties to fiber diameter in electrospinning of softwood kraft lignin solutions, Ind. Eng. Chem. Res. 53 (2014) 2697-2705. https://doi.org/10.1021/ie403724y.

[133] I.M. Morrison, D. Stewart, Plant cell wall fragments released on solubilisation in trifluoroacetic acid, Phytochemistry. 49 (1998) 1555-1563. https://doi.org/10.1016/S0031-9422(98)00244-1.

[134] D. Dong, J. Sun, F. Huang, Q. Gao, Y. Wang, R. Li, Using trifluoroacetic acid to pretreat lignocellulosic biomass, Biomass and Bioenergy. 33 (2009) 1719-1723. https://doi.org/10.1016/j.biombioe.2009.07.013.

[135] N. Poirier, S. Derenne, J. Balesdent, a. Mariotti, D. Massiot, C. Largeau, Isolation and analysis of the non-hydrolysable fraction of a forest soil and an arable soil (Lacadée, southwest France), Eur. J. Soil Sci. 54 (2003) 243-255. https://doi.org/10.1046/j.1365-2389.2003.00520.x.

[136] G.F. Fanta, T.P. Abbott, A.I. Herman, R.C. Burr, W.M. Doane, Hydrolysis of wheat straw hemicellulose with trifluoroacetic acid. Fermentation of xylose with Pachysolen tannophilus., Biotechnol. Bioeng. 26 (1984) 1122-5. https://doi.org/10.1002/bit.260260916.

[137] B.V.M. Rodrigues, E.C. Ramires, R.P.O. Santos, E. Frollini, Ultrathin and nanofibers via room temperature electrospinning from trifluoroacetic acid solutions of untreated lignocellulosic sisal fiber or sisal pulp, J. Appl. Polym. Sci. 132 (2015) 41826. https://doi.org/10.1002/app.41826.

[138] R.P.O. Santos, B.V.M. Rodrigues, E.C. Ramires, A.C. Ruvolo-Filho, E. Frollini, Bio-based materials from the electrospinning of lignocellulosic sisal fibers and recycled PET, Ind. Crops Prod. 72 (2015) 1-8. https://doi.org/10.1016/j.indcrop.2015.01.024.

[139] S.Y. Gu, J. Ren, G.J. Vancso, Process optimization and empirical modeling for electrospun polyacrylonitrile (PAN) nanofiber precursor of carbon nanofibers, Eur. Polym. J. 41 (2005) 2559-2568. https://doi.org/10.1016/j.eurpolymj.2005.05.008.

[140] Y. Li, Z. Huang, Y. Lu, Electrospinning of nylon-6,66,1010 terpolymer, Eur. Polym. J. 42 (2006) 1696-1704. https://doi.org/10.1016/j.eurpolymj.2006.02.002.

[141] C.J. Thompson, G.G. Chase, A.L. Yarin, D.H. Reneker, Effects of parameters on nanofiber diameter determined from electrospinning model, Polymer. 48 (2007) 6913-6922. https://doi.org/10.1016/j.polymer.2007.09.017.

[142] A. Awal, M. Sain, M. Chowdhury, Preparation of cellulose-based nano-composite fibers by electrospinning and understanding the effect of processing parameters, Compos. Part B Eng. 42 (2011) 1220-1225. https://doi.org/10.1016/j.compositesb.2011.02.011.

[143] P. Heikkilä, A. Harlin, Parameter study of electrospinning of polyamide-6, Eur. Polym. J. 44 (2008) 3067-3079. https://doi.org/10.1016/j.eurpolymj.2008.06.032.

[144] J.Y. Park, I.H. Lee, G.N. Bea, Optimization of the electrospinning conditions for preparation of nanofibers from polyvinylacetate (PVAc) in ethanol solvent, J. Ind. Eng. Chem. 14 (2008) 707-713. https://doi.org/10.1016/j.jiec.2008.03.006.

[145] B. Cramariuc, R. Cramariuc, R. Scarlet, L.R. Manea, I.G. Lupu, O. Cramariuc, Fiber diameter in electrospinning process, J. Electrostat. 71 (2013) 189-198. https://doi.org/10.1016/j.elstat.2012.12.018.

[146] L. Kong, G.R. Ziegler, Quantitative relationship between electrospinning parameters and starch fiber diameter, Carbohydr. Polym. 92 (2013) 1416-1422. https://doi.org/10.1016/j.carbpol.2012.09.026.

[147] O.S. Yördem, M. Papila, Y.Z. Menceloğlu, Effects of electrospinning parameters on polyacrylonitrile nanofiber diameter: An investigation by response surface methodology, Mater. Des. 29 (2008) 34-44. https://doi.org/10.1016/j.matdes.2006.12.013.

[148] K. Minu, K.K. Jiby, V.V.N. Kishore, Isolation and purification of lignin and silica from the black liquor generated during the production of bioethanol from rice straw, Biomass and Bioenergy. 39 (2012) 210-217. https://doi.org/10.1016/j.biombioe.2012.01.007.

[149] M. Azadfar, A.H. Gao, S. Chen, Structural characterization of lignin: A potential source of antioxidants guaiacol and 4-vinylguaiacol., Int. J. Biol. Macromol. 75 (2015) 58-66. https://doi.org/10.1016/j.ijbiomac.2014.12.049.

[150] M. Alekhina, O. Ershova, A. Ebert, S. Heikkinen, H. Sixta, Softwood kraft lignin for value-added applications: Fractionation and structural characterization, Ind. Crops Prod. 66 (2015) 220-228. https://doi.org/10.1016/j.indcrop.2014.12.021.

[151] R.K. Sharma, J.B. Wooten, V.L. Baliga, X. Lin, W. Geoffrey Chan, M.R. Hajaligol, Characterization of chars from pyrolysis of lignin, Fuel. 83 (2004) 1469-1482. https://doi.org/10.1016/j.fuel.2003.11.015.

[152] M. Djebara, J.P. Stoquert, M. Abdesselam, D. Muller, A.C. Chami, FTIR analysis of polyethylene terephthalate irradiated by MeV He+, Nucl. Instruments Methods Phys. Res. Sect. B Beam Interact. with Mater. Atoms. 274 (2012) 70-77. https://doi.org/10.1016/j.nimb.2011.11.022.

[153] H. Watanabe, K. Shimomura, K. Okazaki, Effect of high CO_2 concentration on char formation through mineral reaction during biomass pyrolysis, Proc. Combust. Inst. 34 (2013) 2339-2345. https://doi.org/10.1016/j.proci.2012.07.048.

[154] A. Mancera, V. Fierro, A. Pizzi, S. Dumarçay, P. Gérardin, J. Velásquez, Physicochemical characterisation of sugar cane bagasse lignin oxidized by hydrogen peroxide, Polymer Degrad. Stab. 95 (2010) 470-476. https://doi.org/10.1016/j.polymdegradstab.2010.01.012.

[155] A. García, A. Toledano, L. Serrano, I. Egüés, M. González, F. Marín, J. Labidi, Characterization of lignins obtained by selective precipitation, Sep. Purif. Technol. 68 (2009) 193-198. https://doi.org/10.1016/j.seppur.2009.05.001.

[156] USA National Institute of Standards and Technology. https://webbook.nist.gov/cgi/cbook.cgi?ID=C76051&Mask=80#IR-Spec, (accessed on 28/05/2020).

[157] J.M. Andanson, S.G. Kazarian, In situ ATR-FTIR spectroscopy of poly(ethylene terephthalate) subjected to high-temperature methanol, Macromol. Symp. 265 (2008) 195-204. https://doi.org/10.1002/masy.200850521.

[158] H. Marsh, F. Rodríguez-Reinoso, Chapter 5, in: Activated Carbon, 1st ed., Elsevier, 2006, pp. 243-321. https://doi.org/10.1016/b978-008044463-5/50019-4.

[159] R.M.R. Wellen, E.L. Canedo, Complex cold crystallisation peaks in PET/PS blends, Polym. Test. 41 (2015) 26-32.

[160] A. Tejado, C. Pen, J. Labidi, J.M. Echeverria, I. Mondragon, Physico-chemical characterization of lignins from different sources for use in phenol-formaldehyde resin synthesis, Bioresour. Technol. 98 (2007) 1655-1663. https://doi.org/10.1016/j.biortech.2006.05.042.

[161] V.K. Thakur, M.K. Thakur, P. Raghavan, M.R. Kessler, Progress in green polymer composites from lignin for multifunctional applications: A review, ACS Sustain. Chem. Eng. 2 (2014) 1072-1092. https://doi.org/10.1021/sc500087z.

[162] S. Wang, Y. Li, H. Xiang, Z. Zhou, T. Chang, M. Zhu, Low cost carbon fibers from bio-renewable lignin/poly(lactic acid) (PLA) blends, Compos. Sci. Technol. 119 (2015) 20-25. https://doi.org/10.1515/hf-2017-0191.

[163] O. Gordobil, I. Egüés, R. Llano-ponte, J. Labidi, Physicochemical properties of PLA lignin blends, Polym. Degrad. Stab. 108 (2014) 330-338. https://doi.org/10.1016/j.polymdegradstab.2014.01.002.

[164] T. Chen, J. Zhang, J. Wu, Kinetic and energy production analysis of pyrolysis of lignocellulosic biomass using a three-parallel Gaussian reaction model, Bioresour. Technol. 211 (2016) 502-508. https://doi.org/10.1016/j.biortech.2016.03.091.

[165] J. Kim, K.-H. Kim, E.E. Kwon, Enhanced thermal cracking of VOCs evolved from the thermal degradation of lignin using CO_2, Energy. 100 (2016) 51-57. https://doi.org/10.1016/j.energy.2016.01.075.

[166] B. Chin, L. Fui, S. Yusup, A. Al Shoaibi, Kinetic studies of co-pyrolysis of rubber seed shell with high density polyethylene using thermogravimetric approach, Energy Convers. Manag. 87 (2014) 746-753. https://doi.org/10.1016/j.enconman.2014.07.043.

[167] A. Brems, J. Baeyens, J. Beerlandt, R. Dewil, Thermogravimetric pyrolysis of waste polyethylene-terephthalate and polystyrene: A critical assessment of kinetics modelling, Resour. Conserv. Recycl. 55 (2011) 772-781. https://doi.org/10.1016/j.resconrec.2011.03.003.

[168] K. Ko, A. Rawal, V. Sahajwalla, Analysis of thermal degradation kinetics and carbon structure changes of co-pyrolysis between macadamia nut shell and PET using thermogravimetric analysis and 13 C solid state nuclear magnetic resonance, Energy Convers. Manag. 86 (2014) 154-164. https://doi.org/10.1016/j.enconman.2014.04.060.

[169] J.S. Ye, Z.T. Liu, C.C. Lai, C.T. Lo, C.L. Lee, Diameter effect of electrospun carbon fiber support for the catalysis of Pt nanoparticles in glucose oxidation, Chem. Eng. J. 283 (2015) 304-312. https://doi.org/10.1016/j.cej.2015.07.071.

[170] J.H. He, Y.Q. Wan, L. Xu, Nano-effects, quantum-like properties in electrospun nanofibers, chaos, solitons and fractals. Chaos Solitons Fractals 33 (2007) 26-37. https://doi.org/10.1016/j.chaos.2006.09.023.

[171] S. Mazinani, A. Ajji, C. Dubois, Fundamental study of crystallization, orientation, and electrical conductivity of electrospun PET/carbon nanotube nanofibers, J. Polym. Sci. Part B Polym. Phys. 48 (2010) 2052-2064. https://doi.org/10.1002/polb.22085.

[172] D. Thomas, C. Schick, P. Cebe, Novel method for fast scanning calorimetry of electrospun fibers, Thermochim. Acta. 667 (2018) 65-72. https://doi.org/10.1016/j.tca.2018.07.001.

[173] S. Dong, Y. Jia, X. Xu, J. Luo, J. Han, X. Sun, Crystallization and properties of poly(ethylene terephthalate)/layered double hydroxide nanocomposites, J. Colloid Interface Sci. 539 (2019) 54-64. https://doi: 10.1016/j.jcis.2018.12.030.

[174] P. Sun, H. Lu, W. Zhang, H. Wu, S. Sun, X. Liu, Poly(ethylene terephthalate): Rubbish could be low cost anode material of lithium ion battery, Solid State Ionics. 317 (2018) 164-169. https://doi.org/10.1016/j.ssi.2018.01.024.

[175] H. Marsh, F. Rodriquez-Reinoso, Chapter 4, in: Activated Carbon, 1st ed, Elsevier, 2006, pp. 143-242. https://doi.org/10.1016/B978-0-08-044463-5.50017-0.

[176] A. Ghosh, C. do A. Razzino, A. Dasgupta, K. Fujisawa, L.H.S. Vieira, S. Subramanian, R.S. Costa, A.O. Lobo, O.P. Ferreira, J. Robinson, M. Terrones, H. Terrones, B.C. Viana, Structural and electrochemical properties of babassu coconut mesocarp-generated activated carbon and few-layer graphene, Carbon 145 (2019) 175-186. https://doi.org/10.1016/j.carbon.2018.12.114.

[177] P. Li, T.J. Zhao, J.H. Zhou, Z.J. Sui, Y.C. Dai, W.K. Yuan, Characterization of carbon nanofiber composites synthesized by shaping process, Carbon 43 (2005) 2701-2710. https://doi.org/10.1016/j.carbon.2005.05.038.

[178] S. Leyva-García, E. Morallón, D. Cazorla-Amorós, F. Béguin, D. Lozano-Castelló, New insights on electrochemical hydrogen storage in nanoporous carbons by in situ Raman spectroscopy, Carbon 69 (2014) 401-408. https://doi.org/10.1016/j.carbon.2013.12.042.

[179] T.A. Saleh, G.I. Danmaliki, Adsorptive desulfurization of dibenzothiophene from fuels by rubber tyres-derived carbons: Kinetics and isotherms evaluation, Process Saf. Environ. Prot. 102 (2016) 9-19. https://doi.org/10.1016/j.psep.2016.02.005.

[180] X. Li, H. Zhu, C. Liu, P. Yuan, Z. Lin, J. Yang, Y. Yue, Z. Bai, T. Wang, X. Bao, Synthesis, modification, and application of hollow mesoporous carbon submicrospheres for adsorptive desulfurization, Ind. Eng. Chem. Res. 57 (2018) 15020-15030. https://doi.org/10.1021/acs.iecr.8b02780.

[181] T.A. Saleh, G.I. Danmaliki, Influence of acidic and basic treatments of activated carbon derived from waste rubber tires on adsorptive desulfurization of thiophenes, J. Taiwan Inst. Chem. Eng. 60 (2016) 460-468. https://doi.org/10.1016/j.jtice.2015.11.008.

[182] Z.C. Kampouraki, D.A. Giannakoudakis, K.S. Triantafyllidis, E.A. Deliyanni, Catalytic oxidative desulfurization of a 4,6-DMDBT containing model fuel by metal-free activated carbons: the key role of surface chemistry, Green Chem. 21 (2019) 6685-6698. https://doi.org/10.1039/c9gc03234g.

[183] H. Marsh, F. Rodríguez-Reinoso, Chaper 6, in: Activated Carbon, 1st ed. Elsevier, 2006, pp. 322-365. https://doi.org/10.1016/B978-0-08-044463-5.50020-0.

[184] A.M. Soliman, H.M. Elwy, T. Thiemann, Y. Majedi, F.T. Labata, N.A.F. Al-Rawashdeh, Removal of Pb(II) ions from aqueous solutions by sulphuric acid-treated palm tree leaves, J. Taiwan Inst. Chem. Eng. 58 (2016) 264-273. https://doi.org/10.1016/j.jtice.2015.05.035.

[185] S.A. Ganiyu, K. Alhooshani, K.O. Sulaiman, M. Qamaruddin, I.A. Bakare, A. Tanimu, T.A. Saleh, Influence of aluminium impregnation on activated carbon for enhanced desulfurization of DBT at ambient temperature: Role of surface acidity and textural properties, Chem. Eng. J. 303 (2016) 489-500. https://doi.org/10.1016/j.cej.2016.06.005.

[186] R.N. Fallah, S. Azizian, G. Reggers, R. Carleer, S. Schreurs, J. Ahenach, V. Meynen, J. Yperman, Effect of aromatics on the adsorption of thiophenic sulfur compounds from model diesel fuel by activated carbon cloth, Fuel Process. Technol. 119 (2014) 278-285. https://doi.org/10.1016/j.fuproc.2013.11.016.

[187] Z. Yu, D. Wang, Y. Yang, X. Meng, N. Liu, L. Shi, Excellent adsorption performance of dibenzothiophene on functionalized low-cost activated carbons with different oxidation methods, Environ. Technol. 40 (2019) 1686-1696. https://doi.org/10.1080/09593330.2018.1427802.

[188] M. Seredych, E. Deliyanni, T.J. Bandosz, Role of microporosity and surface chemistry in adsorption of 4,6-dimethyldibenzothiophene on polymer-derived activated carbons, Fuel. 89 (2010) 1499-1507. https://doi.org/10.1016/j.fuel.2009.09.032.

[189] C.O. Ania, T.J. Bandosz, Importance of structural and chemical heterogeneity of activated carbon surfaces for adsorption of dibenzothiophene, Langmuir. 21 (2005) 7752-7759. https://doi.org/10.1021/la050772e.

[190] K.S. Triantafyllidis, E.A. Deliyanni, Desulfurization of diesel fuels: Adsorption of 4,6-DMDBT on different origin and surface chemistry nanoporous activated carbons, Chem. Eng. J. 236 (2014) 406-414. https://doi.org/10.1016/j.cej.2013.09.099.

[191] T. Nunthaprechachan, S. Pengpanich, M. Hunsom, Adsorptive desulfurization of dibenzothiophene by sewage sludge-derived activated carbon, Chem. Eng. J. 228 (2013) 263-271. https://doi.org/10.1016/j.cej.2013.04.067.

[192] R.N. Fallah, S. Azizian, Removal of thiophenic compounds from liquid fuel by different modified activated carbon cloths, Fuel Process. Technol. 93 (2012) 45-52. https://doi.org/10.1016/j.fuproc.2011.09.012.

[193] Q. Wang, X. Liang, W. Qiao, C. Liu, X. Liu, L. Zhan, L. Ling, Preparation of polystyrene-based activated carbon spheres with high surface area and their adsorption to dibenzothiophene, Fuel Process. Technol. 90 (2009) 381-387. https://doi.org/10.1016/j.fuproc.2008.10.008.

[194] S. Kumagai, H. Ishizawa, Y. Toida, Influence of solvent type on dibenzothiophene adsorption onto activated carbon fiber and granular coconut-shell activated carbon, Fuel. 89 (2010) 365-371. https://doi.org/10.1016/j.fuel.2009.08.013.

[195] S.A. Ganiyu, O.O. Ajumobi, S.A. Lateef, K.O. Sulaiman, I.A. Bakare, M. Qamaruddin, K. Alhooshani, Boron-doped activated carbon as efficient and selective adsorbent for ultra-deep desulfurization of 4,6-dimethyldibenzothiophene, Chem. Eng. J. 321 (2017) 651-661. https://doi.org/10.1016/j.cej.2017.03.132.

[196] N.A. Khan, H.J. An, D.K. Yoo, S.H. Jhung, Polyaniline-derived porous carbons: Remarkable adsorbent for removal of various hazardous organics from both aqueous and non-aqueous media, J. Hazard. Mater. 360 (2018) 163-171. https://doi.org/10.1016/j.jhazmat.2018.08.001.

[197] J.A. Arcibar-Orozco, A.A. Acosta-Herrera, J.R. Rangel-Mendez, Simultaneous desulfuration and denitrogenation of model diesel fuel by Fe-Mn microwave modified activated carbon: Iron crystalline habit influence on adsorption capacity, J. Clean. Prod. 218 (2019) 69-82. https://doi.org/10.1016/j.jclepro.2019.01.202.

[198] C. Shalaby, X. Ma, A. Zhou, C. Song, Preparation of organic sulfur adsorbent from coal for adsorption of dibenzothiophene-type compounds in diesel fuel, Energy and Fuels. 23 (2009) 2620-2627. https://doi.org/10.1021/ef801135t.

[199] E. Deliyanni, M. Seredych, T.J. Bandosz, Interactions of 4,6-dimethyldibenzothiophene with the surface of activated carbons, Langmuir. 25 (2009) 9302-9312. https://doi.org/10.1021/la900854x.

[200] D. Iruretagoyena, K. Bikane, N. Sunny, H. Lu, S.G. Kazarian, D. Chadwick, R. Pini, N. Shah, Enhanced selective adsorption desulfurization on CO2 and steam treated activated carbons: Equilibria and kinetics, Chem. Eng. J. 379 (2020) 122356. https://doi.org/10.1016/j.cej.2019.122356.

[201] E.S. Moosavi, S.A. Dastgheib, R. Karimzadeh, Adsorption of thiophenic compounds from model diesel fuel using copper and nickel impregnated activated carbons, Energies. 5 (2012) 4233-4250. https://doi.org/10.3390/en5104233.

[202] A.A. Iravani, K. Gunda, F.T.T. Ng, Adsorptive removal of refractory sulfur compounds by tantalum oxide modified activated carbons, AIChE J. 63 (2017) 5044-5053. https://doi.org/10.1002/aic.15852.

[203] W. Choi, I. Lahiri, R. Seelaboyina, Y.S. Kang, Synthesis of graphene and its applications: A review, Crit. Rev. Solid State Mater. Sci. 35 (2010) 52-71. https://doi.org/10.1080/10408430903505036.

[204] H.S. Song, C.H. Ko, W. Ahn, B.J. Kim, E. Croiset, Z. Chen, S.C. Nam, Selective dibenzothiophene adsorption on graphene prepared using different methods, Ind. Eng. Chem. Res. 51 (2012) 10259-10264. https://doi.org/10.1021/ie301209c.

[205] M. Seredych, J. Rawlins, T.J. Bandosz, Investigation of the thermal regeneration efficiency of activated carbons used in the desulfurization of model diesel fuel, Ind. Eng. Chem. Res. 50 (2011) 14097-14104. https://doi.org/10.1021/ie202159a.

[206] M. Yu, Z. Li, Q. Ji, S. Wang, D. Su, Y.S. Lin, Effect of thermal oxidation of activated carbon surface on its adsorption towards dibenzothiophene, Chem. Eng. J. 148 (2009) 242-247. https://doi.org/10.1016/j.cej.2008.08.018.

[207] H. Song, J. Gao, X. Chen, J. He, C. Li, Removal of thiophenic sulfur compounds from oil using chlorinated polymers and Lewis acid mixture via adsorption and Friedel-crafts alkylation reaction, Chinese J. Chem. Eng. 22 (2014) 713-720. https://doi.org/10.1016/S1004-9541(14)60093-8.

[208] J. Wen, X. Han, H. Lin, Y. Zheng, W. Chu, A critical study on the adsorption of heterocyclic sulfur and nitrogen compounds by activated carbon: Equilibrium, kinetics and thermodynamics, Chem. Eng. J. 164 (2010) 29-36. https://doi.org/10.1016/j.cej.2010.07.068.

[209] P. Atkins, J. De Paula, Chapter 23 in: Physical Chemistry, 9th ed., W. H. Freeman and Company, New York, 2010, pp. 876-908.

[210] T.A. Saleh, Simultaneous adsorptive desulfurization of diesel fuel over bimetallic nanoparticles loaded on activated carbon, J. Clean. Prod. 172 (2018) 2123-2132. https://doi.org/10.1016/j.jclepro.2017.11.208.

[211] T.A. Saleh, S.A. Al-Hammadi, A. Tanimu, K. Alhooshani, Ultra-deep adsorptive desulfurization of fuels on cobalt and molybdenum nanoparticles loaded on activated carbon derived from waste rubber, J. Colloid Interface Sci. 513 (2018) 779-787. https://doi.org/10.1016/j.jcis.2017.11.076.

[212] B. Cabal, C.O. Ania, J.B. Parra, J.J. Pis, Kinetics of naphthalene adsorption on an activated carbon: Comparison between aqueous and organic media, Chemosphere. 76 (2009) 433-438. https://doi.org/10.1016/j.chemosphere.2009.04.002.

[213] C. Valderrama, X. Gamisans, X. de las Heras, A. Farrán, J.L. Cortina, Sorption kinetics of polycyclic aromatic hydrocarbons removal using granular activated carbon: Intraparticle diffusion coefficients, J. Hazard. Mater. 157 (2008) 386-396. https://doi.org/10.1016/j.jhazmat.2007.12.119.

[214] Y.S. Al-Degs, M.A. Al-Ghouti, Influence of diesel acidification on dibenzothiophene removal: A new desulfurization practice, Sep. Purif. Technol. 139 (2015) 1-4. https://doi.org/10.1016/j.seppur.2014.10.027.

[215] D. Qu, X. Feng, N. Li, X. Ma, C. Shang, X.D. Chen, Adsorption of heterocyclic sulfur and nitrogen compounds in liquid hydrocarbons on activated carbons modified by oxidation: Capacity, selectivity and mechanism, RSC Adv. 6 (2016) 41982-41990. https://doi.org/10.1039/c6ra06108g.

[216] H. Farag, Selective adsorption of refractory sulfur species on active carbons and carbon based CoMo catalyst, J. Colloid Interface Sci. 307 (2007) 1-8. https://doi.org/10.1016/j.jcis.2006.11.024.

[217] J. Bu, G. Loh, C.G. Gwie, S. Dewiyanti, M. Tasrif, A. Borgna, Desulfurization of diesel fuels by selective adsorption on activated carbons: Competitive adsorption of polycyclic aromatic sulfur heterocycles and polycyclic aromatic hydrocarbons, Chem. Eng. J. 166 (2011) 207-217. https://doi.org/10.1016/j.cej.2010.10.063.

[218] A. Zhou, X. Ma, C. Song, Liquid-phase adsorption of multi-ring thiophenic sulfur compounds on carbon materials with different surface properties, J. Phys. Chem. B. 110 (2006) 4699-4707. https://doi.org/10.1021/jp0550210.

[219] G.I. Danmaliki, T.A. Saleh, Effects of bimetallic Ce/Fe nanoparticles on the desulfurization of thiophenes using activated carbon, Chem. Eng. J. 307 (2017) 914-927. https://doi.org/10.1016/j.cej.2016.08.143.

[220] L. Xiong, F.X. Chen, X.M. Yan, P. Mei, The adsorption of dibenzothiophene using activated carbon loaded with cerium, J. Porous Mater. 19 (2012) 713-719. https://doi.org/10.1007/s10934-011-9523-4.

[221] M.A. Al-Ghouti, Y.S. Al-Degs, A novel desulfurization practice based on diesel acidification prior to activated carbon adsorption, Korean J. Chem. Eng. 32 (2015) 685-693. https://doi.org/10.1007/s11814-014-0303-0.

[222] Z. Yu, X. Meng, N. Liu, L. Shi, A novel disposal approach of deactivated resin catalyst for methyl tert-butyl ether synthesis: Preparation of low-cost activated carbons with remarkable performance on dibenzothiophene adsorption, Fuel. 207 (2017) 47-55. https://doi.org/10.1016/j.fuel.2017.05.053.

[223] C. He, G. Men, B. Xu, J. Cui, J. Zhao, Phenolic resin-derived activated carbon-supported divalent metal as efficient adsorbents (M-C, M=Zn, Ni, or Cu) for dibenzothiophene removal, Environ. Sci. Pollut. Res. 24 (2017) 782-794. https://doi.org/10.1007/s11356-016-7795-6.

List of Publications

Svinterikos, E., Zuburtikudis, I., Al-Marzouqi, M., Fabricating carbon nanofibers from a lignin/r-PET blend: the synergy of mass ratio with the average fiber diameter, Appl. Nanosci. 10 (2019) 1331-1343. https://doi.org/10.1007/s13204-019-01235-7.

Svinterikos, E., Zuburtikudis, I., Al-Marzouqi, M., The nanoscale dimension determines the carbonization outcome of electrospun lignin/recycled-PET fibers, Chem. Eng. Sci. 202 (2019) 26-35. https://doi.org/10.1016/j.ces.2019.03.013.

Svinterikos, E., Zuburtikudis, I., Al-Marzouqi, M., Carbon nanomaterials for the adsorptive desulfurization of fuels, J. Nanotechnol. (2019) 2809867. https://doi.org/10.1155/2019/2809867.

Svinterikos, E., Zuburtikudis, I., Al-Marzouqi, M., Different carbon fibrous morphologies triggered by varying the average diameter of precursor electrospun fibers, J. Phys.: Conf. Ser. 1310 (2019) 012009. doi:10.1088/1742-6596/1310/1/012009.

Svinterikos, E., Zuburtikudis, I., Tailor-made electrospun nanofibers of biowaste lignin/recycled poly(ethylene terephthalate), J. Polym. Environ. 25 (2017) 465-478. DOI 10.1007/s10924-016-0806-3.

Svinterikos E, Zuburtikudis I, Carbon nanofibers from renewable bioresources (lignin) and a recycled commodity polymer [poly(ethylene terephthalate)]. J Appl. Polym. Sci 133 (2016) 43936. DOI: 10.1002/app.43936.